Carbon from Space: determining the biological controls on the ocean sink of CO_2 from satellites, in the Atlantic and Southern Ocean

Submitted by **Daniel John Ford** to the University of Exeter

as a thesis for the degree of

Doctor of Philosophy in Physical Geography

In June 2022

In collaboration with

Plymouth Marine Laboratory

I certify that all material in this thesis which is not my own work has been identified and that no material has previously been submitted and approved for the award of a degree by this or any other University.

Signature:…  ……

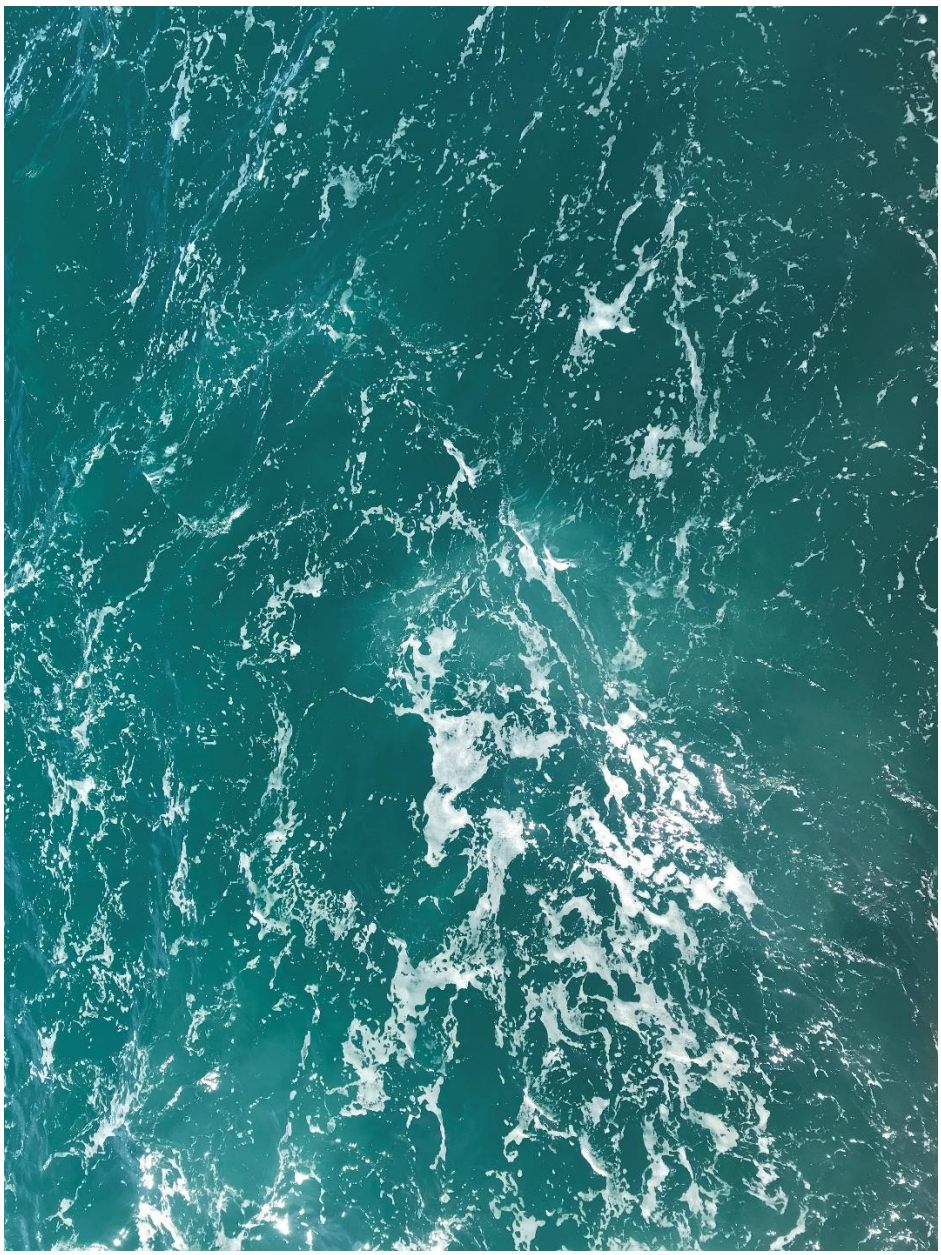

UNIVERSITY OF EXETER

NERC GW4+ Doctoral Training Partnership

PML | Plymouth Marine Laboratory

Abstract

Increasing anthropogenic carbon dioxide (CO_2) emissions to the atmosphere have partially been absorbed by the global oceans. The role which the plankton community contributes to this net CO_2 sink, and how it may change under climate change has been identified as a key issue to address within the United Nations decade of ocean science (2021-2030) Integrated Ocean Carbon Research (IOC-R) programme. This thesis sets out to explore how the net community production (NCP; the balance between photosynthesis and respiration) of the plankton community contributes to the variability in air-sea CO_2 flux in the South Atlantic Ocean.

In Chapter 2, NCP is shown to be accurately and precisely estimated from satellite measurements with respect to in situ observations. For this, weighted statistics are used to account for satellite, in situ and model uncertainties. The accuracy of satellite NCP could be improved by up to 40% by reducing uncertainties in net primary production (NPP). In Chapter 3, these satellite NCP observations were then used within a feed forward neural network scheme (SA-FNN) to extrapolate partial pressure of CO_2 in seawater ($pCO_{2\,(sw)}$) over space and time, which is a key component to estimating the CO_2 flux. NCP improved the accuracy and precision of $pCO_{2\,(sw)}$ fields compared to using chlorophyll *a* (Chl *a*); the primary pigment in phytoplankton which is often used as a proxy for the biological CO_2 drawdown. Compared to in situ observations, the seasonal variability in $pCO_{2\,(sw)}$ was improved using the SA-FNN in key areas such as the Amazon River plume and Benguela upwelling, which make large regional contributions to the air-sea CO_2 flux in the South Atlantic Ocean. In Chapter 4, these complete $pCO_{2\,(sw)}$ fields were used with a timeseries decomposition method to determine the drivers of air-sea CO_2 flux over seasonal, interannual and multi-year timescales. NCP was shown to correlate with the variability in CO_2 flux on a seasonal basis. At interannual and mutli-year timescales, NCP became a more important contributor to variability in CO_2 flux. This has not been previously analysed for this region.

Mesoscale eddies in the global ocean can modify the biological, physical, and chemical properties and therefore may modify the CO_2 flux. In Chapter 5, the cumulative CO_2 flux of 67 long lived eddies (lifetimes > 1 year) was estimated

using Lagrangian tracking with satellite observations. The eddies could enhance the CO_2 flux into the South Atlantic Ocean by up to 0.08 %, through eddy modification of biological and physical properties. Collectively this research has shown that the plankton community plays a more significant role in modulating the air-sea CO_2 flux in the South Atlantic Ocean, which has significant implications for the global ocean.

Table of Contents

Acknowledgements

Firstly, a massive thank you to my supervisors Gavin Tilstone, Jamie Shutler, Vas Kitidis, and Katy Sheen – you have always provided encouragement and pushed me to produce a higher quality of work than I thought was possible, especially throughout a pandemic. Without your support, this PhD would not have been as successful and enjoyable as it has been. Secondly, I must thank all my friends who have celebrated the achievements and helped me through the tougher times of the last 4 years. You have all encouraged and supported, and I am truly grateful! Finally, I thank my family who never had a doubt that I would succeed and finish this PhD, when I may have thought otherwise!

This research was funded by a NERC GW4+ Doctoral Training Partnership studentship from the UK Natural Environment Research Council (NE/L002434/1) which I am extremely grateful for. I must thank Emmi Palk and Sara Tonge for their support, and for working tirelessly to provide extensions to the GW4+ students due to the pandemic.

Acknowledgements for Chapter 2

DF was supported by a GW4+ Doctoral Training Partnership studentship from the UK Natural Environment Research Council (NERC; NE/L002434/1). GT was supported by the AMT4SentinelFRM (ESRIN/RFQ/3-14457/16/I-BG) and AMT4OceanSatFlux (4000125730/18/NL/FF/gp) contracts from the European Space Agency and by NERC National Capability funding to Plymouth Marine Laboratory for the Atlantic Meridional Transect (AMT). PL was supported by SPBU travel grant # 41128672. GT and MK were also funded by NERC International Opportunity Fund Grant Satellite estimates of marine net community production in the South Atlantic from Sentinel-3 (SemSAS; NE/P00878X/1). MK was partially funded by P&D ANP/BRASOIL Project no. 48610.011013/2014-66; Dalio Foundation Proj. Amazon Reefs. FB and MC were supported by four Oceanographic Institute of the University of São Paulo (IOUSP) projects (FAPESP 2015/01373-0; CNPq 442926/2015-4; FAPESP 2014/50820-7; CNPq 565060/2010-4) for the collection of the Chl *a* data used in the BRAZ dataset. We would like to thank the captain and crew of *RRS Discovery, RRS James Clark Ross and RRS James Cook* for conducting the AMTs. We also thank the Natural Environment Research Council Earth

Observation Data Acquisition and Analysis Service (NEODAAS) for use of the Linux cluster to process the MODIS-A satellite imagery. The altimeter products were produced by Ssalto/Duacs and distributed by AVISO+, with support from Cnes (https://www.aviso.altimetry.fr). The AMT is funded by NERC through its National Capability Long-term Single Centre Science Programme, Climate Linked Atlantic Sector Science (NE/R015953/1). This study contributes to the international IMBeR project and is contribution number 354 of the AMT programme. We graciously thank Giorgio Dall'Olmo for providing the AMT AC-S Chl a data.

Acknowledgements for Chapter 3

DF was supported by a NERC GW4+ Doctoral Training Partnership studentship from the UK Natural Environment Research Council (NERC; NE/L002434/1). GT and VK were supported by the AMT4OceanSatFlux (4000125730/18/NL/FF/gp) contract from the European Space Agency and NERC National Capability funding to Plymouth Marine Laboratory for the Atlantic Meridional Transect (CLASS-AMT).

We would like to thank the captain and crew of *RRS Discovery, RRS James Clark Ross* and *RRS James Cook* for conducting the Atlantic Meridional Transects (AMT). We also thank the Natural Environment Research Council Earth Observation Data Acquisition and Analysis Service (NEODAAS) for use of the Linux cluster to process the MODIS-A satellite imagery. We also thank Giorgio Dall'Olmo for collecting the *in situ* Chl *a* data on AMT 22, and Pablo Serret and Jose Lozano for collecting the *in situ* NCP data on AMTs 22 and 23.

The Surface Ocean CO_2 Atlas (SOCAT) is an international effort, endorsed by the International Ocean Carbon Coordination Project (IOCCP), the Surface Ocean Lower Atmosphere Study (SOLAS) and the Integrated Marine Biosphere Research (IMBeR) program, to deliver a uniformly quality-controlled surface ocean CO_2 database. The many researchers and funding agencies responsible for the collection of data and quality control are thanked for their contributions to SOCAT. The AMT is funded by NERC through its National Capability Long-term Single Centre Science Programme, Climate Linked Atlantic Sector Science (NE/R015953/1). This study contributes to the international IMBeR project and is contribution number 366 of the AMT programme. We thank Jonathan Sharp

and an anonymous reviewer for their valuable comments that improved the final manuscript.

Acknowledgements for Chapter 4

Daniel J. Ford was supported by a NERC GW4+ Doctoral Training Partnership studentship from the UK Natural Environment Research Council (NERC; NE/L002434/1). Gavin H. Tilstone and Vassilis Kitidis were supported by the AMT4CO_2Flux (4000125730/18/NL/FF/gp) contract from the European Space Agency and by the NERC National Capability funding to Plymouth Marine Laboratory for the Atlantic Meridional Transect (CLASS-AMT). The Atlantic Meridional Transect is funded by the UK Natural Environment Research Council through its National Capability Long-term Single Centre Science Programme, Climate Linked Atlantic Sector Science (grant number NE/R015953/1). This study contributes to the international IMBeR project and is contribution number 372 of the AMT programme. We also thank the Natural Environment Research Council Earth Observation Data Acquisition and Analysis Service (NEODAAS) for use of the Linux cluster to process the MODIS-A satellite imagery. We thank two anonymous reviewers for their comments, which have improved the manuscript.

The Surface Ocean CO_2 Atlas (SOCAT) is an international effort, endorsed by the International Ocean Carbon Coordination Project (IOCCP), the Surface Ocean Lower Atmosphere Study (SOLAS) and the Integrated Marine Biosphere Research (IMBeR) program, to deliver a uniformly quality-controlled surface ocean CO_2 database. The many researchers and funding agencies responsible for the collection of data and quality control are thanked for their contributions to SOCAT.

Acknowledgements for Chapter 5

DJF was supported by a NERC GW4+ Doctoral Training Partnership studentship from the UK Natural Environment Research Council (NERC; NE/L002434/1). GHT, VK and GD were supported by the AMT4CO2Flux (4000125730/18/NL/FF/gp) contract from the European Space Agency and by

the NERC National Capability funding to Plymouth Marine Laboratory for the Atlantic Meridional Transect (CLASS-AMT). The Atlantic Meridional Transect is funded by the UK Natural Environment Research Council through its National Capability Long-term Single Centre Science Programme, Climate Linked Atlantic Sector Science (grant number NE/R015953/1). This study contributes to the international IMBeR project and is contribution number 380 of the AMT programme. We also thank the Natural Environment Research Council Earth Observation Data Acquisition and Analysis Service (NEODAAS) for use of the Linux cluster to process the MODIS-A satellite imagery.

The Surface Ocean CO_2 Atlas (SOCAT) is an international effort, endorsed by the International Ocean Carbon Coordination Project (IOCCP), the Surface Ocean Lower Atmosphere Study (SOLAS) and the Integrated Marine Biosphere Research (IMBeR) program, to deliver a uniformly quality-controlled surface ocean CO_2 database. The many researchers and funding agencies responsible for the collection of data and quality control are thanked for their contributions to SOCAT. The altimetric Mesoscale Eddy Trajectories Atlas (META3.1exp DT) was produced by SSALTO/DUACS and distributed by AVISO+ (https://aviso.altimetry.fr) with support from CNES, in collaboration with IMEDEA (DOI: 10.24400/527896/a01-2021.001 for the META3.1exp DT allsat version and 10.24400/527896/a01-2021.002 for the META3.1exp DT twosat version)

Author Declaration

My thesis is presented as four research papers (two published, one under review, and one prepared for submission). All work has been the product of my planning and implementation, and I am the lead author on all the presented papers. The contributions from my supervisors and co-authors are described at the beginning of each chapter. Papers have been reformatted to provide a single editorial and referencing style, with figures embedded within the text.

List of definitions and abbreviations

ANTA	Antarctica
AMT	Atlantic Meridional Transect
APD	Absolute percentage difference
BATS	Bermuda Ocean Time Series
BENG	Benguela Current coastal upwelling
BODC	British Oceanographic Data Centre
BRAZ	Brazilian Current coastal
CARIACO	Carbon retention in a colored ocean site
CCDS	Copernicus Climate Data Store
CDOM	Coloured dissolved organic matter
Chl *a*	Chlorophyll a
CI	Color Index
CO_2	Carbon dioxide
CMEMS	Copernicus Marine Environmental Monitoring Service
CZCS	Coastal zone colour scanner
DIC	Dissolved Inorganic Carbon
DL	Daylength
DMSO	Di-methyl-sulphoxide
ECMWF	European Centre for Medium Range Weather Forecasts
ENSO	El Niño Southern Oscillation
EPTOMS	Earth Total Ozone Mapping Spectrometer
ESA	European Space Agency
ETRA	Eastern Tropical Atlantic
F	Air-sea CO_2 flux
fCO_2	Fugacity of CO_2
$fCO_{2\,(atm)}$	Fugacity of CO_2 in the atmosphere
$fCO_{2\,(sw)}$	Fugacity of CO_2 in seawater
FFN	Feed forward neural network
FKLD	Southwest Atlantic shelves
FORSA	Following Ocean Rings in the South Atlantic
FRM	Fiducial Reference Measurement
GO-SHIP	Global ocean ship-based hydrographic investigations program
HPLC	High Performance Liquid Chromatography
HOTS	Hawaii Ocean Timeseries

I_0	Daily surface PAR
IOC-R	Integrated Ocean Carbon Research
IPCC	Intergovernmental panel on climate change
ISAR	Infrared SST autonomous radiometer
k	Gas transfer velocity
K_d	Downwelling diffuse attenuation coefficient
Log-RMS	$\log_{10}$ root mean square difference
LUT	Look up table
M	Mean of $\log_{10}$ difference
MBL	Mass boundary layer
MEI	Multivariate ENSO Index
MERIS	Medium Resolution Imaging Spectroradiometer
MODIS-A	Moderate Resolution Imaging Spectroradiometer on Aqua
NAO	North Atlantic Oscillation
NASA	National Aeronautics and Space Administration
NCEP	National Centres for Environmental Prediction
NCP	Net community production
nL_w	Normalised water leaving radiance
NPP	Net primary production
O_2	Oxygen
O_2/Ar	Oxygen to Argon Ratio
OLCI	Ocean and Land Colour Instrument
PAR	Photosynthetically active radiation
P^B_m	Maximum photosynthetic rate
P^B_{opt}	Biomass specific optimum photosynthetic rate
pCO_2	Partial pressure of CO_2
$pCO_{2\ (atm)}$	Partial pressure of CO_2 in the atmosphere
$pCO_{2\ (sw)}$	Partial pressure of CO_2 in seawater
P-I	Photosynthesis-irradiance
PIRATA	Prediction and Research Moored Array in the Atlantic
PSM	Platt and Sathyendranath model
PUR	Photosynthetic usable radiation
R	Pearson correlation coefficient
R^2	Coefficient of determination
RMSD	Root mean square difference

r_{opt}	Optimal split
R_{rs}	Remote sensing reflectance
R_s	Spearman correlation coefficient
S	Standard deviation of $\log_{10}$ difference
SAM	Southern Annular Mode
SANT	Sub Antarctic
SA-FNN	South Atlantic feed forward neural network
SATL	South Atlantic Gyre
SeaWiFS	Sea Viewing Wide Field of View Sensor
SOCAT	Surface Ocean CO_2 Atlas
SOM	Self organising map
SOM-FNN	Self organising map feed forward neural network
SLHA	Sea level height anomaly
SSS	Sea surface salinity
S_t	Seasonal component
SST	Sea surface temperature
SSTC	South Subtropical Convergence
TA	Total Alkalinity
T_t	Interannual component
VGPM	Vertical generalized production model
VIIRS	Visible Infrared Imaging Radiometer Suites
WRM	Wavelength resolving model
WTRA	Western Tropical Atlantic
X_t	Initial timeseries
z	Depth
z_{eu}	Euphotic zone depth
α	CO_2 solubility
α^B	Initial slope of the light-dependent photosynthetic rate
a^*_{max}	Maximum phytoplankton Chl *a* -specific absorption coefficient
ΔpCO_2	Partial pressure of CO_2 difference between ocean and atmosphere.
Ɛa	Algorithm uncertainty
ƐC	Combined uncertainty
Ɛins	In situ uncertainty
ƐR	MODIS-A retrieval uncertainty
Ɛs	Spatial uncertainty

Φ_m	Maximum quantum yield for growth

List of Figures

List of Tables

Chapter 1: General Introduction

Since the industrial revolution, anthropogenic carbon dioxide (CO_2) emissions have resulted in a ~47 % increase in atmospheric CO_2 concentration from ~280 µatm in 1750 to ~410 µatm in 2019 (IPCC, 2021). As a result, global air temperatures have increased by 1.09 °C and sea surface temperatures have risen by 0.8 °C since 1850 (IPCC, 2021). This warming is leading to unprecedented change in the global climate, affecting the atmosphere, oceans, cryosphere and biospheres as outlined in the Intergovernmental Panel on Climate Change (IPCC) AR6 report (IPCC, 2021).

Terrestrial and oceanic ecosystems are a net sink for CO_2 having absorbed ~56 % of anthropogenic emissions between 1959 and 2019, of which the global ocean has absorbed 24 % and terrestrial land has drawn down 32 % (Friedlingstein et al., 2020). The oceans have absorbed CO_2 at a rate between 1 and 3.5 Pg C yr^{-1} (1 Pg=10^{15} g), and the rate appears to be increasing (Watson et al., 2020b; Friedlingstein et al., 2020; Landschützer et al., 2016). Future projections suggest that this absorption will continue to increase in the short term due to increasing atmospheric CO_2 concentrations effectively forcing more CO_2 into the oceans (IPCC, 2021), but the precise response of the ocean under reduced, or even decreasing, anthropogenic CO_2 emissions is currently unknown.

The long-term absorption of CO_2 into the oceans does not occur without negative effects. The long-term dissolution of CO_2 into the oceans is altering the marine carbonate chemistry of the ocean, resulting in a lowering of pH; and a decrease in carbonate ions; a process known as ocean acidification (Raven et al., 2005). Decreasing surface ocean pH, and carbonate ions, have negative impacts for calcifying organisms, such as corals and coccolithophores, which affects their ability to form calcium carbonate structures at lower pH (IPCC, 2021). The effect of decreasing seawater pH on other phytoplankton and the marine food web in general, is currently unknown (Dutkiewicz et al., 2015). Understanding the current drivers of the oceanic CO_2 sink, and predicting how these may change under future climate change scenarios, is pivotal to identifying the consequences of these changes on the ocean CO_2 sink (Aricò et al., 2021).

1.1 Air-sea gas exchange of CO_2

The air-sea gas exchange of CO_2 or the CO_2 flux (F), that collectively results in the ocean CO_2 sink, is controlled by the CO_2 concentration difference between the base ($[CO_{2\,(sw)}]$) and top ($[CO_{2\,(atm)}]$) of a thin mass boundary layer (MBL; 20-200 µm in thickness) at the sea surface (Fig. 1.1), alongside the gas transfer velocity (k). The CO_2 flux can therefore be expressed as:

$$F = k([[CO_{2\,(sw)}] - [CO_{2\,(atm)}]) \quad (1.1)$$

The CO_2 concentration in seawater is a function of the CO_2 solubility (α) and the fugacity of CO_2 (fCO_2). Therefore Eq. 1.1 can be rewritten in the form

$$F = k(\alpha_{sw} fCO_{2\,(sw)} - \alpha_{atm} fCO_{2\,(atm)}) \quad (1.2)$$

where the subscripts denote seawater (sw) and atmosphere (atm). The fCO_2 corrects the partial pressure of CO_2 (pCO_2) for the non-ideal behaviour of CO_2.

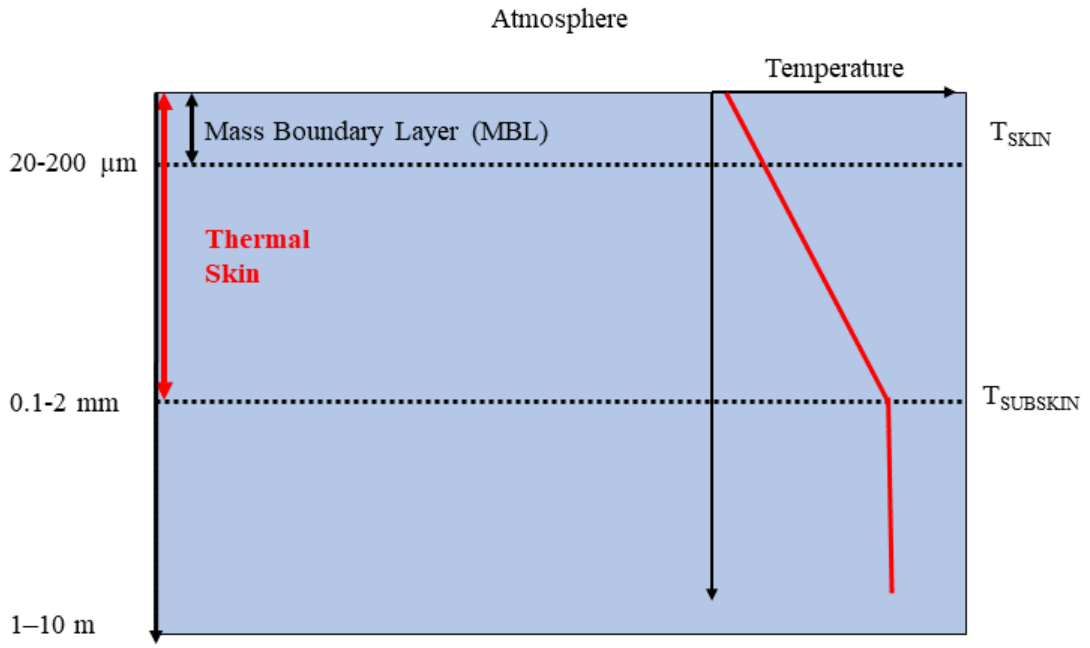

Figure 1.1 – Schematic of the ocean's surface, highlighting the mass boundary layer (MBL; black arrow) embedded within the thermal skin (red arrow). Depth profile on right side of schematic shows an idealised temperature profile from the air-sea interface to the sub skin temperature ($T_{SUBSKIN}$), highlighting the vertical temperature gradient. Exemplar depths of each idealised layer are shown on left of figure. Schematic developed from Donlon et al. (2007) and Woolf et al. (2016) and is not to scale.

fCO_2 and pCO_2 vary by <0.5% (Mcgillis and Wanninkhof, 2006) over the temperature range in the ocean, therefore fCO_2 is commonly substituted with pCO_2 such that Eq. 1.2 becomes:

$$\mathrm{F} = \mathrm{k}\left(\alpha_{\mathrm{sw}} pCO_{2\,(\mathrm{sw})} - \alpha_{\mathrm{atm}} pCO_{2\,(\mathrm{atm})}\right) \quad (1.3)$$

Another popular rearrangement of Eqs 1.2 and 1.3 ignores the differences between the solubilities at the base and top of the MBL, and uses only the solubility at the base (α_{sw}), resulting in

$$\mathrm{F} = \mathrm{k}\,\alpha_{\mathrm{sw}}(fCO_{2\,(\mathrm{sw})} - fCO_{2\,(\mathrm{atm})}) \quad (1.4)$$

and

$$\mathrm{F} = \mathrm{k}\,\alpha_{\mathrm{sw}}(pCO_{2\,(\mathrm{sw})} - pCO_{2\,(\mathrm{atm})}) \quad (1.5)$$

These formulations are commonly referred to as the “bulk” parameterisation of the CO_2 flux. Eqs 1.4 and 1.5 are also commonly condensed to the form

$$\mathrm{F} = \mathrm{k}\,\alpha_{\mathrm{sw}}\,\Delta fCO_2 \quad (1.6)$$

and

$$\mathrm{F} = \mathrm{k}\,\alpha_{\mathrm{sw}}\,\Delta pCO_2 \quad (1.7)$$

ΔfCO_2 is the difference in fugacity of CO_2 between the seawater and atmosphere, and ΔpCO_2 is the partial pressure of CO_2 difference.

The solubility of CO_2 is strongly dependent on temperature, and to a lesser extent salinity (Weiss, 1974), such that CO_2 is more soluble in colder, less saline waters. The MBL is embedded within the thermal skin layer (Fig. 1.1), where due to the cool skin (T_{SKIN}) (Donlon et al., 1999, 2002), vertical temperature gradients exist across the MBL (Woolf et al., 2016). Therefore, using only the sub skin temperature ($T_{SUBSKIN}$), and the resulting solubility, will introduce a bias in the CO_2 flux estimates, which can be substantial on the global scale (Watson et al., 2020b; Woolf et al., 2019). For accurate gas flux calculations, the solubility at the base and top of the MBL should be included, as in Eq. 1.2 and 1.3, as opposed to the commonly used expressions of Eq 1.4 – 1.7 which neglect this difference in solubilities. For this thesis, as fCO_2 and pCO_2 are similar for the temperature range found in the ocean (Mcgillis and

Wanninkhof, 2006), pCO_2 will be used, and therefore Eq. 1.3 is used for air-sea CO_2 flux calculations.

The air-sea CO_2 flux is also controlled by the gas transfer coefficient. Gas exchange is influenced by bubbles (Woolf, 1997), wave breaking (Woolf, 2005) and surface turbulence, which are typically linked to wind speed. The gas transfer coefficient is generally parameterised as a function of wind speed (Nightingale et al., 2000; Wanninkhof, 2014, 1992). Spatial and temporal variability in wind speeds will therefore also play a role in determining the air-sea CO_2 flux variability (Keppler and Landschützer, 2019; Takahashi et al., 2002; Wanninkhof and Triñanes, 2017), and a large concentration difference will not necessarily mean a high rate of exchange (Kitidis et al., 2019).

1.2 Controls on $pCO_{2\,(sw)}$ variability

The previous section described how the air-sea CO_2 flux is determined by the CO_2 concentration difference across the MBL and the gas transfer coefficient. The concentration of CO_2 in seawater is a function of the $pCO_{2\,(sw)}$ and the solubility, therefore $pCO_{2\,(sw)}$ variability is an important control on the CO_2 concentration. The atmospheric concentration of CO_2 is fairly homogenous spatially in comparison to the $pCO_{2\,(sw)}$, which shows seasonal and regional variability.

The global distribution of $pCO_{2\,(sw)}$ is spatially heterogenous, which is controlled and modulated by ocean physics and biological activity. Temperature is a dominant control, through the strong dependence on the solubility of CO_2 (Weiss, 1974), which leads to increased $pCO_{2\,(sw)}$ with increasing temperature. Biological activity in the surface waters, in the form of photosynthesis by phytoplankton and the respiration of the entire plankton community modifies the $pCO_{2\,(sw)}$. Photosynthesis, or net primary production (NPP), draws down CO_2 and nutrients to form organic carbon, which lowers $pCO_{2\,(sw)}$. Respiration releases CO_2 back into the seawater through the remineralisation of the fixed organic carbon, raising $pCO_{2\,(sw)}$. A varying proportion of the fixed organic carbon can be exported into the deeper ocean where it is remineralised back to CO_2 (Laws et al., 2000; Henson et al., 2011; Sarmiento and Gruber, 2004). The rate of NPP and respiration is seasonally and spatially variable and will be discussed in more detail in section 1.4.

The upwelling of deeper water masses into the surface waters brings cooler, CO_2 rich waters to the surface through coastal, equatorial and wind driven upwelling (Arnone et al., 2017; Lefèvre et al., 2002, 2008; Parard et al., 2010). The increase in CO_2 concentrations elevates $pCO_{2\,(sw)}$, and the warming of these waters will amplify the $pCO_{2\,(sw)}$ increase. These upwelled waters are nutrient rich and can stimulate elevated NPP, which can sequester a portion of the upwelled CO_2 (Kim et al., 2019)

The addition of freshwater through riverine (Lefèvre et al., 2020; Chen et al., 2012a) and rainfall inputs has the opposite effect of upwelling by introducing CO_2 depleted fresh waters into the surface ocean which lowers $pCO_{2\,(sw)}$. Riverine inputs can also introduce substantial nutrient inputs that can fuel NPP (Smith and Demaster, 1996; Lefèvre et al., 2017), amplifying the depressed $pCO_{2\,(sw)}$ (Ibánhez et al., 2016; Körtzinger, 2003).

The spatial distribution of $pCO_{2\,(sw)}$ is therefore a complex balance between different amplifying or counteracting contributions from multiple driving mechanisms. These drivers will have regionally differing contributions to the $pCO_{2\,(sw)}$ spatial variability but also the temporal variability on seasonal (Takahashi et al., 2002), interannual (Henson et al., 2018) and decadal timescales (Landschützer et al., 2014, 2016).

1.3 Estimating the global air-sea CO_2 flux

Early assessments of the global ocean CO_2 sink were limited to ocean biogeochemical models (Wanninkhof et al., 2013), atmospheric (Peylin et al., 2013) and oceanic (Gruber et al., 2009) inversions or the binning of sparse in situ $pCO_{2\,(sw)}$ observations into long-term climatology assessments (Tans et al., 1990; Takahashi et al., 1997, 2009, 2002, 1999). More recently due to the availability of large community collated in situ datasets (Bakker et al., 2016; Takahashi et al., 2017) and satellite observations, methods which intelligently extrapolate in situ $pCO_{2\,(sw)}$ measurements for regional or global analyses, are now routinely employed (Shutler et al., 2020; Friedlingstein et al., 2020).

Stephens et al. (1995) extrapolated in situ observations in the North Pacific using seasonal linear regressions between SST and $pCO_{2\,(sw)}$ to produce basin scale fields from monthly satellite SST estimates. Regional SST based linear regressions have also been parameterised for the Caribbean Sea (Olsen et al.,

2004), Chilean upwelling (Lefèvre et al., 2002) and Atlantic Ocean (Lefèvre and Taylor, 2002). The addition of further parameters into multi-linear regression models have also included sea surface salinity (SSS) (Lefèvre et al., 2002) and chlorophyll *a* (Chl *a*) (Ono et al., 2004) as a proxy for biological production, which improved regional estimates of $pCO_{2\,(sw)}$, by accounting for a higher proportion of the $pCO_{2\,(sw)}$ variability.

In the pursuit of further improvements, different extrapolation methods were employed. These moved away from linear and multi-linear regression of $pCO_{2\,(sw)}$ and extrapolation parameters, towards neural networks (Lefèvre et al., 2005; Telszewski et al., 2009) which could effectively capture non-linear relationships. These methods have provided accurate $pCO_{2\,(sw)}$ estimates on both regional and global scales as quality controlled global dataset of $pCO_{2\,(sw)}$ became available.

Global estimates of $pCO_{2\,(sw)}$ based on the extrapolation of in situ $pCO_{2\,(sw)}$ using satellite observations did not appear until after the release of the Surface Ocean CO_2 Atlas (SOCAT) v1.5 in 2011 (Pfeil et al., 2013; Sabine et al., 2013). SOCAT provided a database of quality controlled global in situ $fCO_{2\,(sw)}$ observations (that can be converted to $pCO_{2\,(sw)}$), which has been continually updated since the first release to add more in situ observations (Bakker et al., 2016) and is now updated annually (https://www.socat.info/). The first global multiyear $pCO_{2\,(sw)}$ data-based estimate of the global ocean carbon sink were produced by Rodenbeck et al. (2013) using a mixed layer based diagnostic model that was fit to SOCAT $pCO_{2\,(sw)}$. An increase in the number of data-based estimates followed using a multitude of different methods and parameter combinations to extrapolate the $pCO_{2\,(sw)}$ observations (Rödenbeck et al., 2015; Landschützer et al., 2014; Iida et al., 2015; Denvil-Sommer et al., 2019; Zeng et al., 2015).

These global $pCO_{2\,(sw)}$ estimates, based on SOCAT in situ observations, allowed the investigation of seasonal, interannual, decadal and long-term trends in the global ocean CO_2 sink. For example, Landschützer et al. (2015, 2016) identified decadal changes in the Southern Ocean CO_2 sink strength, a region that had not been studied well, using a self-organising map coupled to a feed forward neural network approach. These global approaches followed the regional approaches incorporating physical parameters, including SST, SSS

and mixed layer depths, into the extrapolation schemes. The biological contribution to $pCO_{2\,(sw)}$ variability was either assumed to be driven by changes in the physical parameters (Watson et al., 2020b), or Chl *a* (Landschützer et al., 2014), the dominant pigment in phytoplankton which has been widely used as a proxy for the balance between photosynthesis and respiration within the plankton community, or the net community production (NCP). Chl *a* does not quantify the biological exchange of CO_2 however, since it does not quantify both the carbon uptake and that respired by the plankton community. This is discussed in further detail in the following section.

1.4 Biological controls on $pCO_{2\,(sw)}$

Biological activity in the surface ocean can modify the concentration of CO_2, and therefore the $pCO_{2\,(sw)}$. The balance between the NPP and respiration by the whole plankton community determines NCP. When NCP is positive, NPP is greater than respiration, and the plankton community is predominantly autotrophic, and a net drawdown of CO_2 is observed. Where NCP is negative, respiration outweighs NPP, heterotrophy is dominant and a net release of CO_2 from the plankton community is observed. Therefore, the NCP of the plankton community quantifies the balance between the biological drawdown or release of CO_2 from the surface ocean.

The NPP rate of a particular plankton community is determined by the phytoplankton biomass in the community as a first order approximation, hence why Chl *a* is regularly used as a proxy for NPP. However, the rate of NPP is not solely determined by the phytoplankton biomass and can be modified by the phytoplankton community composition (Bouman et al., 2005) and environmental conditions including, for example, SST (Behrenfeld and Falkowski, 1997b; Bouman et al., 2005; Eppley et al., 1985; Bouman et al., 2018), light availability (Dogliotti et al., 2014; Poulton et al., 2006; Sathyendranath et al., 1989), and macro (nitrate, phosphate and silicate) (Marañón et al., 2003; Poulton et al., 2006; Marañón et al., 2018) and micro nutrient availability (e.g. iron) (Behrenfeld and Milligan, 2012; Boyd et al., 2000; Coale et al., 1996; Behrenfeld et al., 2009). Thus elevated phytoplankton biomass (or as a proxy; elevated Chl *a*) does not always equate to an equal increase in the overall NPP (Poulton et al., 2006; Dogliotti et al., 2014; Kulk et al., 2020).

NPP rates are determined by a balance between limiting processes that will control the overall NPP rate of a phytoplankton community. Empirical models that relate Chl *a* concentrations to the NPP rate are able to account for some of the variability in NPP (Tilstone et al., 2009; Eppley et al., 1985). More complex models that incorporate light and photosynthetic rate parameters, are able to predict a higher proportion of the observed variability in NPP rates (Tilstone et al., 2009; Campbell et al., 2002; Carr et al., 2006; Friedrichs et al., 2009; Behrenfeld and Falkowski, 1997b; Dogliotti et al., 2014). This highlights that Chl *a*, although important for determining NPP, is not the sole parameter controlling the variability in NPP, and changes in Chl *a* do not necessarily indicate an equal response in NPP rates. Whereas the NCP is the balance between phytoplankton NPP and the respiration of heterotrophic organisms, and therefore the variability in NCP is not only determined by NPP but also by the respiration rate of the plankton community (Serret et al., 2015). Respiration rates have been shown to increase with increasing NPP rates, but this is not proportional, and NPP tends to increase more than respiration rates (Duarte et al., 2013; Williams, 1998; Serret et al., 2009, 2015; Williams et al., 2013). However, in situ comparisons of NPP to respiration relationships show substantial variability, indicating that NPP is not the sole determining variable for respiration variability (Serret et al., 2015, 2009; Tilstone et al., 2015b; Yvon-Durocher et al., 2012).

Other controls on respiration rates can include temperature where higher temperatures support greater respiration rates (Regaudie-De-Gioux and Duarte, 2012; García-Corral et al., 2014; Tilstone et al., 2015b), and therefore modify the NPP to respiration relationship. Variability in these relationships has also been observed due to temporal lags between NPP increases and a subsequent increase in respiration as organic matter flows through the community (Robinson and Williams, 2005), especially surrounding the spring bloom (Serret et al., 1999). Geographical differences also introduce variability when scaling to basin wide estimates, for example between the North and South Atlantic gyres due to differences in the respiration rate (Serret et al., 2002, 2015).

NCP rates are therefore determined by changes in both NPP and respiration (Serret et al., 2015). NPP is related to Chl *a*, but other processes can modify the NPP rate for a given Chl *a* concentration as discussed previously. Community

respiration has been shown to weakly relate to Chl *a* concentrations (Robinson and Williams, 2005; Robinson et al., 2002b, a), but is more closely related to the NPP rates (Tilstone et al., 2015b; Serret et al., 2009; Duarte et al., 2013). Therefore, using Chl *a* as a proxy for NCP, will miss variability in NCP driven not only by differences in NPP, but also due to differences in respiration rates.

1.5 Satellite estimates of phytoplankton biomass and rates

Though in situ data is essential in understanding the variability in NCP, NPP, Chl *a*, and respiration, it does not capture the large-scale variability in these parameters over space and time. To synoptically assess NCP on a basin scale, and therefore to include NCP within schemes to extrapolate $pCO_{2\,(sw)}$ observations, satellite estimates are required. Satellite based ocean colour, the optical signal from the ocean water leaving radiance at visible wavelengths, was unlocked in 1979 with the launch of the experimental Coastal Zone Color Scanner (CZCS) on the Nimbus 7 satellite. This satellite sensor provided the first synoptic global scale estimates of ocean colour, as proof of concept, until its demise in 1986. In 1997, the National Aeronautics and Space Administration (NASA) launched the Sea Viewing Wide Field of View Sensor (SeaWiFS) on the Orbview-2 satellite which allowed the synoptic and routine estimation of ocean colour within the global oceans. Following the success of SeaWiFS, the Moderate Resolution Imaging Spectroradiometer on the Aqua satellite (MODIS-A) was launched in 2002 providing continued ocean colour data until the present day, making MODIS-A the longest single sensor record of ocean colour. Other ocean colour sensors, including for example the Visible Infrared Imaging Radiometer Suite (VIIRS), Medium Resolution Imaging Spectrometer (MERIS) and Ocean Colour Land Imager (OLCI), have since followed. To achieve longer timeseries of ocean colour observations, individual sensor data has been merged into combined multisensor timeseries. These include the Ocean Colour Climate Change Initiative (OC-CCI; Sathyendranath et al., 2019), Copernicus Marine Environmental Monitoring Service (CMEMS) and GlobColour (Garnesson et al., 2019) services. However, the focus of this thesis will be MODIS-A.

Downwelling irradiance from the sun crosses the air-sea interface, interacts with the ocean, and a small proportion of this is reflected back to the atmosphere which is detected by ocean colour satellites. When light from the sun enters the

ocean it is either absorbed or scattered by optically active in water constituents, that include Chl *a* in phytoplankton, coloured dissolved organic matter (CDOM), suspended sediments and the water molecules (Morel and Prieur, 1977). Each constituent has an optical signature that will modify the received light and allows the estimation of that constituent (Fig. 1.2). In the case of Chl *a*, it absorbs strongly in the blue and red relative to green wavelengths (Fig. 1.2a) and the ratio or relationship between the reflected light at these wavelengths can be used to estimate the concentration of Chl *a*. Ocean colour satellites are however restricted in the wavelengths of light that can be sampled due to atmospheric opacity in the ultraviolet and infrared wavelengths. The wavelengths (or bands) generally coincide with signatures of in water constituents (Fig. 1.2d). The properties of constituents will therefore be imprinted on the received light at the satellite, dependent on the concentration of the constituent (Fig. 1.2d).

1.5.1 Chlorophyll *a*

Empirical (O'Reilly et al., 1998; O'Reilly and Werdell, 2019; Hu et al., 2012; Gohin et al., 2002) and semi analytical (Maritorena et al., 2010, 2002; Werdell et al., 2013) algorithms have been developed and refined over the last three decades to estimate the Chl *a* concentrations based on this distinct absorption (Fig. 1.2a). These algorithms perform well in the open ocean (Brewin et al., 2015, 2016) where Chl *a* and covarying phytoplankton products dominate the optical signal received by the satellite (Case-1 waters) (Morel and Prieur, 1977). However, degraded performance and higher uncertainties are observed in coastal regions (Lavender et al., 2004) where other in water substances, such as suspended sediments and CDOM, have a more dominant role in determining the optical properties of the water (Case-2 waters) (Morel and Prieur, 1977) and therefore the light received at the satellite.

The accuracy and precision of these Chl *a* algorithm types and formulation must be assessed with respect to in situ observations of Chl *a*. Globally, large in situ datasets of Chl *a* observations have been compiled (Werdell and Bailey, 2005; Valente et al., 2016, 2019) for the purpose of assessing the performance of algorithms. In a recent study by Brewin et al. (2015) the global accuracy of 15 algorithms were assessed, indicating the majority of algorithms were able to estimate Chl *a* with a similar accuracy.

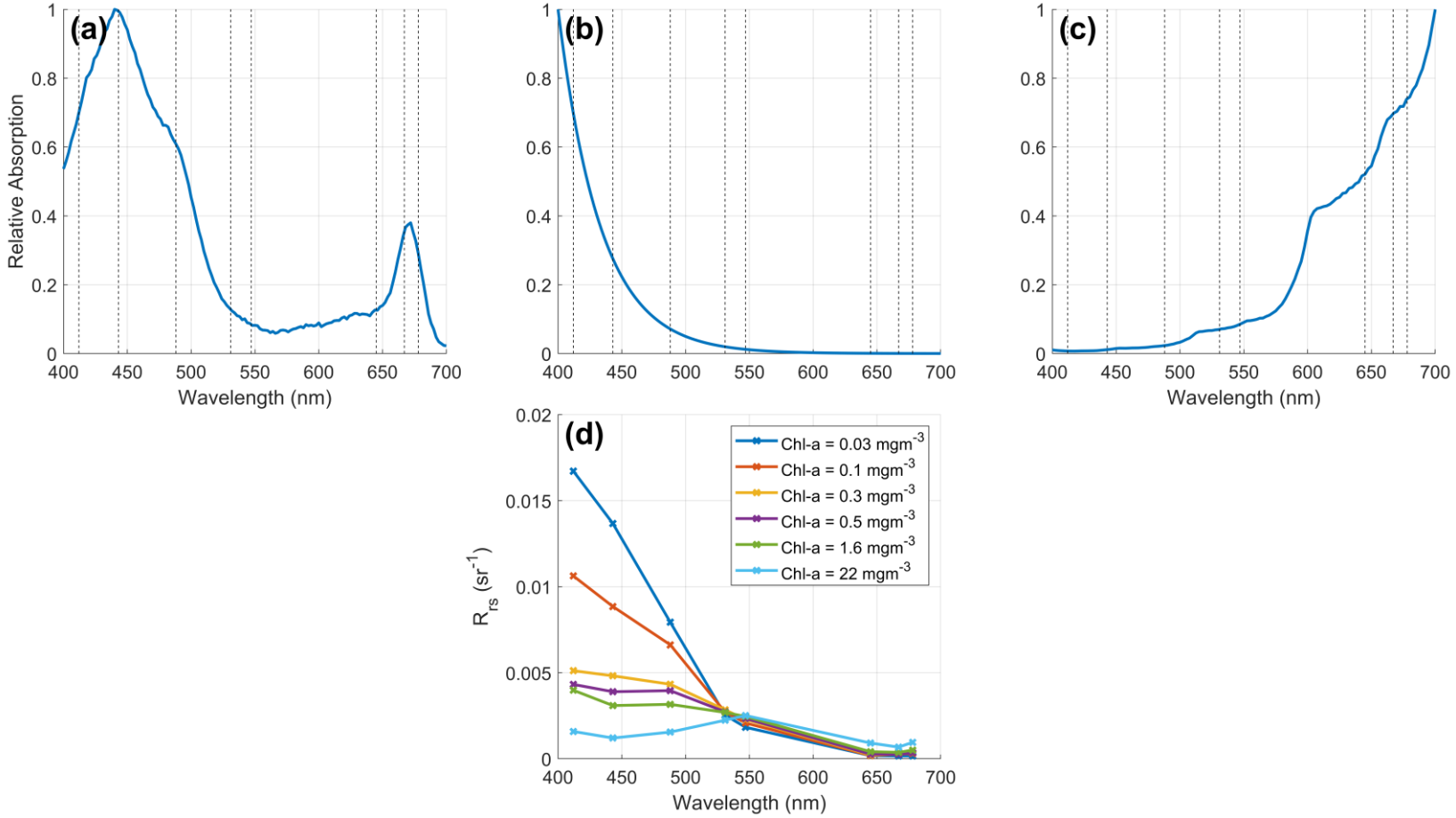

Figure 1.2 - Relative absorption spectra of (a) Chl *a*, (b) Coloured Dissolved Organic Matter and (c) pure water (Pope and Fry, 1997). Black dashed lines indicate the central wavelength of MODIS-A spectral bands. (d) Remote sensing reflectance (R_{rs}) from MODIS-A for in situ Chl *a* concentrations ranging from 0.03 to 22 mgm^{-3} in the South Atlantic Ocean, extracted from data used in Chapter 2.

However, regionally algorithms have shown higher or lower accuracies (Brewin et al., 2016; Dogliotti et al., 2009; Tilstone et al., 2011; Garcia et al., 2006; Kampel et al., 2009b) compared to the global accuracy. This highlights the need to assess the accuracy of satellite Chl *a* algorithms using high quality in situ data for regional analyses, to select the best performing algorithm.

1.5.2 Net Primary Production

The first global oceanic NPP estimate of between 45 to 50 Pg C yr^{-1} using satellite observations were made by Longhurst et al. (1995). Concerted efforts over the last 30 years have made advances in the estimation of NPP from satellite observations, and upwards of 20 algorithms have been developed and refined, with a comprehensive series of round-robin inter-comparisons at both global and regional scales to determine both the accuracy and limitations of the algorithms tested (Carr et al., 2006; Saba et al., 2010; Friedrichs et al., 2009; Campbell et al., 2002; Saba et al., 2011).

Early estimates of NPP from satellite observations by the CZCS were based on empirical relationships to Chl *a* concentrations (Eppley et al., 1985). These empirical methods only accounted for ~30 % of the seasonal variability in NPP at single stations (Campbell and O'Reilly, 1988), highlighting that changes in photosynthetic rates are important for the accurate estimation of NPP (Behrenfeld and Falkowski, 1997b). More complex algorithms which incorporated in situ photosynthetic rates (Bouman et al., 2018; Kulk et al., 2020; Longhurst et al., 1995), models of the phytoplankton photosynthetic response to the light spectra (Platt and Sathyendranath, 1988; Sathyendranath et al., 2020; Morel, 1991; Smyth et al., 2005), temperature (Behrenfeld and Falkowski, 1997b) and other environmental conditions (Behrenfeld et al., 2002), alongside vertical changes in these parameters (Sathyendranath et al., 1995), were developed to improve the accuracy of satellite derived NPP. Algorithm complexity also increased by resolving these photosynthetic responses through time, wavelength and depth, or combinations of the three (Behrenfeld and Falkowski, 1997a).

A series of algorithm intercomparisons performed by NASA compared the accuracy of a large selection of these algorithms with different structures and complexities (Campbell et al., 2002; Carr et al., 2006; Saba et al., 2010;

Friedrichs et al., 2009; Saba et al., 2011). These intercomparisons showed an increase in the accuracy of the NPP algorithms from the first comparison by Campbell et al. (2002) to the study by Saba et al. (2011). On the global scale, algorithms tended to have a similar accuracy compared to in situ observations, however regional differences between algorithms were still apparent. For example, Friedrich et al. (2009) showed a tendency to overestimate the NPP rate but underestimate the NPP variability in the Equatorial Pacific. However, Saba et al. (2010) reported that NPP was underestimated at two stations in the oligotrophic, low NPP regions, namely the Bermuda Atlantic Time Series (BATS) and Hawaii Ocean Time series (HOTS), compared to two decades of in situ observations. These differences are reinforced by independent regional studies, such as those in the Atlantic Ocean (Tilstone et al., 2009; Dogliotti et al., 2014; Tilstone et al., 2015a; Lobanova et al., 2018). And these regional differences lead to a global NPP estimate between 49 to 60 Pg C yr^{-1} across the NPP algorithms tested (Carr et al., 2006).

Friedrich et al. (2009) and Saba et al. (2011) assessed the impact of uncertainties in the input parameters, on the NPP algorithm accuracy. Friedrich et al. (2009) showed that more than 50% of the deviations between in situ and satellite NPP estimates could be attributed to the algorithm input parameters. Saba et al. (2011) reported a larger value of 72%, however. Both studies identified Chl *a* as the largest contribution to uncertainty, which was between 25 % and 35 % of the uncertainty in NPP estimates. Geographical differences in the accuracy of satellite Chl *a* algorithms, as described in the previous section, highlights the need to select the most accurate Chl *a* algorithm for the region of study, as well as the most accurate NPP algorithm.

1.5.3 Net Community Production

Satellite algorithms of NCP are still in their infancy compared to NPP (Serret et al., 2009; Tilstone et al., 2015b), and the first NCP algorithms have only been recently applied to satellite data (Tilstone et al., 2015b). Tilstone et al. (2015b) presented algorithms to estimate NCP in the Atlantic Ocean from an empirical power law relationship to NPP based upon in situ analyses. An additional algorithm including a relationship between NCP and SST within the power law, was shown to perform most accurately in the Atlantic Ocean, compared to in

situ observations. The SST relationship improved the accuracy of these algorithms, by capturing more of the temperature dependency in respiration rates (Regaudie-De-Gioux and Duarte, 2012; García-Corral et al., 2014).

Although these NCP algorithms are in their infancy, their good performance (when assessed against in situ data) means that these estimates are useful. Clear differences in the relationships between NPP and NCP exist in the North and South Atlantic oceans (Serret et al., 2015; Gist et al., 2009). It is therefore of paramount importance to assess the NCP algorithm performance and to quantify the uncertainties, with respect to in situ observations, prior to using these approaches to ensure that the satellite NCP regional estimates are reliable and accurate.

1.6 The South Atlantic Ocean

The South Atlantic Ocean is a dynamic system with regions of high and very low biological activity but is under sampled with limited in situ observations. Satellite observations provide a mechanism to study this region in greater detail and at higher resolution (Fig. 1.3). In the Equatorial region, the seasonal upwelling brings CO_2 rich water to the surface between June and September (Parard et al., 2010; Lefèvre et al., 2008), which also enhances the biological activity through nutrient inputs. In the western Equatorial Atlantic the Amazon River delivers ~20% of all the global freshwater riverine inputs into the oceans (Cai et al., 2013). The freshwater input produces an extensive plume, that extends offshore following the North Brazil current retroflection during August to November (Ibánhez et al., 2016). This riverine input also supplies nutrients that enhance biological activity within the plume (Smith and Demaster, 1996). Strong biological activity is observed on the southeastern shelf within the Benguela upwelling system (Lamont et al., 2014), on the southwestern shelf and offshore into the Brazil Malvinas confluence (Dogliotti et al., 2014). These features will all contribute to $pCO_{2\,(sw)}$ variability both spatially and temporally, and therefore influence the air-sea CO_2 flux.

1.6.1 Mesoscale features in the oceans

Mesoscale features, of the order 100 km and timescales of days to years, are prevalent in the global oceans and especially in the South Atlantic Ocean.

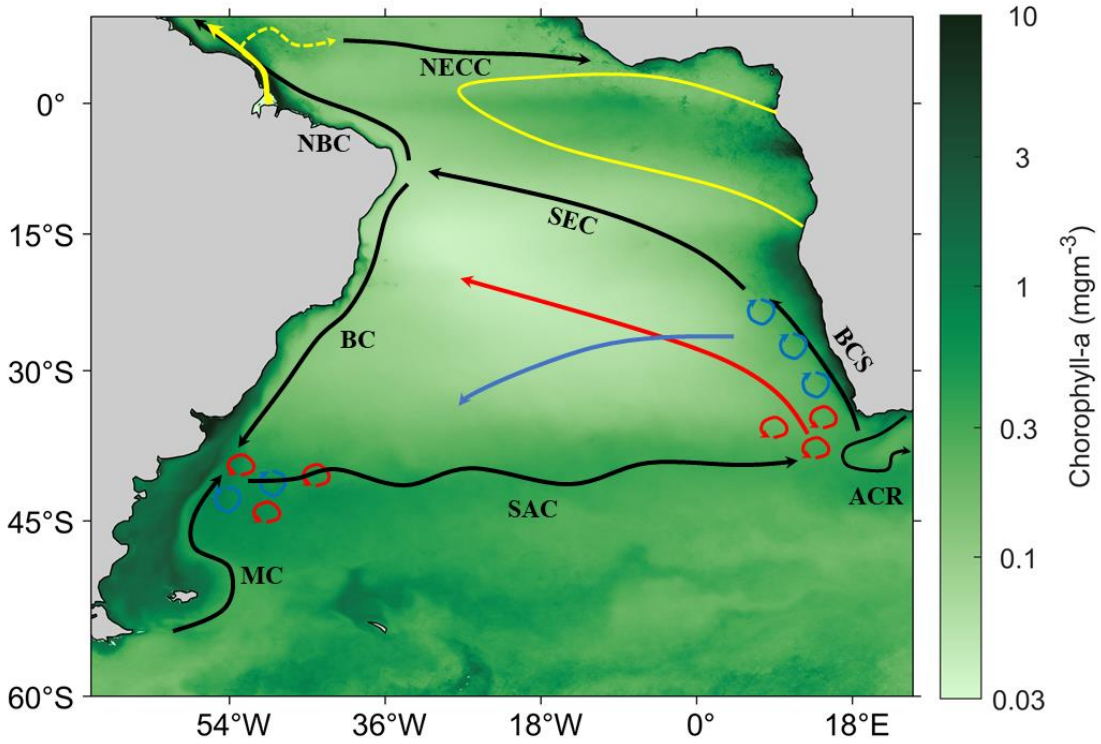

Figure 1.3 – Map of the South Atlantic Ocean, overlaid on a MODIS-A mission long composite of Chl a. Solid yellow arrow indicates the flow of the Amazon Plume, and dashed arrow indicates the flow during the North Brazil Current Retroflection. Yellow bounding indicates the region under the influence of the Equatorial Upwelling. The black arrows represent the main surface currents which are North Equatorial Counter Current (NECC), North Brazil Current (NBC), South Equatorial Current (SEC), Brazil Current (BC), Benguela Current (BCS), Malvinas Current, (MC), South Atlantic Current (SAC) and Agulhas Current Retroflection (ACR). Red circles indicate eddies formed at the ACR. Blue circles indicate eddies forming from the Benguela Upwelling System. Both types of eddy follow their idealised trajectories (solid arrows) across the South Atlantic Ocean (Chelton et al., 2011; Guerra et al., 2018). Red and blue circles at the Brazil-Malvinas Confluence (BC-MC) indicate the intense mesoscale eddy formation, and re-circulation in the region.

These features occur as eddies (Chelton et al., 2011; Pegliasco et al., 2022; Chaigneau et al., 2009), filaments (Rubio et al., 2009), meanders (Lefèvre et al., 2020; Lefévre et al., 2010), and fronts. They can modify the physical (Laxenaire et al., 2019; Nencioli et al., 2018), chemical (Orselli et al., 2019a; Arhan et al., 2011; Orselli et al., 2019b; Pezzi et al., 2021),and biological (Carvalho et al., 2019; Hernández-Hernández et al., 2020; Dufois et al., 2016; Gaube et al., 2014; Roughan et al., 2017; Lehahn et al., 2011) oceanic conditions as well as the overlying atmospheric conditions (Frenger et al., 2013; Pezzi et al., 2021; Souza et al., 2021) compared to the surrounding environment. It is likely that these features will also modify the air-sea CO_2 flux, however few studies have

investigated the effect of these mesoscale features in controlling the CO_2 flux (Pezzi et al., 2021; Chen et al., 2007; Song et al., 2016; Orselli et al., 2019b; Sarma et al., 2019). These features exist in the South Atlantic Ocean, for example, Agulhas retroflection eddies (Guerra et al., 2018), filaments and eddies forming from the Benguela upwelling front (Rubio et al., 2009) and intense eddies, fronts and filaments in the Brazil-Malvinas confluence (Mason et al., 2017) (Fig. 1.3). Few studies have analysed the effects of these features on air-sea CO_2 flux.

1.7 Thesis Objectives

In this thesis, the biological contribution to the air-sea CO_2 flux in the South Atlantic Ocean is explored. The objectives of the thesis are:

1. To assess the accuracy of satellite Chl *a*, NPP and NCP using a comprehensive dataset of in situ observations.
2. To identify whether using satellite NCP, as the quantified biological contribution to $pCO_{2\,(sw)}$, instead of Chl *a* will improve basin scale estimates of $pCO_{2\,(sw)}$ from satellite observations.
3. To identify the seasonal, interannual and multi-year drivers of changes in the air-sea CO_2 flux
4. To assess the contribution of mesoscale features to the air-sea CO_2 flux using satellite and in situ observations.

Chapter 2, "Wind speed and mesoscale features drive net autotrophy in the South Atlantic Ocean", is published as Ford et al (2021a), and identifies the most accurate satellite estimates of Chl *a*, NPP and NCP whilst accounting for the *in situ* observation uncertainties. In this process the satellite uncertainties for each parameter are determined. A 16 year satellite-based NCP timeseries was constructed to explore the environmental and climate drivers of NCP variability in the South Atlantic Ocean, whilst accounting for the uncertainties in the satellite NCP estimates.

Chapter 3, "Derivation of seawater pCO_2 from net community production identifies the South Atlantic Ocean as a CO_2 source", is published as Ford et al. (2022, 2021b), and presents a novel comparison of spatially and temporally complete $pCO_{2\,(sw)}$ fields estimated using a neural network extrapolation scheme which applies satellite Chl *a*, NPP, or NCP as the

estimator of the biological contribution to $pCO_{2\,(sw)}$ variability. The satellite uncertainties for Chl *a*, NPP and NCP determined in Chapter 2 are used to investigate the potential reductions in the $pCO_{2\,(sw)}$ uncertainties that could be attributed to the biological parameter, and where future efforts should focus to improve $pCO_{2\,(sw)}$ estimates.

Chapter 4, "Identifying the biological control of the annual and multi-year variations in South Atlantic air-sea CO_2 flux" presents a timeseries decomposition approach applied to complete $pCO_{2\,(sw)}$ fields estimated in Chapter 3 from NCP, to assess the seasonal and interannual drivers of ΔpCO_2 and the CO_2 flux in the South Atlantic Ocean. The multi-year trends in ΔpCO_2 and the CO_2 flux are identified and suggest that biological contributions are an important control of these changes.

Chapter 5, "Mesoscale eddies enhance the air-sea CO_2 sink in the South Atlantic Ocean" presents a novel Lagrangian tracking approach applied to long lived mesoscale eddies as they transit across the South Atlantic Ocean. The cumulative air-sea CO_2 flux is estimated throughout their respective lifetimes using the neural network approach in Chapter 3 to estimate $pCO_{2\,(sw)}$ and assess the contribution of mesoscale eddies to the CO_2 flux.

Chapter 2: Wind speed and mesoscale features drive net autotrophy in the South Atlantic Ocean

This chapter is a reformatted version of my publication:
Ford, D., Tilstone, G. H., Shutler, J. D., Kitidis, V., Lobanova, P., Schwarz, J., Poulton, A. J., Serret, P., Lamont, T., Chuqui, M., Barlow, R., Lozano, J., Kampel, M. and Brandini, F. (2021): Wind speed and mesoscale features drive net autotrophy in the South Atlantic Ocean, Remote Sensing of the Environment, 260, 112435, https://doi.org/10.1016/j.rse.2021.112435

DJF processed and analysed the data, prepared the figures, and wrote the paper. DJF, GHT, JDS and VK conceived and directed the research. DJF and JS directed the basin scale time series analysis. PL processed and extracted the VGPM and PSM primary production algorithms. DJF, PS, JL, VK, GHT, AJP, MC, FB, MK, RB and TL collected in situ data used within the manuscript.

Abstract: A comprehensive *in situ* dataset of chlorophyll *a* (Chl *a*; N=18,001), net primary production (NPP; N=165) and net community production (NCP; N=95), were used to evaluate the performance of Moderate Resolution Imaging Spectroradiometer on Aqua (MODIS-A) algorithms for these parameters, in the South Atlantic Ocean, to facilitate the accurate generation of satellite NCP time series. For Chl *a*, five algorithms were tested using MODIS-A data, and OC3-CI performed best, which was subsequently used to compute NPP. Of three NPP algorithms tested, a Wavelength Resolved Model (WRM) was the most accurate, and was therefore used to estimate NCP with an empirical relationship between NCP with NPP and sea surface temperature (SST). A perturbation analysis was deployed to quantify the range of uncertainties introduced in satellite NCP from input parameters. The largest reductions in the uncertainty of satellite NCP came from MODIS-A derived NPP using the WRM (40 %) and MODIS-A Chl *a* using OC3-CI (22 %).

The most accurate NCP algorithm, was used to generate a 16 year time series (2002 to 2018) from MODIS-A to assess climate and environmental drivers of NCP across the South Atlantic basin. Positive correlations between wind speed anomalies and NCP anomalies were observed in the central South Atlantic Gyre (SATL), and the Benguela Upwelling (BENG), indicating that autotrophic conditions may be fuelled by local wind-induced nutrient inputs to the mixed

layer. Sea Level Height Anomalies (SLHA), used as an indicator of mesoscale eddies, were negatively correlated with NCP anomalies offshore of the BENG upwelling fronts into the SATL, suggesting autotrophic conditions are driven by mesoscale features. The Agulhas bank and Brazil-Malvinas confluence regions also had a strong negative correlation between SLHA and NCP anomalies, similarly, indicating that NCP is forced by mesoscale eddy generation in this region. Positive correlations between SST anomalies and the Multivariate ENSO Index (MEI) in the SATL, indicated the influence of El Niño events on the South Atlantic Ocean, however the plankton community response was less clear.

2.1 Introduction

Autotrophic plankton produce up to 50% of the net organic carbon on our planet (Field et al., 1998), as they draw down carbon dioxide (CO_2) from the atmosphere into the ocean. A proportion of this NPP is respired by heterotrophic plankton, which results in a re-release of some of the fixed CO_2 back into the atmosphere. The balance between autotrophic production and heterotrophic respiration determines NCP. Measurements of NCP made on research ships, though essential to understanding the dynamics of NCP, provides only a snapshot of the system rather than broader temporal-spatial dynamics. Such measurements can be estimated by observing ocean colour from space (Tilstone et al., 2015b). The use of *in situ* data to identify the most accurate ocean colour satellite algorithms, will facilitate the generation of reliable synoptic-scale NCP time series. Such data are needed for identifying trends in the metabolic balance of the oceans, and understanding the biological draw down and release of CO_2 from the oceans.

The estimation of NCP from satellite ocean colour is dependent on the accurate quantification of NPP, which is derived from Chl *a*, photo-physiological parameters (e.g.: maximum photosynthetic rate, P^B_m; initial slope of the light-dependent photosynthetic rate, α^B), and photosynthetically active radiation (PAR), and the estimation of the relationship between NPP and heterotrophic respiration from proxy parameters such as SST. Chl *a*, as the dominant pigment in phytoplankton, has been routinely monitored on a global scale using satellite data since the launch of the National Aeronautics and Space Administration (NASA) Sea Viewing Wide Field of View Sensor (SeaWiFS) on the Orbview-2

satellite in 1997. Following the success of SeaWiFS, MODIS-A was launched in 2002 providing continued monitoring of Chl *a* globally. Concerted efforts over the last three decades to estimate NPP from Chl *a* on a global scale resulted in the development of 20 models that use a variety of algorithm architecture (Carr et al., 2006; Friedrichs et al., 2009). A series of inter-comparisons performed by NASA indicated that NPP models of different complexities performed similarly (Friedrichs et al., 2009), though they displayed regional dependencies (Campbell et al., 2002). These inter-comparisons also highlighted that up to 50 % of model uncertainties could be attributed to uncertainty in the input parameters, with by far the largest contribution coming from Chl *a* (Saba et al., 2011). Such differences in algorithm performance highlight the need to identify the best performing NPP and Chl *a* algorithms regionally, to reduce the uncertainty attributed to input parameters.

Recently NCP has been estimated from ocean colour data using empirical or semi-analytical algorithms based on NPP (Chang et al., 2014; Li and Cassar, 2016; Serret et al., 2009; Tilstone et al., 2015b). Regional empirical NCP algorithms for the Atlantic Ocean have been derived from *in vitro* ^{14}C-based NPP and O_2-based NCP estimates (Serret et al., 2009; Tilstone et al., 2015b). However, these empirical algorithms assume a spatially homogenous relationship between photosynthesis and respiration that has been shown to be variable, for example between the North and South Atlantic Oceans (Serret et al., 2015). This reinforces the need to identify the most accurate algorithms for a particular geographical region.

According to Saba et al. (2011), 22 % of the uncertainty in NPP models could be attributed to the *in situ* NPP measurements uncertainty. Chl *a*, NPP and NCP algorithms will all have uncertainties in both the algorithm input parameters, and the uncertainty of the *in situ* measurements, used to assess their performance. Previous statistical assessments have assumed that all uncertainty resides in the satellite retrievals, and consider the *in situ* measurements to be truth (i.e. ‘100% accurate’). Neglecting the *in situ* uncertainty could result in a reduction in algorithm performance, especially when limited *in situ* data exist to either calibrate or validate the algorithm.

The South Atlantic Ocean is under sampled and few *in situ* datasets are available. It is however an exceptionally dynamic and varied system, that

includes the seasonal Equatorial upwelling, high productivity on the southwestern (Dogliotti et al., 2014; Garcia et al., 2004) and the southeastern shelf (Hutchings et al., 2009; Lamont et al., 2018a), as well as the propagation of Agulhas Current eddies through the basin (Guerra et al., 2018). NCP variability can feasibly be observed using ocean colour remote sensing, to assess principal environmental drivers, assuming the performance of ocean colour algorithms have been evaluated. There are few studies however, that have assessed the performance of ocean colour satellite algorithms in the South Atlantic Ocean. These have been focused mainly on the southwestern shelf and Brazilian Coast, but with conflicting results (Dogliotti et al., 2014, 2009; Garcia et al., 2005; Kampel et al., 2009a, b). Dogliotti et al. (2014, 2009) showed that the MODIS-A OC3M, underestimates Chl *a* on the southwestern shelf, over a range of *in situ* values spanning 0.1 to 11 mg m^{-3}. By contrast, Kampel et al. (2009a) showed that OC3M overestimates Chl *a* on the Brazilian Coast, but over a much smaller range of *in situ* values from 0.08 to 0.20 mg m^{-3}.

The objectives of this paper are to investigate the NCP dynamics in the South Atlantic Ocean, using MODIS-A multi-spectral observations, in order to assess the principal environmental drivers of NCP over a 16 year period. In order to generate accurate satellite NCP time series, the performance of MODIS-A estimates of Chl *a*, NPP and NCP for the South Atlantic Ocean are assessed, whilst also accounting for the *in situ* uncertainty. Weighted statistics are computed to account for the uncertainty in both the satellite and *in situ* data to evaluate algorithm performance. Following selection of the most accurate algorithms, a perturbation analysis to determine the magnitude of the uncertainty induced on satellite NCP by each input parameter, and on the *in situ* measurements themselves was conducted. The uncertainty analysis identifies where future efforts should focus on reducing the uncertainties in these parameters.

2.2 Methods

2.2.1 Chlorophyll *a*

Chl *a* was measured semi-autonomously and continuously along seven Atlantic Meridional Transects (AMT; data available from BODC; https://www.bodc.ac.uk/) from 2009 to 2018 (Fig. 2.1a). Chl *a* was derived from

total particulate absorption coefficients, measured using a WetLabs AC-S connected to the ships clean flow through system, which sampled the surface seawater continuously from a depth of approximately 5 m.

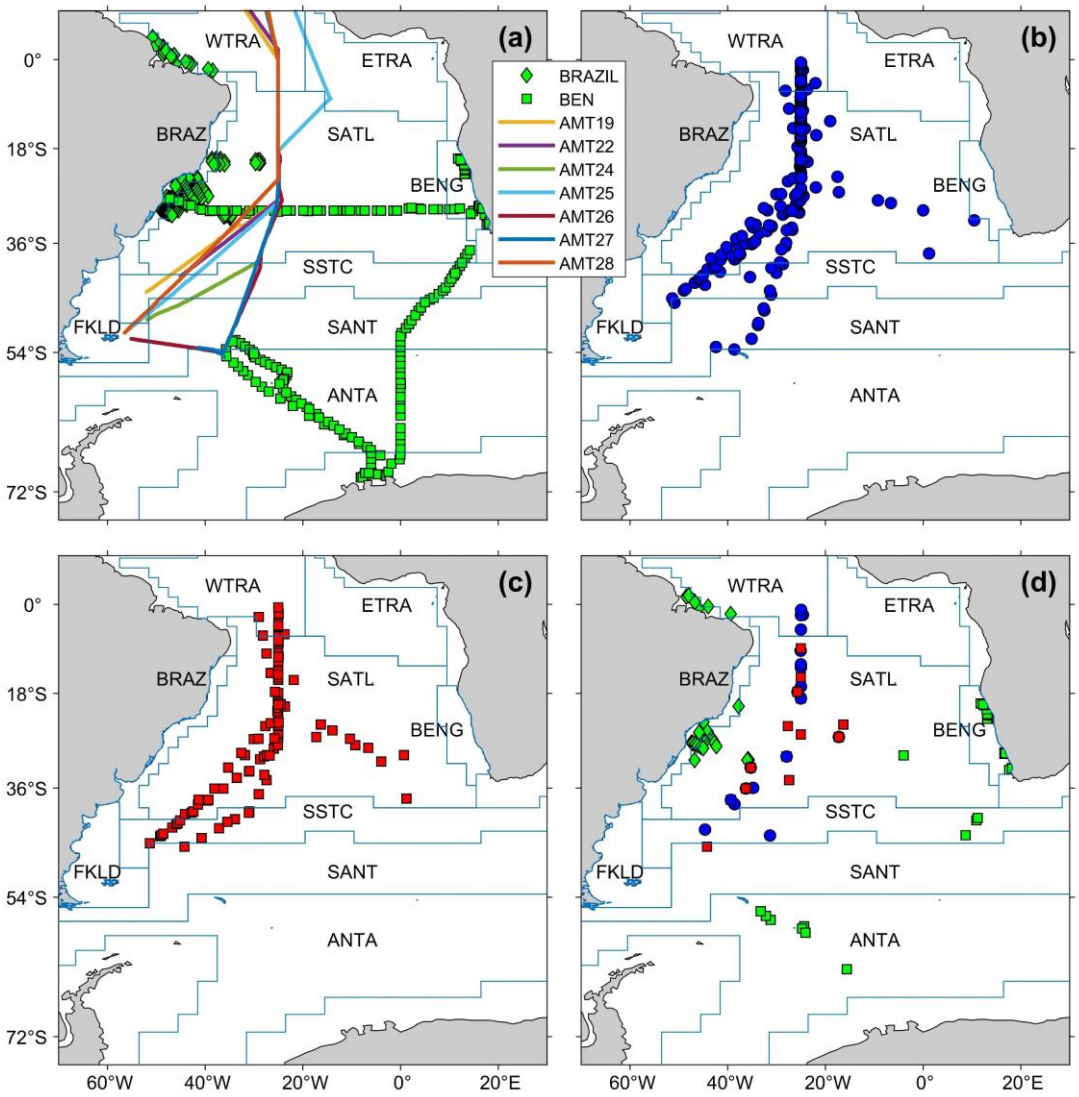

Figure 2.1 - Sampling locations for measurements of (a.) in situ chlorophyll a (Chl *a*) collected at discrete stations along the Brazilian coast (BRAZIL dataset, green diamonds), Benguela and Southern Ocean (BEN dataset, green squares) and continuous underway estimates collected on seven Atlantic Meridional Transect (AMT) cruises (coloured lines); (b.) in vitro net primary production and (c.) in vitro net community production both determined at discrete stations on AMT cruises between 2002 and 2019. (d) indicates discrete Chl *a*, net primary production and net community production stations with satellite matchups. The province areas are from Longhurst (1998) as follows: WTRA is Western Tropical Atlantic; ETRA is Eastern Tropical Atlantic; BRAZ is Brazilian Current coastal; SATL is South Atlantic Gyre; BENG is Benguela Current coastal upwelling; FKLD is Southwest Atlantic shelves; SSTC is South Subtropical Convergence; SANT is Sub Antarctic and ANTA is Antarctic.

Further details of this method are given in Brewin et al. (2016) following methods of Dall'Olmo et al. (2009), Slade et al. (2010) and Dall'Olmo et al. (2012). The AC-S Chl *a* method provided ~80,000 measurements in the study area. The *in situ* uncertainty (Ɛins_{CHL}) in the measurements were assessed using the $\log_{10}$ root mean square difference between the HPLC Chl *a* and AC-S estimated Chl *a* for each cruise, ranging from 0.06 to 0.26 $\log_{10}(\text{mg m}^{-3})$.

A further 211 discrete Chl *a* measurements were collected along the South American coast (BRAZIL dataset) on six cruises between 2012 and 2018. For each measurement, between 0.5 and 1 L of seawater was filtered onto 25 mm GF/F filters and stored in liquid nitrogen until analysis in the laboratory. Chl *a* was extracted in a solution of acetone and di-methyl sulphoxide (DMSO) and estimated fluorometrically following the method of Welschmeyer (1994) on a 10 AU Turner Fluorometer. No replicate measurements were taken to assess the uncertainty of these values.

Additionally, 223 discrete Chl *a* measurements were collected in the South Atlantic (November 2003), Benguela upwelling system (October 2002, May 2014 and September 2014) and the Atlantic sector of the Southern Ocean (January - February 2009) on five cruises (BEN dataset). For these samples, between 1.5 and 2.4 L of seawater was filtered onto 25 mm GF/F filters and the filters were stored in liquid nitrogen until analysis ashore. Frozen filters were added to 90% acetone to extract pigments for analysis using the reverse-phase HPLC procedures outlined by Barlow et al. (1997) or Zapata et al. (2000). No replicate measurements were taken to assess the uncertainty for these estimates.

2.2.2 In vitro NPP

In vitro ^{14}C NPP incubations were conducted at 165 stations (Fig. 2.1b), from 15 AMT cruises between 2002 and 2019, following the protocols outlined in Poulton et al. (2006) and Tilstone et al. (2009). The *in situ* uncertainty (Ɛins_{NPP}) was estimated by propagating the triplicate standard deviations of the discrete depth measurements, through the water column, using the same integration scheme, for each station. Ɛins_{NPP} was on average 49 mg C m^{-2} d^{-1}, and ranged between 5 and 300 mg C m^{-2} d^{-1}.

2.2.3 In vitro NCP

In vitro NCP measurements were conducted at 95 stations (Fig. 2.1c) on 10 AMT cruises between 2003 and 2019 using *in vitro* changes in dissolved oxygen (O_2), following the procedures described in Gist et al. (2009). The *in situ* uncertainty ($Ɛins_{NCP}$) was assessed by integrating the combined standard errors of the initial and light replicate bottles, at discrete depths through the water column, following the same integration scheme, for each station. $Ɛins_{NCP}$ was on average 20 mmol O_2 m^{-2} d^{-1} and ranged between 5 and 114 mmol O_2 m^{-2} d^{-1}. The *in situ* NCP dataset contains a subset of the data present in Tilstone et al. (2015b; N = 50), alongside an additional 45 stations from four AMT cruises; AMT 22 (2012), AMT 23 (2013), AMT 24 (2014) and AMT 29 (2019).

2.2.4 Chl *a* Algorithms

Satellite Chl *a* was estimated using five algorithms. The OC algorithms are based on an empirical relationship between the log-transformed blue to green remote sensing reflectance (R_{rs}) ratio and the *in situ* Chl *a* concentration (O'Reilly et al., 1998). For MODIS-A, the OC3Mv6 algorithm uses the log-transformed maximum band ratio (R) from two bands, $R_{rs}(443)$ and $R_{rs}(448)$ using $R_{rs}(547)$ as the denominator as follows:

$$R = log_{10}(\frac{\max[R_{rs}(443), R_{rs}(488)]}{R_{rs}(547)}), \quad (2.1)$$

Chl *a* was estimated according to:

$$\text{Chl } a = 10^{(a_0 + a_1 R + a_2 R^2 + a_3 R^3 + a_4 R^4)}, \quad (2.2)$$

where a_0 = 0.2424, a_1 = -2.7423, a_2 = 1.8017, a_3 = 0.0015 and a_4 = -1.2280. The algorithm performs well where phytoplankton dominate the optical signal, however in coastal waters the performance decreases, where suspended sediments and coloured dissolved organic matter (CDOM), change the optical properties of the water (Morel and Prieur, 1977).

OC5 is a modification of the OC algorithm, to improve performance in areas with increased absorption by CDOM and scattering by suspended sediments. Chl *a* concentrations are estimated by a triplicate look up table (LUT) approach, using the OC maximum band ratio, normalised water leaving radiance ($nL_w(\lambda)$ at 412 and 555 nm; Gohin et al., 2002). The algorithm was developed using

observations in the English Channel and Bay of Biscay, but has been shown to perform well in other areas with high CDOM and/or sediment loads (Tilstone et al., 2011, 2017).

The GSM semi analytical model (Garver and Siegel, 1997; Maritorena et al., 2002) simultaneously estimates Chl *a*, absorption by detrital and dissolved matter at 443 nm, and particle backscatter at 443 nm using non-linear optimisation of the R_{rs} spectrum. The underlying bio-optical model is:

$$R_{rs}(\lambda) = \left\{\sum_{i=1}^{2} g_i \left[\frac{b_{bw} + b_{bp}(\lambda_0)\left(\frac{\lambda}{\lambda_0}\right)^{-\Upsilon}}{b_{bw} + b_{bp}(\lambda_0)\left(\frac{\lambda}{\lambda_0}\right)^{-\Upsilon} + a_w(\lambda) + chla * a^*_{ph}(\lambda) + a_{dg}(\lambda_0)\exp[-S_{dg}(\lambda-\lambda_0)]}\right]^i\right\} 0.5238 \quad (2.3)$$

Where $\lambda_0 = 443$, and g_i, γ, S_{dg} and $a^*_{ph}(\lambda)$ are predefined values (Maritorena et al., 2002) and 0.5238 is a conversion from below water to above water R_{rs}. The GSM has the advantage of solving for multiple parameters simultaneously.

The Color Index (CI) method was developed for the clearest waters (Hu et al., 2012) to reduce impacts from artefacts and biases due to residual glint, stray light, and atmospheric correction errors in the R_{rs} spectra. A three band reflectance difference method was used between $R_{rs}(555)$ and a linear baseline between $R_{rs}(443)$ and $R_{rs}(670)$. For MODIS-A, the associated bands are band shifted to those required by the CI. The approach is merged with the OC algorithm (OCI) in the standard NASA Chl *a* algorithm to improve retrievals in the oligotrophic gyres (Hu et al., 2012). For this work, the CI was merged with OC3 and OC5 (OC3-CI and OC5-CI) blending linearly between 0.15 and 0.2 mg m^{-3}.

2.2.5 NPP Algorithms

NPP was determined using three algorithms, which have previously shown to be accurate regionally in the Atlantic Ocean and/or the South Atlantic Ocean (Campbell et al., 2002; Carr et al., 2006; Dogliotti et al., 2014; Friedrichs et al., 2009; Lobanova et al., 2018; Tilstone et al., 2015a, 2009). In each case, satellite Chl *a* determined by the best performing algorithm was used as input. The Vertical Generalized Production Model (VGPM; Behrenfeld and Falkowski, 1997) estimates NPP in the euphotic zone (1% light level) taking the form:

$$NPP_{VGPM} = Chla\ z_{eu}\ 0.66125\ \left[P^B_{opt}\frac{I_0}{4.1+I_0}\right]DL \quad (2.4)$$

Where DL is the day length, z_{eu} is the euphotic zone depth and I_0 is the daily surface PAR. P^B_{opt} is the biomass specific optimum photosynthetic rate retrieved as a function of SST (Behrenfeld and Falkowski, 1997b).

The Platt and Sathyendranath model (PSM; Platt et al., 1991) estimates daily NPP at a specific depth (z), based on an exponential photosynthetic-irradiance (P-I) function (square brackets):

$$NPP(z)_{PSM} = Chla(z)\left[P^B_m\left(1-\exp\left(-\frac{\alpha^B I(z)}{P^B_m}\right)\right)\right]DL \quad (2.5)$$

where, I(z) is PAR at z. The P-I function is driven by two parameters: the biomass specific maximum photosynthetic rate (P^B_m) and the initial slope of the light-dependent photosynthetic rate (α^B). These parameters cannot be determined using remote sensing, therefore *in situ* values were used from a published database (Bouman et al., 2018) averaged across the provinces (Fig. 2.1) and seasons in which the *in situ* NPP were sampled; P^B_m = 3.43 mg C (mg Chl)$^{-1}$ h^{-1} and α^B = 0.039 mg C (mg Chl)$^{-1}$ h^{-1} (µEm^{-2}s^{-1})$^{-1}$. $NPP(z)_{PSM}$ was integrated to z_{eu} to provide total water column NPP_{PSM} (Lobanova et al., 2018).

The P-I function was propagated through the water column using the Beer-Lambert-Bouguer law, as a function of surface PAR (I_0):

$$I(z) = I_0\exp(-K_d z) \quad (2.6)$$

Where K_d is the downwelling diffuse attenuation coefficient of PAR. Z_{eu} for the VGPM and PSM was estimated using the following equation, derived from equation 2.6, assuming I_0 is 100% of the surface PAR and PAR at the euphotic zone depth is 1%:

$$z_{eu} = -\frac{\ln(0.01)}{K_d} = \frac{4.6}{K_d} \quad (2.7)$$

Where K_d for the PAR spectrum was calculated as a function of K_d at 490 nm (Morel et al., 2007) available from satellite estimates (see Section 2.2.7 for data source). The PSM was therefore run as a broad-band model using PAR as the input light parameter.

The Wavelength Resolved Model (WRM) of Morel (1991), implemented following Smyth, Tilstone and Groom (2005), spectrally resolves the irradiance and associated phytoplankton response. The WRM takes the form:

$$NPP_{WRM} = 12\, a^{*}_{max}\phi_m \int_0^{DL} \int_0^{z_{eu}} \int_{400}^{700} Chl\, a(z)\, PUR\,(z,t,\lambda)\, f\big(x(z,t)\big)\, d\lambda\, dz\, dt \quad (2.8)$$

where, a^{*}_{max} is the maximum phytoplankton Chl *a* -specific absorption coefficient and Φ_m is the maximum quantum yield for growth, both parametrised using Chl *a* following Morel et al. (1996), and PUR is the phytoplankton usable radiation. The PSM can also be run in a wavelength resolving configuration. The above-water incident PAR was computed from the Gregg and Carder (1990) model at 5 nm wavelength and 1 minute time resolution. Meteorological and ozone data were obtained from the National Centres for Environmental Prediction (NCEP) and Earth Total Ozone Mapping Spectrometer data (EPTOMS), respectively. Cloud cover fields were obtained from the European Centre for Medium Range Weather Forecasts (ECMWF) ERA5 model reanalysis product, downloaded from the Copernicus Climate Data Store (CCDS; https://cds.climate.copernicus.eu/), and used to modify the light field following Reed (1977). NPP_{WRM} was integrated to the same z_{eu} as the VGPM and PSM, computed using equation 7.

2.2.6 NCP Algorithms

NCP was estimated using four empirical algorithms as described in Tilstone et al. (2015b). All four algorithms are based on a power law relationship between NPP and NCP. NCP-A was derived using data from mainly net heterotrophic areas of the North Atlantic Ocean (negative NCP). NCP-B was derived using data from mainly net autotrophic areas of the North Atlantic Ocean (positive NCP; Serret et al., 2009). These algorithms take the form:

$$NCP_A = 49.53 * \int {}^{14}C\, NPP^{0.48} - 300 \quad \text{(AMT6 Model)} \quad (2.9)$$

$$NCP_B = 212.01 * \int {}^{14}C\, NPP^{0.15} - 300 \quad \text{(AMT11 Model)} \quad (2.10)$$

Two further algorithms, NCP-C and NCP-D, were developed using data spanning net autotrophic and net heterotrophic regimes in the Atlantic Ocean, but weighted towards the North Atlantic Ocean. An additional relationship between NCP and SST is included in the NPP exponent for NCP-D (Tilstone et al., 2015b):

$$NCP_C = 163.83 * \int {}^{14}C\ NPP^{0.2035} - 300 \quad (2.11)$$

$$NCP_D = 179.86 * \int {}^{14}C\ NPP^{(0.2487+(-0.0036*SST))} - 300 \quad (2.12)$$

2.2.7 MODIS-A Data

MODIS-A Level 1 images downloaded from the NASA Ocean Colour website (https://oceancolor.gsfc.nasa.gov) were processed to Level 2 (Reprocessing 2018) 1 km products using SeaDAS v7.5 using the standard atmospheric correction and projected onto a linearly spaced 1 km grid for matchup analysis. PAR, $K_d(490)$ and SST were processed alongside Chl *a* using standard MODIS-A algorithms, as described on the NASA Ocean Colour website (https://oceancolor.gsfc.nasa.gov/atbd/), as inputs to the NPP and NCP algorithms. The AMT, BEN and BRAZ Chl *a* datasets used 56, 38 and 30 images respectively for matchup analysis.

The procedure for matchup analysis described in Brewin et al. (2016) was followed using level 2, 1 km products. Although Brewin et al. (2016) highlighted that level 3, 4 km products could be used to evaluate the continuously measured AMT Chl *a* dataset, NPP and NCP *in situ* measurements represent discrete water samples, driving the choice of level 2, 1 km products. Discrete station data were subjected to the same quality checks (Brewin et al., 2016), including the elimination of data collected at night, leading to an approximate time window of ± 8 hours, to remain consistent between continuous and discrete datasets. A 3 × 3 pixel window centred on each 1 km station-matchup pixel was selected to test for spatial homogeneity, and matchups with fewer than 5 valid pixels within the 3 × 3 pixel windows (after standard L2 flags were applied), were excluded from further analysis (Bailey and Werdell, 2006).

After selection of the most accurate algorithms, MODIS-A monthly 4 km Chl *a* composites were produced for the entire South Atlantic domain using OC3-CI. Monthly composites of NPP were computed with the WRM using the LUT described in Smyth et al. (2005), using additional input composites of MODIS-A PAR, $K_d(490)$ and SST downloaded from the NASA Ocean Colour website (https://oceancolor.gsfc.nasa.gov/l3/). Monthly NCP composites were assembled using NCP-D, to perform a monthly time series analysis against climate indices and environmental drivers between July 2002 and December 2018. Monthly NCP anomalies were calculated on a per pixel basis, by

subtracting from the monthly NCP the corresponding month's climatological NCP value computed using a time series between 2002 and 2018.

2.2.8 Uncertainties in satellite data

The combined uncertainty in the satellite measurements ($\text{Ɛ}C_{ALGORITHM}$) was estimated as the combination of three components (BIPM, 2008). Firstly, the stated uncertainty of the algorithm ($\text{Ɛ}a_{ALGORITHM}$) during the parameterisation with *in situ* data was taken from the literature (see Table 1). Secondly, the spatial uncertainty in the satellite data ($\text{Ɛ}s_{ALGORITHM}$) were estimated using the standard deviation of the 3 × 3 pixel grid used to test for homogeneity. Finally, the uncertainty attributed to the satellite input parameters ($\text{Ɛ}i_{ALGORITHM}$) was calculated as follows: In the case of Chl *a*, Ɛi is the R_{rs} uncertainty, which is outside the scope of the work; For NPP and NCP algorithms Ɛi was estimated using a Monte Carlo uncertainty propagation, where 1000 calculations were made perturbing the input products using random noise representing the uncertainty on the MODIS-A retrieval of each parameter ($\text{Ɛ}R_{PARAMETER}$). ƐR for Chl *a* and NPP were assessed in this paper as $\log_{10}$ root mean square difference (log-RMS) values. ƐR for SST was taken as the RMS value of a comparison of MODIS-A SST to *in situ* skin SST (details in Appendix 2.3; Table A2.7). ƐR for PAR and $K_d(490)$ were estimated using SeaWiFS Bio-optical Archive and Storage System (SeaBASS) matchups between *in situ* and MODIS-A data from a global dataset (PAR ƐR = 5.6 Einstein $m^{-2}\,d^{-1}$, and $K_d(490)$ ƐR = 0.257 in $\log_{10}$ space).

The three components (Ɛa, Ɛs and Ɛi) are assumed to be independent, and combined in quadrature (Taylor, 1997) to estimate $\text{Ɛ}C_{ALGORITHM}$ for each matchup:

$$\text{Ɛ}C = \sqrt{\text{Ɛ}a^2 + \text{Ɛ}s^2 + \text{Ɛ}i^2} \qquad (2.13)$$

2.2.9 Weighted Statistical Analyses

Measured and satellite estimates of each parameter were compared in $\log_{10}$ space. To enable $\log_{10}$ transformation of NCP estimates, the minimum value of the satellite matchups (-170 mmol O_2 $m^{-2}\,d^{-1}$) was added to each value.
The measured and satellite estimates were first evaluated using a non-weighted statistical approach to assess the performance of satellite algorithms (e.g:

Brewin et al., 2015; Dogliotti et al., 2014, 2009). A Type-II regression analysis was employed to calculate the slope, intercept and the percentage variability explained by the linear regression (R^2). To evaluate the accuracy of each model, the absolute percentage difference (APD), log-RMS and the mean (M) and standard deviation (S) of the $\log_{10}$ difference were calculated. Following the methods of Campbell et al. (2002) the inverse $\log_{10}$ difference between the *in situ* and satellite values of 10^{M} (F_{med}), 10^{M+S} (F_{max}) and 10^{M-S} (F_{min}) were calculated. The number of matchups used to compute the statistics (N) is also given.

Table 2.1 – Tabulated algorithm uncertainties (Ɛa) used for parameterisation with in situ data from the literature. * indicates for OC3-CI and OC5-CI the uncertainty is assumed to be the same as the non-CI version. ** indicates for the PSM an uncertainty value to our knowledge is unavailable, and therefore assume the same value as the VGPM.

Algorithm	Algorithm Uncertainty (Ɛa)	Reference
Chl *a* Algorithms Uncertainty units: $\log_{10}$(mg m^{-3})		
OC3 + OC3CI*	0.255	NASA Oceancolour Website
GSM	0.156	(Maritorena et al., 2002)
OC5 + OC5CI*	0.220	(Gohin et al., 2002)

NPP Algorithms Uncertainty units: $\log_{10}$(mg C m^{-2} d^{-1})		
VGPM	0.24	(Friedrichs et al., 2009)
PSM	0.24**	N/A
WRM	0.16	(Smyth et al., 2005)

NCP Algorithms Uncertainty units: mmol O_2 m^{-2} d^{-1}		
NCP-A	103	(Tilstone et al., 2015b)
NCP-B	46	(Tilstone et al., 2015b)
NCP-C	40	(Tilstone et al., 2015b)
NCP-D	35	(Tilstone et al., 2015b)

The estimates were then evaluated by a weighted statistical approach using weighted variants of the previously mentioned statistics. The weights for each matchup were computed using Ɛins and ƐC:

$$weight = \frac{1}{\sqrt{\varepsilon\text{ins}^2 + \varepsilon\text{C}^2}} \quad (2.14)$$

The weights were rescaled between zero and one. This approach allows the satellite and *in situ* uncertainties to be accounted for in the statistical analysis, which was not previously possible, because *in situ* data uncertainties were not determined. The approach emphasises matchups where both the satellite and *in situ* measurements are more certain, while less certain matchups produce a smaller effect on the overall statistics. For the BRAZIL and BEN datasets, no *in situ* uncertainty could be calculated, and therefore the weighting uses only the satellite uncertainty (Appendix 2.2). NCP algorithms were assessed firstly driven using *in situ* NPP and *in situ* SST, and secondly driven by MODIS-A estimates.

2.2.10 Uncertainty Perturbation Analysis

Following the methods of Saba et al. (2011), a perturbation analysis was conducted to determine the potential reduction in NCP-D log-RMS which could be attributed to uncertainties in the satellite input parameters and *in situ* NCP. This analysis quantifies the range of uncertainty introduced in satellite NCP estimates from the input parameters, including the *in situ* NCP used to validate these estimates. Each of the input parameters; Chl *a*, PAR and SST can have three possible values for each NCP measurement (original value, original – ƐR and original + ƐR). The WRM algorithm used to determine NPP also has an uncertainty (log-RMS found in this paper, using weighted statistics: 0.20; Table 2.3), and therefore three values are also possible. For each NCP measurement, 81 perturbations of the input data were calculated. Similarly, each *in situ* NCP measurement could also have three perturbations (original value, original - $\varepsilon\text{ins}_{\text{NCP}}$, original + $\varepsilon\text{ins}_{\text{NCP}}$). Log-RMS was used to assess the performance of NCP-D under different scenarios. For each NCP measurement, the 81 perturbations were examined and the perturbation that produced the lowest log-RMS from 4 scenarios was selected, in order to assess the potential reduction in log-RMS that could be attributed to each of the parameters. The 4 scenarios tested were: (1) uncertainty in individual input parameters (Chl *a*, PAR, SST and

NPP algorithm), (2) uncertainty in all input parameters together, (3) uncertainty in *in situ* NCP measurements and (4) uncertainty in all input parameters *and in situ* NCP. The analysis focused on the reduction in log-RMS, however considering the uncertainties from the input parameters could also increase log-RMS. The input parameter uncertainties that have the greatest control on satellite NCP uncertainties were therefore indicated. Additionally, for scenarios two and four the combination of multiple parameter perturbations could lead to compensating effects (i.e. one parameter reducing and another increasing the log-RMS reduction). These scenarios provide a useful indicator of the overall impact of satellite data (scenario two) and satellite with *in situ* data uncertainties (scenario four).

2.2.11 Climate Indices and Environmental Drivers

Climate indices indicate large-scale variability in physical parameters in the ocean. Satellite estimated NCP anomalies were compared to three climate indices: the North Atlantic Oscillation (NAO), indicating atmospheric pressure conditions in the North Atlantic, downloaded from http://www.cgd.ucar.edu/cas/catalog/; the Multivariate ENSO Index (MEI) as an indicator of El Niño Southern Oscillation (ENSO) phases, downloaded from https://www.esrl.noaa.gov/psd/enso/mei and the Southern Annular Mode (SAM), indicating the displacement of the westerly winds in the Southern Ocean, downloaded from http://www.nerc-bas.ac.uk/icd/gjma/sam.html.

Changes in wind forcing can affect the distribution of phytoplankton through changes in the mixed layer. ECMWF ERA5 monthly wind speeds were downloaded from the CCDS (https://cds.climate.copernicus.eu/), with a resolution of 0.25°, coincident with the MODIS-A NCP time series (July 2002 – December 2018). Wind speed anomalies were calculated by subtracting from the monthly wind speed, the corresponding monthly climatology value calculated from the ECMWF ERA5 wind speed.

Sea Level Height Anomalies (SLHA) can be associated with mesoscale processes and water mass changes, which can contribute to changes in phytoplankton distributions across basins. Monthly mean SLHA were downloaded from AVISO+ (https://www.aviso.altimetry.fr/) coinciding with the

MODIS-A NCP time series at a resolution of 0.25°. Anomalies were calculated by AVISO+ with respect to a 25 year climatology between 1993 and 2018.

2.2.12 Time series Analysis

Mean monthly NCP anomalies were averaged from 4 km monthly NCP anomaly maps for the South Atlantic Longhurst provinces; WTRA, ETRA, SATL, BRAZ, BENG, FKLD and SSTC (Fig. 2.1; Longhurst, 1998). The potential drivers of NCP variability were explored firstly by calculating Spearman correlation coefficients between monthly province-averaged NCP anomalies, climate indices and environmental drivers. The use of anomalies to determine correlations reduces the effect of temporal autocorrelation which may complicate interpretation.

Averaging NCP anomalies over the provinces may highlight the dominant drivers of variability but mask the effects of opposing trends within a province as well as the more subtle and localised drivers, such as mesoscale eddies. The localised forcing is explored using a per pixel correlation approach, where a monthly time series of NCP anomalies is generated for each 4 km pixel for comparison against environmental drivers (Spearman correlation, $\alpha = 0.05$). Spatial autocorrelation was tested using the method of field significance (Wilks, 2006).

The uncertainties in NCP anomalies were propagated through the Spearman correlations using a Monte Carlo uncertainty propagation. Each monthly NCP measurement in the time series, was perturbed with random noise representing the uncertainty of the MODIS-A NCP estimate 1000 times as in Section 2.2.8, and the Spearman correlations were repeated. The 95% confidence interval was calculated from the resulting distribution of the correlations. The correlation was deemed significant ($\alpha = 0.05$), where the 95% confidence interval remained significant. The per pixel analysis was repeated for NPP and SST anomalies.

2.3 Results

2.3.1 Accuracy assessment of MODIS-A Chl *a*.

Weighted regression analysis between *in situ* Chl *a* and five MODIS-A algorithms for data collected on seven AMT campaigns is given in Fig. 2.2, and the associated statistical analysis are given in Table 2.2. Using the weighted

approach to determine the algorithm performance, all five algorithms performed similarly, with $R^2 > 0.9$ and log-RMS < 0.20. OC3-CI, the standard MODIS-A algorithm, showed the best performance with the lowest log-RMS, slope close to 1 and F_{min}, F_{med} and F_{max} close to 1. All algorithms had positive M indicating a tendency to underestimate Chl *a*. OC5-CI, GSM and OC5 were characterised by higher values of M compared to OC3-CI and OC3, and by F_{med} and F_{max} values greater than 1, highlighting that these three algorithms perform worse compared to OC3-CI and OC3 at the medium and maximum range Chl *a* values (Table 2.2). OC3-CI and OC5-CI showed lower scatter at Chl *a* < 0.15 mg m^{-3} (Fig. 2.2a, e), compared to OC3 and OC5 (Fig. 2.2b, d), which resulted in a lower S over this range (Table 2.2).

For both the BEN and BRAZIL datasets the weighting used only the satellite uncertainty. For the BEN, the trend in MODIS-A Chl *a* algorithms was similar to that of the AMT dataset except for the GSM (Appendix 2.2 Table A2.6), which had a higher log-RMS, higher S and negative M and a tendency to overestimate Chl *a* above 3 mg m^{-3} (Fig. 2.2c). For the BRAZIL dataset, the trends were different (Appendix 2.2 Table A2.5); the GSM exhibited the worst performance with lowest R^2, highest log-RMS, M and S, indicating a failure in the algorithm to estimate Chl *a* accurately in this region (Fig. 2.2c).

Table 2.2 – Performance indices for satellite chlorophyll a algorithms using the AMT dataset. Log-differences uncertainties in satellite estimates are mean (M), standard deviation (S) and Root Mean Square (log-RMS). The mean and one sigma range of the difference are given as; F_{med}, F_{min} and F_{max}; values closer to 1 indicate greater accuracy. APD is the Absolute Percentage Difference. N indicates the number of matchups used to compute statistics. The most accurate algorithm for each statistic is highlighted in bold. Statistics were computed by weighting each station based on the in situ and satellite uncertainty (weighted). The statistics were performed on firstly, all the available matchups, and secondly, on matchups where in situ Chl a < 0.15 mg m^{-3}.

Weighted (All)												
	Model	R^2	Slope	Intercept	log-RMS	APD	M	S	F_{min}	F_{med}	F_{max}	N
AMT	OC3-CI	**0.93**	**0.96**	**-0.08**	**0.16**	**123**	**0.06**	**0.14**	0.83	1.16	**1.61**	1440
	OC3	0.91	**0.96**	**-0.08**	**0.17**	**122**	**0.05**	0.16	0.78	**1.13**	1.65	1440
	GSM	0.91	**0.96**	**-0.10**	0.18	144	0.09	0.16	0.84	1.22	1.77	1440
	OC5	0.91	0.92	-0.13	0.19	166	0.08	0.17	0.82	1.21	1.79	1440
	OC5-CI	**0.93**	0.93	-0.12	0.18	163	0.09	**0.15**	**0.87**	1.23	1.74	1440
Weighted (Chl < 0.15 mg m^{-3})												
AMT	OC3-CI	**0.87**	**1.05**	0.04	**0.10**	**6.9**	**0.01**	**0.10**	**0.81**	1.03	**1.30**	884
	OC3	0.74	1.05	0.06	0.14	9.4	**0.00**	0.14	0.72	**1.00**	1.40	884
	GSM	0.72	1.02	**0.00**	0.14	9.5	0.03	0.14	0.79	1.08	1.48	884
	OC5	0.74	1.04	0.03	0.14	8.6	**0.01**	0.14	0.75	**1.02**	1.40	884
	OC5-CI	**0.87**	**1.05**	0.04	**0.10**	**7.0**	**0.02**	**0.10**	**0.83**	1.05	**1.33**	884

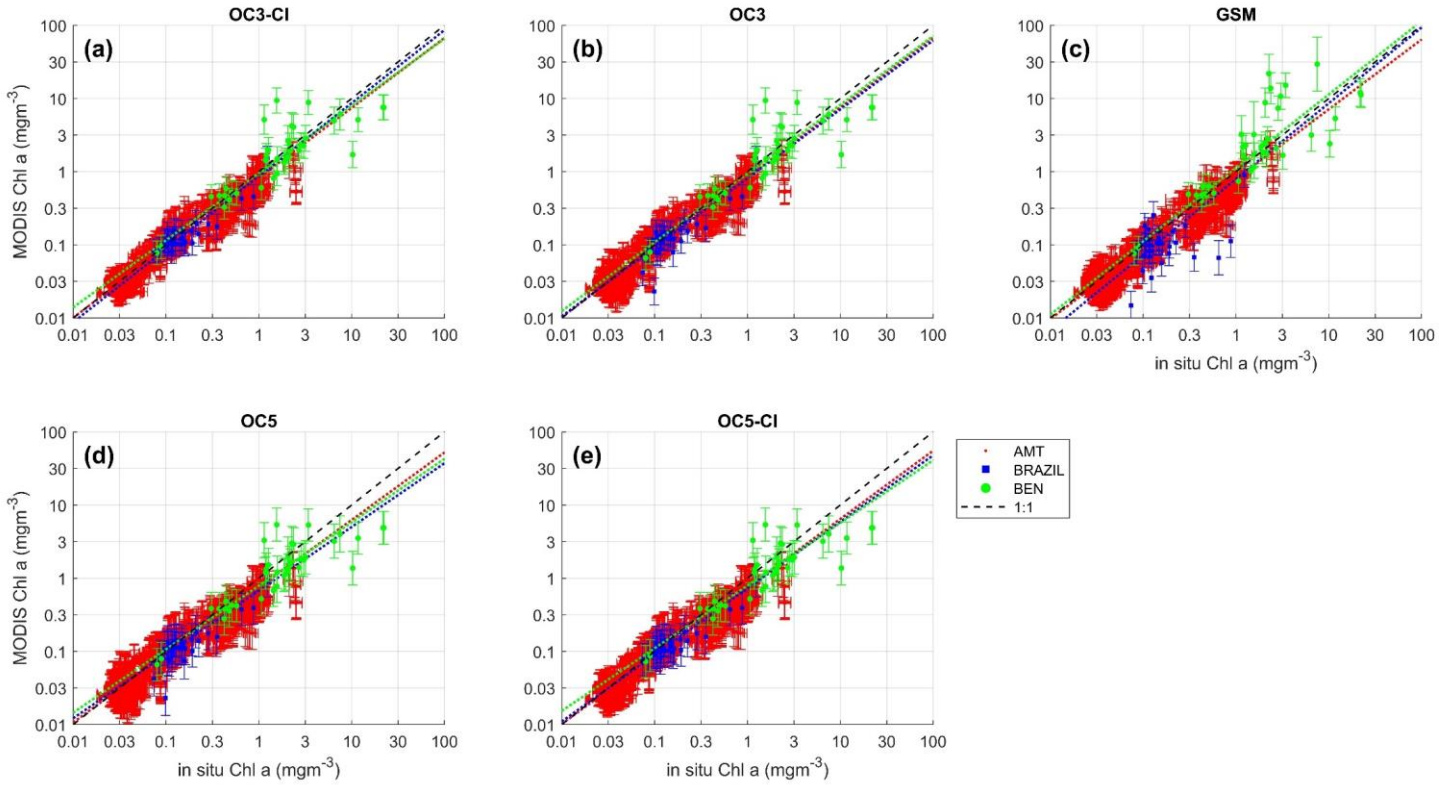

Figure 2.2 - Comparison of in situ and MODIS-A estimates of chlorophyll a for: (a) OC3-CI, (b) OC3, (c) GSM, (d) OC5 and (e) OC5-CI. Algorithms are described in section 2.2.3. Red points indicate satellite matchups with the continuous Atlantic Meridional Transect (AMT) dataset, blue squares the Brazilian dataset (BRAZIL) and green squares the Benguela dataset (BEN). Black dashed line is 1:1 line, red dashed line is a weighted Type-II linear regression for the AMT dataset, blue dashed line is a weighted Type-II linear regression for the Brazilian dataset and green dashed line the weighted Type-II linear regression for the Benguela dataset. Horizontal error bars indicate in situ uncertainty ($Ɛins_{CHLA}$). Vertical error bars indicate the combined satellite uncertainty (ƐC).

2.3.2 Accuracy assessment of MODIS-A NPP

There was a high variability in the *in situ* NPP uncertainty at each station. This was accounted for using the weighted method, which then showed that the WRM exhibited the best performance (Table 2.3, Fig. 2.3) with the lowest log-RMS, slope closest to 1 and intercept closest to 0. The VGPM also had low log-RMS and M equal to 0 but displayed the lowest R^2 and the highest S (Table 2.3). The PSM had high R^2 but systematically underestimated NPP with F_{min}, F_{med} and F_{max} greater than 1.

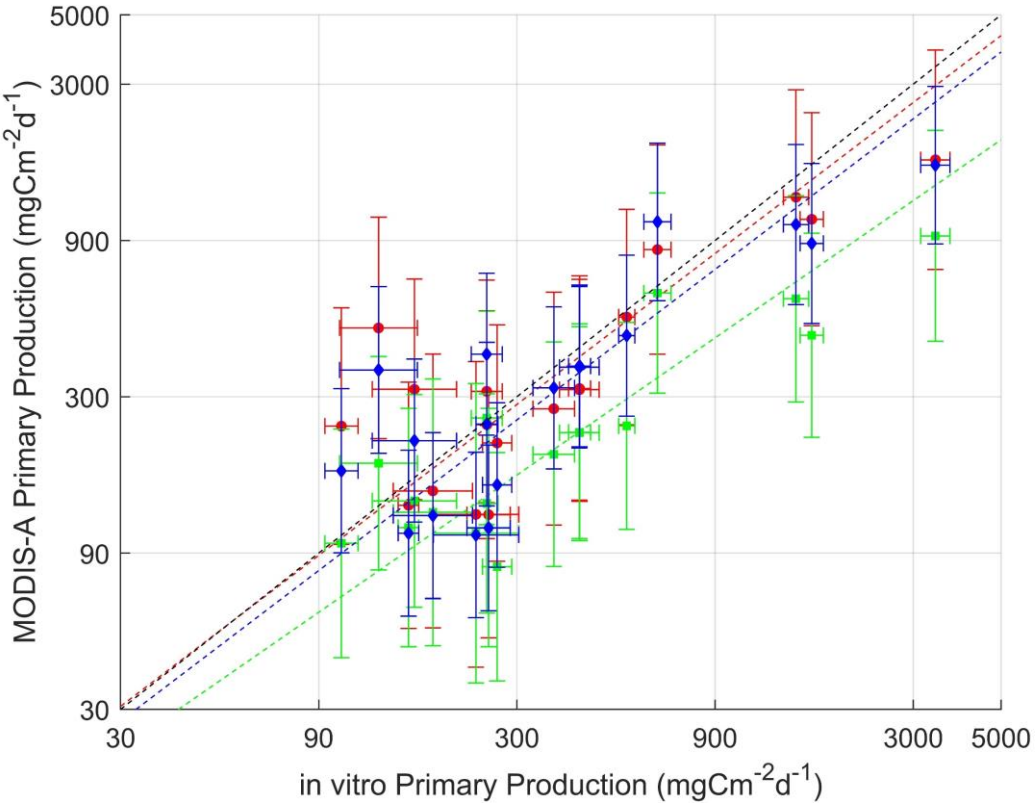

Figure 2.3 – Comparison of in vitro and MODIS-A estimated net primary production. Algorithms are described in section 2.5. Black dashed line is the 1:1 line. Red, green and blue dashed lines indicate a weighted Type-II linear regression for the VGPM, PSM and WRM respectively. Horizontal error bars indicate in situ uncertainty (Ɛins$PP). Vertical error bars indicate the combine satellite uncertainty (ƐC).

Table 2.3 - Performance indices for satellite net primary production algorithms. Log-differences uncertainties in satellite estimates are mean (M), standard deviation (S) and Root Mean Square (log-RMS). The mean and one sigma range of the difference are given as; Fmed, Fmin and Fmax; values closer to 1 indicate greater accuracy. APD is the Absolute Percentage Difference. N indicates the number of matchups used to compute statistics. The most accurate algorithm for each statistic is highlighted in bold. Statistics were computed by weighting each station based on the in situ and satellite uncertainty (weighted).

Weighted											
Model	R^2	Slope	Intercept	Log-RMS	APD	M	S	F_{min}	F_{med}	F_{max}	N
VGPM	0.72	**0.97**	0.06	**0.22**	**6.9**	**0.00**	0.22	0.61	**1.01**	**1.68**	18
PSM	**0.79**	0.88	0.05	0.32	9.6	0.25	0.20	**1.11**	1.77	2.82	18
WRM	**0.81**	**0.96**	**0.02**	**0.20**	**6.3**	0.07	**0.18**	0.78	1.18	1.79	18

2.2.3 Accuracy assessment of MODIS-A NCP

The four NCP algorithms were firstly run using *in situ* NPP and *in situ* SST (N = 84) to assess their accuracy (Fig. 2.4, Table 2.4). Using the weighted approach NCP-C was the most accurate, with low log-RMS and S and the highest R^2. NCP-D had a higher log-RMS and lower R^2. NCP-B tended to overestimate NCP, indicated by F_{min} and F_{med} less than 1 but had a similar log-RMS to NCP-C and NCP-D. NCP-A had the highest slope, log-RMS, M and S indicating a tendency to underestimate NCP with F_{min}, F_{med} and F_{max} all greater than 1.

MODIS-A SST and NPP using the WRM model were then applied to estimate NCP (N = 14; Fig. 2.5; Table 2.5). Using the weighted approach, NCP-D showed the highest R^2, low log-RMS and lowest S, and of all four algorithms was the most accurate. NCP-C showed a similar accuracy, but the slope deviated further from 1. Both algorithms tended to underestimate NCP when driven by MODIS-A NPP, compared to the *in situ* NPP. NCP-B tended to overestimate NCP, indicated by F_{min} less than 1. NCP-A tended to underestimate NCP indicated by F_{med} and F_{max} greater than 1, low R^2 and high log-RMS.

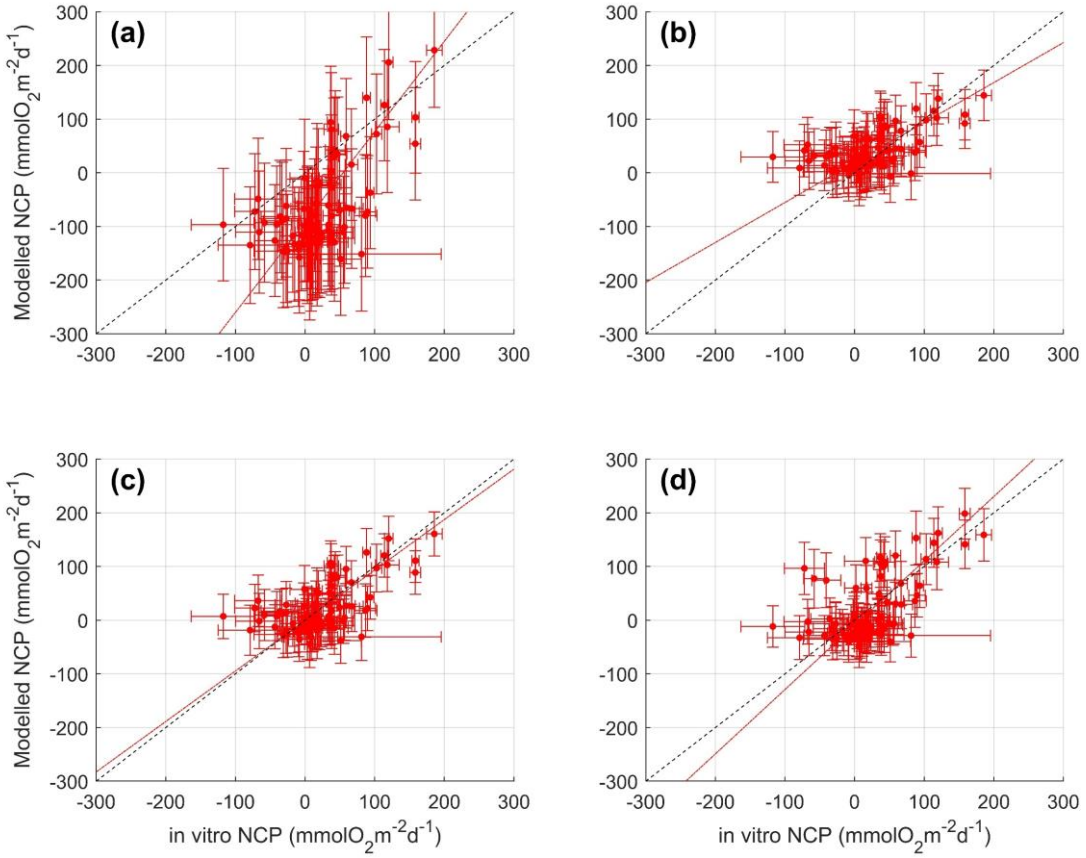

Figure 2.4 - Comparison of net community production (NCP) algorithms driven using in situ net primary production and sea surface temperature where each scatter plot refers to (a) NCP-A, (b) NCP-B, (c) NCP-C and (d) NCP-D. Algorithms are described in section 2.2.6. Black dashed line is the 1:1 line. Red dashed line indicates a weighted Type-II linear regression. Horizontal error bars indicate in situ uncertainty (Ɛins$NCP). Vertical error bars indicates the in situ uncertainty in NPP and SST propagated through the NCP algorithms.

Table 2.4 - Performance indices for net community production (NCP) algorithms driven by in situ net primary production and in situ sea surface temperature. To log transform negative NCP values, we added the minimum value (-170 mmol O_2 $m^{-2}d^{-1}$) to all values. Log-differences uncertainties in satellite estimates are mean (M), standard deviation (S) and Root Mean Square (log-RMS). The mean and one sigma range of the difference are given as; Fmed, Fmin and Fmax; values closer to 1 indicate greater accuracy. APD is the Absolute Percentage Difference. N indicates the number of matchups used to compute statistics. The most accurate algorithm for each statistic is highlighted in bold. Statistics were computed by weighting each station based on the in situ and satellite uncertainty (weighted).

Weighted											
Model	R^2	Slope	Intercept	Log-RMS	APD	M	S	F_{min}	F_{med}	F_{max}	N
A	0.17	1.17	-0.68	0.53	18.11	0.39	0.36	**1.09**	2.47	5.60	84
B	**0.30**	**0.93**	0.16	**0.11**	**3.4**	-0.04	**0.10**	0.72	0.90	**1.14**	84
C	**0.31**	**0.95**	**0.09**	**0.10**	**3.5**	**0.00**	**0.10**	0.79	**1.00**	1.28	84
D	0.26	0.90	0.17	**0.12**	**4.2**	**0.02**	**0.12**	0.80	1.05	1.37	84

2.3.4 Uncertainty Perturbation Analysis

For the scenario in which the uncertainty in both the input parameters and *in situ* NCP measurements were considered, log-RMS decreased by 87% (Table 2.6). The uncertainties in the NPP model (40%) and *in situ* NCP (36%) accounted for the largest reduction in log-RMS. Chl *a* uncertainties accounted for a reduction in log-RMS of 22%, whereas PAR and SST contributed the smallest reductions in the log-RMS of 2.8% and 3.5% respectively.

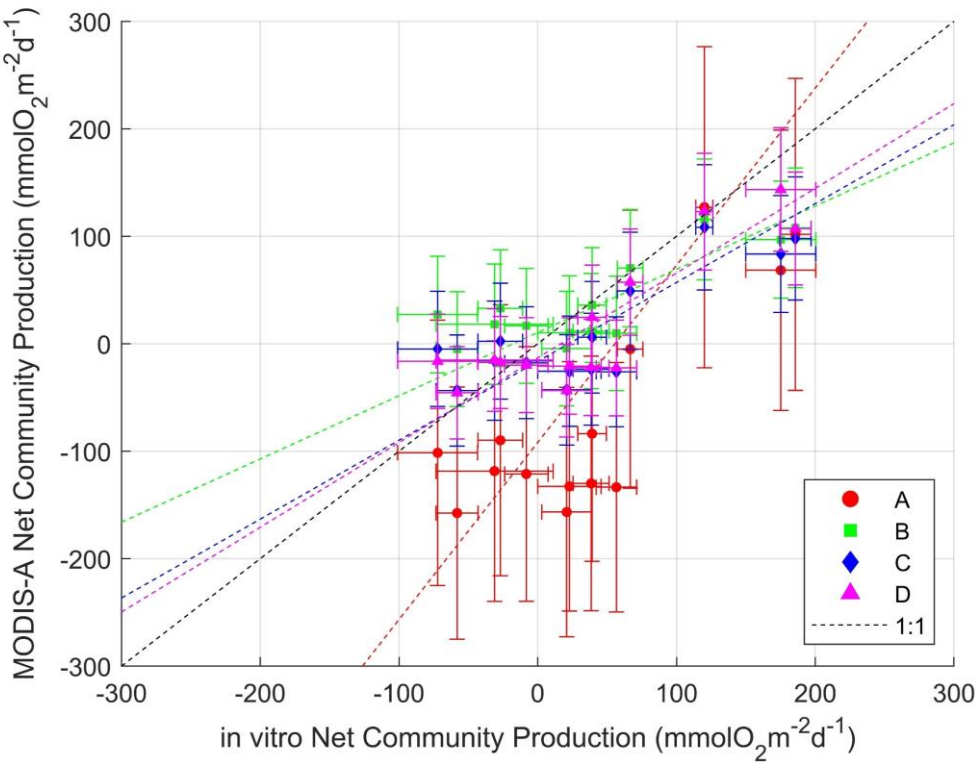

Figure 2.5 – Comparison of in vitro and MODIS-A estimated net community production (NCP). Algorithms are described in section 2.2.6. Black dashed line is the 1:1 line. Red, green, blue and pink dashed lines indicate a weighted Type-II linear regression for the A, B, C and D respectively. Horizontal error bars indicate in situ uncertainty (Ɛins$_{NCP}$). Vertical error bars indicate the combine satellite uncertainty (ƐC).

Table 2.5 – Performance indices for satellite net community production (NCP) algorithms. To log transform negative NCP values, we added the minimum value (-170 mmol O_2 $m^{-2}d^{-1}$) to all values. Log-differences uncertainties in satellite estimates are mean (M), standard deviation (S) and Root Mean Square (log-RMS). The mean and one sigma range of the difference are given as; F_{med}, F_{min} and F_{max}; values closer to 1 indicate greater accuracy. APD is the Absolute Percentage Difference. N indicates the number of matchups used to compute statistics. The most accurate algorithm for each statistic is highlighted in bold. Statistics were computed by weighting each station based on the in situ and satellite uncertainty (weighted).

Weighted											
Model	R^2	Slope	Intercept	Log-RMS	APD	M	S	F_{min}	F_{med}	F_{max}	N
A	0.54	**0.99**	-0.11	0.48	14.4	0.33	0.34	**0.97**	2.14	4.70	14
B	0.64	0.96	0.04	**0.10**	**3.4**	**0.01**	**0.10**	0.81	**1.03**	**1.30**	14
C	0.62	0.96	**0.01**	**0.12**	**4.5**	0.07	**0.10**	0.93	1.17	1.48	14
D	**0.70**	**0.98**	**0.00**	**0.11**	**3.5**	0.06	**0.09**	0.93	1.14	1.40	14

Table 2.6 – Perturbation analysis results showing the percentage reduction in NCP-D log-RMS under different scenarios as described in section 2.2.10. The first five scenarios use single parameter perturbations to determine the individual reductions in log-RMS when accounting for the uncertainties. The further two scenarios determine the reduction in log-RMS when firstly all input parameters (Chl *a*, PAR, SST and NPP) are perturbed by their uncertainties, and secondly when all input parameters and the in situ NCP uncertainties are perturbed.

Scenario	Percentage reduction in log-RMS
Chl *a*	22%
SST	3.5%
PAR	2.8%
NPP	40%
in situ NCP	36%
All Input	61%
All Input and *in situ* NCP	87%

2.3.5 NCP Time series Analysis

Since NCP-D was the most accurate NCP algorithm, it was applied to the MODIS-A time series. There were no significant correlations between province-averaged NCP anomalies, climate indices and environmental drivers, when the uncertainties were accounted for.

On a per pixel basis and accounting for the uncertainties, there were significant correlations between NCP anomalies, with SLHA, wind speed anomalies, and the MEI (Fig. 2.6a, b, c). NCP anomalies were positively correlated with wind speed anomalies along the BENG coast (Fig. 2.6b). Negative correlations between NCP anomalies and SLHA occurred offshore in the BENG extending to the SATL (Fig. 2.6a). Significant negative correlations between NCP anomalies and SLHA, were also observed along the boundary between the SATL and SSTC. Positive correlations between NCP anomalies and wind speed anomalies, occurred in the SATL, especially around the centre of the South Atlantic gyre (Fig. 2.6b) which extended north into the WTRA. Patchy negative correlations between NCP anomalies and the MEI were observed (Fig. 2.6c), but were at the limits of significance (Wilks, 2006). No significant correlations were found between NCP anomalies and the NAO and SAM.

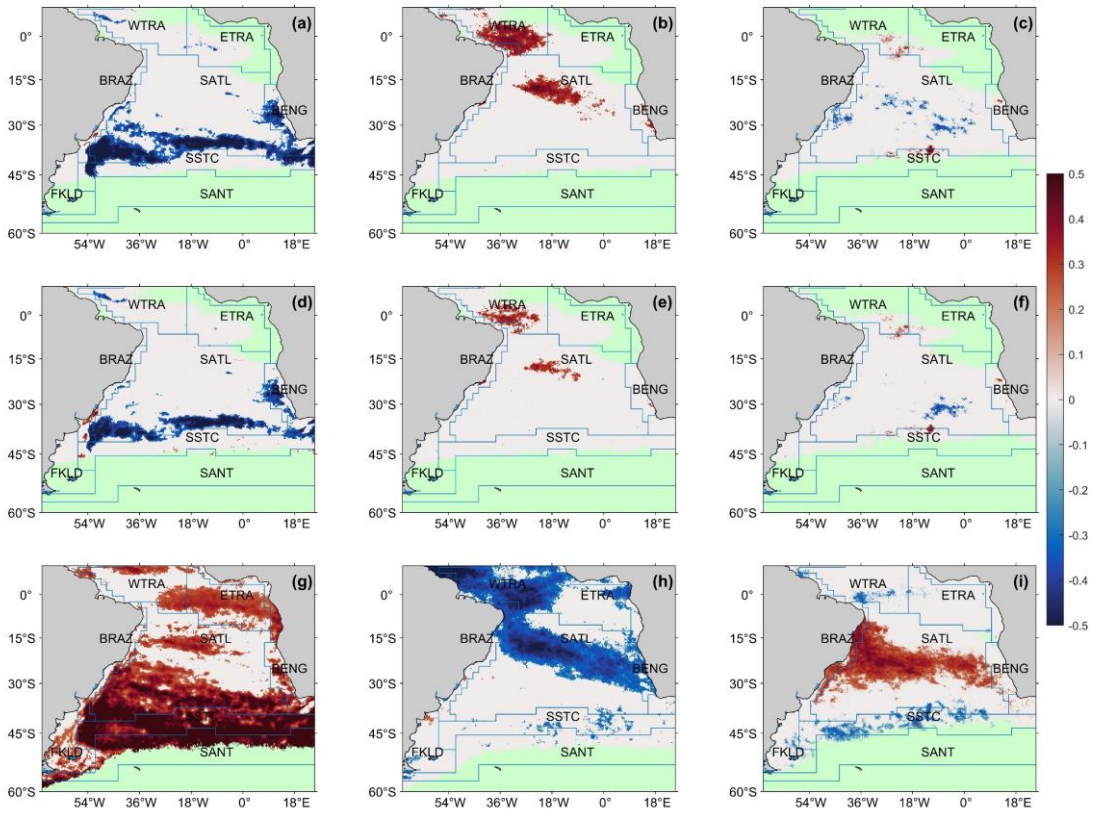

Figure 2.6 – Significant per pixel Spearman correlations between monthly satellite net community production (NCP-D) anomalies and (a) sea level height anomaly, (b) wind speed anomaly and (c) Multivariate ENSO Index (MEI). (d), (e) and (f) show the same for monthly satellite net primary production (WRM) anomalies and (g), (h) and (i) for monthly satellite sea surface temperature anomalies. The correlations were deemed significant when the 95% confidence interval of the Spearman correlation, determined through a Monte Carlo uncertainty propagation, remained significant (α = 0.05). Light grey regions indicate no significant correlation. Green areas indicate where more than 24 months of data are missing (N = 168 to 192).

2.4 Discussion

2.4.1 Satellite Uncertainty Analysis

This is one of the first studies to evaluate the performance of and uncertainties in MODIS-A Chl *a*, NPP and NCP over the entire South Atlantic basin, using a comprehensive *in situ* dataset. In the following sections the reasons for the algorithms performance and where and why some of them fail is explored.

2.4.1.1 Accuracy assessment of MODIS-A Chl *a*

Previous studies in this region showed that MODIS-A OC3M tends to underestimate Chl *a* on the Patagonian Shelf over a Chl *a* range of 0.2 to 6 mg

m^{-3} (Dogliotti et al., 2009) and 0.3 to 11 mg m^{-3} (Dogliotti et al., 2014). Dogliotti et al. (2009) suggested that the underestimate is caused by increased aerosol loading off the Patagonian deserts, generating lower than expected $R_{rs}(412)$ and $R_{rs}(443)$ retrievals. Our results would suggest that this is not a local underestimation. In this study, we found that OC3-CI performed most accurately out of the five algorithms tested. There was, however, a tendency in all algorithms tested to underestimate Chl *a*, especially at concentrations > 0.3 mg m^{-3} (Fig. 2.2).

Szeto et al. (2011) found that the Chl *a* in the Atlantic Ocean was generally overestimated, however the majority of their Atlantic data were from the North American coast. Brewin et al. (2016) showed that using the same AC-S derived Chl *a*, OC3M Chl *a* were close to the 1:1 line and had a low bias. Compared to our results this could suggest bio-optical differences between the North and South Atlantic, resulting in an underestimation that may relate to changes in CDOM to Chl *a* ratios (Szeto et al., 2011), driven by changes in the phytoplankton community structure (Organelli and Claustre, 2019).

MODIS-A is now in its 18th year of operation and has known degradation in the blue bands (412 and 443 nm; Meister and Franz, 2014). NASA have corrected for some of this and conducted a vicarious calibration for these bands; the newly reprocessed data (R2018) prove to be accurate (MODIS-A Reprocessing R2018, 2020). The OC5 algorithm uses the 412 nm band to account for atmospheric overcorrection and/or CDOM absorption. Anomalies with this band have previously been reported, associated with the performance of the GSM (Maritorena et al., 2010), and may explain why OC5 performs worse than the other algorithms tested. Differences in the reprocessing versions may account for the difference found in this study to previous studies (Brewin et al., 2016; Dogliotti et al., 2014, 2009; Kampel et al., 2009a). The regional bias for the South Atlantic shown in this study highlights the on-going need to monitor the performance of satellite ocean colour data, especially in regions where *in situ* data are sparse.

2.4.1.2 Accuracy assessment of MODIS-A NPP

Using MODIS-A OC3-CI Chl *a* as input to the NPP models, the WRM was the most accurate algorithm for this area, followed by the VGPM, similar to findings

of Tilstone et al. (2009) for the entire Atlantic basin. The general trend in all three algorithms was an underestimation of NPP, especially at higher values, and reflects the trend in MODIS-A Chl *a*. Platt and Sathyendranath (1988) showed that the largest contributor to NPP variability is Chl *a*. Using *in situ* Chl *a* data, Tilstone et al. (2009) showed that the WRM and VGPM tend to overestimate NPP in the SATL during the period 1998 to 2005. This contrasts our results using MODIS-A Chl *a*, which showed an underestimate in NPP, during 2002 to 2019, by a similar amount. Stations at which *in situ* NPP exceeded 700 mg C m^{-2} d^{-1} exhibited an underestimation in MODIS-A Chl *a*, whereas the remaining stations both over and under estimated satellite Chl *a*.

The PSM showed a systematic bias (Fig. 2.3) resulting in a higher underestimation of NPP compared to the WRM and VGPM. The photosynthetic parameters, P^B_m and α^B, used to parameterise the rate of photosynthesis in the PSM, are not used in the other models. Our data suggest that the regionally-averaged values of these parameters used in this study may be underestimated for the South Atlantic. Dogliotti et al. (2014) reported that the PSM performed well on the Patagonian Shelf when using *in situ* P^B_m and α^B, collected at the same time as Chl *a* data used for validation of NPP algorithms, but it is not possible to run the PSM at the basin scale in this way. To assess this further, the PSM was run using *in situ* P^B_m and α^B from the season and province of each individual station, but there was no improvement and an even higher systematic bias (M = 0.37, log-RMS = 0.41, N=17), indicating that the variability in the two photosynthetic parameters is not sufficiently represented by the available *in situ* data for the South Atlantic (Bouman et al., 2018; Platt and Sathyendranath, 1988).

2.4.1.3 Accuracy assessment of NCP

The NCP algorithms tested in this study are still in their infancy compared to NPP models, but the results are promising. Running the NCP algorithms with *in situ* NPP and SST showed that NCP-C performs slightly better than NCP-D (Table 2.4). This contrasts with Tilstone et al. (2015b), who found that over the entire Atlantic Ocean NCP-D was more accurate since it includes a temperature function which theoretically captures more of the natural variability in respiration rates. Howard et al. (2017) observed net autotrophic conditions in the SATL during austral autumn, which are also represented more accurately by NCP-C,

but observed NCP closer to estimates of NCP-D in the SSTC. Serret et al. (2015) highlighted that NCP is not just determined by NPP, with a heterogeneous relationship between NPP and respiration and substantial differences between the North and South Atlantic. The relationship between NPP and respiration could also change with the season (Serret et al., 2015), while the majority of the calibration data for NCP-C and NCP-D occurs in austral spring. Using satellite data alone however, NCP-D was the best performing algorithm (Table 2.5), and when driven with *in situ* NPP the differences to NCP-C were small.

2.4.1.4 Weighted Statistics and Perturbation Analysis

In situ measurements used to assess satellite algorithm performance have their own uncertainties (e.g. mean Ɛins_{NPP} in this study = 15%) and should not be assumed to be "100% accurate" as is common practice (e.g. Brewin et al., 2015; Dogliotti et al., 2014, 2009). The perturbation analysis conducted in this paper showed that 36% of the NCP algorithm uncertainty could be attributed to the *in situ* NCP uncertainty (Table 2.6), indicating that this is the highest accuracy that a satellite NCP algorithm can currently achieve (equivalent to 0.03 $\log_{10}$ mmol O_2 m^{-2} d^{-1}). A further 61% of the uncertainty was attributed to all of the satellite input parameters (Table 2.6), reinforcing the need to account for *in situ* as well as satellite uncertainties when assessing satellite algorithm performance, and therefore to use weighted statistics to account for the uncertainties in both the *in situ* data used to evaluate algorithm performance, and the satellite data used to run the algorithm. Differences between the unweighted and weighted statistics are clearer for discrete station measurements, such as NPP (Table 2.3; Appendix 2.1 Table A2.2) and NCP (Table 2.4, 2.5; Appendix 2.1 Table A2.3, A2.4), where uncertainties are unlikely to be constant.

Large *in situ* datasets have been compiled for Chl *a* to test the performance of satellite algorithms (e.g. Valente et al., 2019, 2016). These datasets contain discrete station measurements across the globe, but do not include the associated uncertainties. A weighted approach could also be expanded for algorithm development, where uncertainties in both the *in situ* calibration and validation datasets could also be used to evaluate the algorithm performance.

Uncertainties in the satellite data make the largest contribution to the total uncertainty. In this study we have not included the uncertainties associated with atmospheric correction and the resulting satellite R_{rs} (Li et al., 2019). Land et al. (2018) proposed a promising statistical approach to estimate some of these uncertainties in Chl *a* alone. This is beyond the scope of this study, but is an important topic to pursue in the future to trace the uncertainties in R_{rs} through Chl *a* to NPP to NCP.

2.4.2 Climate Indices and Environmental Drivers of NCP

Applying the most accurate satellite NCP and input parameter algorithms to the 16 year MODIS-A time series, enables the exploration of climate indices and environmental drivers that may modulate NCP in the South Atlantic. Tilstone et al. (2015b) showed correlations between monthly province-averaged NCP anomalies and climate indices for the SeaWiFS time series between 1998 and 2010 in the Atlantic Ocean.

Conducting the correlation analysis on province-averaged NCP anomalies, between 2002 and 2018, we showed no significant correlations between NCP anomalies and wind speed anomalies, SLHA and the climate indices, when the NCP uncertainties were accounted for. Tilstone et al. (2015b) showed significant correlation between NCP anomalies and the MEI in the SATL, which may become non-significant if the uncertainties are accounted for. Correlations with the environmental drivers at local scales may however, still be significant. This was therefore studied in more detail, by conducting a correlation analysis on a per pixel basis across the region (Fig. 2.6). This technique has previously proved effective for determining trends in phytoplankton pigments and production (e.g.: Behrenfeld et al., 2006; Dunstan et al., 2018; Kahru et al., 2010).

Significant positive correlations were found between wind speed and NCP anomalies, along the BENG coast (Fig. 2.6b). An increase in upwelling conducive wind speeds enhances the upwelling of colder, nutrient rich waters, causing an increase in NPP (Chen et al., 2012b; Lamont et al., 2019) and therefore potentially in NCP. The negative correlations between wind speed and SST anomalies (Fig. 2.6h) indicate the enhancement of nutrient rich, cold water

at the surface, under elevated wind speeds, which in turn drive the correlations between wind speed and NPP anomalies (Fig. 2.6e).

Negative correlations between NCP anomalies and SLHA were observed offshore in the BENG, extending into the SATL (Fig. 2.6a). SLHA show substantial mesoscale activity in the form of eddies and filaments that propagate away from the upwelling front and advect more productive, cooler waters (negative SLHA; positive NCP anomalies) into the SATL (Rubio et al., 2009). The positive correlations between SST anomalies and SLHA (Fig. 2.6g; negative SST anomalies; negative SLHA) extended offshore of the BENG, but to a lesser extent than negative correlations between NPP anomalies and SLHA (Fig. 2.6d). Rubio et al. (2009) indicated that these eddies and filaments can advect a significant volume of nutrient rich water into the SATL, which potentially enhances NPP and NCP offshore. Lamont et al. (2019) showed that long-term trends in Chl *a* and phytoplankton size structure differed between open ocean (> 1000 m) and shelf (< 1000 m) regions of the BENG, suggesting different driving mechanisms between shelf and open ocean regions.

In the SATL, an area of positive correlations between NCP anomalies and wind speed anomalies were observed (Fig. 2.6b). Productivity in this region is influenced by the equatorial upwelling and South Equatorial current, both of which are wind-driven (Hooker et al., 2000). Wind speed anomalies were positively correlated with both NPP and NCP anomalies (Fig. 2.6b), suggesting a connection between wind induced mixing of nutrients to the photic zone which in turn fuels NPP and NCP. Negative correlations between SST anomalies and wind speed anomalies have a larger regional influence (Fig. 2.6h) than correlations with NCP and NPP anomalies (Fig. 2.6b, e).

In the SSTC, significant negative correlations between NCP anomalies and SLHA were observed, extending north into the SATL (Fig. 2.6a). From 30° S to 40° S, the western region between 54° W and 36° W, is influenced by mesoscale eddies from the Brazil-Malvinas confluence, where the deflection of the two currents generates, anticyclonic (positive SLHA; negative NCP anomalies) and cyclonic (negative SLHA; positive NCP anomalies) eddies (Garcia et al., 2004).

The leakage of Indian Ocean waters into the South Atlantic is facilitated by Agulhas eddies, shed from the Agulhas Current, at the southern tip of South Africa (Guerra et al., 2018). These rings propagate across the South Atlantic, reaching the Brazilian coast between 15° S and 30° S. A band of significant positive correlations between SST anomalies and SLHA (Fig. 2.6g), are an indication of the presence of mesoscale eddies, which start at the southern tip of Africa, and end near the Brazilian coast. This is consistent with the basin-scale propagation of these Agulhas rings. These rings are anticyclonic 'warm' eddies, generally associated with positive SLHA, which induce downwelling of nutrients that potentially decreases NPP (He et al., 2016). The response of the plankton community to these Agulhas eddies in both NPP and NCP anomalies is clear at the southern tip of Africa, with negative correlations between NPP/NCP anomalies and SLHA (Fig. 2.6a, d; positive SLHA; negative NPP/NCP anomalies). The response as these Agulhas eddies propagate across the South Atlantic is less clear however, with some patchy negative correlations between NCP anomalies and SLHA (Fig. 2.6a), and to a lesser extent between NPP anomalies and SLHA (Fig. 2.6d). The influence of oceanic mesoscale eddies on phytoplankton production varies with the structure and age of the feature (Liu et al., 2018; Nencioli et al., 2018).

On a per pixel basis, patchy negative correlations between NCP anomalies and the MEI were observed in the SATL (Fig. 2.6c), reciprocated in correlations between NPP anomalies and the MEI (Fig. 2.6f). El Niño periods are coupled with variability in SST in the South Atlantic, leading to higher temperatures in the SATL (Rodrigues et al., 2015), which are evident in the positive correlations between SST anomalies and the MEI in this region (Fig. 2.6i). Higher SST in the SATL is associated with stronger stratification and decreased nutrient supply, which can reduce NPP and NCP, but this was not seen in our analysis of the South Atlantic.

Future climate change effects could drive changes in environmental forcing, which we have shown to control the metabolic state of the South Atlantic. Oceanic wind speeds have increased from 1985 to 2018 (Young and Ribal, 2019) and if this trend continues, it may suggest that areas of the South Atlantic become more autotrophic, driven by nutrient enrichment from upwelling and water column mixing. Upwelling favourable winds may become more prevalent

along eastern boundary upwelling systems (Aguirre et al., 2019), inducing a further increase in these autotrophic communities in the Benguela system.

2.5 Conclusions

In this paper, we perform a comprehensive uncertainty analysis of ocean colour parameters for MODIS-A in the South Atlantic Ocean, to enable the generation of an accurate satellite NCP time series, to investigate the effect of environmental drivers on NCP. Five Chl *a*, three NPP and four NCP satellite algorithms were assessed using a weighted statistical analysis which takes into account the uncertainty in both the satellite and *in situ* data. For Chl *a*, OC3-CI showed the best performance, however all algorithms showed a large underestimation at higher Chl *a* concentrations. For NPP, the WRM showed the best performance, however it underestimated NPP at more productive stations. For NCP, NCP-D showed the highest accuracy and NCP-C was also similar. Up to 61% of the uncertainty in satellite NCP could be attributed to uncertainties in the input parameters. The uncertainties in the NPP model (40%) and Chl *a* (22%) accounted for the greatest reduction in the log-RMS, indicating that these need to be reduced to improve the derivation of NCP using satellite data.

Using NCP-D, in conjunction with the most accurate input parameters, a 16 year monthly time series of NCP anomalies was produced for the South Atlantic Ocean, to investigate the effect of climate indices and environmental drivers on NCP. The central SATL showed significant positive correlations between wind speed and NCP anomalies. Similarly, in the Benguela region, significant positive correlations between wind speed and NCP anomalies dominated the coastal regions, indicating that wind driven upwelling controls autotrophic NCP in this region. Offshore SLHA had significant negative correlation with NCP anomalies which extended into the South Atlantic gyre. This correlation suggests that the propagation of mesoscale eddies and filaments from the BENG, modifies the autotrophic metabolic state of the plankton community offshore and into the SATL. Significant negative correlations between NCP anomalies and SLHA were also observed at the southern tip of Africa, highlighting that anticyclonic Agulhas Current rings and their associated fronts control NCP in this region. Significant negative correlations between SLHA and NCP anomalies also occur in the Brazil-Malvinas Confluence region through persistent eddy generation.

Appendices

Appendix 2.1 – Unweighted Statistics

Table A2.1- Performance indices for satellite chlorophyll a algorithms using AMT dataset. Log-differences uncertainties in satellite estimates are mean (M), standard deviation (S) and Root Mean Square (log-RMS). The mean and one sigma range of the difference are given as; Fmed, Fmin and Fmax; values closer to 1 indicate greater accuracy. APD is the Absolute Percentage Difference. N indicates the number of matchups used to compute statistics. The most accurate algorithm for each statistic is highlighted in bold. Statistics were computed using a standard unweighted procedure.

Unweighted												
	Model	R^2	Slope	Intercept	log-RMS	APD	M	S	F_{min}	F_{med}	F_{max}	N
AMT	OC3-CI	0.94	0.92	-0.14	0.15	125	0.07	0.14	0.85	1.17	1.60	1440
	OC3	0.92	0.91	-0.14	0.16	126	0.06	0.15	0.80	1.14	1.63	1440
	GSM	0.92	0.94	-0.15	0.18	143	0.09	0.15	0.87	1.24	1.75	1440
	OC5	0.92	0.86	-0.21	0.18	162	0.09	0.16	0.84	1.22	1.77	1440
	OC5-CI	0.93	0.87	-0.21	0.17	161	0.09	0.14	0.89	1.24	1.73	1440

Table A2.2- Performance indices for satellite net primary production algorithms. Log-differences uncertainties in satellite estimates are mean (M), standard deviation (S) and Root Mean Square (log-RMS). The mean and one sigma range of the difference are given as; Fmed, Fmin and Fmax; values closer to 1 indicate greater accuracy. APD is the Absolute Percentage Difference. N indicates the number of matchups used to compute statistics. The most accurate algorithm for each statistic is highlighted in bold. Statistics were computed using a standard unweighted procedure.

Unweighted											
Model	R^2	Slope	Intercept	log-RMS	APD	M	S	F_{min}	F_{med}	F_{max}	N
VGPM	0.68	0.86	0.33	0.23	7.4	0.02	0.23	0.62	1.05	1.79	18
PSM	0.78	0.76	0.37	0.31	9.7	0.24	0.20	1.12	1.75	2.75	18
WRM	0.71	0.91	0.16	0.22	7.6	0.06	0.22	0.69	1.15	1.90	18

Table A2.3- Performance indices for net community production (NCP) algorithms driven by in situ net primary production and in situ sea surface temperature. To log transform negative NCP values, we add the minimum value (-170 mmol O_2 $m^{-2}d^{-1}$) to all values. Log-differences uncertainties in satellite estimates are mean (M), standard deviation (S) and Root Mean Square (log-RMS). The mean and one sigma range of the difference are given as; F_{med}, F_{min} and F_{max}; values closer to 1 indicate greater accuracy. APD is the Absolute Percentage Difference. N indicates the number of matchups used to compute statistics. The most accurate algorithm for each statistic is highlighted in bold. Statistics were computed using a standard unweighted procedure.

Unweighted											
Model	R^2	Slope	Intercept	log-RMS	APD	M	S	F_{min}	F_{med}	F_{max}	N
A	0.14	3.00	-4.93	0.53	18.2	0.39	0.36	1.08	2.48	5.70	84
B	0.23	0.53	1.11	0.12	3.8	-0.05	0.11	0.69	0.89	1.16	84
C	0.23	0.74	0.58	0.12	3.9	0.00	0.12	0.76	0.99	1.31	84
D	0.21	0.95	0.10	0.13	4.6	0.01	0.13	0.75	1.02	1.38	84

Table A2.4- Performance indices for satellite net community production (NCP) algorithms. To log transform negative NCP values, we added the minimum value (-170 mmol O_2 $m^{-2}d^{-1}$) to all values. Log-differences uncertainties in satellite estimates are mean (M), standard deviation (S) and Root Mean Square (log-RMS). The mean and one sigma range of the difference are given as; F_{med}, F_{min} and F_{max}; values closer to 1 indicate greater accuracy. APD is the Absolute Percentage Difference. N indicates the number of matchups used to compute statistics. The most accurate algorithm for each statistic is highlighted in bold. Statistics were computed using a standard unweighted procedure.

Unweighted											
Model	R^2	Slope	Intercept	log-RMS	APD	M	S	F_{min}	F_{med}	F_{max}	N
A	0.35	3.53	-6.32	0.79	27.0	0.59	0.54	1.12	3.92	13.69	14
B	0.50	0.48	1.20	0.13	4.6	-0.03	0.13	0.69	0.94	1.27	14
C	0.49	0.69	0.65	0.13	5.0	0.05	0.13	0.84	1.12	1.50	14
D	0.61	0.81	0.40	0.11	4.0	0.04	0.11	0.85	1.10	1.42	14

Appendix 2.2 – Chl *a* Statistics for BRAZ and BEN datasets

Table A2.5– Performance indices for satellite chlorophyll a algorithms using BRAZIL dataset. Log-differences uncertainties in satellite estimates are mean (M), standard deviation (S) and Root Mean Square (log-RMS). The mean and one sigma range of the difference are given as; F_{med}, F_{min} and F_{max}; values closer to 1 indicate greater accuracy. APD is the Absolute Percentage Difference. N indicates the number of matchups used to compute statistics. The most accurate algorithm for each statistic is highlighted in bold. Statistics were computed firstly assuming all stations have equal weighting (unweighted) and secondly weighting each station based only on the satellite uncertainty (ℰC) (weighted).

Unweighted												
	Model	R^2	Slope	Intercept	log-RMS	APD	M	S	F_{min}	F_{med}	F_{max}	N
BRAZIL	OC3-CI	0.83	0.90	-0.15	0.13	35	0.07	0.12	0.88	1.16	1.53	30
	OC3	0.73	1.07	-0.03	0.19	38	0.09	0.16	0.85	1.24	1.80	30
	GSM	0.22	1.01	-0.22	0.38	104	0.23	0.30	0.85	1.71	3.42	30
	OC5	0.72	0.96	-0.16	0.20	46	0.13	0.16	0.94	1.35	1.93	30
	OC5-CI	0.86	0.78	-0.27	0.15	42	0.09	0.12	0.94	1.24	1.63	30

Weighted												
	Model	R^2	Slope	Intercept	log-RMS	APD	M	S	F_{min}	F_{med}	F_{max}	N
BRAZIL	OC3-CI	0.86	1.00	-0.06	0.13	39	0.08	0.11	0.92	1.19	1.54	30
	OC3	0.81	0.94	-0.09	0.15	39	0.07	0.13	0.86	1.17	1.58	30
	GSM	0.43	1.04	-0.10	0.26	38	0.16	0.21	0.90	1.45	2.32	30
	OC5	0.81	0.87	-0.17	0.17	48	0.11	0.13	0.95	1.28	1.72	30
	OC5-CI	0.88	0.91	-0.14	0.14	44	0.09	0.11	0.97	1.24	1.59	30

Table A2.6 - Performance indices for satellite chlorophyll a algorithms using BEN dataset. Log-differences uncertainties in satellite estimates are mean (M), standard deviation (S) and Root Mean Square (log-RMS). The mean and one sigma range of the difference are given as; F_{med}, F_{min} and F_{max}; values closer to 1 indicate greater accuracy. APD is the Absolute Percentage Difference. N indicates the number of matchups used to compute statistics. The most accurate algorithm for each statistic is highlighted in bold. Statistics were computed firstly assuming all stations have equal weighting (unweighted) and secondly weighting each station based only on the satellite uncertainty (ℰC) (weighted).

Unweighted												
	Model	R^2	Slope	Intercept	log-RMS	APD	M	S	F_{min}	F_{med}	F_{max}	N
BEN	OC3-CI	0.74	0.92	0.00	0.28	108	0.02	0.28	0.55	1.05	2.00	38
	OC3	0.75	0.94	-0.01	0.28	108	0.02	0.28	0.55	1.06	2.02	38
	GSM	0.69	1.10	0.09	0.35	109	-0.11	0.34	0.36	0.78	1.71	38
	OC5	0.76	0.85	-0.11	0.30	103	0.14	0.27	0.74	1.37	2.57	38
	OC5-CI	0.76	0.84	-0.10	0.30	103	0.14	0.27	0.73	1.37	2.56	38

Weighted												
	Model	R^2	Slope	Intercept	log-RMS	APD	M	S	F_{min}	F_{med}	F_{max}	N
BEN	OC3-CI	0.80	0.92	-0.02	0.25	89	0.03	0.25	0.61	1.08	1.93	38
	OC3	0.80	0.94	-0.03	0.25	89	0.04	0.25	0.61	1.09	1.95	38
	GSM	0.75	1.00	0.05	0.30	92	-0.06	0.30	0.44	0.86	1.71	38
	OC5	0.80	0.87	-0.10	0.29	94	0.14	0.25	0.78	1.39	2.48	38
	OC5-CI	0.80	0.86	-0.10	0.29	94	0.14	0.25	0.78	1.38	2.47	38

Appendix 2.3 – Satellite skin sea surface temperature uncertainty

Sea surface temperature (SST) is a key variable for both NPP and NCP algorithms, and therefore the performance of MODIS-A SST retrievals were assessed. SST measurements by infrared radiometers, such as MODIS-A, are a measurement of the SST at the oceans skin (~10 µm), but are usually compared to *in situ* buoy measurements of temperature below the surface (~5 m). These temperature measurements can introduce additional uncertainty through vertical temperature gradients in the water column, and therefore a measurement of skin SST should be used in determining the uncertainty of MODIS-A SST.

Skin SST measurements made on three AMT cruise in 2017, 2018 and 2019 (AMT 27, 28, 29) using an infrared SST autonomous radiometer (ISAR) as outlined in Donlon et al. (2008), were downloaded from the Ships4SST website (http://ships4sst.org/). Each individual measurement was provided with an uncertainty using the statistical model outlined in Wimmer and Robinson (2016).

In situ measurements were subjected to the same matchup protocol as the ocean colour component, as described in section 2.2.7. Satellite uncertainties were determined following the same approach as the ocean colour component, with Ɛi assumed to be negligible, and Ɛa assigned a value of 0.345 °C (Brown and Minnett, 1999).

Weighted linear regression analysis is shown in Fig. A2.1 with associated statistics tabulated in Table A2.7. Our results show MODIS-A SST measurements are accurate having no bias and little scatter, falling on the 1:1 line.

Table A2.7- Performance indices for satellite sea surface temperature (SST). Log-differences uncertainties in satellite estimates are mean (M) and standard deviation (S). Root Mean Square Error (RMS) was computed as opposed to log-RMS. The mean and one sigma range of the difference are given as; F_{med}, F_{min} and F_{max}; values closer to 1 are more accurate. APD is the Absolute Percentage Difference. N indicates the number of matchups used to compute statistics. Statistics were computed firstly assuming all stations have equal weighting (unweighted) and secondly weighting each station based on the in situ and satellite uncertainty (weighted).

Unweighted											
	R^2	Slope	Intercept	RMS	APD	M	S	F_{min}	F_{med}	F_{max}	N
SST	0.99	1.01	-0.16	0.41	1.4	0.00	0.01	0.98	1.00	1.02	362

Weighted											
	R^2	Slope	Intercept	RMS	APD	M	S	F_{min}	F_{med}	F_{max}	N
SST	0.99	1.00	-0.08	0.41	1.4	0.00	0.01	0.98	1.00	1.02	362

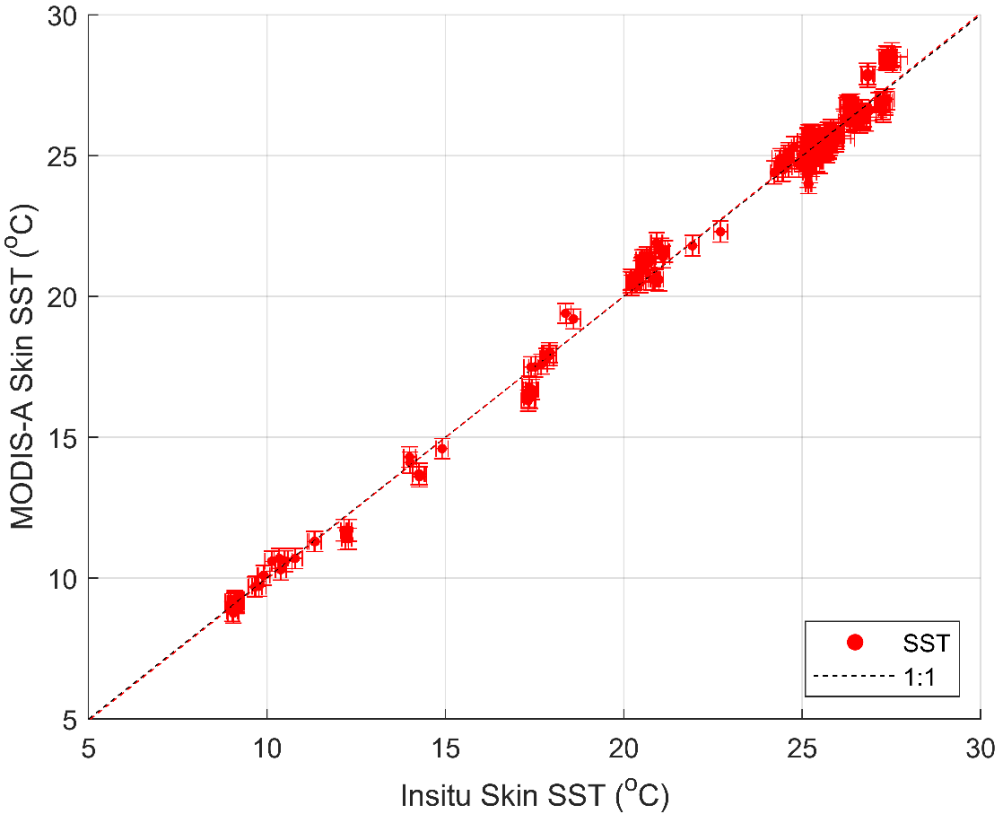

Figure A2.1 – Comparison of ISAR and MODIS-A skin sea surface temperature (SST). Black dashed line is the 1:1 line. Red dashed line is a weighted Type-II linear regression between the ISAR and MODIS-A skin SST. Horizontal error bars indicate in situ uncertainty (Ɛins). Vertical error bars indicate the combine satellite uncertainty (ƐC).

Chapter 3: Derivation of seawater pCO_2 from net community production identifies the South Atlantic Ocean as a CO_2 source

This chapter is a reformatted version of my publication:
Ford, D. J., Tilstone, G. H., Shutler, J. D., and Kitidis, V. (2022): Derivation of seawater pCO_2 from net community production identifies the South Atlantic Ocean as a CO_2 source, Biogeosciences, 19, 93–115, https://doi.org/10.5194/bg-19-93-2022
The data produced within this publication was published in:
Ford, D. J., Tilstone, G. H., Shutler, J. D., and Kitidis, V. (2021): Interpolated surface ocean carbon dioxide partial pressure for the South Atlantic Ocean (2002-2018) using different biological parameters. PANGAEA, https://doi.org/10.1594/PANGAEA.935936
DJF, GHT, JDS and VK conceived and directed the research. DJF developed the code and prepared the manuscript. GHT, JDS and VK provided comments that shaped the final manuscript.

Abstract: A key step in assessing the global carbon budget is the determination of the partial pressure of CO_2 in seawater ($pCO_{2\,(sw)}$). Spatially complete observational fields of $pCO_{2\,(sw)}$ are routinely produced for regional and global ocean carbon budget assessments by extrapolating sparse *in situ* measurements of $pCO_{2\,(sw)}$ using satellite observations. As part of this process, satellite chlorophyll *a* (Chl *a*) is often used as a proxy for the biological drawdown or release of CO_2. Chl *a* does not however quantify carbon fixed through photosynthesis and then respired, which is determined by net community production (NCP).

In this study, $pCO_{2\,(sw)}$ over the South Atlantic Ocean is estimated using a feed forward neural network (FNN) scheme and either satellite derived NCP, net primary production (NPP) or Chl *a* to compare which biological proxy produces the most accurate fields of $pCO_{2\,(sw)}$. Estimates of $pCO_{2\,(sw)}$ using NCP, NPP or Chl *a* were similar, but NCP was more accurate for the Amazon Plume and upwelling regions, which were not fully reproduced when using Chl *a* or NPP. A perturbation analysis assessed the potential maximum reduction in $pCO_{2\,(sw)}$ uncertainties that could be achieved by reducing the uncertainties in the satellite biological parameters. This illustrated further improvement using NCP compared to NPP or Chl *a*. Using NCP to estimate $pCO_{2\,(sw)}$ showed that the South Atlantic Ocean is a CO_2 source, whereas if no biological parameters are used in the FNN (following existing annual carbon assessments), this region appears to be a sink for CO_2. These results highlight that using NCP improved the accuracy of estimating $pCO_{2\,(sw)}$ and changes the South Atlantic Ocean from a CO_2 sink to a source. Reducing the uncertainties in NCP derived from satellite

parameters will ultimately improve our understanding and confidence in quantification of the global ocean as a CO_2 sink.

3.1 Introduction

Since the industrial revolution, anthropogenic CO_2 emissions have resulted in an increase in atmospheric CO_2 concentrations (IPCC, 2013; Friedlingstein et al., 2020). By acting as a sink for CO_2, the oceans have buffered the increase in anthropogenic atmospheric CO_2, without which the atmospheric concentration would be 42-44 % higher (DeVries, 2014). The long-term absorption of CO_2 by the oceans is altering the marine carbonate chemistry of the ocean, resulting in a lowering of pH, a process known as ocean acidification (Raven et al., 2005). Observational fields of the partial pressure of CO_2 in seawater ($pCO_{2\,(sw)}$) are one of the key datasets needed to routinely assess the strength of the oceanic CO_2 sink (Rödenbeck et al., 2015; Landschützer et al., 2014; Watson et al., 2020b; Landschützer et al., 2020; Friedlingstein et al., 2020). These methods are reliant on the extrapolation of sparse *in situ* observations of $pCO_{2\,(sw)}$ using satellite observations of parameters which account for the variability of, and the controls on, $pCO_{2\,(sw)}$ (Shutler et al., 2020). These parameters include sea surface temperature (SST; e.g. Landschützer et al., 2013; Stephens et al., 1995), salinity and chlorophyll *a* (Chl *a*) (Rödenbeck et al., 2015). SST and salinity control $pCO_{2\,(sw)}$ by changing the solubility of CO_2 in seawater (Weiss, 1974), whilst biological processes such as photosynthesis and respiration contribute by modulating its concentration.

Chl *a* is routinely used as a proxy for the biological activity (Rödenbeck et al., 2015), but it does not distinguish between carbon fixation through photosynthesis and the carbon respired by the plankton community. Net primary production (the net carbon fixation rate; NPP) is determined by the standing stock of phytoplankton, for which the Chl *a* concentration is used as a proxy, and modified by the photosynthetic rate and the available light in the water column (Behrenfeld et al., 2016). Photosynthetic rates are, in turn, modified by ambient nutrient and temperature conditions (Behrenfeld and Falkowski, 1997b; Marañón et al., 2003). Elevated Chl *a* does not always equate to elevated NPP (Poulton et al., 2006), and for the same Chl *a* concentrations, NPP can vary depending on the health and metabolic state of the plankton community. All of these controls are captured by the net community production (NCP), which is

the metabolic balance of the plankton community resulting from the carbon fixed through photosynthesis and that lost through respiration. Where NCP is positive, the plankton community is autotrophic which implies that there is a drawdown of CO_2 from seawater (since the plankton reduce the CO_2 in the water column). Where NCP is negative the community is heterotrophic implying a release of CO_2 into the ocean (as the plankton produce or release CO_2) which can then be released into the atmosphere (Schloss et al., 2007; Jiang et al., 2019). Using NCP to estimate $pCO_{2\,(sw)}$ compared to Chl *a* should theoretically lead to an improvement in the derivation of $pCO_{2\,(sw)}$.

Many studies have used satellite Chl *a* to estimate $pCO_{2\,(sw)}$ at both regional (Benallal et al., 2017; Moussa et al., 2016; Chierici et al., 2012), and global scales (Landschützer et al., 2014; Liu and Xie, 2017). Chierici et al. (2012) attempted to use satellite NPP to estimate $pCO_{2\,(sw)}$ in the southern Pacific Ocean, but there was no significant improvement over using satellite Chl *a*. This is not surprising as NPP captures more of the biological signal, but still lacks any inclusion of respiration which results in the release of CO_2 into the water column. To our knowledge the use of satellite NCP to estimate $pCO_{2\,(sw)}$ has not been attempted before and could be a means of improving estimates of $pCO_{2\,(sw)}$ as long as satellite NCP observations are accurate (Ford et al., 2021b; Tilstone et al., 2015a). These satellite measurements may improve the estimation of $pCO_{2\,(sw)}$ as NCP includes the full biological control on $pCO_{2\,(sw)}$. This is particularly important in regions where *in situ* $pCO_{2\,(sw)}$ observations are sparse and where interpolation and neural network techniques are therefore likely to struggle (Watson et al., 2020b).

The South Atlantic Ocean is under sampled with limited $pCO_{2\,(sw)}$ observations (e.g. Fay and McKinley, 2013; Watson et al., 2020b). The region is varied and dynamic as it includes the seasonal Equatorial upwelling, high biological activity on the south-western (Dogliotti et al., 2014) and south-eastern shelves (Lamont et al., 2014), as well as the propagation of the Amazon Plume into the western Equatorial Atlantic (Ibánhez et al., 2015). This dynamic biogeochemical variability in conjunction with a comprehensive database of satellite observation-based data with associated uncertainties (Ford et al., 2021a) provides the potential to identify the improvement to $pCO_{2\,(sw)}$ estimates that could be made from using NCP.

The objective of this paper is to compare the estimation of $pCO_{2\,(sw)}$ using either NCP, NPP or Chl *a* to determine which biological descriptor produces the most accurate and complete $pCO_{2\,(sw)}$ fields. A 16 year time series of $pCO_{2\,(sw)}$ was generated for the South Atlantic Ocean using satellite NCP, NPP or Chl *a*, as the biological input, alongside two approaches with no biological input parameters. Regional differences in the resulting $pCO_{2\,(sw)}$ fields are assessed. The seasonal and interannual variability in $pCO_{2\,(sw)}$ estimated from NCP, NPP, Chl *a* and the approaches with no biological parameters were also compared. A perturbation analysis was conducted to evaluate the potential reduction in the uncertainty in the $pCO_{2\,(sw)}$ fields when estimated from NCP, NPP or Chl *a*. This is discussed in the context of reducing uncertainties in these input variables for future improvements in spatially complete fields of $pCO_{2\,(sw)}$, and the effect on estimates of the oceanic carbon sink.

3.2 Methods

3.2.1 Surface Ocean Carbon Atlas (SOCAT) $pCO_{2\,(sw)}$ and atmospheric CO_2

SOCATv2020 (Bakker et al., 2016; Pfeil et al., 2013) individual fugacity of CO_2 in seawater ($fCO_{2\,(sw)}$) observations were downloaded from https://www.socat.info/index.php/data-access/. Data were extracted from 2002 to 2018 for the South Atlantic Ocean (10º N-60º S, 25º E–80º W; Fig. 3.1b). The individual cruise observations were collected from different depths, and are not representative of the $fCO_{2\,(sw)}$ in the top ~100 µm of the ocean, where gas exchange occurs (Goddijn-Murphy et al., 2015; Woolf et al., 2016). Therefore, the SOCAT observations were re-analysed to a standard temperature dataset and depth (Reynolds et al., 2002) that is considered representative of the bottom of the mass boundary layer (Woolf et al., 2016). This was achieved using the 'fe_reanalyse_socat' utility in the open source FluxEngine toolbox (Shutler et al., 2016; Holding et al., 2019), which follows the methodology described in Goddijn-Murphy et al. (2015). The reanalysed $fCO_{2\,(sw)}$ observations were converted to $pCO_{2\,(sw)}$, and gridded onto 1º monthly grids following SOCAT protocols (Sabine et al., 2013). The uncertainties in the *in situ* data were taken as the standard deviation of the observations in each grid cell, or where a single observation exists were set as 5 µatm following Bakker et al. (2016).

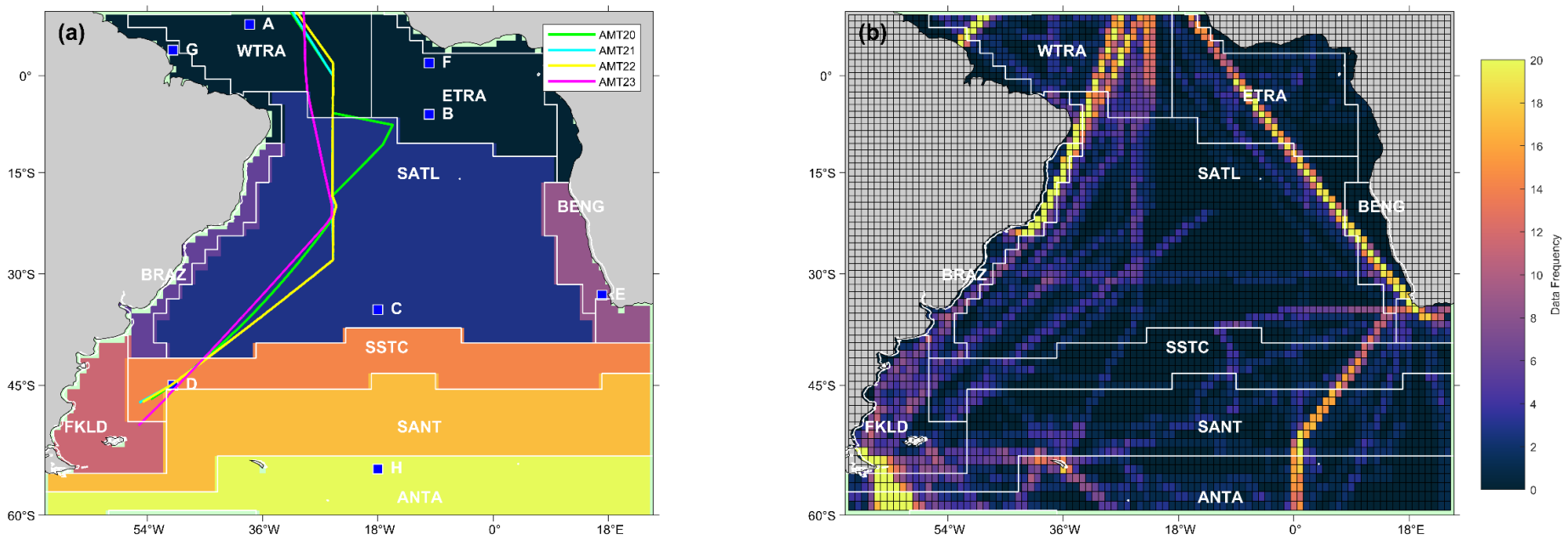

Figure 3.1 - (a) Map of the 8 static biogeochemical provinces in the South Atlantic Ocean, following Longhurst et al. (1995) and Longhurst (1998). Markers and letters indicate the locations of timeseries extracted from Fig. 3. The four Atlantic Meridional Transect (AMT) cruise tracks are also overlaid (b) Map showing the spatial distribution of the SOCATv2020 dataset used, where the data frequency is the number of available months of data within each 1° pixel. The province areas acronyms are: WTRA is Western Tropical Atlantic; ETRA is Eastern Equatorial Atlantic; SATL is South Atlantic Gyre; BRAZ is Brazilian current coastal; BENG is Benguela Current coastal upwelling; FKLD is Southwest Atlantic shelves; SSTC is South Subtropical Convergence; SANT is Sub Antarctic and ANTA is Antarctic.

Monthly 1º grids of atmospheric pCO_2 ($pCO_{2\,(atm)}$) were extracted from v5.5 of the global estimates of $pCO_{2\,(sw)}$ dataset (Landschützer et al., 2017, 2016). $pCO_{2\,(atm)}$ was estimated using the dry mixing ratio of CO_2 from the NOAA-ESRL marine boundary layer reference (https://www.esrl.noaa.gov/gmd/ccgg/mbl/), Optimum Interpolated SST (Reynolds et al., 2002) and sea level pressure following Dickson et al. (2007).

3.2.2 Moderate Resolution Spectroradiometer on Aqua (MODIS-A) satellite observations

4 km resolution monthly mean Chl *a* were calculated from MODIS-A Level 1 granules, retrieved from National Aeronautics and Space Administration (NASA) Ocean Colour website (https://oceancolor.gsfc.nasa.gov/) using SeaDAS v7.5, and applying the standard OC3-CI Chl *a* algorithm (https://oceancolor.gsfc.nasa.gov/atbd/chlor_a/). In addition, monthly mean MODIS-A SST and photosynthetically active radiation (PAR) were also downloaded from the NASA Ocean Colour website. Mean monthly NPP were generated from MODIS-A Chl *a*, SST and PAR using the Wavelength Resolving Model (Morel, 1991) with the look up table described in Smyth et al. (2005). Coincident mean monthly NCP using the algorithm NCP-D described in Tilstone et al. (2015a) were generated using the MODIS-A NPP and SST data. Further details of the satellite algorithms are given in O'Reilly et al. (1998; 2019) and Hu et al. (2012) for Chl *a*, Smyth et al. (2005) and Tilstone et al. (2005, 2009) for NPP and Tilstone et al. (2015a) for NCP. These satellite algorithms were shown to be the most accurate for the South Atlantic Ocean in an algorithm inter-comparison which accounted for the uncertainties in both *in situ*, model and input data (Ford et al., 2021a). All monthly mean data were generated between July 2002 and December 2018 and were re-gridded onto the same 1º grid as the $pCO_{2\,(sw)}$ observations. The assessed uncertainties from the literature for each of the input parameters used are given in Table 3.1.

Table 3.1 - Uncertainties in the input parameters of the Feed Forward Neural Network used in Monte Carlo uncertainty propagation and perturbation analysis.

Parameter	Algorithm Uncertainty	Reference
Chlorophyll *a*	0.15 $\log_{10}$(mg m^{-3})	(Ford et al., 2021a)
Net Primary Production	0.20 $\log_{10}$(mg C m^{-2} d^{-1})	(Ford et al., 2021a)
Net Community Production	45 mmol O_2 m^{-2} d^{-1}	(Ford et al., 2021a)
SST	0.41 ºC	(Ford et al., 2021a)
$pCO_{2\ (atm)}$	1 µatm	Takahashi et al. (2009)

3.2.3 Feed forward neural network scheme

The South Atlantic Ocean was partitioned into 8 biogeochemical provinces (Fig. 3.1a), following Longhurst et al. (1995) and Longhurst (1998). The $pCO_{2\ (sw)}$ observations in the eastern Equatorial Atlantic were sparse, and therefore the Equatorial region was merged into 1 province. In each province the available monthly $pCO_{2\ (sw)}$ observations were matched to temporally and spatially coincident $pCO_{2\ (atm)}$, MODIS-A, NCP and SST, to provide training data for the feed forward neural network (FNN). Observations in coastal regions (< 200 m water depth) were removed from the analysis, due to the increased uncertainty in ocean colour observations in these areas (e.g. Lavender et al., 2004). Due to constraints on the coverage of ocean colour data, no data were available in austral winter below ~50º S.

The coincident observations in each province were randomly split into 3 datasets: 1.) A training dataset (50 % of the observations) used to train the FNNs; 2.) A validation dataset (30 % of the observations) used to assess the performance of the FNN and to prevent the networks from overfitting; 3.) An independent test dataset (20 % of the observations) to assess the final performance of the FNN, with observations that are independent of the network training. The optimal split (r_{opt}) method of Amari et al. (1997) was used to partition the input data into these three sets, as follows:

$$r_{opt} = 1 - \frac{1}{\sqrt{2m}} \tag{3.1}$$

where m is number of input parameters. For our three input parameters, an optimal split of 60 % training data to 40 % validation data would occur, where

we removed 10 % from each dataset to provide a further independent test dataset. A pre-training step was used to determine the optimum number of hidden neurons in the FNN (Moussa et al., 2016; Benallal et al., 2017; Landschützer et al., 2013), to provide the best fit for the observations, whilst preventing over fitting (Demuth et al., 2008).

The FNNs consist of 1 hidden layer with between 2 and 30 nodes depending on the pre-training step and 1 output layer. The networks were trained using the optimum number of hidden neurons, in an iterative process until the Root Mean Square Difference (RMSD) remained unchanged for 6 iterations. The best performing FNN, with the lowest RMSD was then used to estimate $pCO_{2\,(sw)}$. The uncertainties in the input parameters were propagated through the FNN, using a Monte Carlo uncertainty propagation, where 1000 calculations were made perturbing the input parameters, using random noise for their uncertainty (Table 3.1). The output from the 8 province FNNs were then combined and weighted statistics, which account for both the satellite and *in situ* uncertainty, were used to assess the overall performance of the FNN (as also used in Ford et al., 2021b). The combined 8 FNNs approach will hereafter be referred to as SA-FNN.

The approach to training the FNNs was repeated replacing NCP with Chl *a* or NPP sequentially (Table 3.2), to determine if there was an improvement by using NCP. Chl *a* and NPP estimates were $\log_{10}$ transformed before input into the FNN, due to their respective uncertainties being determined in $\log_{10}$ space (Table 3.1). A baseline SA-FNN with no biological parameters as input was trained using $pCO_{2\,(atm)}$ and MODIS-A SST ($SA\text{-}FNN_{NO\text{-}BIO\text{-}1}$; Table 3.2). A second SA-FNN with no biological parameters ($SA\text{-}FNN_{NO\text{-}BIO\text{-}2}$; Table 3.2) was trained with the addition of sea surface salinity and mixed layer depth from the Copernicus Marine Environment Modelling Service (https://resources.marine.copernicus.eu/) global ocean physics reanalysis product (GLORYS12V1). This parameter combination ($pCO_{2\,(atm)}$, SST, salinity and mixed layer depth) has recently been included within a neural network scheme to estimate global fields of $pCO_{2\,(sw)}$ (Watson et al., 2020b).

Following these methods, a monthly mean time-series of $pCO_{2\,(sw)}$ was generated in the South Atlantic Ocean, applying the SA-FNN approach using NCP ($SA\text{-}FNN_{NCP}$), NPP ($SA\text{-}FNN_{NPP}$), Chl *a* ($SA\text{-}FNN_{CHLA}$) or no biological

Table 3.2 - The input parameters of the neural network variants described in section 3.2.3. and 3.2.6. xCO_2 is the atmospheric mixing ratio of CO_2.

Neural Network Variant	Input parameters
SA-FNN$_{NCP}$	$pCO_{2\,(atm)}$, SST and NCP
SA-FNN$_{NPP}$	$pCO_{2\,(atm)}$, SST and NPP
SA-FNN$_{CHLA}$	$pCO_{2\,(atm)}$, SST and Chl *a*
SA-FNN$_{NO-BIO-1}$	$pCO_{2\,(atm)}$ and SST
SA-FNN$_{NO-BIO-2}$	$pCO_{2\,(atm)}$, SST, salinity, and mixed layer depth
W2020 (Watson et al., 2020a)	$xCO_{2\,(atm)}$, SST, salinity, and mixed layer depth

parameters (SA-FNN$_{NO-BIO-1}$ and SA-FNN$_{NO-BIO-2}$). The $pCO_{2\,(sw)}$ fields were spatially averaged using a 3×3 pixel filter, but were not averaged temporally as in previous studies (Landschützer et al., 2014, 2016) because averaging temporally could mask features that occur within single months of the year. The uncertainties in the input parameters (Table 3.1) were propagated through the neural network on a per pixel basis, and combined in quadrature with the RMSD of the test dataset, to produce a combined uncertainty budget for each pixel, assuming all sources of uncertainty are independent and uncorrelated (Taylor, 1997; BIPM, 2008).

3.2.4 Atlantic Meridional Transect *in situ* data

To assess the accuracy of the SA-FNN, coincident *in situ* measurements of NCP, NPP, Chl *a*, SST, $pCO_{2\,(atm)}$ and $pCO_{2\,(sw)}$, with uncertainties, were provided by Atlantic Meridional Transects 20, 21, 22 and 23 in 2010, 2011, 2012 and 2013, respectively. All the Atlantic Meridional Transect data described in this section can be obtained from the British Oceanographic Data Centre (https://www.bodc.ac.uk/). Chl *a* was computed following the methods of Brewin et al. (2016), using underway continuous spectrophotometric measurements from AMT 22, and uncertainties were estimated as ~0.06 $\log_{10}$(mg m^{-3}) (Ford et al., 2021a). ^{14}C based NPP measurements were made based on dawn to dusk simulated *in situ* incubations, following the methods given in Tilstone et al. (2017), at 56 stations with a per station uncertainty. Uncertainties ranged between 8 and 213 mg C m^{-2} d^{-1} and were on average 53 mg C m^{-2} d^{-1}. NCP was estimated using *in vitro* changes in dissolved O_2, following the methods of

Gist et al. (2009) and Tilstone et al. (2015a) at 51 stations with a per station uncertainty calculated. Uncertainties ranged between 5 and 25 mmol O_2 m^{-2} d^{-1} and were on average 14 mmol O_2 m^{-2} d^{-1}.

Underway measurements of $pCO_{2\,(sw)}$ and $pCO_{2\,(atm)}$ were performed continuously, following the methods of Kitidis et al. (2017). SST was continuously measured alongside all observations (SeaBird SBE45), with a factory calibrated uncertainty of ±0.01 °C. The mean of underway $pCO_{2\,(sw)}$, $pCO_{2\,(atm)}$, SST and Chl *a* were taken ±20 minutes around each station where NCP and NPP were measured. These $pCO_{2\,(sw)}$ observations (N≈200) were removed from the SOCATv2020 dataset so that the Atlantic Meridional Transect data remained independent from the training and validation datasets.

3.2.5 Perturbation analysis

Following the approach of Saba et al. (2011), a perturbation analysis was conducted, to evaluate the potential reduction in SA-FNN $pCO_{2\,(sw)}$ RMSD that could be attributed to the input parameters. The analysis indicates the maximum reduction in RMSD that could be achieved if uncertainties in the input parameters were reduced to ~0. Each of the input parameters; NCP, SST and $pCO_{2\,(atm)}$ can have three possible values for each *in situ* $pCO_{2\,(sw)}$ observation (original value, original ± uncertainty; Table 3.1), enabling 27 perturbations of the input data as input to the SA-FNN. For each *in situ* $pCO_{2\,(sw)}$ observation, the 27 perturbations of SA-FNN $pCO_{2\,(sw)}$ were examined, and the perturbation that produced the lowest RMSD and bias combination was selected. The RMSD and bias were calculated between all the *in situ* $pCO_{2\,(sw)}$ and the selected perturbations. The percentage difference between this RMSD and the original RMSD when training the SA-FNN was calculated to indicate the maximum achievable reduction. This approach was conducted for two scenarios; (1) uncertainty in individual input parameters (NCP, SST and $pCO_{2\,(atm)}$) and (2) uncertainty in all input parameters together. The approach was conducted on all three training datasets, and on the Atlantic Meridional Transect *in situ* data. The analysis was repeated sequentially replacing NCP with Chl *a* and NPP, to determine if there was a greater maximum reduction in RMSD using NCP. The analysis was also conducted allowing for a 10 % reduction in input parameter uncertainties, to indicate the short-term reduction in $pCO_{2\,(sw)}$ RMSD that could be achieved by reducing the input parameter uncertainties.

3.2.6 Comparison of the SA-FNN$_{NCP}$ with the SA-FNN$_{NO-BIO}$, SA-FNN$_{CHLA}$, SA-FNN$_{NPP}$ and 'state of the art' data for the South Atlantic

The most comprehensive $pCO_{2\,(sw)}$ fields to date are from Watson et al. (2020b, a). The 'standard method' $pCO_{2\,(sw)}$ fields within the Watson et al. (2020b, 2020a) data were produced by extrapolating the *in situ* reanalysed SOCATv2019 $pCO_{2\,(sw)}$ observations using a self-organising map feed forward neural network approach (Landschützer et al., 2016), hereafter referred to as 'W2020'. A time-series was extracted from the W2020 data, coincident with SA-FNN$_{NCP}$, SA-FNN$_{NPP}$, SA-FNN$_{CHLA}$ and the two SA-FNN$_{NO-BIO}$ variants. For the six methods, a monthly climatology referenced to the year 2010 was computed, assuming an atmospheric CO_2 increase of 1.5 µatm yr^{-1} (Takahashi et al., 2009; Zeng et al., 2014). The climatology should be insensitive to the assumed rise in atmospheric CO_2 due to the reference year being central to the time series. The standard deviation of this climatology was also computed on a per pixel basis.

The stations (Fig. 3.1) are representative of locations from previous literature that analysed the variability of *in situ* $pCO_{2\,(sw)}$ in the South Atlantic Ocean. For each station, the monthly climatology of $pCO_{2\,(sw)}$, representing the average seasonal cycle of $pCO_{2\,(sw)}$, and the standard deviation of the climatology, as an indication of the interannual variability, were extracted from the six approaches. The $pCO_{2\,(sw)}$ value for each station was the statistical mean of the four nearest data points weighted by their respective proximity to the station coordinate. *In situ* $pCO_{2\,(sw)}$ observations from the SOCATv2020 Flag E dataset were also extracted for stations A and B (Fig. 3.1a), and a climatology was generated. These observations represent data from the Prediction and Research Moored Array in the Atlantic (PIRATA) buoys at these locations (Bourlès et al., 2008).

The station climatologies for the SA-FNN$_{NO-BIO-1}$, SA-FNN$_{NO-BIO-2}$, W2020, SA-FNN$_{CHLA}$, and SA-FNN$_{NPP}$ were compared to the SA-FNN$_{NCP}$, by testing for significant differences in the seasonal cycle and annual $pCO_{2\,(sw)}$ (offset). The seasonal cycles (seasonality) were compared using a non-parametric Spearman's correlation and deemed statistically different where the correlation was not significant ($\alpha < 0.05$). A non-parametric Kruskal-Wallis was used to test for significant ($\alpha < 0.05$) differences in the annual $pCO_{2\,(sw)}$, indicating an offset between the two tested climatologies. The Southern Ocean station (station H) was excluded from the statistical analysis due to missing data in the SA-FNN.

3.2.7 Estimation of the bulk CO_2 flux

The flux of CO_2 (F) between the atmosphere and ocean (air-sea) can be expressed in a bulk parameterisation as:

$$F = k\ (\alpha_W\ pCO_{2\ (sw)} - \alpha_s\ pCO_{2\ (atm)}) \quad (2)$$

Where k is the gas transfer velocity, and α_w and α_s are the solubility of CO_2 at the base and top of the mass boundary layer at the sea surface respectively (Woolf et al., 2016). k was estimated from ERA5 monthly reanalysis wind speed (downloaded from the Copernicus Climate Data Store; https://cds.climate.copernicus.eu/) following the parameterisation of Nightingale et al. (2000). The parameter α_w was estimated as a function of SST and sea surface salinity (Weiss, 1974) using the monthly Optimum Interpolated SST (Reynolds et al., 2002) and sea surface salinity from the Copernicus Marine Environment Modelling Service global ocean physics reanalysis product (GLORYS12V1). The α_s parameter was estimated using the same temperature and salinity datasets but included a gradient from the base to the top of mass boundary layer of -0.17 K (Donlon et al., 1999) and +0.1 salinity units (Woolf et al., 2016). $pCO_{2\ (atm)}$ was estimated using the dry mixing ratio of CO_2 from the NOAA-ESRL marine boundary layer reference, Optimum Interpolated SST (Reynolds et al., 2002) applying a cool skin bias (0.17K; Donlon et al., 1999) and sea level pressure following Dickson et al. (2007). Spatially and temporally complete $pCO_{2\ (sw)}$ fields, which are representative of $pCO_{2\ (sw)}$ at the base of the mass boundary layer, were extracted from the SA-FNN_{NCP}, SA-FNN_{NPP}, SA-FNN_{CHLA}, SA-$FNN_{NO\text{-}BIO\text{-}1}$, SA-$FNN_{NO\text{-}BIO\text{-}2}$ and W2020.

The monthly CO_2 flux was calculated using the open source FluxEngine toolbox (Holding et al., 2019; Shutler et al., 2016) between 2003 and 2018 for the six $pCO_{2\ (sw)}$ inputs, using the 'rapid transport' approximation (described in Woolf et al., 2016). The net annual flux was determined for the South Atlantic Ocean (10° N-44° S; 25° E-70° W) using the 'fe_calc_budgets.py' utility within FluxEngine with the supplied area and land percentage masks. The mean net annual flux was calculated as the mean of the 15 year net annual fluxes. Positive net fluxes indicate a net source to the atmosphere, and negative net fluxes represent a sink.

3.3 Results

3.3.1 SA-FNN performance and perturbation analysis

The performance of the SA-FNN trained using $pCO_{2\,(atm)}$, SST and NCP for the three training datasets are given in Fig. 3.2. The $SA\text{-}FNN_{NCP}$ had an accuracy (RMSD) of 21.68 µatm and a precision (bias) of 0.87 µatm, which was determined with the independent test data (N = 1300). Training the SA-FNN using Chl *a* or NPP instead of NCP, resulted in a similar performance (Appendix 3.1 Fig. A3.1, Fig. A3.2). The RMSD for the independent test data was within ~1.5 µatm for Chl *a* (19.88 µatm), NPP (20.48 µatm) and NCP (21.68 µatm) and bias near zero.

The reduction in $pCO_{2\,(sw)}$ RMSD that could be achieved if input parameter uncertainties were reduced to ~0 was assessed using the perturbation analysis (Table 3.3, Appendix 3.1 Table A3.1). This showed that a reduction in $pCO_{2\,(sw)}$ RMSD of 36% was achieved by eliminating satellite NCP uncertainties, 34% by eliminating satellite NPP uncertainties, and 19% by eliminating satellite Chl *a* uncertainties. The bias remained near zero for all parameters indicating good precision of the SA-FNN approach (not shown). Applying the Atlantic Meridional Transect *in situ* data as input to the SA-FNN and using the perturbation analysis, a decrease in $pCO_{2\,(sw)}$ RMSD of 25 % for NCP, 13 % for NPP and 7 % for Chl *a* was observed.

The reduction in $pCO_{2\,(sw)}$ RMSD from reducing input parameter uncertainties by 10 % was also assessed through the perturbation analysis (Table 3.4). This indicated a decrease in $pCO_{2\,(sw)}$ RMSD of 8 % for NCP, 5 % for NPP and 2 % for Chl *a*, again indicating that improving NCP uncertainties has the largest impact on improving the estimated $pCO_{2\,(sw)}$ fields.

Table 3.3 - The percentage reduction in $pCO_{2\,(sw)}$ RMSD by reducing NCP, NPP and Chl *a* uncertainties to ~0 as described in Section 2.5. The full results can be found in Appendix Table A3.1.

Parameter	Training	Validation	Independent Test	AMT *in situ*
NCP	32 %	40 %	36 %	25 %
NPP	31 %	37 %	36 %	13 %
Chl *a*	17 %	21 %	20 %	7 %

Table 3.4 - The percentage reduction in $pCO_{2\,(sw)}$ RMSD by reducing NCP, net primary production and chlorophyll a uncertainties by 10 % as described in Section 2.5.

Parameter	Training	Validation	Independent Test	AMT *in situ*
NCP	7 %	8 %	8 %	3 %
NPP	5 %	6 %	5 %	1.5 %
Chl *a*	2 %	2 %	2 %	0.5 %

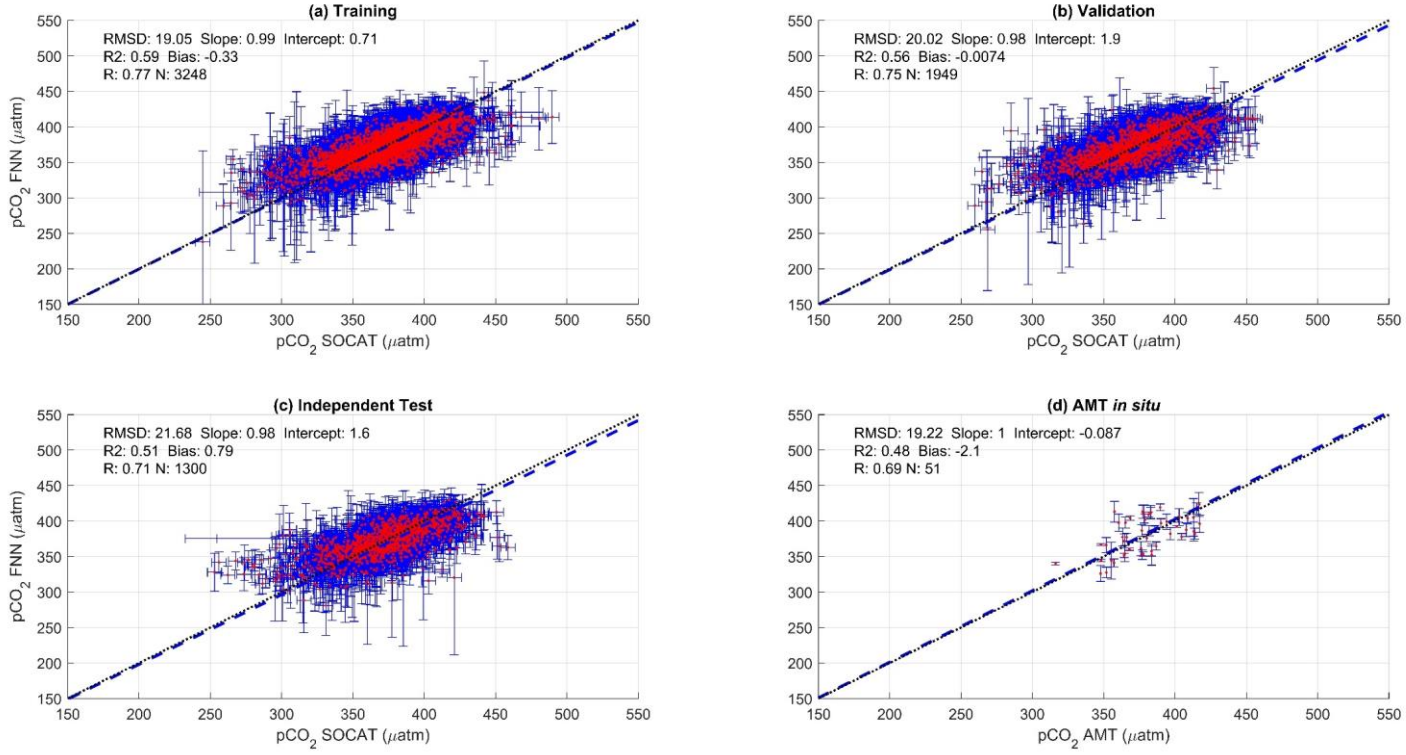

Figure 3.2 - Scatter plots showing the combined performance of the 8 feed forward neural networks trained using NCP for each biogeochemical province (Fig. 1) using 4 separate training and validation datasets; (a) Training, (b) Validation, (c) Independent Test and (d) Atlantic Meridional Transect (AMT) in situ. The data points are highlighted in red to distinguish them from the error bars in blue. The blue dashed line is the Type II regression and the black dashed line is the 1:1 line. Horizontal error bars indicate the uncertainty of the SOCATv2020 $pCO_{2\,(sw)}$. Vertical error bars indicate the uncertainty attributed to the input parameter uncertainty propagated through the feed forward neural networks. The statistics within each plot are; Root Mean Square Difference (RMSD), Slope and Intercept of the Type II regression, Coefficient of Determination (R2), Pearson's Correlation Coefficient (R), Bias and number of samples (N).

3.3.2 Comparison between SA-FNN$_{NCP}$ and other methods

The monthly climatologies of $pCO_{2\,(sw)}$ generated using the SA-FNN$_{NCP}$ and referenced to the year 2010 showed differences with two published climatologies, especially in the Equatorial region (Appendix 3.2). The monthly climatology for 8 stations (Fig. 3.1) were extracted from the SA-FNN$_{NCP}$, SA-FNN$_{NPP}$, SA-FNN$_{CHLA}$, SA-FNN$_{NO\text{-}BIO\text{-}1}$, SA-FNN$_{NO\text{-}BIO\text{-}2}$ and the W2020, to assess differences between the $pCO_{2\,(sw)}$ estimates (Fig. 3.3). The SA-FNN$_{NCP}$ and SA-FNN$_{NO\text{-}BIO\text{-}1}$ showed significant divergence in the Equatorial Atlantic (Figs. 3.3b, f, g; Fig. 3.4). At the eastern equatorial station, the interannual variability in $pCO_{2\,(sw)}$ from the SA-FNN$_{NCP}$ was high and a minimum occurred between January and April, which gradually increased to a maximum in September and October (Fig. 3.3b). The SA-FNN$_{NO\text{-}BIO\text{-}1}$ showed no seasonality in the $pCO_{2\,(sw)}$ and was consistently below the SA-FNN$_{NCP}$ $pCO_{2\,(sw)}$. The Gulf of Guinea station showed a similar variability in the SA-FNN$_{NCP}$ $pCO_{2\,(sw)}$ except that the maxima was lower at this station (Fig. 3.3f). The SA-FNN$_{NO\text{-}BIO\text{-}1}$ indicated $pCO_{2\,(sw)}$ below the SA-FNN$_{NCP}$ throughout the year. The greatest divergence occurred near the Amazon plume (Fig. 3.3g) where SA-FNN$_{NCP}$ $pCO_{2\,(sw)}$ was below or at $pCO_{2\,(atm)}$ for all months and there was a large interannual variability in $pCO_{2\,(sw)}$. The SA-FNN$_{NO\text{-}BIO\text{-}1}$ displayed higher $pCO_{2\,(sw)}$ and a lower interannual variability (Fig. 3.3g).

The SA-FNN$_{NCP}$ and SA-FNN$_{NO\text{-}BIO\text{-}1}$ showed no significant difference in the seasonal patterns of $pCO_{2\,(sw)}$ at stations south of 20 °S (Figs. 3.3c, d, e; Fig. 3.4). There was, however, a significant offset at some stations where the SA-FNN$_{NCP}$ generally exhibited lower $pCO_{2\,(sw)}$ in austral summer and a higher interannual variation. The SA-FNN$_{NCP}$ was significantly different to W2020 and SA-FNN$_{NO\text{-}BIO\text{-}2}$ at similar stations to those at which SA-FNN$_{NO\text{-}BIO\text{-}1}$ were different (Fig. 3.3, Fig. 3.4).

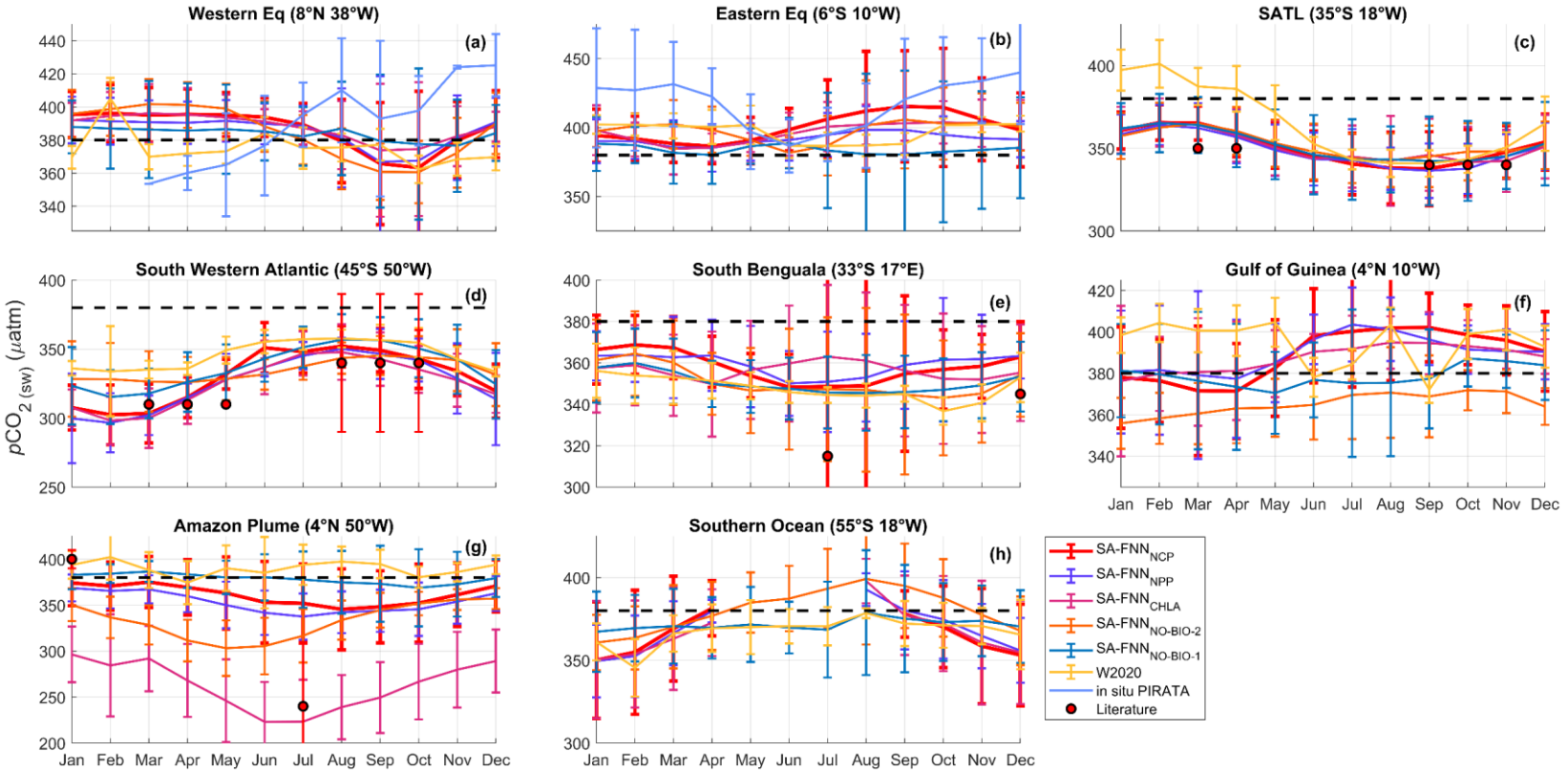

Figure 3.3 - Monthly climatologies of $pCO_{2\,(sw)}$ referenced to the year 2010 for the 8 stations marked in Fig. 1 from the SA-FNN$_{NCP}$, SA-FNN$_{NPP}$, SA-FNN$_{CHLA}$, SA-FNN$_{NO\text{-}BIO\text{-}1}$, SA-FNN$_{NO\text{-}BIO\text{-}2}$ and W2020 (Watson et al., 2020b). Light blue lines in Fig. 3a, b indicate the in situ $pCO_{2\,(sw)}$ observations from PIRATA buoys. The atmospheric CO_2 increase was set as 1.5 µatm yr^{-1}. Black dashed line indicates the atmospheric pCO_2 (~380 µatm). Error bars indicate the 2 standard deviation of the climatology (~95% interval), where larger error bars indicate a larger interannual variability. Red circles indicate the literature values of $pCO_{2\,(sw)}$ described in section 4.2. Note the different y-axis limits in each plot.

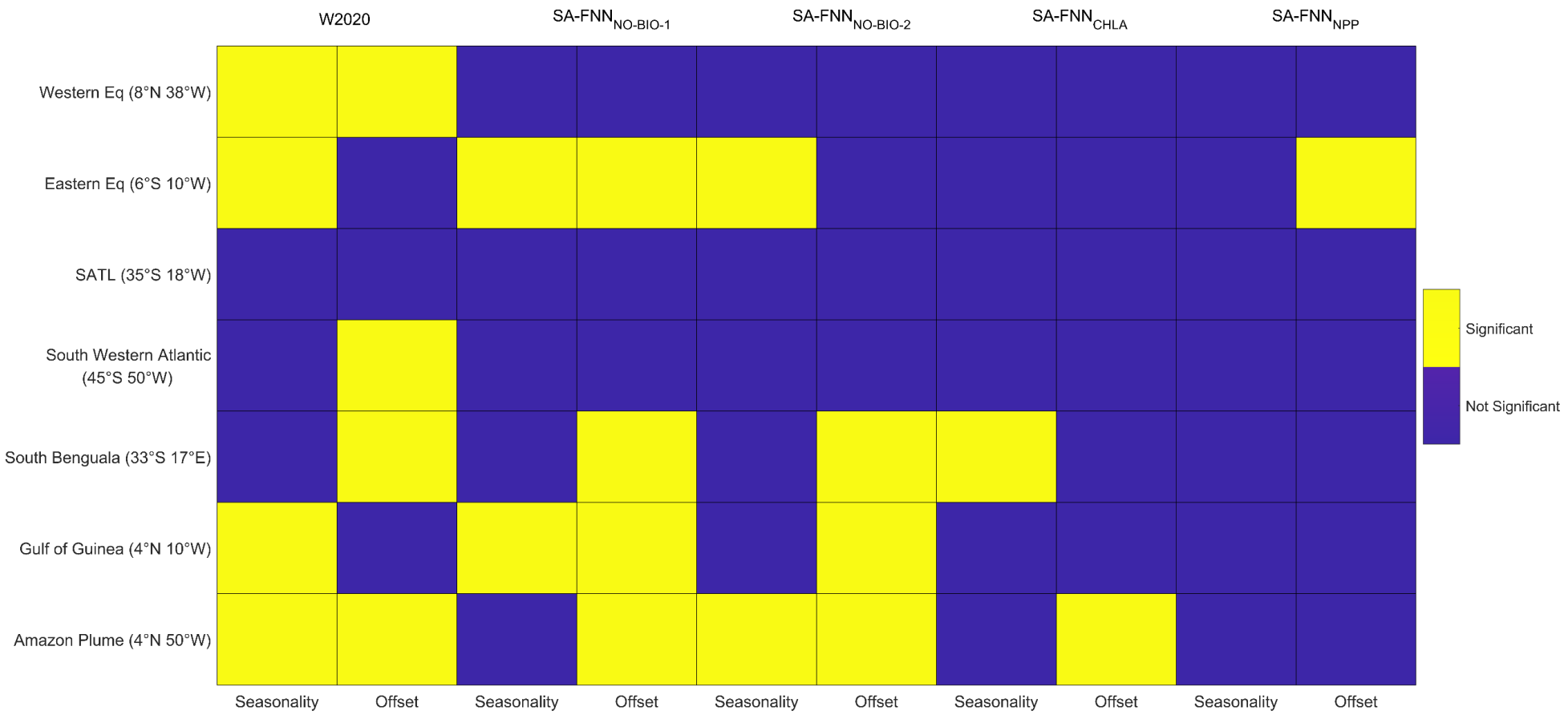

Figure 3.4 - Statistical comparison of the SA-FNN$_{NCP}$ with the W2020, SA-FNN$_{NO-BIO-1}$, SA-FNN$_{NO-BIO-2}$, SA-FNN$_{CHLA}$ and SA-FNN$_{NPP}$ climatologies, where yellow blocks indicate a significant difference ($\alpha = 0.05$). Seasonality indicates a difference in the seasonal cycle and offset indicates a difference between the mean $pCO_{2\,(sw)}$ of the climatologies.

The SA-FNN$_{NCP}$ and SA-FNN$_{CHLA}$ showed significant differences in $pCO_{2\,(sw)}$ values in the South Benguela and Amazon Plume. In the South Benguela (Fig. 3.3e; Fig. 3.4), SA-FNN$_{NCP}$ had $pCO_{2\,(sw)}$ maxima in austral summer, whereas the SA-FNN$_{CHL}$ maximum occurs in austral winter. In the Amazon Plume there was significant offset between the two methods and the SA-FNN$_{CHL}$ resulted in lower $pCO_{2\,(sw)}$ compared to the SA-FNN$_{NCP}$ (Fig. 3.3g; Fig. 3.4). The SA-FNN$_{NCP}$ and SA-FNN$_{NPP}$ had a significant offset at the Eastern Equatorial station (Fig. 3.3c; Fig. 3.4), where the SA-FNN$_{NPP}$ indicated lower $pCO_{2\,(sw)}$. For the other stations, no significant differences were observed.

3.4 Discussion

3.4.1 Assessment of biological parameters to estimate $pCO_{2\,(sw)}$

In this paper, the differences in estimating $pCO_{2\,(sw)}$ using FNNs with satellite derived NCP, NPP or Chl *a* were assessed. The SA-FNN$_{NCP}$ had an overall accuracy (21.68 µatm; Fig. 3.2) that is consistent with other approaches that have been developed for the Atlantic (22.83 µatm; Landschützer et al., 2013), and slightly lower than the published global result of 25.95 µatm (Landschützer et al., 2014). Training the SA-FNN using Chl *a* or NPP showed comparable broad-scale accuracy to NCP. When the uncertainties in the input parameters were investigated however, differences in the estimates of $pCO_{2\,(sw)}$ were apparent. The perturbation analysis indicated that up to a 36 % improvement in estimating $pCO_{2\,(sw)}$ could be achieved if NCP data uncertainties were reduced (Table 3.3). A similar improvement could be obtained if the NPP uncertainties were reduced (Table 3.3). Ford et al. (2021a) showed that up to 40 % of the uncertainty in satellite NCP is attributed to the uncertainty in satellite NPP, which is an input to the NCP approach. This suggests that improvements in estimating NPP from satellite data will lead to a further improvement in estimating $pCO_{2\,(sw)}$ from NCP. These improvements could be achieved through better estimates of the water column light field (e.g. Sathyendranath et al., 2020), and the vertical variability of input parameters or assignment of photosynthetic parameters (e.g. Kulk et al., 2020), for example. For a discussion on improving satellite NPP estimates we refer the reader to Lee et al. (2015).

To uncouple the Chl *a*, NPP and NCP estimates and their uncertainties, the perturbation analysis was also conducted on Atlantic Meridional Transect *in situ* observations. This showed that reducing *in situ* NCP uncertainties provided the greatest reduction in $pCO_{2\,(sw)}$ RMSD, which was three times the reduction achievable using Chl *a* (Table 3.3; Table 3.4). This indicates that the optimal predictive power of Chl *a* to estimate $pCO_{2\,(sw)}$ has been reached and to achieve further improvements in estimates of $pCO_{2\,(sw)}$ and reduction in its associated uncertainty, requires the use of NCP.

A reduction of input uncertainties to ~0 is near impossible, but a reduction by 10 % could be feasible (e.g. NCP uncertainty reduced from 45 to 40.5 mmol O_2 m^{-2} d^{-1}; Table 3.1). A perturbation analysis conducted for this showed similar results, with NCP producing the greatest reduction in $pCO_{2\,(sw)}$ RMSD of 8 % compared to 2 % for Chl *a* (Table 3.4). Thus reducing NCP uncertainties will provide a greater improvement in $pCO_{2\,(sw)}$ compared to reducing the uncertainties in Chl *a*.

These improvements in estimating NCP could be achieved through many components. Ford et al. (2021a) showed that 40 % of satellite NCP uncertainties were attributed to *in situ* NCP uncertainties. The *in situ* bottle incubation measurements could be improved using the principles of Fiducial Reference Measurements (FRM; Banks et al., 2020), which are traceable to metrology standards, referenced to inter-comparison exercises, with a full uncertainty budget. This becomes complicated however, when considering the number of different methods to measure NCP and the large divergence between them (Robinson et al., 2009). A review of these methods has already been conducted (Duarte et al., 2013; Ducklow and Doney, 2013; Williams et al., 2013). The methods broadly fall into the following categories: a.) *in vitro* incubations of samples under light/dark treatments (Gist et al., 2009) and b.) *in situ* observations of oxygen to argon (O_2/Ar) ratios (Kaiser et al., 2005) or the observed isotopic signature of oxygen (Luz and Barkan, 2000; Kroopnick, 1980). All of these methods are subject to, but do not account for, the photochemical sink which may lead to underestimation of *in vitro* NCP by up to 22 % (Kitidis et al., 2014). Independent ground measurements that use accepted protocols for the *in vitro* method are currently made on the Atlantic Meridional Transect, however a community consensus should consider a

consistent methodology for NCP. Increasing the number of such observations for the purpose of algorithm development, would further constrain the NCP, but also provide observations across the lifetime of newly launched satellites. The uncertainties on each *in vitro* measurement are assessed through replicate bottles which could be used to calculate a full uncertainty budget for each NCP measurement when combined with analytical uncertainties.

Serret et al. (2015) indicated that NCP is controlled by both the heterogeneity in NPP and respiration. The satellite NCP algorithm applied in this study accounts for some of the heterogeneity in respiration, through an empirical SST to NCP relationship (Tilstone et al., 2015a). Quantifying the variability in respiration could further improve NCP estimates when coupled with NPP rates from satellite observations.

3.4.2 Accuracy of SA-FNN$_{NCP}$ $pCO_{2\,(sw)}$ at seasonal and interannual scales

The seasonal and interannual variability of $pCO_{2\,(sw)}$ estimated using the SA-FNN$_{NCP}$ was compared with the SA-FNN$_{NO\text{-}BIO}$, W2020 (Watson et al., 2020b), SA-FNN$_{CHL}$ and SA-FNN$_{NPP}$ at 8 stations. The stations (Fig. 3.1) represent locations of previous studies into *in situ* $pCO_{2\,(sw)}$ variability allowing comparisons with literature values. Significant differences between the SA-FNN$_{NCP}$ and SA-FNN$_{NO\text{-}BIO}$ were observed at four stations (Fig. 3.4), especially in the Equatorial Atlantic.

At 8° N 38° W (Fig. 3.3a), Lefèvre et al. (2020) reported $pCO_{2\,(sw)}$ to be stable at ~400 µatm, between June and August 2013, and to decrease in September to ~360 µatm, which is attributed to the Amazon Plume propagating into the western Equatorial Atlantic (Coles et al., 2013). Bruto et al. (2017) indicated however, that elevated $pCO_{2\,(sw)}$ at ~430 µatm was observed in September for 2008 to 2011. The errorbars on the PIRATA buoy $pCO_{2\,(sw)}$ observations (Fig. 3.3a) clearly highlight the differences between Lefèvre et al. (2020) and Bruto et al. (2017), but there are less than 4 years of monthly observations available, which do not resolve the full seasonal cycle. For the station in the Amazon Plume at 4° N 50° W (Fig. 3.3g), where the effects of the plume extend northwest towards the Caribbean (Coles et al., 2013; Varona et al., 2019), Lefèvre et al. (2017) indicated that this region acts as a sink for CO_2 ($pCO_{2\,(sw)} < pCO_{2\,(atm)}$), especially between May to July, coincident with maximum discharge

from the Amazon River (Dai and Trenberth, 2002). Valerio et al. (2021) indicated $pCO_{2\,(sw)}$ varied at and below $pCO_{2\,(atm)}$ at 4° N 50° W consistent with the SA-FNN_{NCP}. The interannual variability of $pCO_{2\,(sw)}$ has been shown to be high in this region in all months (Lefèvre et al., 2017). The SA-FNN_{NCP} provided a better representation of the seasonal and interannual variability induced by the Amazon River discharge and associated plume at these two stations compared to the SA-$FNN_{NO\text{-}BIO}$, although differences were small at 8° N 38° W.

The station in the Eastern Tropical Atlantic at 6° S 10° W (Fig. 3.3b), is under the influence of the equatorial upwelling (Lefèvre, Guillot, Beaumont, & Danguy, 2008), which is associated with the upwelling of CO_2 rich waters between June and September. Lefèvre et al. (2008) indicated that peak $pCO_{2\,(sw)}$ of ~440 µatm was observed in September, and remained stable until December, before decreasing to a minima of ~360 µatm in May (Parard et al., 2010). Lefèvre et al. (2016) showed however, that the influence of the equatorial upwelling does not reach the buoy in all years, and in some years lower $pCO_{2\,(sw)}$ is observed. The PIRATA buoy observations (Fig. 3.3b) clearly show this seasonality but also highlight the interannual variability in *in situ* $pCO_{2\,(sw)}$. Further north at 4° N 10° W (Fig. 3.3f), Koffi et al. (2010) suggested that this region follows a similar seasonal cycle as the station at 6° S 10° W, but that $pCO_{2\,(sw)}$ is ~30 µatm lower (Koffi et al., 2016). The interannual variability in SA-FNN_{NCP} $pCO_{2\,(sw)}$ clearly shows the influence of the equatorial upwelling at these stations, with latitudinal gradients in $pCO_{2\,(sw)}$ during the upwelling period (Lefèvre et al., 2016), but struggles to identify elevated $pCO_{2\,(sw)}$ between December to April shown by the PIRATA buoy observations (Fig. 3.3b). By contrast, the SA-$FNN_{NO\text{-}BIO\text{-}1}$ indicated little influence from the equatorial upwelling and a depressed $pCO_{2\,(sw)}$ during the upwelling season.

The two methods converge on the seasonal cycle at the remaining stations although significant offsets in the mean annual $pCO_{2\,(sw)}$ remain. The station at 35° S 18° W (Fig. 3.3c) has consistently been implied as a sink for CO_2. Lencina-Avila et al. (2016) showed the region to have 340 µatm $pCO_{2\,(sw)}$ and to be a sink for CO_2 between October to December. Similarly, Kitidis et al. (2017) implied that the region is a sink for CO_2 during March to April. The region has depressed $pCO_{2\,(sw)}$ due to high biological activity that originates from the Patagonian shelf and the South Subtropical Convergence Zone. The station at

45° S 50° W (Fig. 3.3d), has also been implied as a strong, but highly variable sink, where $pCO_{2\,(sw)}$ can be between ~280 µatm and ~380 µatm during austral spring, and is constant at ~310 µatm during austral autumn (Kitidis et al., 2017). The SA-FNN_{NCP} and SA-$FNN_{NO\text{-}BIO\text{-}1}$ methods reproduced the seasonal variability in the $pCO_{2\,(sw)}$ at these two stations accurately, but only the SA-FNN_{NCP} captures the magnitude of the depressed $pCO_{2\,(sw)}$ at 45° S.

Within the southern Benguela upwelling system, $pCO_{2\,(sw)}$ at station 33° S 17° E (Fig. 3.3e) is influenced by gradients in the seasonal upwelling (Hutchings et al., 2009). Santana-Casiano et al. (2009) showed that $pCO_{2\,(sw)}$ varies from ~310 µatm in July to ~340 µatm in December and that the region is a CO_2 sink through the year. González-Dávila et al. (2009) suggested however, that this CO_2 sink is highly variable during upwelling events, and that recently upwelled waters act as a source ($pCO_{2\,(sw)} > pCO_{2\,(atm)}$) of CO_2 to the atmosphere (Gregor and Monteiro, 2013). Arnone et al. (2017) indicated elevated $pCO_{2\,(sw)}$ during austral spring and autumn at the station, with a ~40 µatm seasonal cycle amplitude. The SA-FNN_{NCP} and SA-$FNN_{NO\text{-}BIO\text{-}1}$ were able to reproduce the seasonal cycle, although the SA-FNN_{NCP} correctly represented the seasonal magnitude in $pCO_{2\,(sw)}$ as reported by Santana-Casiano et al. (2009) and Arnone et al. (2017).

In summary, for these stations, the SA-FNN_{NCP} better represents the seasonality and the interannual variability of $pCO_{2\,(sw)}$ in the South Atlantic Ocean compared to the SA-$FNN_{NO\text{-}BIO\text{-}1}$, especially in the Equatorial Atlantic. The SA-$FNN_{NO\text{-}BIO\text{-}2}$ also displayed significant differences to SA-FNN_{NCP}, indicating that the variability in $pCO_{2\,(sw)}$ has a strong biological contribution which is not fully represented and explained by the additional physical parameters included in the FNN. The SA-$FNN_{NO\text{-}BIO\text{-}2}$ and W2020 both displayed significant differences to the SA-FNN_{NCP} at specific stations (Fig. 3.4). There are methodological differences between these approaches however. The SA-FNN method uses only *in situ* $pCO_{2\,(sw)}$ observations from the South Atlantic Ocean to train the FNNs. The W2020 uses global *in situ* $pCO_{2\,(sw)}$ observations to train FNNs for 16 provinces with similar seasonal cycles (Landschützer et al., 2014; Watson et al., 2020b). The W2020 will therefore be weighted to $pCO_{2\,(sw)}$ variability in regions of relatively abundant *in situ* observations (i.e. Northern Hemisphere) and may not be fully representative of the South Atlantic Ocean.

This would explain the SA-FNN$_{NO-BIO-2}$ and W2020 differences, when driven using the same input variables.

Comparing the SA-FNN$_{NCP}$ and SA-FNN$_{CHLA}$ there were two significant differences (Fig. 3.4). A difference in the seasonal cycle in the southern Benguela (Fig. 3.3e) was observed. Santana-Casiano et al. (2009) showed that the minima $pCO_{2\,(sw)}$ in July and maxima in December, consistent with the SA-FNN$_{NCP}$ and SA-FNN$_{NPP}$ whereas the SA-FNN$_{CHL}$ estimated the opposite scenario. Lamont et al. (2014) reported Chl *a* concentrations to remain consistent in May and October, but NPP rates were significantly higher in October, associated with increased surface PAR and enhanced upwelling. The disconnect between Chl *a* and NPP can also be observed in the satellite observations (Appendix 3.3 Fig. A3.8) limiting the ability of Chl *a* to estimate $pCO_{2\,(sw)}$, which is highlighted by the failure of the SA-FNN$_{CHLA}$ to identify the seasonal $pCO_{2\,(sw)}$ cycle.

A Chl *a* to NPP disconnect has also been reported in the Amazon Plume (Smith and Demaster, 1996), where Chl *a* concentrations can be similar but NPP rates significantly different due to light limitation caused by suspended sediments. A significant offset between the SA-FNN$_{NCP}$ and SA-FNN$_{CHLA}$ was observed in this region (Fig. 3.3g; Fig. 3.4). Lefèvre et al. (2017) reported $pCO_{2\,(sw)}$ values ranging from 400 ± ~10 µatm in January to ~240 ± ~70 µatm in May. Although, the SA-FNN$_{NCP}$ January estimates are consistent, the May estimates are higher than these *in situ* measurements. These observations were made further north (6° N) where the turbidity within the plume has decreased sufficiently for irradiance to elevate NPP rates (Smith and Demaster, 1996), which decrease $pCO_{2\,(sw)}$. Chl *a* remains relatively consistent across the plume (not shown), suggesting a disconnect between Chl *a* and NPP at 4° N 50° W which would lead to lower $pCO_{2\,(sw)}$ estimates by the SA-FNN$_{CHLA}$, where NPP rates are low due to light limitation (Smith and Demaster, 1996; Chen et al., 2012a). Respiration would be elevated from the decomposition of riverine organic material reducing NCP further (Lefèvre et al., 2017; Cooley et al., 2007; Jiang et al., 2019). It is noted that the Amazon Plume is a dynamic region with transient, localised biological and $pCO_{2\,(sw)}$ features (Ibánhez et al., 2015; Lefèvre et al., 2017; Valerio et al., 2021; Cooley et al., 2007) that may be masked by the coarse resolution of estimates available using satellite data. The SA-FNN$_{NCP}$

however, agreed with *in situ* $pCO_{2\,(sw)}$ observations at 4° N 50° W where $pCO_{2\,(sw)}$ varied at or below $pCO_{2\,(atm)}$ (Valerio et al., 2021).

Though the differences between the SA-FNN_{NCP} and SA-FNN_{CHLA} may appear small, the Amazon Plume and Benguela Upwelling have a higher intensity in the CO_2 flux per unit area compared to the open ocean, illustrating a disproportionate contribution to the overall global CO_2 sink than their small areal coverage implies (Laruelle et al., 2014). The differences in the $pCO_{2\,(sw)}$ estimates result in a 22 Tg C yr^{-1} alteration in the annual CO_2 flux for the South Atlantic Ocean (SA-FNN_{NCP} = +14 Tg C yr^{-1}; SA-FNN_{CHLA} = -9 Tg C yr^{-1}; Fig. 3.5f). This unequivocally reinforces the use of NCP to improve basin scale estimates of $pCO_{2\,(sw)}$, especially in regions where Chl *a*, NPP and NCP become disconnected.

Recent assessments of the strength of the global oceanic CO_2 sink have been made using $pCO_{2\,(sw)}$ fields estimated using no biological parameters as input (Watson et al., 2020b). Our results indicate that the SA-FNN_{NCP} more accurately represented the $pCO_{2\,(sw)}$ variability in the South Atlantic Ocean compared to the SA-$FNN_{NO\text{-}BIO\text{-}2}$, which included additional physical parameters. Estimating the South Atlantic Ocean net CO_2 flux with the SA-FNN_{NCP} $pCO_{2\,(sw)}$ produced a 14 Tg C yr^{-1} source compared to a 10 Tg C yr^{-1} sink indicated by the SA-$FNN_{NO\text{-}BIO\text{-}2}$ (Fig. 3.5f). The incremental inclusion of parameters to account for the biological signal starting with Chl *a* (-9 Tg C yr^{-1}) then NPP (-7 Tg C yr^{-1}) then NCP (+14 Tg C yr^{-1}) switched the South Atlantic Ocean from a CO_2 sink to a source, which is driven by differences in the $pCO_{2\,(sw)}$ estimates in regions that are biologically controlled. This 21 Tg C yr^{-1} difference between the SA-FNN_{NCP} and SA-FNN_{NPP} is due to additional outgassing in the Equatorial Atlantic provinces of the WTRA and ETRA (Fig 3.1a; Fig. 3.5f). Compared to the *in situ* $pCO_{2\,(sw)}$ observations at the Equatorial stations (Fig. 3.3a, b), it is likely that the outgassing is still underestimated by the SA-FNN_{NCP} but does improve these estimates within the upwelling season (June – September).

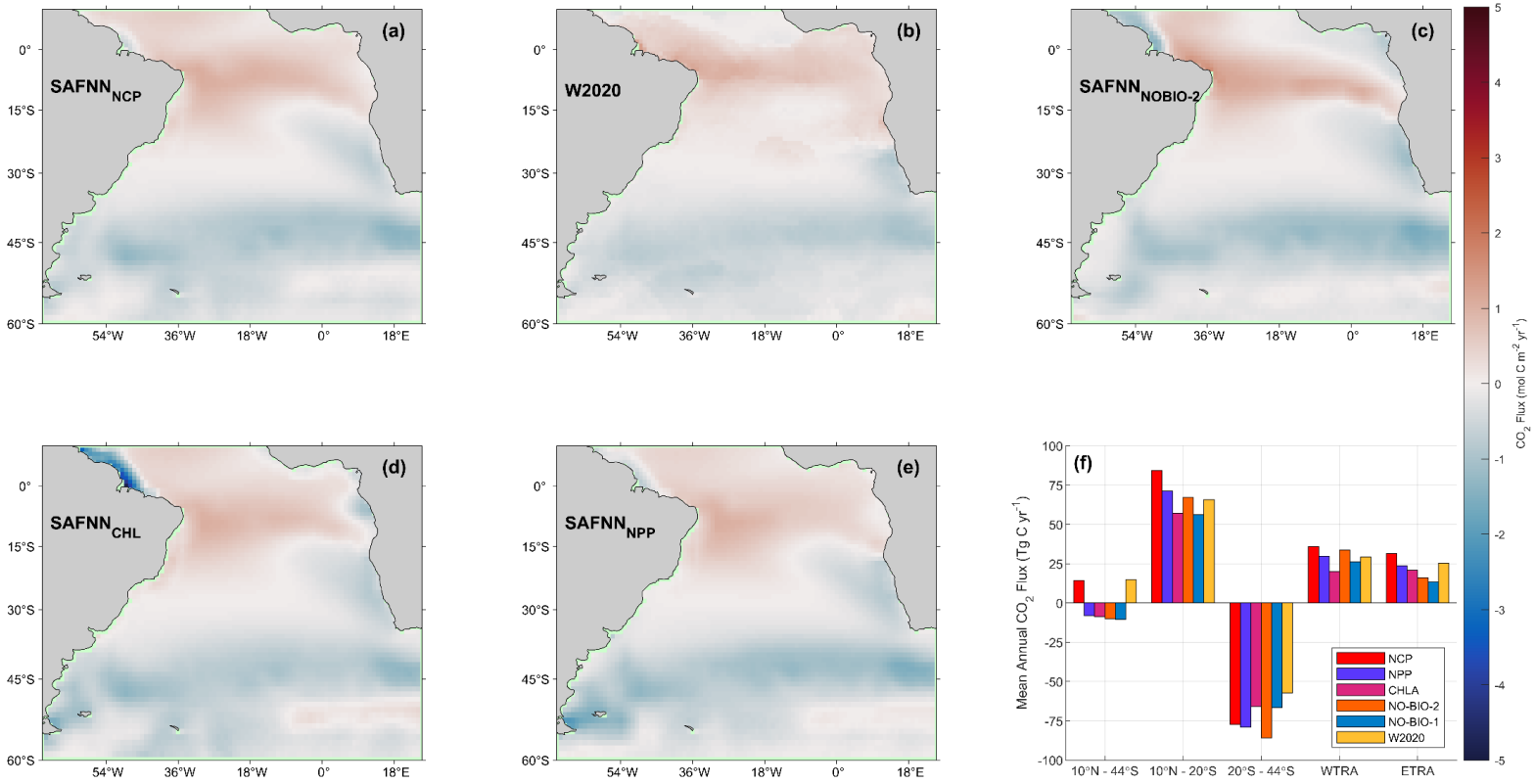

Figure 3.5 - Long term average annual mean CO_2 flux for the South Atlantic Ocean, using $pCO_{2\,(sw)}$ estimates from (a) SA-FNN$_{NCP}$, (b) W2020 (Watson, et al., 2020a), (c) SA-FNN$_{NO\text{-}BIO\text{-}2}$, (d) SA-FNN$_{CHLA}$ and (e) SA-FNN$_{NPP}$. (f) Bar chart displaying the mean annual CO_2 flux for different regions of the South Atlantic Ocean including 10° N to 44° S (Whole South Atlantic Ocean), 10° N to 20° S, 20° S to 44° S, alongside the WTRA and ETRA biogeochemical provinces (Fig. 3.1a).

The W2020 identified the South Atlantic Ocean as a source for CO_2 of 15 Tg C yr^{-1}, which is consistent with the SA-FNN_{NCP} (Fig. 3.5f). The SA-FNN_{NCP} however, indicated the Equatorial Atlantic (10° N to 20° S) as a 20 Tg C yr^{-1} stronger source and south of 20° S (20° S to 44° S) as a 20 Tg C yr^{-1} stronger sink. These differences indicate that biologically induced variability in $pCO_{2\,(sw)}$ would not be captured by the W2020 and could reduce the variability in the global ocean CO_2 sink. A further SA-FNN trained with $pCO_{2\,(atm)}$, SST, salinity, mixed layer depth and NCP indicated a similar CO_2 source of 12 Tg C yr^{-1} (data not shown) as the SA-FNN_{NCP} for the South Atlantic Ocean, highlighting that additional physical parameters cannot fully account for the biological contribution to the variability in $pCO_{2\,(sw)}$. This further confirms the importance of using NCP within estimates of the global ocean CO_2 sink.

2.5 Conclusions

In this paper, we compare neural network models of $pCO_{2\,(sw)}$ parameterised separately using either satellite Chl *a*, NPP or NCP as biological proxies to estimate complete fields of $pCO_{2\,(sw)}$. The results suggest that using NCP improved the estimation of $pCO_{2\,(sw)}$. The differences between satellite Chl *a*, NPP or NCP were initially small, but the use of a perturbation analysis to assess the uncertainties in these parameters, showed that NCP has a greater potential uncertainty reduction of up to ~36 % of the RMSD, compared to a ~19 % for Chl *a*. These results were verified using *in situ* observations from the Atlantic Meridional Transect, which resulted in a 25 % improvement in $pCO_{2\,(sw)}$ RMSD when the *in situ* NCP uncertainties were reduced to ~0, compared to 7 % for Chl *a* and 13 % for NPP.

Monthly climatological estimates of $pCO_{2\,(sw)}$ at 8 stations in the South Atlantic Ocean, calculated using satellite NCP were compared with the NPP and the Chl *a* approaches and two neural networks that do not use biological parameters. The NCP approach significantly improved on both approaches with no biological parameters at 4 stations in reconstructing the seasonal and interannual variability, compared to *in situ* $pCO_{2\,(sw)}$ observations. At the remaining 4 stations, differences were also observed although these were not statistically significant. In the eastern Equatorial Atlantic, in the upwelling region, a significant difference between the NCP and NPP approaches occurred. Significant differences between the NCP and Chl *a* approaches were also

observed in the Benguela upwelling and Amazon Plume, where $pCO_{2\,(sw)}$ from Chl *a* suggested that photosynthetic rates were not solely controlled by Chl *a*. Using NCP to estimate $pCO_{2\,(sw)}$ the South Atlantic Ocean was characterised as a net source of CO_2, whereas methods that only include physical controls have indicated the region to be a small sink for CO_2. Sequentially using Chl *a* to estimate $pCO_{2\,(sw)}$, then NPP incrementally reduced the South Atlantic CO_2 sink and finally using NCP the area switched to being a source of CO_2. These results indicate that in regions where biological activity is important in controlling the variability in $pCO_{2\,(sw)}$, the use of NCP, which is available from satellite data, is important for quantifying the ocean carbon pump, and for providing data in areas that are sparsely covered by observations such as the Southern Ocean.

Appendices

Appendix 3.1 - Feed forward neural network training and perturbation analysis

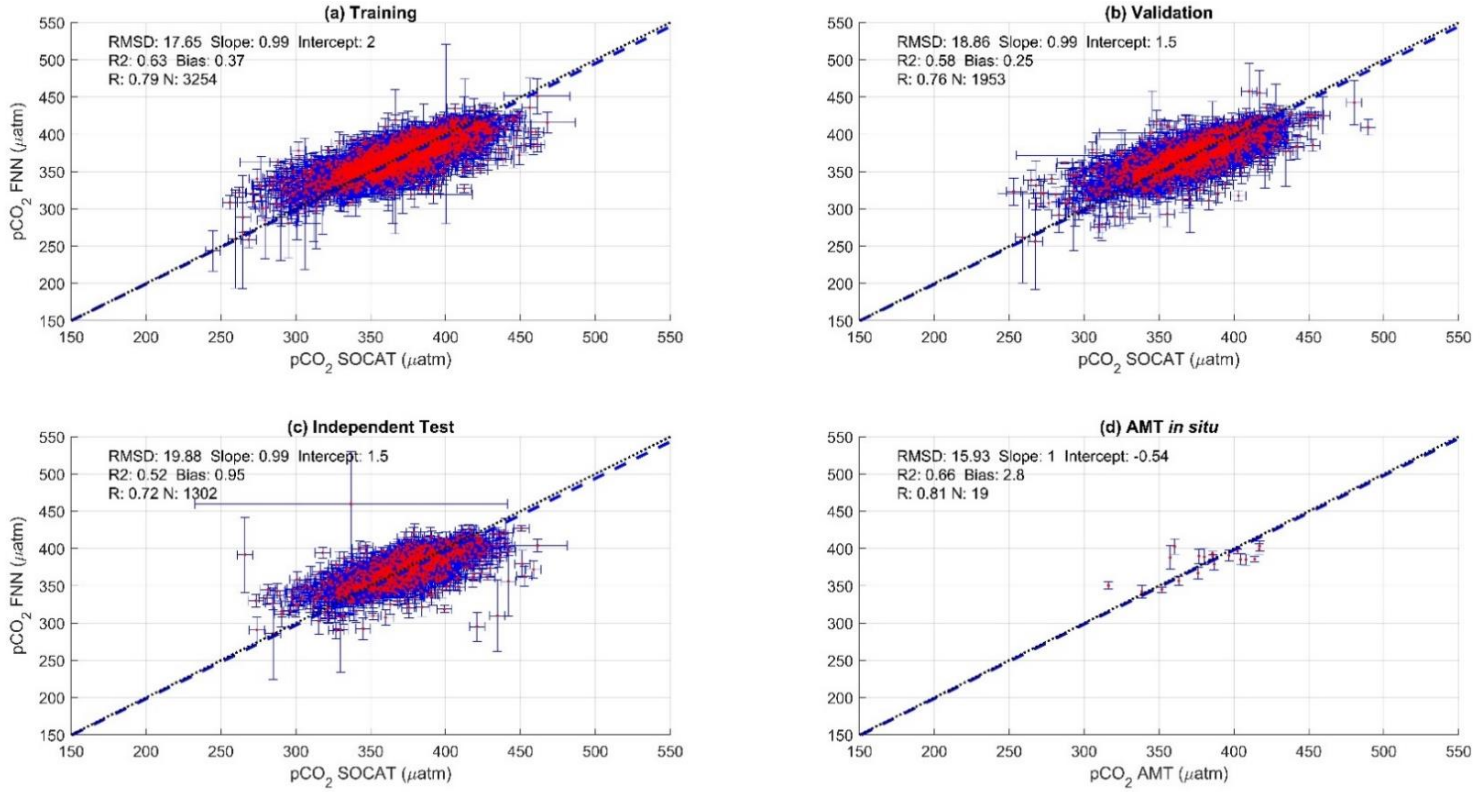

Figure A3.1 - Scatter plots showing the combined performance of the 8 feed forward neural networks trained using chlorophyll a for 4 separate training and validation datasets; (a) Training, (b) Validation, (c) Independent Test and (d) Atlantic Meridional Transect (AMT) in situ. The blue dashed line is the Type II regression and the black dashed line is the 1:1 line. Horizontal error bars indicate the uncertainty of the SOCATv2020 $pCO_{2\,(sw)}$. Vertical error bars indicate the uncertainty attributed to the input parameter uncertainty propagated through the feed forward neural networks. The statistics within each plot are; Root Mean Square Difference (RMSD), Slope and Intercept of the Type II regression, Coefficient of Determination (R2), Pearson's Correlation Coefficient (R), Bias and number of samples (N).

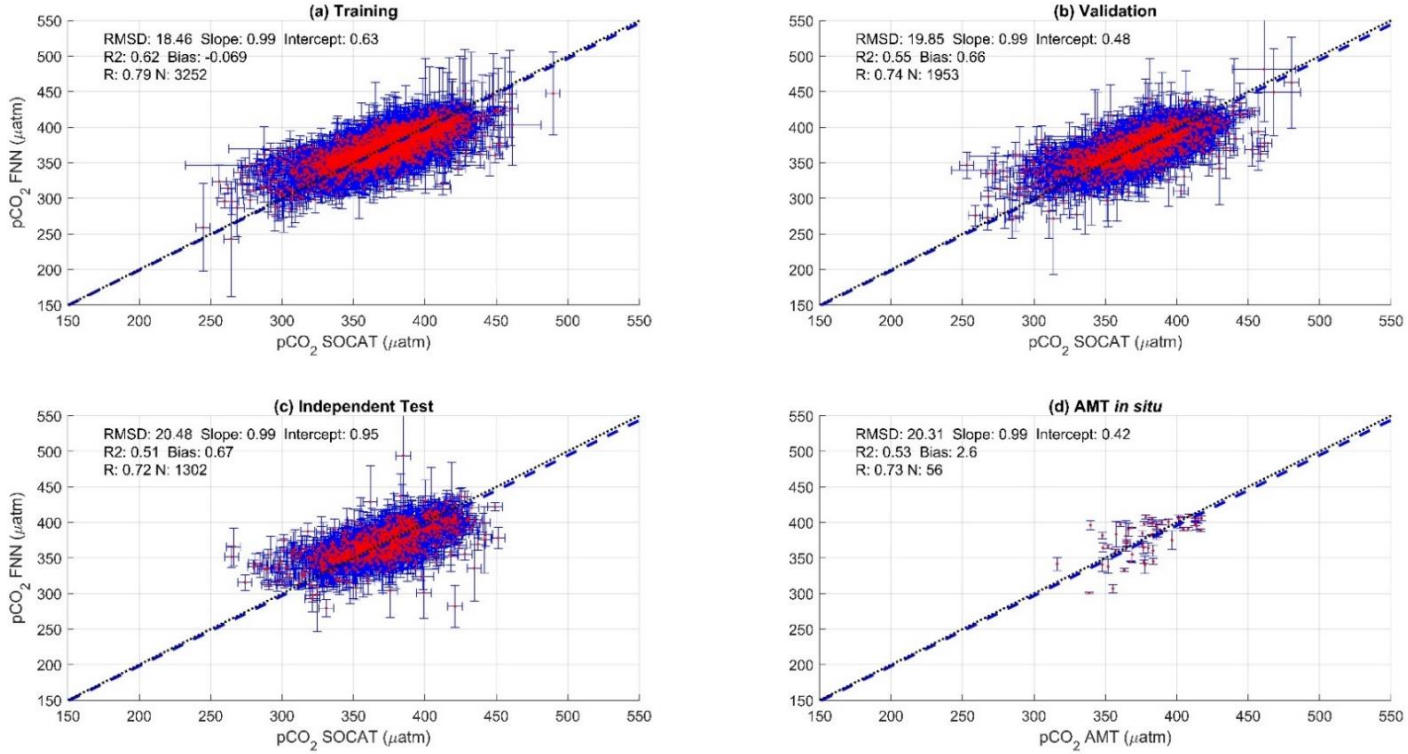

Figure A3 2 - Scatter plots showing the combined performance of the 8 feed forward neural networks trained using net primary production for 4 separate training and validation datasets; (a) Training, (b) Validation, (c) Independent Test and (d) Atlantic Meridional Transect (AMT) in situ. The blue dashed line is the Type II regression and the black dashed line is the 1:1 line. Horizontal error bars indicate the uncertainty of the SOCATv2020 $pCO_{2\,(sw)}$. Vertical error bars indicate the resulting uncertainty attributed to the input parameter uncertainty propagated through the feed forward neural networks. The statistics within each plot are; Root Mean Square Difference (RMSD), Slope and Intercept of the Type II regression, Coefficient of Determination (R2), Pearson's Correlation Coefficient (R), Bias and number of samples (N).

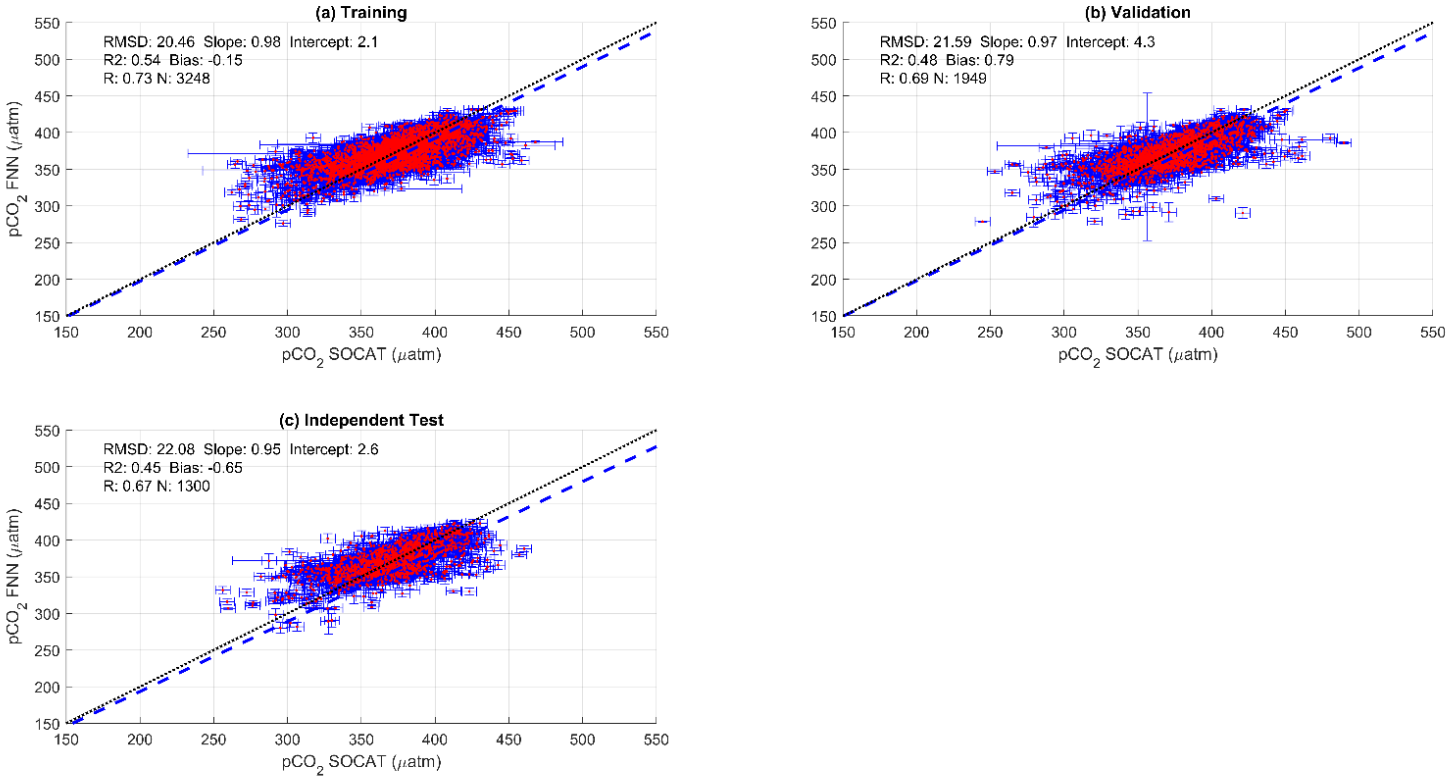

Figure A3.3 - Scatter plots showing the combined performance of the 8 feed forward neural networks trained using no biological parameters (SA-FNN$_{NO\text{-}BIO\text{-}1}$) for 3 separate training and validation datasets; (a) Training, (b) Validation and (c) Independent Test. The blue dashed line is the Type II regression and the black dashed line is the 1:1 line. Horizontal error bars indicate the uncertainty of the SOCATv2020 $pCO_{2\ (sw)}$. Vertical error bars indicate the resulting uncertainty attributed to the input parameter uncertainty propagated through the feed forward neural networks. The statistics within each plot are; Root Mean Square Difference (RMSD), Slope and Intercept of the Type II regression, Coefficient of Determination (R2), Pearson's Correlation Coefficient (R), Bias and number of samples (N).

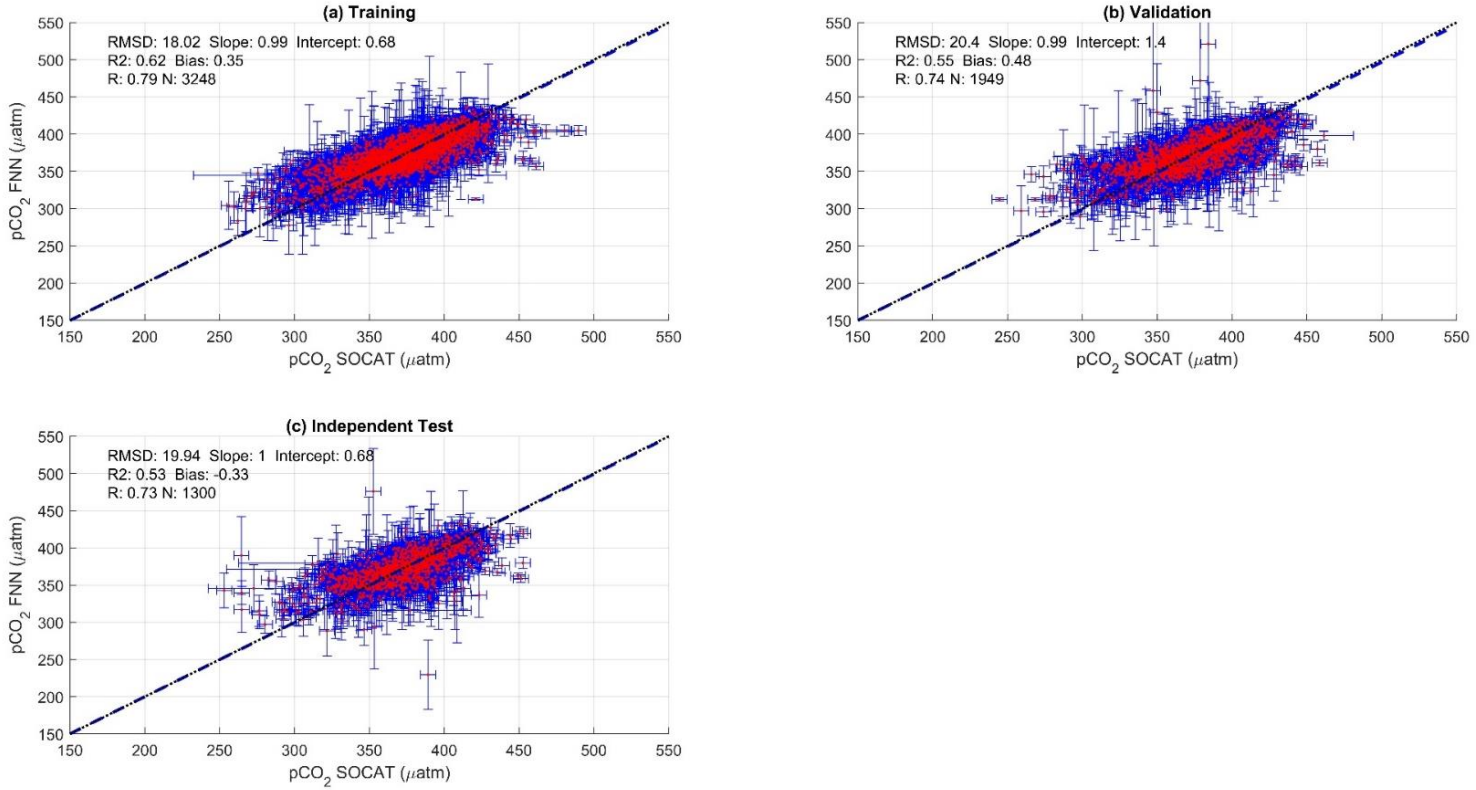

Figure A3.4 - Scatter plots showing the combined performance of the 8 feed forward neural networks trained using no biological parameters (SA-FNN$_{NO\text{-}BIO\text{-}2}$) for 3 separate training and validation datasets; (a) Training, (b) Validation and (c) Independent Test. The blue dashed line is the Type II regression and the black dashed line is the 1:1 line. Horizontal error bars indicate the uncertainty of the SOCATv2020 $pCO_{2\,(sw)}$. Vertical error bars indicate the resulting uncertainty attributed to the input parameter uncertainty propagated through the feed forward neural networks. The statistics within each plot are; Root Mean Square Difference (RMSD), Slope and Intercept of the Type II regression, Coefficient of Determination (R2), Pearson's Correlation Coefficient (R), Bias and number of samples (N).

Table A3.1 - The percentage reduction in Root Mean Square Difference (RMSD) attributable to the uncertainties in the input parameter for each training and validation datasets determined from a perturbation analysis as described in Sect. 3.2.5.

	Parameter	Training	Validation	Independent Test	AMT *in situ*
Net Community Production	ALL	33 %	42 %	38 %	28 %
	SST	10 %	12 %	10 %	0.5 %
	Net Community Production	32 %	40 %	36 %	25 %
	$pCO_{2\ (atm)}$	6 %	7 %	6 %	9 %
Net Primary Production	ALL	34 %	40 %	40 %	17 %
	SST	9 %	10 %	10 %	0.4 %
	Net Primary Production	31 %	37 %	36 %	13 %
	$pCO_{2\ (atm)}$	6 %	6 %	6 %	9 %
Chlorophyll *a*	ALL	22 %	26 %	25 %	29 %
	SST	9 %	10 %	9 %	0.4 %
	Chlorophyll *a*	17 %	21 %	20 %	7 %
	$pCO_{2\ (atm)}$	8 %	9 %	9 %	16 %

Appendix 3.2 - Climatology comparison

A monthly climatology was generated from the SA-FNN$_{NCP}$ monthly timeseries (Fig. A3.5), referenced to the year 2010, assuming an atmospheric CO_2 increase of 1.5 µatm yr^{-1} (Takahashi et al., 2009; Zeng et al., 2014). The standard deviation of the monthly climatology was computed, as an indication of the interannual variations in the climatology. The ability of the SA-FNN$_{NCP}$ to estimate the spatial distribution of $pCO_{2\,(sw)}$ was compared to two methods.

Firstly, the SA-FNN$_{NCP}$ climatology was compared to the climatology from Woolf et al. (2019), produced following the statistical 'ordinary block kriging' approach described in Goddijn-Murphy et al. (2015), using the SOCATv4 reanalysed data. The method provides an interpolation uncertainty where in regions of sparse data this becomes larger. Fig. A3.6 shows the methods produce similar climatological $pCO_{2\,(sw)}$ values for the South Atlantic Ocean, with some clear differences along the African coastline, and equatorial region.

Secondly, the SA-FNN$_{NCP}$ was compared to a climatology calculated from the 'standard method', a Self Organising Map Feed Forward Neural Network presented in Watson et al. (2020b; W2020). Fig. A3.7 shows the methods produce similar climatological $pCO_{2\,(sw)}$ values for the South Atlantic Ocean, however, clear differences in the Equatorial region occur across all months. In the central South Atlantic Ocean, artefacts form the self organising map can be seen during January and February.

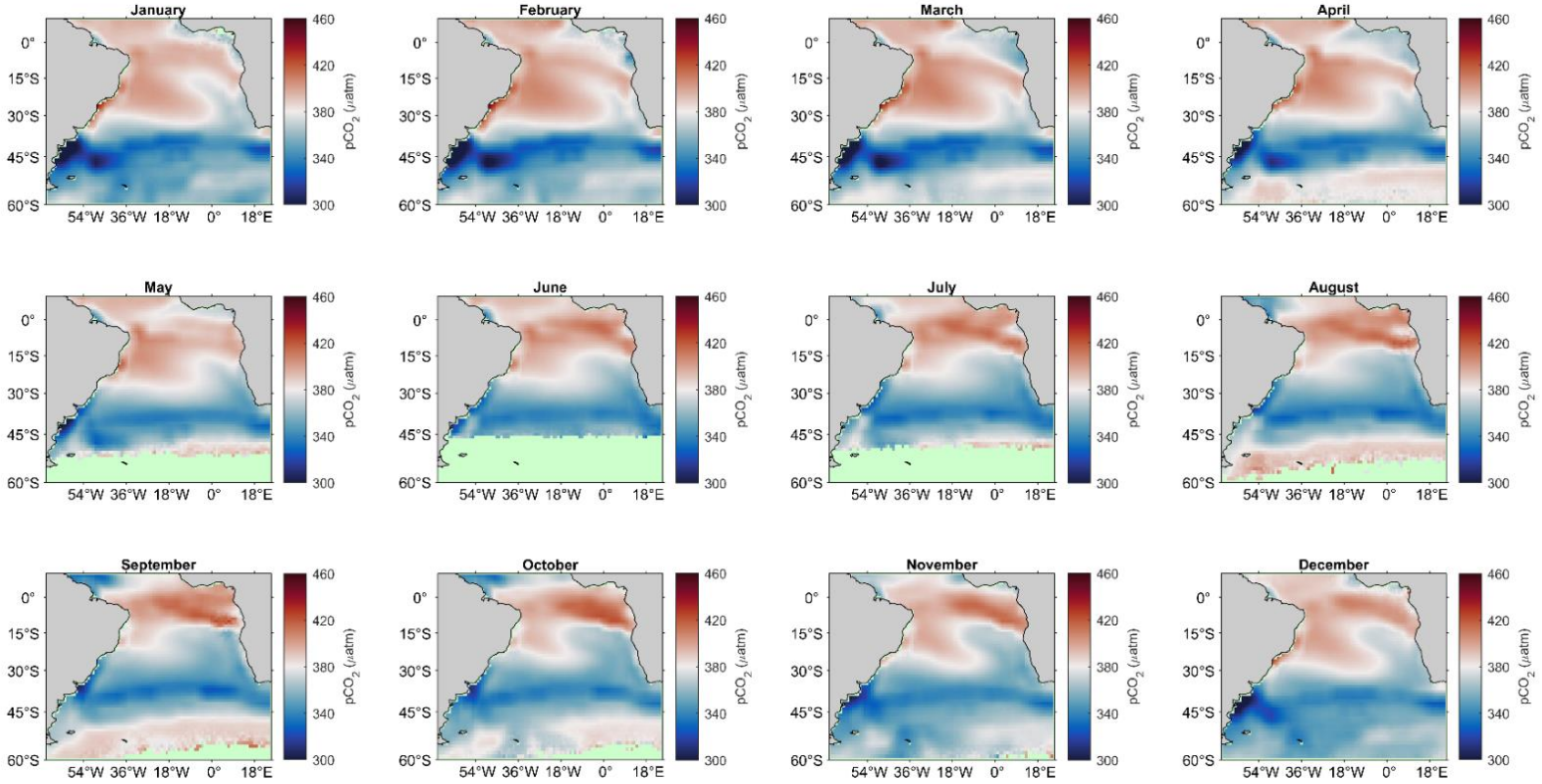

Figure A3.5 - Monthly climatologies of $pCO_{2\,(sw)}$ between July 2002 and December 2018 estimated by the SA-FNN$_{NCP}$ approach referenced to 2010. The atmospheric CO_2 increase was set as 1.5 µatm yr^{-1}. The colour scale is centred on the atmospheric concentration for 2010 (~380 µatm). Red shaded areas indicate oversaturated regions, and blue shaded areas indicate under saturated regions. Light green areas indicate where no input data to compute $pCO_{2\,(sw)}$ are available.

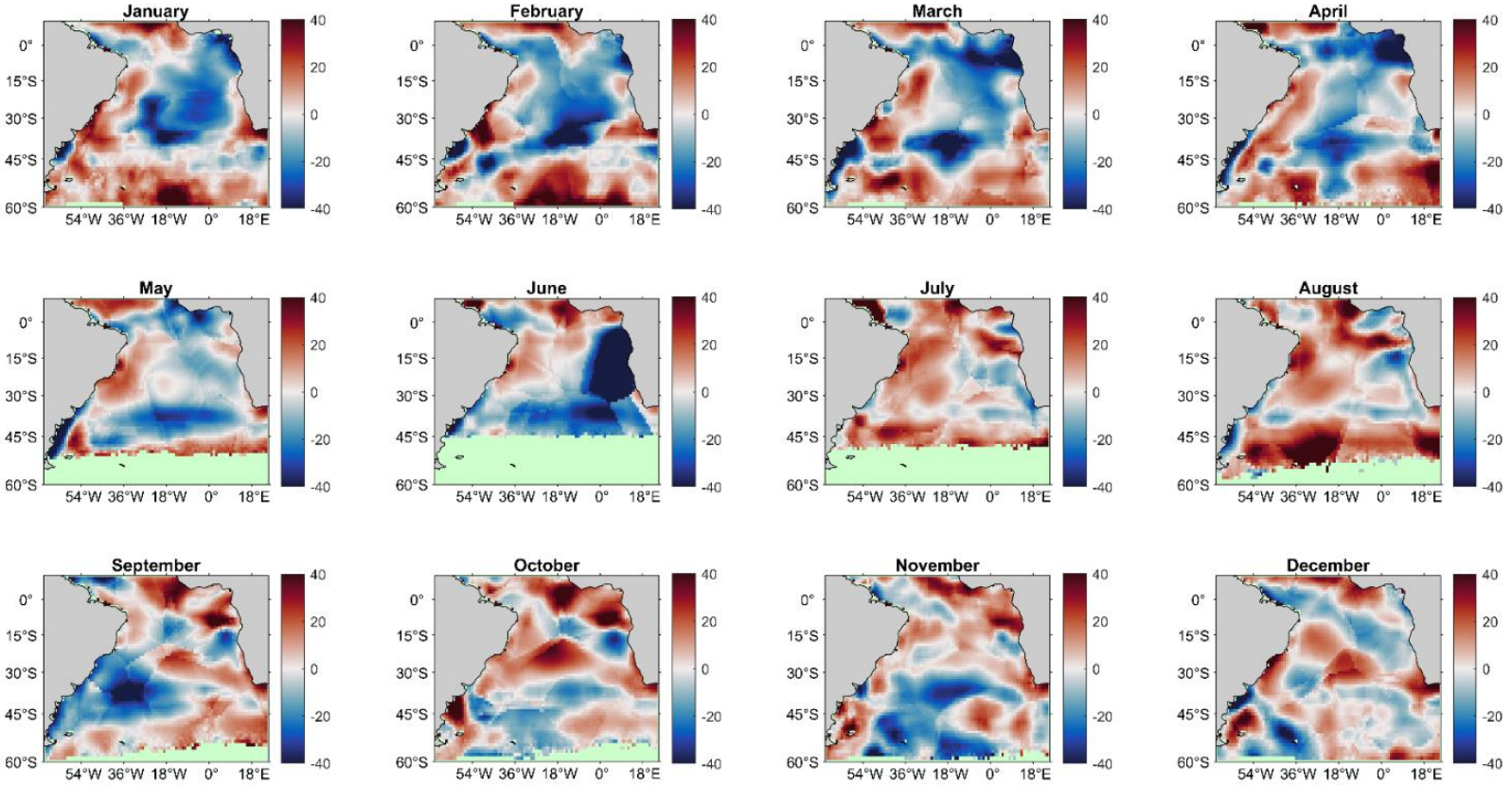

Figure A3.6 - Monthly comparison between $pCO_{2\,(sw)}$ climatology estimated by the SA-FNN_{NCP} and Woolf et al (2019) climatology referenced to 2010 (SA-FNN_{NCP} pCO_2 – Woolf pCO_2). Red (Blue) shades indicate regions where SA-FNN is greater (less) than the Woolf climatology.

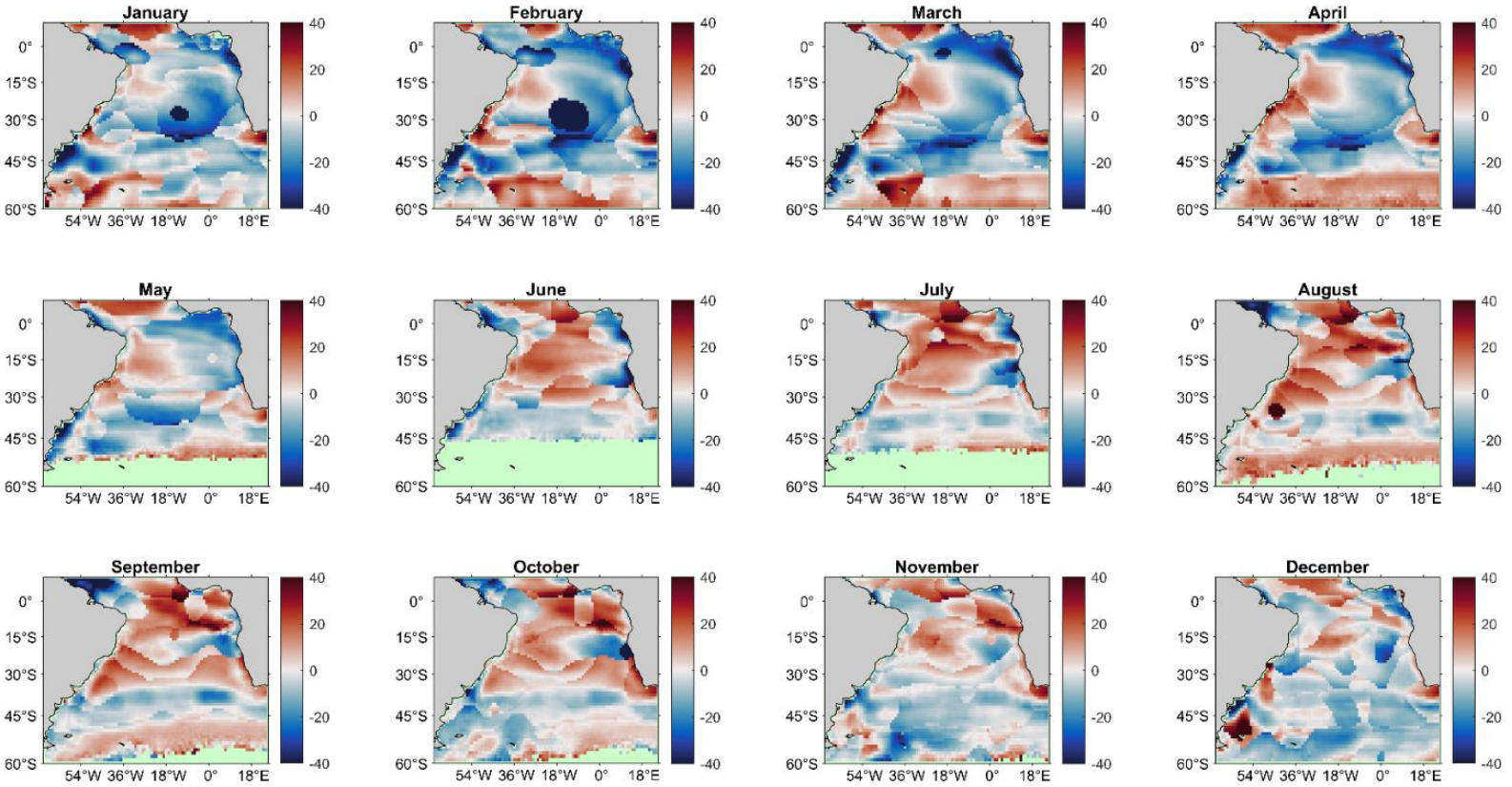

Figure A3.7 - Monthly comparison between $pCO_{2\,(sw)}$ climatologies estimated by the SA-FNN_{NCP} and W2020 (Watson et al, 2020a) climatology referenced to 2010 (SA-FNN_{NCP} pCO_2 – W2020 pCO_2). Red (Blue) shades indicate regions where SA-FNN_{NCP} is greater (less) than the W2020 climatology.

Appendix 3.3 – Biological parameter climatologies

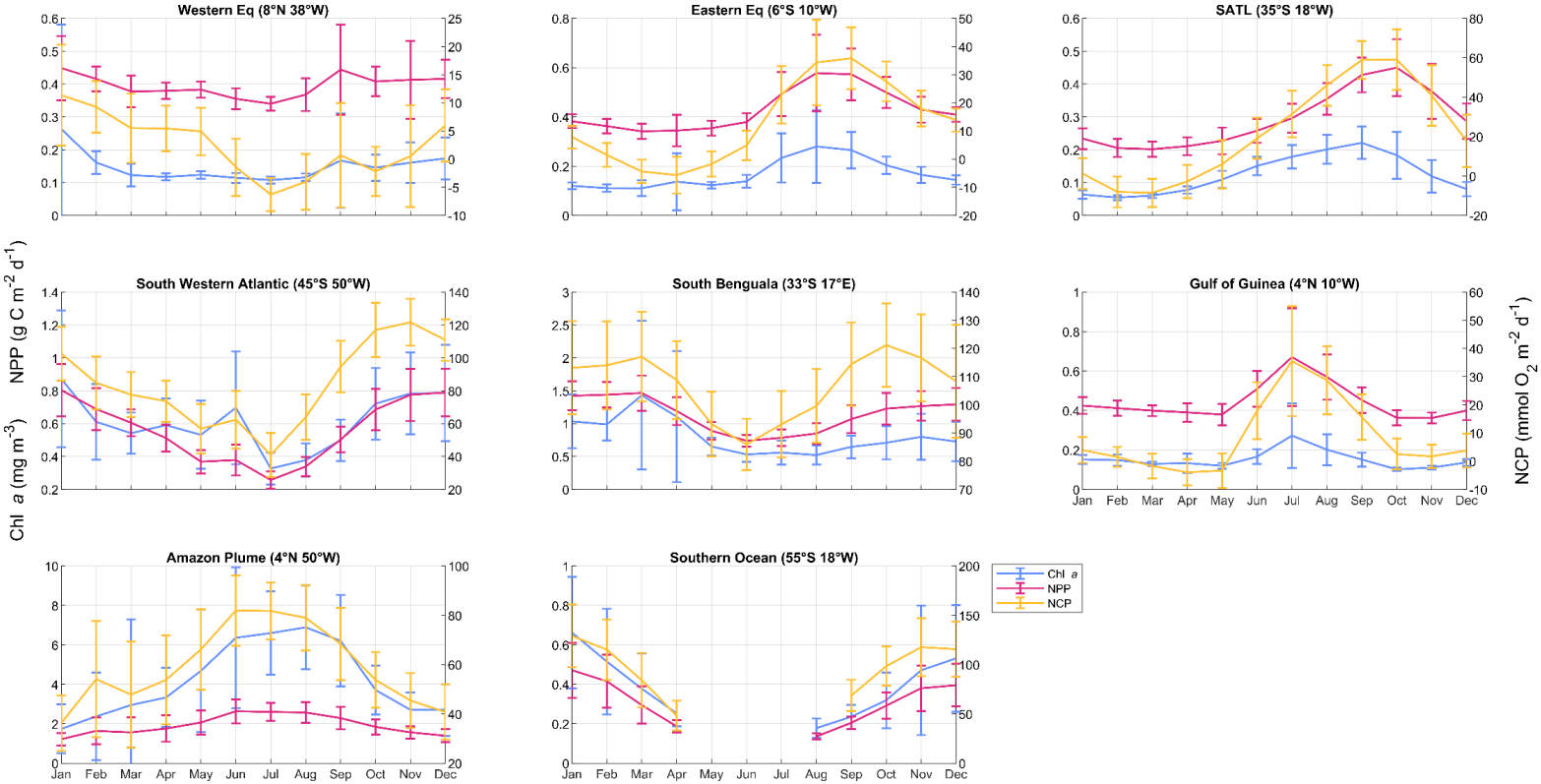

Figure A3.8 - Monthly climatologies of the biological parameters (Chl *a*, NPP and NCP) for the 8 stations (Fig. 3.1a). Chl *a* and NPP scale on the left axis, and NCP on the right. Note the different axis limits on each plot.

Chapter 4: Identifying the biological control of the annual and multi-year variations in South Atlantic air-sea CO_2 flux

This chapter is a reformatted version of my in review publication:
Ford, D. J., Tilstone, G. H., Shutler, J. D., and Kitidis, V. (2022): Identifying the biological control of the annual and multi-year variations in South Atlantic air-sea CO_2 flux, Biogeosciences Discussions,

DJF, GHT, JDS and VK conceived and directed the research. DJF developed the code and prepared the manuscript. GHT, JDS and VK provided comments that shaped the final manuscript.

Abstract: The accumulation of anthropogenic CO_2 emissions in the atmosphere has been buffered by the absorption of CO_2 by the global ocean which acts as a net CO_2 sink. The CO_2 flux between the atmosphere and the ocean, that collectively results in the oceanic carbon sink, is spatially and temporally variable, and fully understanding the driving mechanisms behind this flux is key to assessing how the sink may change in the future. In this study a time series decomposition analysis was applied to satellite observations to determine the drivers that control the sea-air difference of CO_2 partial pressure (ΔpCO_2) and the CO_2 flux on seasonal and interannual time scales in the South Atlantic Ocean. Linear trends in ΔpCO_2 and the CO_2 flux were calculated to identify key areas of change.

Seasonally, changes in both the ΔpCO_2 and CO_2 flux were dominated by sea surface temperature (SST) in the subtropics (north of 40 ^{o} S) and were correlated with biological processes in the subpolar regions (south of 40 °S). In the Equatorial Atlantic, analysis of the data indicated that biological processes are likely a key driver, as a response to upwelling and riverine inputs. These results highlighted that seasonally ΔpCO_2 can act as an indicator to identify drivers of the CO_2 flux. Interannually, the SST and biological contributions to the CO_2 flux in the subtropics were correlated with the Multivariate ENSO Index (MEI) which leads to a weaker (stronger) CO_2 sink in El Niño (La Niña) years.

The 16-year time-series identified significant trends in ΔpCO_2 and CO_2 flux, however, these trends were not always consistent in spatial extent. Therefore, predicting the oceanic response to climate change requires the examination of CO_2 flux rather than ΔpCO_2. Positive CO_2 flux trends (weakening sink for atmospheric CO_2) were identified within the Benguela upwelling system,

consistent with increased upwelling and wind speeds. Negative trends in the CO_2 flux (intensifying sink for atmospheric CO_2) offshore into the South Atlantic Gyre, were consistent with an increase in the export of nutrients in mesoscale features, which drives the biological drawdown of CO_2. These multi-year trends in the CO_2 flux indicate that the biological contribution to changes in the air-sea CO_2 flux cannot be overlooked when scaling up to estimates of the global ocean carbon sink.

4.1 Introduction

Since the industrial revolution, anthropogenic CO_2 emissions have increased unabated and continue to raise atmospheric CO_2 concentrations (IPCC, 2021). The global oceans have buffered the rise by acting as a sink for atmospheric CO_2 at a rate of between 1 and 3.5 Pg C yr^{-1} (e.g. Friedlingstein et al., 2020; Landschützer et al., 2014; Watson et al., 2020). The strength of the ocean as a sink for CO_2 appears to be increasing with time (Friedlingstein et al., 2020; Watson et al., 2020b). Regionally this can vary hugely, however and the ocean can oscillate between a source or sink of atmospheric CO_2. The difference in the partial pressure of CO_2 (pCO_2) between the seawater and atmosphere (ΔpCO_2) is used as an indicator or proxy, for the net direction of air-sea CO_2 flux during gas exchange.

In the open ocean, changes in physical and biogeochemical processes that control seawater pCO_2 ($pCO_{2\,(sw)}$) also modify ΔpCO_2 as the atmospheric pCO_2 ($pCO_{2\,(atm)}$) is less variable (e.g. Henson et al., 2018; Landschützer et al., 2016). ΔpCO_2 can therefore be controlled by changes in sea surface temperature (SST), because the pCO_2 is proportional to the temperature. In addition, plankton net community production (NCP) modifies the concentration of CO_2 in the seawater depending on the balance between net primary production (NPP; uptake of CO_2 via photosynthesis) and respiration (release of CO_2 into the water). The NCP describes the overall metabolic balance of the plankton community, where positive (negative) NCP indicates a drawdown (or release) of CO_2 from (or into) the water contributing to a decrease (increase) in ΔpCO_2. Physical processes, including riverine input (e.g. Ibánhez et al., 2016; Lefèvre et al., 2020; Valerio et al., 2021), and upwelling (e.g. González-Dávila et al., 2009; Lefèvre et al., 2008; Santana-Casiano et al., 2009) can alter $pCO_{2\,(sw)}$ and ΔpCO_2 directly through the entrainment of high-CO_2 water or indirectly by

modifying NCP through nutrient supply (enhancing photosynthesis) and/or organic material supply (enhancing respiration).

The air-sea CO_2 flux is more precisely a function of the difference in CO_2 concentrations across the mass boundary layer at the ocean's surface, with any turbulent exchange characterised by the gas transfer velocity. The CO_2 concentration difference is determined by the pCO_2 at the base ($pCO_{2\,(sw)}$) and top ($pCO_{2\,(atm)}$) of the mass boundary layer and the respective solubilities (Weiss, 1974), and must be carefully calculated due to vertical thermo-haline gradients existing across the mass boundary layer (Woolf et al., 2016). The gas transfer velocity is usually parameterised as a function of wind speed (e.g. Ho et al., 2006; Nightingale et al., 2000; Wanninkhof, 2014) which accounts for ~75% of the variance in surface turbulent exchange (e,g, Dong et al., 2021; Ho et al., 2006). Therefore, both oceanographic and meteorological conditions are able to modify and control the seasonality, interannual variability and multi-year trends of this flux.

Seasonal drivers of ΔpCO_2 have been explored globally (Takahashi et al., 2002), and regionally in the Atlantic Ocean (Landschützer et al., 2013; Henson et al., 2018). Takahashi et al. (2002) used binned *in situ* $pCO_{2\,(sw)}$ observations to a 4º by 5º global grid, and found that SST drives ΔpCO_2 in the subtropics, and non-SST processes (i.e. biological activity and ocean circulation) dominate in subpolar and equatorial regions. Landschützer et al. (2013) used a self-organising map feed forward neural network (SOM-FNN) technique to extrapolate the *in situ* $pCO_{2\,(sw)}$ observations and reported similar seasonal drivers in the Atlantic Ocean with one exception, that SST and non-SST processes compensated each other in the Equatorial Atlantic. Henson et al. (2018) using binned *in situ* observations for the North Atlantic Ocean, also indicated that the subtropics are driven by SST and that subpolar regions are correlated with biological activity.

The interannual drivers of ΔpCO_2 are different compared to the seasonal drivers in the North Atlantic (Henson et al., 2018), which could be true of the South Atlantic Ocean, though this needs to be further investigated. Landschützer et al. (2016, 2014) postulated the El Niño cycle may influence ΔpCO_2 in the subtropical South Atlantic but did not explore the underlying processes. South of 35° S, Landschützer et al. (2015) indicated that atmospheric forcing could

control the interannual variability of ΔpCO_2 through changes in Ekman transport and upwelling. These interannual drivers of ΔpCO_2 and the CO_2 flux in the South Atlantic Ocean are poorly understood but have key implications for determining how the oceanic CO_2 sink could be impacted by climate change and its evolution over interannual and decadal timescales.

In this study, we investigate the drivers of ΔpCO_2 and the CO_2 flux in the South Atlantic Ocean over both seasonal and interannual timescales using a timeseries decomposition approach. Trends in ΔpCO_2 and the CO_2 flux were calculated from 2002 to 2018, and regions in the South Atlantic Ocean showing the greatest change in the CO_2 flux are investigated**.**

4.2 Data and Methods

4.2.1 pCO_2 data

Satellite estimates of $pCO_{2\,(sw)}$ were retrieved from the South Atlantic Feed Forward Neural Network (SA-FNN) dataset (Ford et al., 2022, 2021a). Ford et al. (2022) showed that the SA-FNN improved on the seasonal $pCO_{2\,(sw)}$ variability in the South Atlantic Ocean compared to current estimates using the 'state of the art' methodology (the SOM-FNN). The SA-FNN estimates $pCO_{2\,(sw)}$ by clustering *in situ* monthly 1° gridded Surface Ocean CO_2 Atlas (SOCAT) v2020 $pCO_{2\,(sw)}$ observations (Bakker et al., 2016; Sabine et al., 2013), that have been reanalysed into a dataset configured using consistent depth and temperature fields (Goddijn-Murphy et al., 2015; Woolf et al., 2016; Reynolds et al., 2002), into eight static provinces in the South Atlantic Ocean (Fig. B1a). The use of eight static provinces allows the SA-FNN to more accurately reproduce the $pCO_{2\,(sw)}$ variability. The nonlinear relationships between $pCO_{2\,(sw)}$ and three environmental drivers; SST, NCP and $pCO_{2\,(atm)}$ were constructed for each province with a feed forward neural network (FNN). The FNN for each province were applied to produce spatially and temporally complete $pCO_{2\,(sw)}$ fields on monthly 1° grids between July 2002 and December 2018, with uncertainties also generated on a per pixel basis as described in Ford et al. (2022). These per pixel uncertainties are displayed in Appendix 4.2 (Fig. A4.3).

Monthly 1º grids of $pCO_{2\,(atm)}$ were extracted from v5.5 of the global estimates of $pCO_{2\,(sw)}$ dataset (Landschützer et al., 2017, 2016) which was calculated using the dry mixing ratio of CO_2 from the NOAA-ESRL marine boundary layer

reference (https://www.esrl.noaa.gov/gmd/ccgg/mbl/; last accessed 25/09/2020), Optimum Interpolated SST (Reynolds et al., 2002) and sea level pressure following Dickson et al. (2007). ΔpCO_2 was calculated from $pCO_{2\,(sw)}$ and $pCO_{2\,(atm)}$ as;

$$\Delta pCO_2 = pCO_{2\,(sw)} - pCO_{2\,(atm)} \quad (4.1)$$

4.2.2 Air-sea CO_2 flux data

The air-sea CO_2 flux (F) can be estimated using a bulk parameterisation as:

$$F = k\,(\alpha_W\, pCO_{2\,(sw)} - \alpha_s\, pCO_{2\,(atm)}) \quad (4.2)$$

Where k is the gas transfer velocity which was estimated from ERA5 monthly reanalysis wind speed (Hersbach et al., 2019) following the parameterisation of Nightingale et al. (2000). α_w and α_s are the solubility of CO_2 at the base and top of the mass boundary layer at the sea surface (Woolf et al., 2016). α_w was calculated as a function of SST and sea surface salinity (SSS) (Weiss, 1974) using the monthly Optimum Interpolated SST (Reynolds et al., 2002) and SSS from the Copernicus Marine Environment Modelling Service global ocean physics reanalysis product (GLORYS12V1; CMEMS, 2021). α_s was calculated using the same temperature and salinity datasets but included a gradient from the base to the top of mass boundary layer of -0.17 K (Donlon et al., 1999) and +0.1 salinity units (Woolf et al., 2016). $pCO_{2\,(atm)}$ was calculated using the dry mixing ratio of CO_2 from the NOAA-ESRL marine boundary layer reference, Optimum Interpolated SST (Reynolds et al., 2002) applying a cool skin bias (0.17K; Donlon et al., 1999) and sea level pressure following Dickson et al. (2007).

All of these calculations along with the resulting monthly CO_2 flux were carried out using the open source FluxEngine toolbox (Holding et al., 2019; Shutler et al., 2016), for the period between July 2002 and December 2018, assuming 'rapid' transfer (as described in Woolf et al., 2016).

4.2.3 Biological data

The 4 km resolution mean monthly chlorophyll *a* (Chl *a*) was calculated from Moderate Resolution Imaging Spectroradiometer on Aqua (MODIS-A) Level 1 granules, retrieved from the National Aeronautics Space Administration (NASA)

Ocean Colour website (https://oceancolor.gsfc.nasa.gov/; last accessed 10/12/2020), using SeaDAS v7.5, and applying the standard OC3-CI algorithm for Chl *a* (https://oceancolor.gsfc.nasa.gov/atbd/chlor_a/; last accessed 15/12/2020). Monthly composites of MODIS-A SST (NASA OBPG, 2015) and photosynthetically active radiation (PAR; NASA OBPG, 2017b) were also downloaded from the NASA Ocean Colour website. Monthly NPP composites were generated from MODIS-A Chl *a*, SST and PAR composites using the Wavelength Resolving Model (Morel, 1991) with the look up table described in Smyth et al. (2005). Coincident monthly composites of NCP using the algorithm NCP-D described in Tilstone et al. (2015b) were generated using the NPP and SST data. Further details of the satellite algorithms are given in O'Reilly et al. (1998), O'Reilly and Werdell (2019) and Hu et al. (2012) for Chl *a*, Smyth et al. (2005), Tilstone et al. (2005, 2009) for NPP and Tilstone et al. (2015b) for NCP. Monthly composites were generated between July 2002 and December 2018 and were re-gridded onto the same 1º grid as the $pCO_{2\,(sw)}$ and flux data. Ford et al. (2021b) showed that these satellite algorithms for Chl *a*, NPP, NCP and SST are accurate compared to *in situ* observations in the South Atlantic Ocean following an algorithm intercomparison which accounted for model, *in situ* and input parameter uncertainties.

4.2.4 Seasonal and interannual driver analysis

The X-11 analytical econometric tool (Shiskin et al., 1967) was used to decompose the timeseries into seasonal, interannual and residual components following the methodology of Pezzulli et al. (2005). In brief, the X-11 method comprises a three step filtering algorithm; (1) The interannual component (T_t) is initially estimated using an annual centred running mean, which is subtracted from the initial timeseries (X_t) and a seasonal running mean applied to estimate the seasonal component (S_t). (2) T_t is revised by applying an annual centred running mean to the X_t minus S_t. The revised T_t is removed from X_t and the final S_t calculated with a seasonal running mean. (3) The final T_t is calculated by applying an annual centred running mean to X_t minus the revised S_t. The analysis has been shown to be effective in the decomposition of environmental time-series (Pezzulli et al., 2005; Vantrepotte & Mélin, 2011; Henson et al., 2018), that allows the seasonal cycle to vary on a yearly basis and, produces an

interannual component that results in a robust representation of the longer-term changes in the timeseries.

The approach was applied to monthly 1° fields of ΔpCO_2 that were estimated from $pCO_{2\,(atm)}$ and SA-FNN $pCO_{2\,(sw)}$, on a per pixel basis. The $pCO_{2\,(atm)}$ and spatially and temporally varying $pCO_{2\,(sw)}$ uncertainties (Table 4.1; Fig. A4.3) were propagated through the X-11 analysis, using a Monte Carlo uncertainty propagation approach. The input time series were randomly perturbed 1000 times within the uncertainties of each parameter, and Spearman correlations calculated for each perturbation. The 95% confidence interval was extracted from the resulting distribution of correlations coefficients, and results were deemed significant ($\alpha < 0.05$) where the confidence interval remained significant. Spatial autocorrelation was tested using the method of field significance (Wilks, 2006). The analysis was then conducted on the CO_2 fluxes, on a per pixel basis. The $pCO_{2\,(sw)}$, $pCO_{2\,(atm)}$, gas transfer velocity, SST and SSS uncertainties (Table 4.1) were propagated through the flux calculations using the same Monte Carlo uncertainty propagation approach used for ΔpCO_2.

The potential drivers tested were MODIS-A skin SST, NCP and NPP alongside SSS from the CMEMS global reanalysis product (GLORYSV12; CMEMS, 2021) and two climate indices: Multivariate ENSO Index (MEI) as an indicator of El Niño Southern Oscillation phases, https://www.esrl.noaa.gov/psd/enso/mei (last accessed: 19/12/2019); Southern Annular Mode (SAM) data, which indicate the displacement of the westerly winds in the Southern Ocean, were downloaded from http://www.nerc-bas.ac.uk/icd/gjma/sam.html (last accessed: 19/12/2019).

Table 4.1 - Uncertainties in the input parameters used in the Monte Carlo uncertainty propagation.

Parameter	Uncertainty	Reference
$pCO_{2\,(sw)}$	Variable (Appendix B)	(Ford et al., 2022)
SST	0.441 °C	(Ford et al., 2021b)
SSS	0.1 psu	(Jean-Michel et al., 2021)
$pCO_{2\,(atm)}$	1 µatm	(Takahashi et al., 2009)
Gas transfer velocity	20 %	(Woolf et al., 2019)

4.2.5 Trend analysis

The linear trend in the interannual components of ΔpCO_2 and the CO_2 flux were calculated on a per pixel basis using the non parametric Mann-Kendall test for trend (Kendall, 1975; Mann, 1945) and Sen's Slope estimates (Sen, 1968), which are less sensitive to outliers in the timeseries. The input parameter uncertainties (Table 4.1) were propagated within this trend analysis using a Monte Carlo uncertainty propagation (n = 1000) to extract the 95% confidence interval on the trends. The overall trend was deemed significant if 95% of the trends were significant ($\alpha = 0.05$), and the uncertainties in these trends are displayed in Appendix B (Fig. A4.4).

4.2.6 Limitations

It should be noted that correlations between the ΔpCO_2 and SST/NCP are expected since the SA-FNN estimates $pCO_{2\,(sw)}$ (the major determinant of ΔpCO_2 variability) using SST and NCP as input parameters which are subsequently interpreted as drivers here. By extension, but to a lesser extent, this also applies to correlations between CO_2 flux and SST/NCP since $pCO_{2\,(sw)}$ is included in the flux calculations. Different lines of evidence suggest that this is not a major limitation of our study. Firstly, any correlation between $\Delta pCO_2/CO_2$ flux and SST/NCP is not determined *a priori*, but is an emerging property of the SA-FNN. Therefore, the driver analysis undertaken here represents an indirect decomposition of the SA-FNN drivers rather than a strict correlation analysis between independent variables. The accurate representation of seasonal $pCO_{2\,(sw)}$ cycles across the South Atlantic Ocean (Ford et al., 2022) provides confidence in the SA-FNN. Secondly, conducting the analysis described by Henson et al. (2018) using *in situ* $pCO_{2\,(sw)}$ to estimate ΔpCO_2 on a per province basis (Longhurst, 1998) for the South Atlantic Ocean, yielded similar seasonal drivers to the SA-FNN (Appendix 4.1). The interannual drivers displayed some differences however, which may be due to the spatial and temporal averaging that is required to construct the *in situ* timeseries.

4.3 Results

4.3.1 Seasonal drivers of ΔpCO_2 and CO_2 flux

The X-11 analysis conducted on ΔpCO_2 indicated significant seasonal correlations (Fig. 4.1), when the uncertainties are accounted for. The subtropics

(10 °S to 40 °S) showed positive correlations between ΔpCO_2, SST and SSS (Fig. 4.1c, d), as well as negative correlations between ΔpCO_2, NCP and NPP (Fig. 4.1a, b). In contrast the subpolar (south of 40 °S) and equatorial regions (10 °N to 10 °S) displayed negative correlations between ΔpCO_2 and SST (Fig. 4.1c). Correlations between ΔpCO_2 and NCP were negative in the subpolar regions and were positive in the Equatorial regions (Fig. 4.1a). There were no significant correlations observed between ΔpCO_2 and MEI or SAM in any of the regions.

Regional deviations were observed in the Amazon Plume, Benguela upwelling, the South American coast, and a band across 40 °S. The region under the influence of the Amazon Plume indicated negative correlations between ΔpCO_2 and NCP in contrast to the surrounding waters which had positive correlations (Fig. 4.1a). The Benguela upwelling displayed positive correlations between ΔpCO_2 and NCP (Fig. 4.1a), no significant correlations between ΔpCO_2 and SST (Fig. 4.1c), and negative correlations between ΔpCO_2 and SSS (Fig. 4.1e). The South American coast between 12 °S and 17 °S displayed positive correlations between ΔpCO_2 and NPP (Fig. 4.1b), along with negative correlations between ΔpCO_2 and SSS (Fig. 4.1e). Negative correlation between ΔpCO_2 and SSS, and positive correlations between NCP, NPP and ΔpCO_2 were also observed in the southwestern Atlantic (Fig. 4.1e). Positive correlations between NCP, NPP and ΔpCO_2 were identified in a band across 40 °S (Fig. 4.1a, b). Performing the X-11 analysis on the CO_2 flux revealed similar and comparable correlations to ΔpCO_2 (Fig. 4.2). Significant driver-flux correlations were observed over a larger area however, compared to ΔpCO_2.

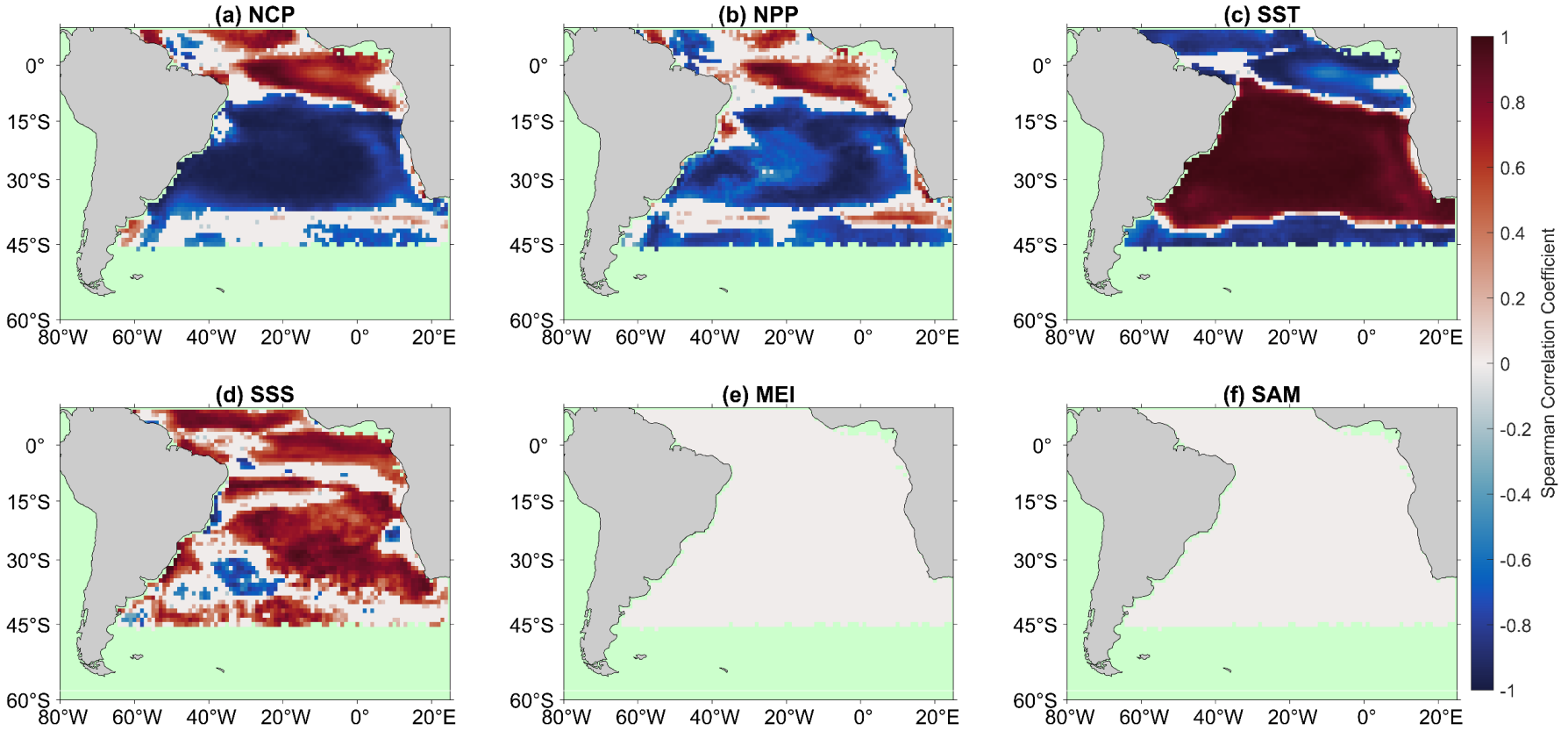

Figure 4.1- Significant Spearman correlations between the ΔpCO_2 seasonal component of the X-11 analysis and (a) net community production (NCP), (b) net primary production (NPP), (c) sea surface temperature (SST), (d) sea surface salinity (SSS), (e) Multivariate ENSO index (MEI) and (f) Southern Annular Mode (SAM) seasonal components. White regions indicate no significant correlations, and green regions indicate no analysis was performed due to missing satellite data.

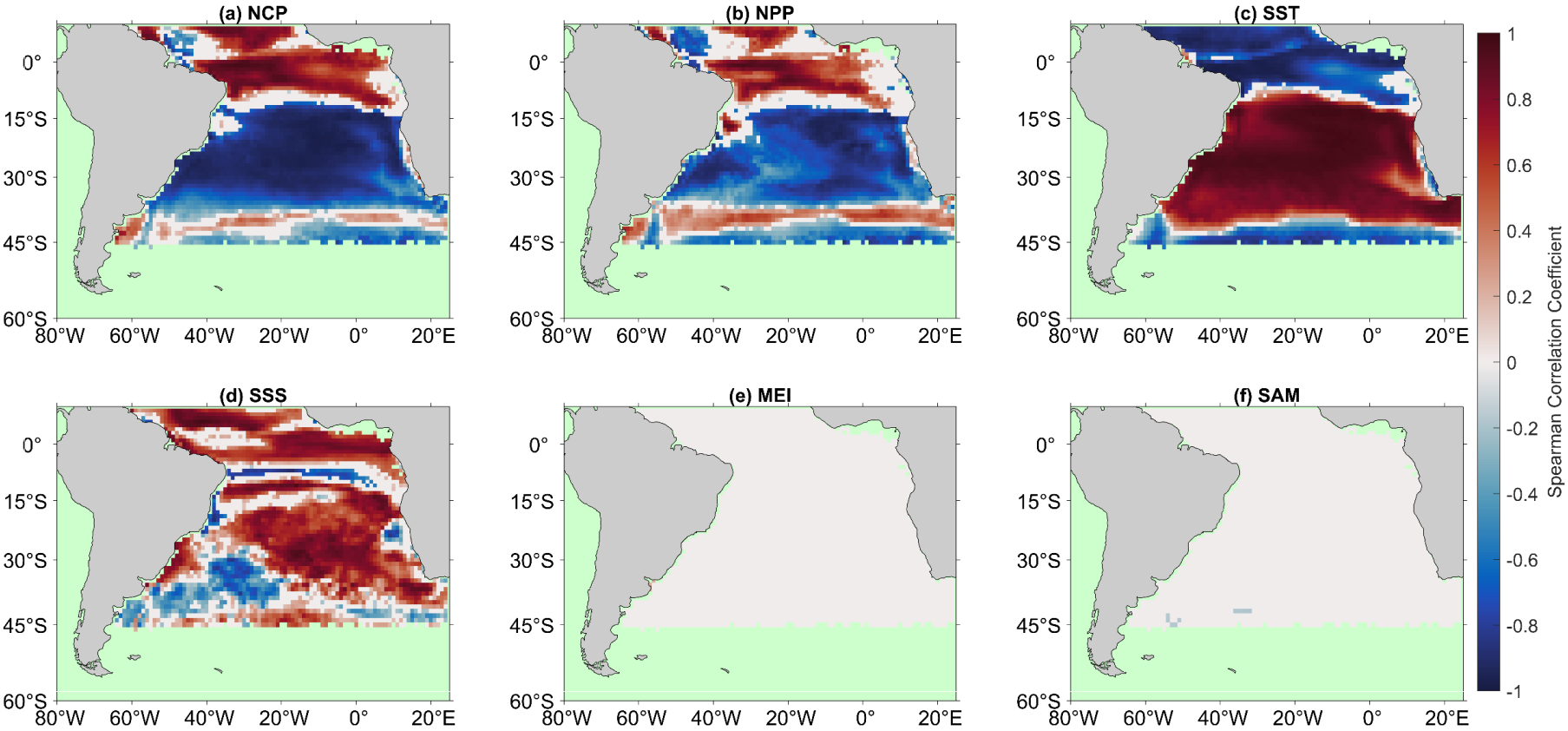

Figure 4.2 - Significant Spearman correlations between the air-sea CO_2 flux seasonal component of the X-11 analysis and (a) net community production (NCP), (b) net primary production (NPP), (c) sea surface temperature (SST), (d) sea surface salinity (SSS), (e) Multivariate ENSO index (MEI) and (f) Southern Annular Mode (SAM) seasonal components. White regions indicate no significant correlations, and green regions indicate no analysis was performed due to missing satellite data.

4.3.2 Interannual drivers of ΔpCO_2 and CO_2 flux

The X-11 analysis identified regionally significant interannual correlations between ΔpCO_2 and SST, MEI and to a lesser extent NCP and SSS (Fig. 4.3). The subtropics displayed positive correlations between SST and ΔpCO_2, which extended across the basin from the South American coast (Fig. 4.3c). Positive correlations were also observed between the MEI and ΔpCO_2 (Fig. 4.3e), with a similar geographic extent as the correlations with SST. In the central South Atlantic gyre spatially variable negative correlations between NCP and ΔpCO_2, and positive correlations between SSS and ΔpCO_2 were observed (Fig. 4.3a, d). The central Equatorial Atlantic displayed spatially variable positive correlations between NCP and ΔpCO_2, which extended south-east towards the African coast (Fig. 4.3a).

Significant interannual correlations for the CO_2 flux were also identified by the X-11 analysis (Fig. 4.4), which generally covered a larger spatial area to the corresponding ΔpCO_2 correlations (Fig. 4.3). Positive correlations between the CO_2 flux and SST were observed in the subtropics (Fig. 4.4c), consistent with the correlations with ΔpCO_2 (i.e. by comparing Fig. 4.4c and Fig. 4.3c). Nevertheless, negative correlations between the CO_2 flux and SST were observed at the border between the equatorial region and subtropics; which was not identified in the ΔpCO_2 correlations. Negative correlations between NCP and the CO_2 flux were also identified over a spatially larger area (Fig. 4.4a, 4.3a). Correlations between the MEI and CO_2 flux were positive in the subtropics (Fig. 4e) and included a band of negative correlations to the south between 35 °S and 45 °S (Fig. 4.4e).

Positive correlations between NCP and CO_2 flux were observed in the western equatorial Atlantic, alongside spatially variable negative correlations to SST (Fig. 4.4a, c). Positive correlations between SSS and CO_2 flux were identified in the region of the Amazon plume (Fig. 4.4d). Weak positive correlations between the SAM and CO_2 flux were identified between 30° S and 45° S (Fig. 4.4f).

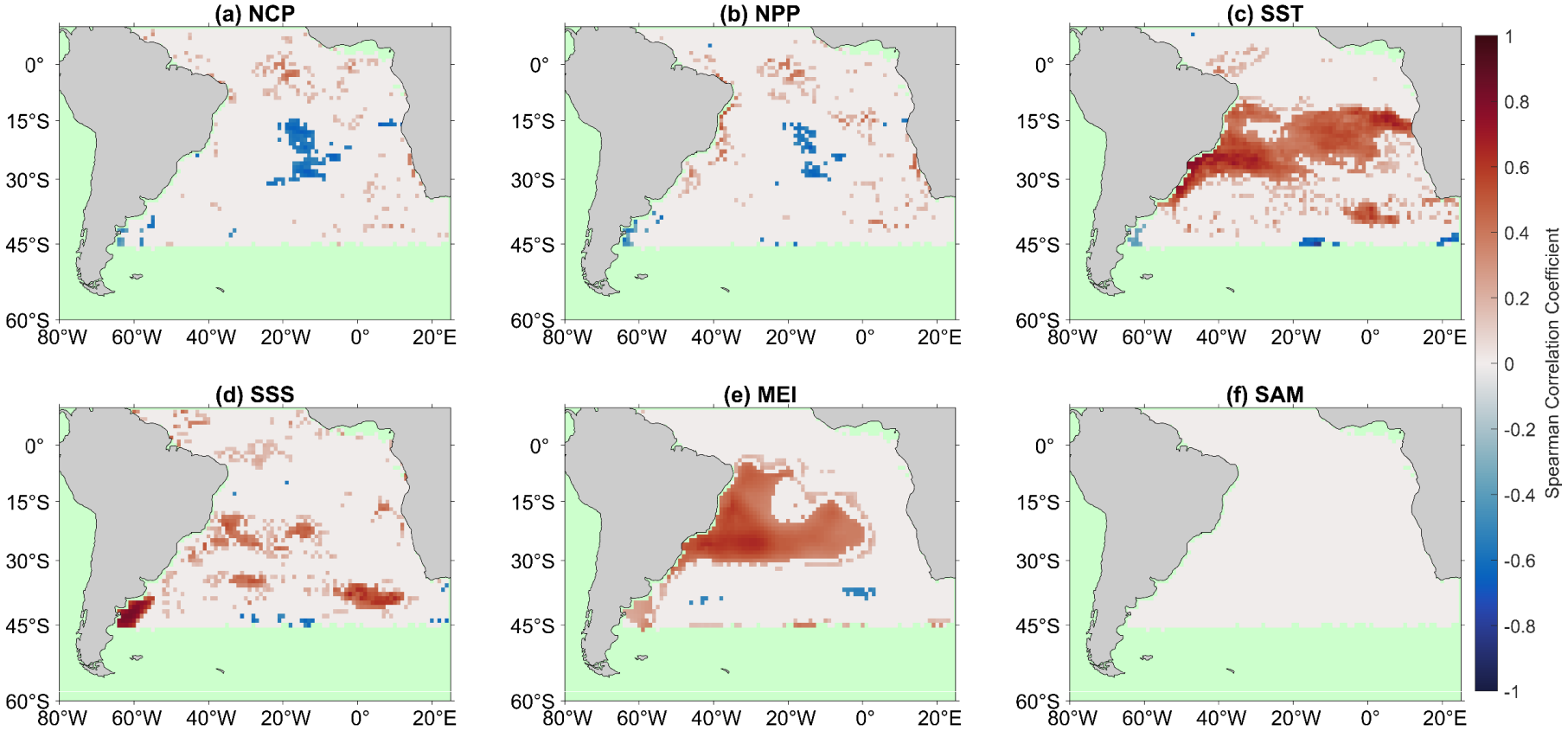

Figure 4.3 - Significant Spearman correlations between the ΔpCO_2 interannual component of the X-11 analysis and (a) net community production (NCP), (b) net primary production (NPP), (c) sea surface temperature (SST), (d) sea surface salinity (SSS), (e) Multivariate ENSO index (MEI) and (f) Southern Annular Mode (SAM) interannual components. White regions indicate no significant correlations, and green regions indicate no analysis was performed due to missing satellite data.

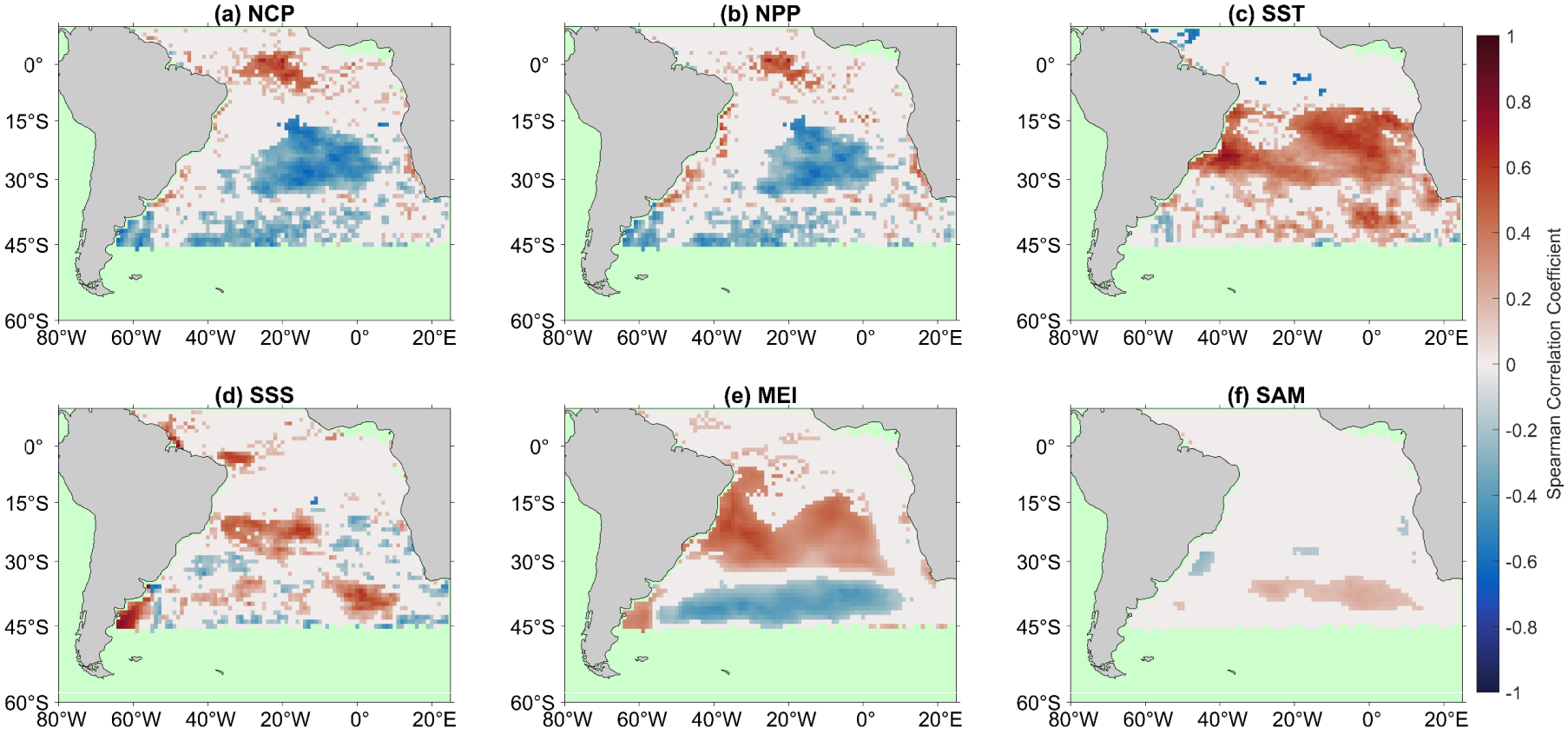

Figure 4.4 - Significant Spearman correlations between the air-sea CO_2 flux interannual component of the X-11 analysis and (a) net community production (NCP), (b) net primary production (NPP), (c) sea surface temperature (SST), (d) sea surface salinity (SSS), (e) Multivariate ENSO index (MEI) and (f) Southern Annular Mode (SAM) interannual components. White regions indicate no significant correlations, and green regions indicate no analysis was performed due to missing satellite data.

4.3.3 Trends in interannual ΔpCO_2 and CO_2 flux

Regions of significant trends in the interannual component of ΔpCO_2 were observed (Fig. 4.5a). Negative trends occurred in the South Atlantic gyre. Positive trends in ΔpCO_2 were identified along the South African coast, which switched to strong negative trends moving offshore into the central South Atlantic gyre. Positive trends were also observed in the Equatorial Atlantic consistent with the positions of the Amazon Plume and Equatorial Upwelling.

Regions of significant trends in the CO_2 flux were identified (Fig. 4.5b), but over much larger spatial areas than evident in the ΔpCO_2 results (i.e. comparing Fig. 4.5a with 4.5b). The trends in CO_2 flux are generally in the same direction as trends in ΔpCO_2. Strong positive trends in the CO_2 flux occurred in the Benguela upwelling region, before switching to a negative trend offshore of similar magnitude but occupying a larger spatial extent.

4.4 Discussion

4.4.1 Seasonal drivers of ΔpCO_2 and CO_2 flux

Previous studies have explored the seasonal drivers of ΔpCO_2 and to a lesser extent the air-sea CO_2 flux . In this study, we investigated the drivers of ΔpCO_2 and CO_2 flux at both seasonal and interannual timescales in the South Atlantic Ocean. In the North Atlantic, Henson et al. (2018) indicated that the seasonal variability in subtropical ΔpCO_2 variability is driven by SST, whereas the variability in ΔpCO_2 in subpolar regions is biologically driven, similar to previous studies (Takahashi et al., 2002; Landschützer et al., 2013). The X-11 analysis conducted on spatially complete ΔpCO_2 and CO_2 flux displayed consistent seasonal results (Fig. 4.1, 4.2), though for the CO_2 flux significant correlations occupied a larger area. These both indicated a similar pattern in seasonal drivers for the South Atlantic Ocean, with subtropical ΔpCO_2 and CO_2 flux driven by SST, and subpolar correlated with biological controls, although the equatorial region exhibited more complex patterns (Fig. 4.1).

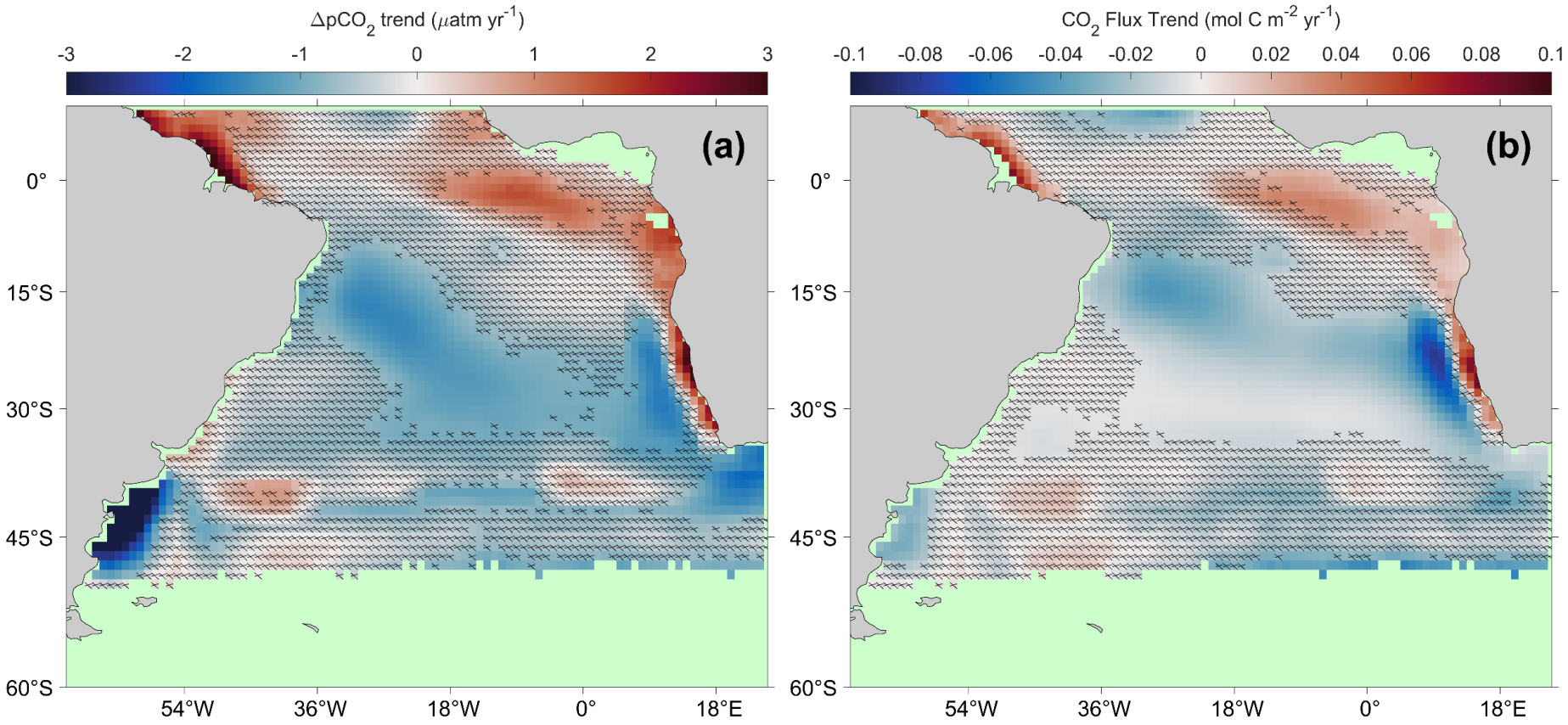

Figure 4.5 - Linear trends in (a) ΔpCO_2 and (b) the air-sea CO_2 flux between 2002 and 2018. Hashed areas indicate non-significant trends when accounting for the uncertainties. Green regions indicate insufficient data to calculate trends.

In the Equatorial Atlantic, the correlations between ΔpCO_2, SST and biological production were spatially variable (Fig. 4.1). Landschützer et al. (2013) suggested that the temperature and non-temperature (i.e. biological and circulation) drivers generally compensated each other. We found positive correlations between the NCP, ΔpCO_2 and CO_2 flux seasonal components, indicating that biological activity is likely a key driver of seasonal variability in response to the equatorial upwelling. Ford et al. (2022) showed that the SA-FNN improved the seasonal $pCO_{2\,(sw)}$ variability in the Equatorial Atlantic compared to the current 'state of the art' SOM-FNN methodology (Watson et al., 2020b). Elevated ΔpCO_2 associated with elevated NCP in the eastern Equatorial Atlantic was consistent with the seasonal equatorial upwelling (Radenac et al., 2020). Parard et al. (2010) indicated strong negative correlations between SST and ΔpCO_2 during the upwelling season (R= -0.76 for June to September), which is also consistent with our results. By contrast, Lefèvre et al. (2016) showed that correlations between $pCO_{2\,(sw)}$ and SST were weak across the whole year (R = -0.13), and SSS (R = 0.93) was the primary driver at the same station.

In the western Equatorial Atlantic, negative correlations between NCP and ΔpCO_2, and positive correlations between the SSS and ΔpCO_2 seasonal component occurred in the vicinity of the Amazon River mouth. The mixing of the Amazon river and oceanic water decreases SSS (Ibánhez et al., 2016; Lefèvre et al., 2020; Bonou et al., 2016; Lefévre et al., 2010), and increases the nutrient supply to the ocean which can in turn enhance NPP and NCP, leading to a decrease in ΔpCO_2 within the Amazon plume (Körtzinger, 2003; Cooley et al., 2007). This coupling produces an extensive area of depressed ΔpCO_2 which is a CO_2 sink (Ibánhez et al., 2016). Lefèvre et al. (2010) indicated that rainfall from the intertropical convergence zone could reduce SSS, with an associated decrease in ΔpCO_2. The Eastern Tropical Atlantic is also subject to large river input, especially from the Congo (Hopkins et al., 2013) and Niger rivers, which could produce nutrient-rich plumes that fuel NCP and decrease ΔpCO_2 (Lefèvre et al., 2016, 2021).

Between 30 °S and 45 °S, dissolved inorganic carbon and SST exert a similar influence on $pCO_{2\,(sw)}$, indicating that seasonal changes in dissolved inorganic carbon driven by biological uptake in the summer and upwelling in winter are

approximately balanced by seasonal changes in SST and their control on the solubility pump (Henley et al., 2020). This likely explains the band of positive correlations between NCP, NPP and ΔpCO_2 and sharp transitions in correlations between SST and ΔpCO_2 across ~40 °S.

Deviations from the expected drivers in the subtropics, occurred within the Benguela upwelling system between 20 °S and 35 °S. Positive correlations between NCP and the CO_2 flux (Fig. 4.2a) alongside negative correlations between SST, SSS and the CO_2 flux (Fig. 4.2c, d) are indicative of upwelled waters that have both elevated $pCO_{2\,(sw)}$ and nutrients, which cause an increase in NPP (Lamont et al., 2014). These upwelled waters move offshore in filaments (Rubio et al., 2009) where NPP decreases, and SST becomes the dominant driver, which is confirmed by the positive correlations between SST and the CO_2 flux further offshore. Ford et al. (2021b) indicated a switch in NCP drivers in the Benguela upwelling from wind driven upwelling on the shelf, to filaments that propagate offshore from the upwelling front, which is consistent with the switch in the drivers observed for the CO_2 flux as these filaments move offshore.

At between 12° S and 17 °S along the South American coast, there were also deviations from the expected drivers as there were positive correlations between NPP and ΔpCO_2 (Fig. 4.1b) and negative correlations between SSS and ΔpCO_2 (Fig. 4.1d), which are consistent with an upwelling signature that occurs along the coast. Aguiar et al. (2018) also showed intense seasonal upwelling events in this region that are driven by wind and currents. The southern coast of South America is strongly influenced by riverine water input that reduces the total alkalinity and therefore causes an increase in $pCO_{2\,(sw)}$ (Liutti et al., 2021). This is associated with an increased supply of nutrients which in turn enhances NPP, though the main drivers of $pCO_{2\,(sw)}$ in this region still remain as total alkalinity and SST (Liutti et al., 2021). This potentially explains the positive correlation between ΔpCO_2 and both NCP and NPP (Fig. 4.1a, b), as well as the negative correlations between ΔpCO_2 and SSS. The extension offshore of this negative correlation between SSS and ΔpCO_2 (Fig. 4.1d) could be caused by the advection of water masses due to intense mesoscale eddy activity arising from the Brazil-Malvinas confluence (Mason et al., 2017).

The seasonal correlations between the CO_2 flux and the drivers were similar to ΔpCO_2, but for CO_2 flux these occurred over a larger spatial area. The South Atlantic subtropical anticyclone (Reboita et al., 2019) which controls wind speeds across the region, and therefore the gas transfer velocity, could enhance the CO_2 flux into the subtropical ocean, through higher (or lower) wind speeds in winter (or summer; Xiong et al., 2015). Since seasonal variations in ΔpCO_2 largely explain the seasonal variability in the CO_2 flux, ΔpCO_2 can be used as a proxy to understand seasonal variations in the CO_2 flux in this region.

4.4.2 Interannual drivers of ΔpCO_2 and CO_2 flux

The larger geographic region of significant correlations for the air-sea CO_2 flux compared to ΔpCO_2, and the consistency between the two results (i.e. comparing the smaller regions of ΔpCO_2 correlations with their equivalent in the flux results; Fig. 4.3, 4.4) suggests that analysing the CO_2 flux is the better dataset to investigate drivers of variations in inter-annual and longer timescales. The results become clearer when analysing the CO_2 flux, where the effects of solubility and gas transfer (estimated via wind speed proxy) could reinforce correlations and multi-year trends, which will be retrieved by performing long timeseries analyses on the CO_2 flux. Landschützer et al. (2015) showed that variations in the Southern Ocean carbon sink were primarily driven by changes in ΔpCO_2, when integrating across basin scales. At localised scales of 1° by 1° as performed in our analysis, changes in surface turbulence and solubility are shown to be important in determining interannual variability, consistent with Keppler and Landschützer (2019). In the North Atlantic Ocean, Henson et al. (2018) showed that the seasonal and interannual drivers of ΔpCO_2 are different, which could arise from the necessity to study CO_2 fluxes over longer timescales.

The interannual component of NCP and the CO_2 flux were negatively correlated in the subtropical gyre (Fig. 4.4a), alongside a positive correlation between SST and CO_2 flux (Fig. 4.4b). El Niño (La Niña) events are known to influence the South Atlantic Ocean, causing an increase (decrease) in SST across the basin (Rodrigues et al., 2015; Colberg et al., 2004), and a decrease (increase) in NPP and NCP (Ford et al., 2021b; Tilstone et al., 2015). Positive correlations between the MEI and CO_2 flux (Fig. 4.4e) indicate that the MEI partially controls the interannual variability in CO_2 flux in the South Atlantic subtropical gyre,

through modulations primarily in SST and to a lesser extent NCP. The South Atlantic Subtropical Anticyclone has been observed to strengthen (weaken) and move south (north) during La Niña (El Niño) events. This displacement increases (decreases) wind speeds across the subtropical South Atlantic, which will enhance (weaken) gas exchange, and elevate (depress) NCP (Ford et al., 2021b). These results suggest a more significant role of NCP in controlling the interannual variability in the CO_2 flux than has previously been thought.

The negative correlation between the CO_2 flux and the MEI in a band between 30° S and 45° S (Fig. 4.4e), indicates that reduced (elevated) wind speeds that occur during La Niña (El Niño) events in this region, suppress (enhance) the gas exchange (Colberg et al., 2004) and therefore acts as a weaker (stronger) CO_2 sink. In the equatorial region, neither ΔpCO_2 or the CO_2 flux were correlated with the MEI, in sharp contrast with Lefèvre et al. (2013) who showed stronger outgassing of CO_2 in the western equatorial Atlantic for the year following the 2009 El Niño. In that respect, it should be noted that our analysis would not identify such lagged correlations.

The SAM has known meteorological connections to the MEI (Fogt et al., 2011), where El Niño (La Niña) events generally coincide with negative (positive) SAM phases, resulting in northward (southward) displacement of the westerly winds in the Southern Ocean. Our results showed positive correlations between the CO_2 flux and the SAM between 30° S and 45° S (Fig. 4.4f) indicating stronger (weaker) CO_2 drawdown into the oceans during negative (positive) SAM phases. Although no significant correlations were found between ΔpCO_2 and the SAM (Fig. 4.3f), the changes in the gas transfer driven by the displacement of the westerly winds could control the CO_2 flux. Landschützer et al. (2015) indicated that the SAM is unlikely to be the main driver of changes in the Southern Ocean CO_2 flux, but an observed zonally asymmetric atmospheric pattern could induce changes in the CO_2 flux (Keppler and Landschützer, 2019; Landschützer et al., 2015). This asymmetric atmospheric pattern, however, may not be captured within the SAM index.

4.4.3 Multi-year trends in ΔpCO_2 and CO_2 flux

The trends in ΔpCO_2 and CO_2 flux over 16 years (Fig. 4.5) showed some similarities to previous trend assessments in the South Atlantic Ocean

(Landschützer et al., 2016). Our results indicated a lower number of significant trends however, since uncertainties in the trend analysis were accounted for. The uncertainties in both the $pCO_{2\,(sw)}$ estimates from extrapolation techniques and the gas transfer velocity are rarely propagated through previous trend analyses. By accounting for these uncertainties, the trend analyses provide a robust depiction of regions that can confidently be determined as changing. As with the seasonal and inter-annual analysis, the CO_2 flux-based trend analysis showed a greater spatial area of significant trends, when compared to ΔpCO_2 (Fig. 4.5).

The strongest trends in ΔpCO_2 and the CO_2 flux were observed in the Benguela upwelling system. Arnone et al. (2017) reported positive trends in *in situ* $pCO_{2\,(sw)}$ of 6.1 ± 1.4 µatm yr^{-1}, between 2005 and 2015. Assuming an atmospheric CO_2 increase of 1.5 µatm yr^{-1} (Takahashi et al., 2002; Zeng et al., 2014), to remove the trend in $pCO_{2\,(atm)}$ from the $pCO_{2\,(sw)}$ and approximate a ΔpCO_2 trend, these results are consistent with the ΔpCO_2 trends observed in this study (1.5 ± 1.1 – 3.8 ± 1.1 µatm yr^{-1}, Fig. 4.5a). Arnone et al. (2017) also suggested that the positive trend was due to a stronger influence of upwelling (Rouault et al., 2010), which injects CO_2 and nutrients into the area that is then not completely removed by the enhanced NPP/NCP. Varela et al. (2015) indicated an increase in the strength of the Benguela upwelling. By contrast, Lamont et al. (2018b) showed no significant change in upwelling in the Southern Benguela but increases in the Northern Benguela which are consistent with our data that highlights an increasing efflux of CO_2 to the atmosphere (Fig. 4.5b). The CO_2 flux trends in this study (0.03 ± 0.01 – 0.09 ± 0.02 mol m^{-2} yr^{-1}, Fig. 4.5b) were also consistent with but slightly lower than the 0.13 ± 0.03 mol m^{-2} yr^{-1} trend in CO_2 flux observed by Arnone et al. (2017). An increase in the strength of the upwelling that injects CO_2 into the surface layer, will be driven by enhanced (upwelling-conducive) winds, that also enhance the gas transfer. This highlights the importance of studying multi-year trends using the CO_2 flux, because the enhancement of these trends by meteorological conditions would not be observed using ΔpCO_2 alone.

Offshore from the upwelling region negative ΔpCO_2 and CO_2 flux trends were observed. Rubio et al. (2009) showed that mesoscale filaments and eddies propagate away from the upwelling front, transporting nutrients offshore into the

South Atlantic gyre. Ford et al. (2021b) showed negative correlations between sea level height anomalies (SLHA), and NPP/NCP anomalies (negative SLHA; positive NCP/NPP), indicating an influence of mesoscale features on ΔpCO_2 and the CO_2 flux. Xiu et al. (2018) indicated that an increase in upwelling conducive winds could increase the number of mesoscale eddies, which would transport nutrients offshore of the Californian upwelling. Although the Benguela and Californian upwelling systems are not identical, these connections could suggest an elevated nutrient export offshore, driving elevated NPP/NCP, which would increase the CO_2 sink. Kulk et al. (2020) showed significant increases in NPP of ~2 % yr^{-1}, between 1998 and 2018 in the region of strong negative trends in the CO_2 flux observed in this study, which supports the contribution of NCP to multi-year trends in the CO_2 flux.

There were also positive trends in ΔpCO_2 and CO_2 flux in the Equatorial Atlantic. In the Eastern Equatorial Atlantic, Lefèvre et al. (2016) previously suggested a negative trend in *in situ* ΔpCO_2, between 2006 and 2013, but indicated that the trend may be biased by extreme events at either end of the record. From 1995 to 2007, Parard et al. (2010) indicated a greater increase in *in situ* $pCO_{2\,(sw)}$ than $pCO_{2\,(atm)}$ (increasing ΔpCO_2), but the trend was derived from data from only two research cruises. For the Equatorial upwelling, an increase in ΔpCO_2 (as shown here and in Landschützer et al., 2016) is counter intuitive because there is evidence that upwelled water has recently been in contact with the atmosphere (~15 years; Reverdin et al., 1993). Dissolved inorganic carbon in these upwelled waters has been shown to increase at a similar rate to the surface waters (e.g Woosley et al., 2016). Therefore, the trend in ΔpCO_2 should be ~0 with increasing $pCO_{2\,(atm)}$. This could suggest a missing component within the SA-FNN to estimate $pCO_{2\,(sw)}$, such as changes in the biological export efficiency (Kim et al., 2019), which could then suppress upwelling induced CO_2 outgassing.

The Western Tropical Atlantic, in the vicinity of the Amazon Plume, also showed positive trends in ΔpCO_2 and CO_2 flux. Previous studies have not investigated the trends in ΔpCO_2 or CO_2 flux in the Amazon Plume, however the carbon retention in a colored ocean site (CARIACO), situated to the northwest, displayed positive trends in $pCO_{2\,(sw)}$ of 2.95 ± 0.43 µatm yr^{-1} (Bates et al., 2014). Araujo et al. (2019) identified a positive trend in $pCO_{2\,(sw)}$ of 1.20 µatm yr^{-}

[1], but a trend in $pCO_{2\,(atm)}$ of 1.70 µatm yr^{-1} (i.e. decreasing ΔpCO_2) for the northeast Brazilian coast, Although, the air-sea CO_2 flux and ΔpCO_2 within the Amazon Plume region is spatially and temporally variable (Valerio et al., 2021; Ibánhez et al., 2016; Bruto et al., 2017).

The South Atlantic gyre exhibited negative trends in ΔpCO_2 and the CO_2 flux indicating an increasing drawdown of atmospheric CO_2 into the ocean, which were consistent with Landschützer et al. (2016) over the period from 1982 and 2011 though the trends were at the limits of the uncertainties (Appendix 4.2; Fig. A4.4). Fay and Mckinley (2013) showed weak negative trends in ΔpCO_2 using *in situ* observations over different time series lengths. Gregor et al. (2019), with an ensemble of complete $pCO_{2\,(sw)}$ fields, indicated negative trends in ΔpCO_2 however there was low confidence in these trends especially in the South Atlantic gyre. By contrast, Kitidis et al. (2017) reported a mean trend in *in situ* ΔpCO_2 between 1995 and 2013, that was not significantly different from zero. These contradictory trends support the conclusion that ΔpCO_2 is unlikely to be representative of the CO_2 flux over multi-year timescales. Therefore, we recommend that the CO_2 flux should be used to assess multi-year variability in the oceanic CO_2 sink, as the importance of changes in solubility and gas transfer velocity (estimated via wind speed) increases (Keppler and Landschützer, 2019).

During the United Nations decade of ocean science (2021-2030) , the Integrated Ocean Carbon Research (IOC-R) highlights that the role of biology is a key issue to understanding the global ocean CO_2 sink (Aricò et al., 2021). The biological contribution to both interannual and multi-year variations in the South Atlantic air-sea CO_2 flux shown in this study, and supported by Ford et al. (2022), indicates that the biology activity through NCP cannot be assumed to be in steady state. The biological effect of NCP on ΔpCO_2 and CO_2 flux should therefore not be overlooked when assessing the interannual and multi-year variations in the global ocean carbon sink.

4.5 Conclusions

In this paper, we have investigated the seasonal and interannual drivers of ΔpCO_2 and the air-sea CO_2 flux in the South Atlantic Ocean using satellite observations. Seasonally, our results indicated that the subtropics were

controlled by SST, and the subpolar regions were correlated with biological processes. Deviations from this trend occurred in the Benguela upwelling where predominately biological processes correlated with variability in the ΔpCO_2 as well as upwelling. The Equatorial Atlantic showed spatially variable drivers associated with the Amazon Plume and Equatorial upwelling which induced a biological effect. These regions imply a strong biological control on ΔpCO_2 through local physical processes. The CO_2 flux had similar seasonal drivers to ΔpCO_2, but with significant correlations over a larger spatial area. This highlights that ΔpCO_2 can be used to indicate the important drivers of the CO_2 flux on seasonal timescales, but it's still possible that ΔpCO_2 will miss some of the spatial correlations and will likely overestimate the strength of these correlations.

The interannual variability of ΔpCO_2 and the CO_2 flux was correlated with the MEI through a reduction (increase) of NCP and increase (decrease) in SST during El Niño (La Niña) events, again highlighting the importance of biology to the interannual variability. The CO_2 flux response extended over a larger geographical region, indicating that the CO_2 flux should be used to assess interannual trends in the oceanic CO_2 sink, as opposed to a proxy such as ΔpCO_2, which may overestimate the strength of the correlations and does not include variability in the solubility and the gas transfer velocity (estimated via wind speed). The 16 year trends in ΔpCO_2 and the CO_2 flux were determined with associated uncertainties which identified negative trends in the CO_2 flux in the South Atlantic gyre. Positive trends in the CO_2 flux were observed in the Benguela upwelling region, which were associated with an increase in the strength and frequency of upwelling. A transition to negative trends offshore were consistent with elevated nutrient export from the upwelling area, and subsequent biological drawdown of CO_2. These results highlight that changes in biological activity in the South Atlantic Ocean can control the interannual and multi-year trends in the oceanic CO_2 flux. This emphasises the importance of biology and specifically NCP in assessing the global ocean carbon sink.

Appendices

Appendix 4.1 – Driver analysis using *in situ* Δ*p*CO_2

Henson et al. (2018) performed the X-11 analysis using *in situ* *p*$CO_{2\,(sw)}$ observations to estimate average Δ*p*CO_2 for the Longhurst provinces (Longhurst, 1998). The in situ *p*$CO_{2\,(sw)}$ observations were obtained from SOCATv2020 (https://www.socat.info/; Bakker et al., 2016), and were reanalysed to a temperature dataset representative for a consistent and fixed depth (Reynolds et al., 2002) which is used to represent the base of the mass boundary layer. The reanalysis method used the 'fe_reanalyse_socat.py' routine within FluxEngine (Holding et al., 2019; Shutler et al., 2016), which follows the methodology of Goddijn-Murphy et al. (2015), and as used in Woolf et al. (2019) and Watson et al (2020b). Δ*p*CO_2 was calculated using the reanalysed *in situ* *p*$CO_{2\,(sw)}$ observations and *p*$CO_{2\,(atm)}$. These Δ*p*CO_2 estimates were used within the driver analysis as described by Henson et al. (2018), using the drivers described in section 4.2.4, for the South Atlantic Longhurst provinces (Longhurst, 1998). The seasonal drivers of *in situ* Δ*p*CO_2 (Fig. A4.1) showed a similar spatial distribution as the SA-FNN Δ*p*CO_2 (Fig. 4.1). The interannual drivers (Fig. A4.2) showed some differences to the SA-FNN (Fig. 4.3). The averaging required to produce the *in situ* Δ*p*CO_2 timeseries may mask interannual signals, and Ford et al. (2021b) indicated that averaging over large province areas could mask correlations, especially in dynamic regions, and locally these correlations may be significant.

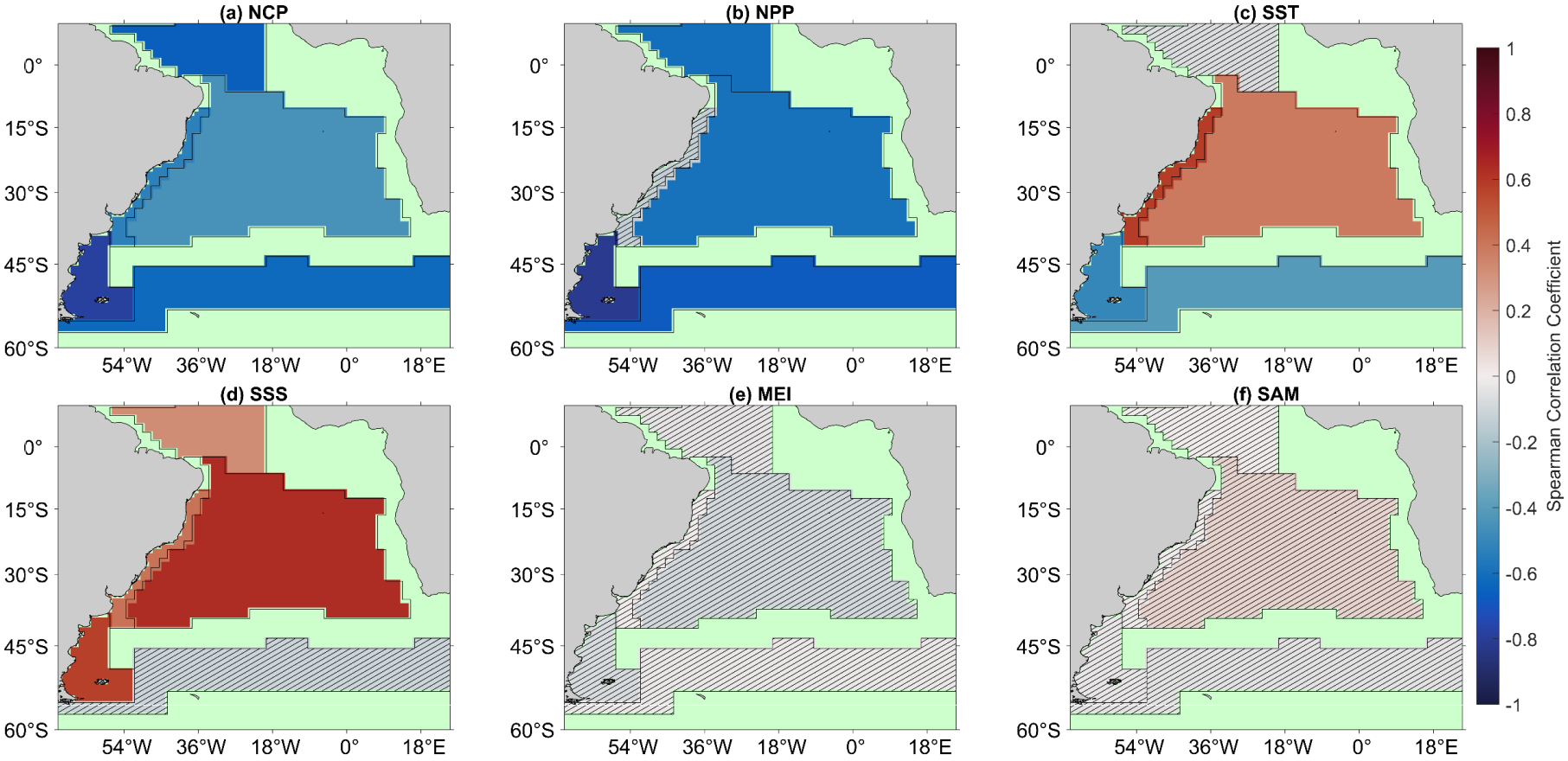

Figure A4.1 - Spearman correlations between the in situ ΔpCO_2 seasonal component of the X-11 analysis and (a) net community production (NCP), (b) net primary production (NPP), (c) sea surface temperature (SST), (d) sea surface salinity (SSS), (e) Multivariate ENSO index (MEI) and (f) Southern Annular Mode (SAM) seasonal components on a per province basis. Hashed areas indicate no significant correlations, and green regions indicate no analysis was performed due to missing data.

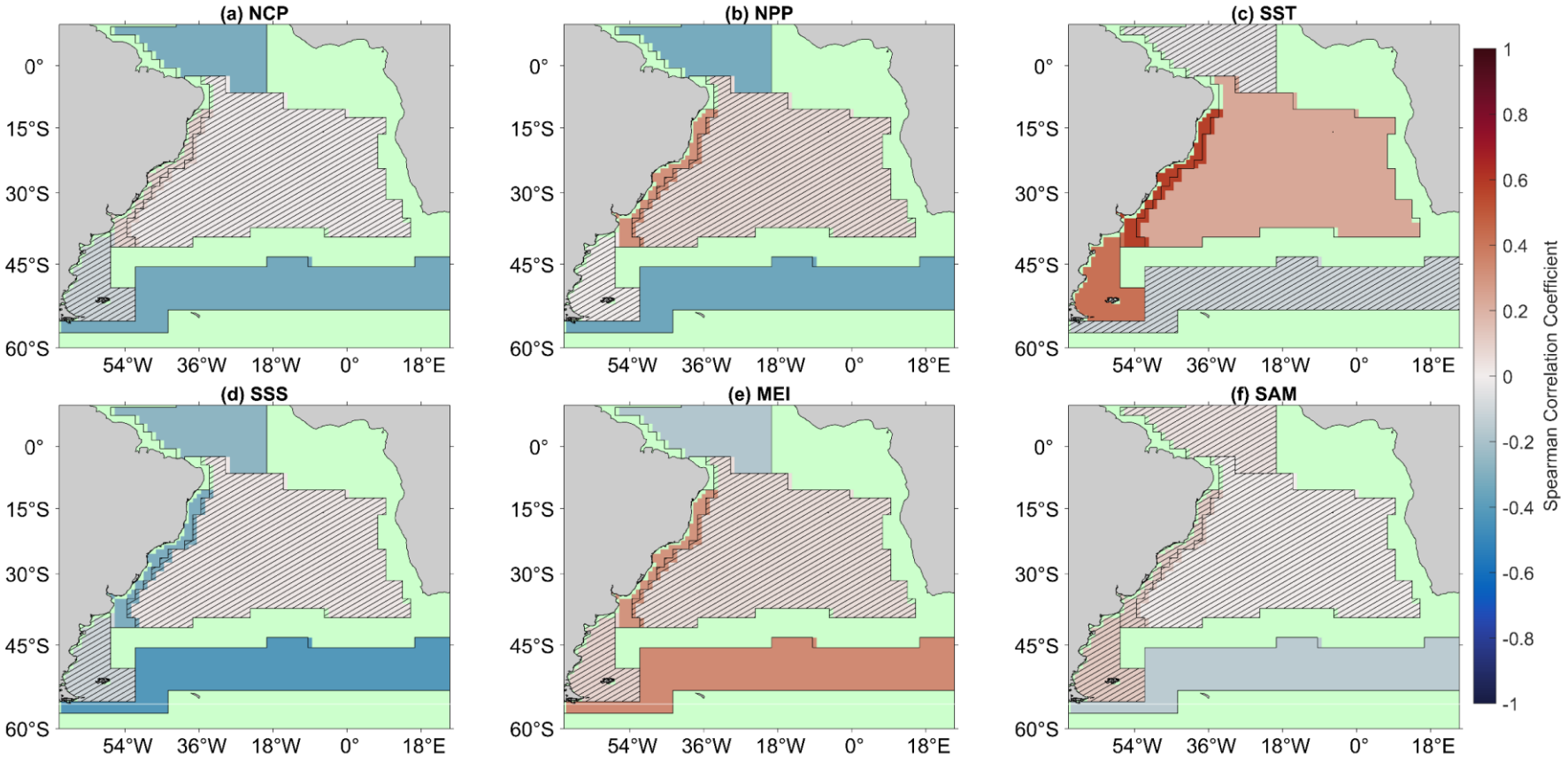

Figure A4.2 - Spearman correlations between the in situ ΔpCO_2 interannual component of the X-11 analysis and (a) net community production (NCP), (b) net primary production (NPP), (c) sea surface temperature (SST), (d) sea surface salinity (SSS) (e) Multivariate ENSO index (MEI) (f) Southern Annular Mode (SAM) interannual components on a per province basis. Hashed areas indicate no significant correlations, and green regions indicate no analysis was performed due to missing data.

Appendix 4.2 – SA-FNN $pCO_{2\,(sw)}$ and trend uncertainties

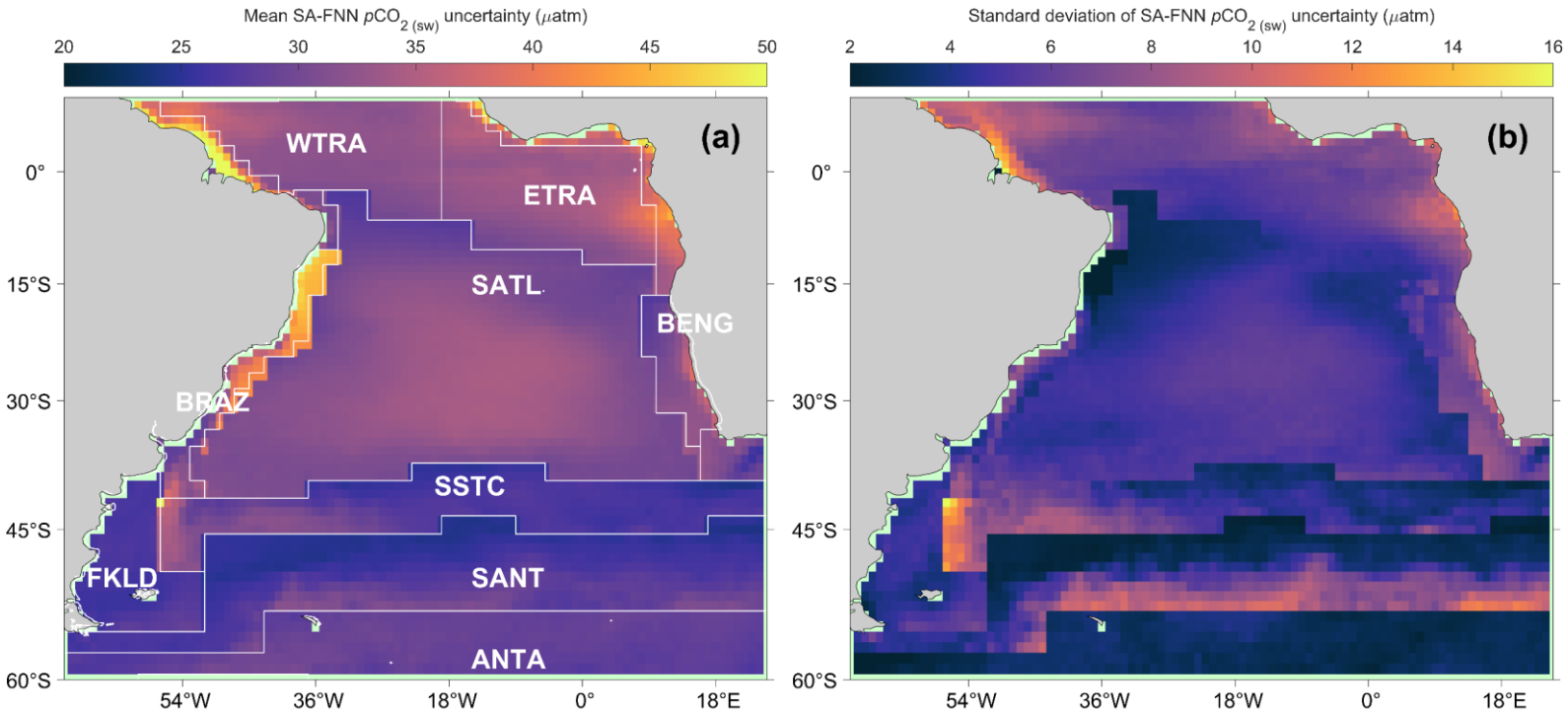

Figure A4.3 - (a) Mean SA-FNN $pCO_{2\,(sw)}$ uncertainty between July 2002 and December 2018. Longhurst provinces (Longhurst, 1998) used within the SA-FNN training described in Ford et al. (2022; note the WTRA and ETRA are merged into one province). The province areas acronyms are listed as follows: WTRA is western tropical Atlantic; ETRA is eastern equatorial Atlantic; SATL is South Atlantic Gyre; BRAZ is Brazilian current coastal; BENG is Benguela Current coastal upwelling; FKLD is Southwest Atlantic shelves; SSTC is South Subtropical Convergence; SANT is sub-Antarctic and ANTA is Antarctic. (b) Standard deviation of SA-FNN $pCO_{2\,(sw)}$ uncertainty.

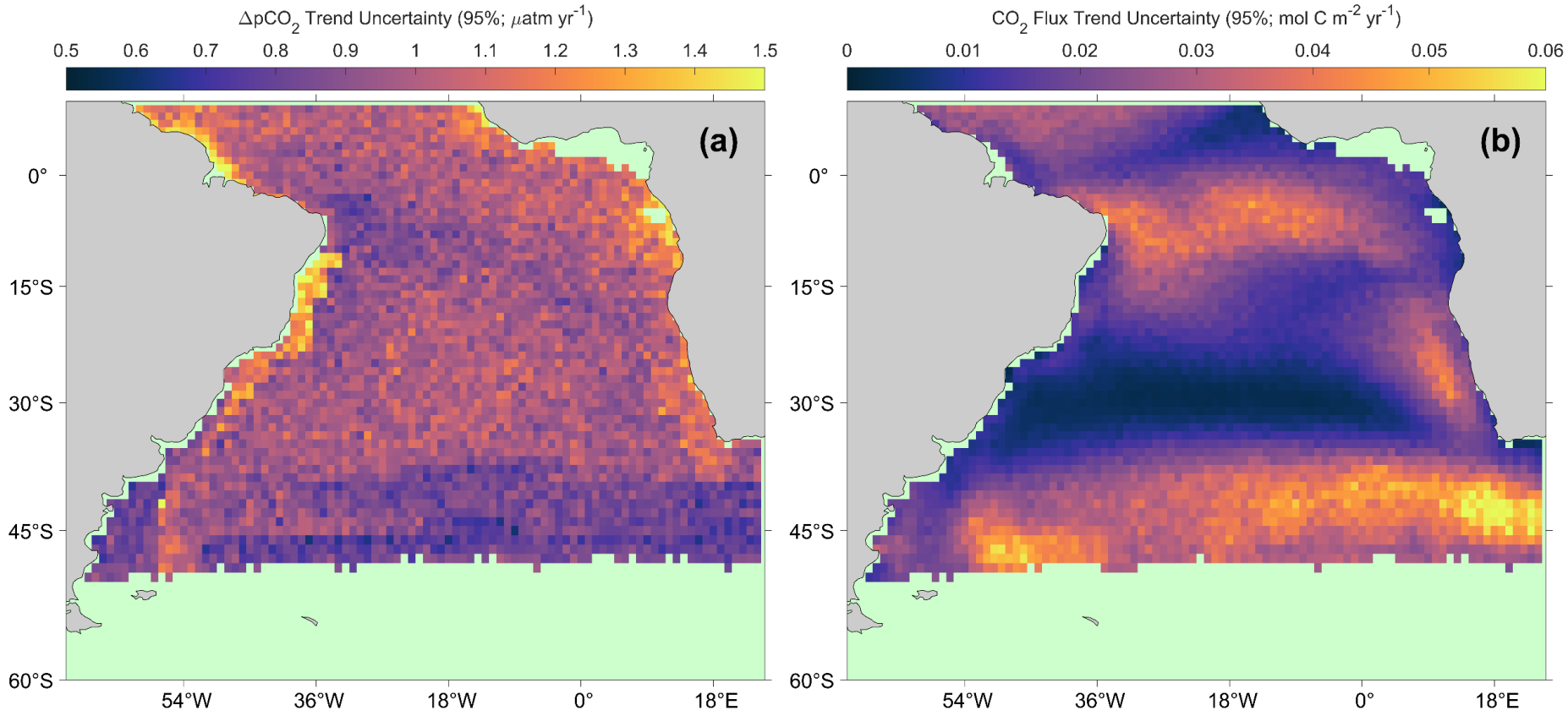

Figure A4.4 - (a) Uncertainty in the ΔpCO_2 trends presented in Fig. 5a (b) Uncertainty in the air-sea CO_2 flux trends presented in Fig. 5b

Chapter 5: Mesoscale eddies enhance the air-sea CO_2 sink in the South Atlantic Ocean

This chapter is a reformatted version of my in prep publication:
Ford, D. J., Tilstone, G. H., Shutler, J. D., Kitidis, V., Sheen, K. L., Dall'Olmo, G. and Orselli, I. B. M. (in prep): Mesoscale eddies enhance the air-sea CO_2 sink in the South Atlantic Ocean

DJF, GHT, JDS, VK and KLS conceived and directed the research. DJF developed the code and prepared the manuscript. GHT, JDS, VK, KLS, GD and IBMO provided comments that have shaped the manuscript.GD provided useful discussions on the Lagrangian tracking and application of the neural network approach. IBMO provided in situ observations from the Following Ocean Rings in the South Atlantic Ocean cruise.

Abstract: Long lived mesoscale eddies are abundant in the global oceans and known to affect marine biogeochemical cycles. Understanding their cumulative impact on modulating the air-sea CO_2 flux would appear important for assessing the global carbon budget. In this study, satellite observations and Lagrangian tracking are used to estimate the air-sea CO_2 flux into long lived mesoscale eddies in the South Atlantic Ocean. Using this technique, we find that anticyclonic eddies originating from the Agulhas retroflection, and cyclonic eddies from the Benguela upwelling act as cumulative net CO_2 sinks over their respective lifetimes. In combination the anticyclonic and cyclonic eddies significantly enhanced the CO_2 sink into the South Atlantic Ocean by 0.08 %. However, these long lived eddies account for 0.4 % of eddies globally, and therefore, the inclusion of mesoscale eddies within models used to estimate the global ocean carbon sink could be important.

Plain Languange Summary: Ocean mesoscale eddies are formed when part of a main current gets pinched off to form circular rotating currents that wander the oceans and last from weeks to years. These eddies can modify the ocean properties and affect the rate at which CO_2 flows between the ocean and the atmosphere, which is known as the global ocean CO_2 sink. Little is known on how these eddies modify the ocean CO_2 sink. Using satellite based observations, to estimate the eddy CO_2 exchange in the South Atlantic Ocean, we show that the eddies enhance the drawdown of CO_2 from the atmosphere, thus modifying the ocean to be a stronger net sink of CO_2. These results are of importance as they quantify how much eddies contribute to the drawdown of

CO_2 from the atmosphere to the ocean. Our results further support the inclusion of these, currently unresolved, features in future global climate models.

5.1 Introduction

Mesoscale eddies are ubiquitous in the global oceans with radii up to 100 km and last for weeks to years (Chelton et al., 2011; Pegliasco et al., 2022). Eddies modify the physical (Laxenaire et al., 2019; Nencioli et al., 2018), biological (Carvalho et al., 2019; Dufois et al., 2016; Lehahn et al., 2011; Roughan et al., 2017), and chemical (Arhan et al., 2011; Orselli et al., 2019a, b; Chen et al., 2007) oceanic conditions compared to the surrounding waters, and can advect these waters far away from the formation regions. Alteration of the ocean surface conditions can modulate the air-sea exchange of CO_2 through changes in the partial pressure of CO_2 ($pCO_{2\,(sw)}$) (Orselli et al., 2019b; Chen et al., 2007; Song et al., 2016; Jones et al., 2017), solubility of CO_2, and the overlying atmospheric conditions (Frenger et al., 2013; Pezzi et al., 2021; Souza et al., 2021). Few studies have investigated the role of eddies in the air-sea exchange of CO_2 (Pezzi et al., 2021; Orselli et al., 2019b; Chen et al., 2007; Jones et al., 2017) and none has identified their cumulative impact on the oceanic CO_2 sink.

Anticyclonic eddies generally display high pressure centres, displace isopycnals downwards, and have higher sea surface temperatures (SST) than the surrounding environment (McGillicuddy, 2016). The solubility of CO_2 in seawater decreases with increasing temperature (Weiss, 1974), and biological activity would hypothetically decrease due to lower nutrient inputs into the surface layer (e.g. Gaube et al., 2014; Liu et al., 2018). Therefore, these anticyclonic features are commonly thought to increase $pCO_{2\,(sw)}$ and considered as weak CO_2 sinks or even sources of CO_2 to the atmosphere. Cyclonic eddies are expected to follow the opposite convention with low pressure centres, lower SST, elevated isopycnals, enhanced biological activity and therefore decreased $pCO_{2\,(sw)}$, potentially enhancing the CO_2 sink.

Mesoscale eddies are, however, intricate structures, and the modification of the air-sea CO_2 fluxes can be more complex. Jones et al. (2017) identified that both anticyclonic and cyclonic eddies were hotspots for CO_2 drawdown in the Southern Ocean. Orselli et al. (2019b) showed that anticyclonic (Agulhas) eddies are stronger CO_2 sinks in the South Atlantic Ocean. By contrast, Pezzi et

al. (2021) identified an anticyclonic eddy acting as a CO_2 source and Chen et al. (2007) reported that a single cyclonic eddy in the North Pacific weakened the CO_2 sink by ~ 17 %. Song et al. (2016) showed that modifications to the air-sea CO_2 flux are seasonally dependent in the Southern Ocean. Anticyclonic (cyclonic) eddies were stronger (weaker) CO_2 sources in winter and stronger (weaker) CO_2 sinks in summer. The ability of mesoscale eddies to modify the CO_2 flux as they age (Orselli et al., 2019b), may also be modified by seasonal variability.

The South Atlantic Ocean contains some of the largest long-lived (> 1 year) anticyclonic eddies globally, originating from the Agulhas retroflection (Guerra et al., 2018), which propagate across the basin to the Brazilian Coast. In conjunction with these, cyclonic eddies forming from the Benguela upwelling system also propagate across the basin (Rubio et al., 2009; Chelton et al., 2011; Pegliasco et al., 2022). The modulation of the air-sea CO_2 flux by eddies, differences between anticyclonic and cyclonic, and their role in the global ocean CO_2 sink requires further investigation, especially since eddy kinetic energy, a proxy for mesoscale eddies, has been increasing globally (Martínez-Moreno et al., 2021).

The objective of this study is to estimate the air-sea CO_2 flux of long-lived mesoscale eddies in the South Atlantic Ocean throughout their lifetimes using satellite observations. In total, 36 Agulhas anticyclonic and 31 Benguela cyclonic eddies were tracked in a Lagrangian mode using satellite observations (2002 - 2018), and the cumulative air-sea CO_2 fluxes of these 67 eddies were estimated in order to assess their role in the South Atlantic CO_2 sink. The $pCO_{2\,(sw)}$ timeseries for each eddy was decomposed into the thermal and non-thermal drivers to assess changes over the lifetime of the respective eddies.

5.2 Data and Methods

5.2.1 Sea surface temperature, salinity, biological and wind speed data

Daily 4 km resolution chlorophyll *a* (Chl *a*) composites were calculated from Moderate Resolution Imaging Spectroradiometer on Aqua (MODIS-A) Level 1 granules, retrieved from the National Aeronautics Space Administration (NASA) Ocean Colour website (https://oceancolor.gsfc.nasa.gov/; accessed 10/12/2020), using SeaDAS v7.5, and applying the standard OC3-CI algorithm

for Chl *a* (https://oceancolor.gsfc.nasa.gov/atbd/chlor_a/; accessed 15/12/2020). Coincident daily composites of SST (NASA OBPG, 2015) and photosynthetically active radiation (PAR) (NASA OBPG, 2017) were retrieved from the NASA ocean colour website (https://oceancolor.gsfc.nasa.gov/; accessed 10/12/2020). SST, PAR and Chl *a* were used to estimate net primary production (NPP) using the Wavelength Resolving Model (Morel, 1991) with the look up table described in Smyth et al. (2005). Daily net community production (NCP) composites were generated using NPP and SST data with the algorithm NCP-D described in Tilstone et al. (2015b). These satellite algorithms were shown to be the best performing with respect to *in situ* data in an algorithm intercomparison which accounted for *in situ*, satellite and algorithm uncertainties (Ford et al., 2021a). Daily 8 km sea surface salinity (SSS) composites were retrieved from the Copernicus Marine Service (CMEMS) physics reanalysis product (GLORYSV12) (CMEMS, 2021). Daily 0.25 ° resolution wind speed at 10 m were downloaded from Remote Sensing Systems Cross-Calibrated Multi-Platform (CCMP) product (Wentz et al., 2015). All data were retrieved for the period July 2002 to December 2018.

5.2.2 AVISO+ Mesoscale Eddy Tracking Product and Lagrangian Tracking

The AVISO+ Mesoscale Eddy Product META3.1exp (Pegliasco et al., 2022; Mason et al., 2014; Pegliasco et al., 2021) was used to identify the trajectories of mesoscale eddies within the South Atlantic Ocean, which provides daily estimates of the eddy location and radius. Anticyclonic (Agulhas) eddies were considered for analysis using three criteria: (1) the eddy trajectory started in a region surrounding the Agulhas retroflection (30 °S – 40 °S; 5 °E – 25 °E; Fig. 1c); (2) the eddy trajectory was longer than 1 year and (3) the trajectory crossed 0 °E into the South Atlantic gyre region. These criteria identified 36 anticyclonic eddies for analysis between July 2002 and December 2018, that entered the South Atlantic Ocean as a single trajectory from formation to dissipation, with limited interactions with other eddies. The selection procedure was repeated for cyclonic eddies originating from the Benguela upwelling system (15 °S – 40 °S; 5 °E – 25 °E; Fig. 1c), which identified 31 cyclonic eddies for further analysis.

For each eddy, a daily timeseries of SST, SSS, NCP and wind speed was constructed using the eddy location and radius estimates from the AVISO+ product. For each parameter, the available data were extracted assuming a

circular eddy and the median value taken when at least 30 % of the data within the eddy were available. An example of the timeseries extraction is presented in Fig. A5.1. A daily timeseries of the environmental conditions surrounding the eddy was also extracted from a circular region three times the radius of eddy, where data inside the eddy radius were excluded. Median calendar month SST, SSS, NCP and wind speeds were calculated from the daily timeseries both for the eddy and the environmental conditions surrounding the eddy.

5.2.3 Sea surface pCO_2 estimates

The sea surface pCO_2 ($pCO_{2\,(sw)}$) was determined for each calendar month of the eddy trajectories using the South Atlantic Feed Forward Neural Network ($SA\text{-}FNN_{NCP}$; Ford et al. 2022). The $SA\text{-}FNN_{NCP}$ estimates $pCO_{2\,(sw)}$ at the base of the mass boundary layer (sub skin $pCO_{2\,(sw)}$) (Woolf et al., 2016) using non-linear relationships between $pCO_{2\,(sw)}$ and three environmental drivers; $pCO_{2\,(atm)}$, SST and NCP, which were constructed for eight static provinces in the South Atlantic Ocean. The $SA\text{-}FNN_{NCP}$ was supplied with the calendar month median SST and NCP, and the monthly $pCO_{2\,(atm)}$ for the mean location of the eddy within the month was estimated using the dry mixing ratio of CO_2 from the NOAA-ESRL marine boundary layer reference, monthly mean skin SST and sea level pressure following Dickson et al. (2007). The $pCO_{2\,(sw)}$ uncertainty was estimated by propagating the $pCO_{2\,(atm)}$ (1 µatm), satellite SST (0.441 °C) and NCP (45 mmol O_2 m^{-2} d^{-1}) (Ford et al., 2021a) uncertainties through the $SA\text{-}FNN_{NCP}$, and combined in quadrature with the $SA\text{-}FNN_{NCP}$ uncertainty (21.48 µatm) (Ford et al., 2022).

5.2.4 Estimation of the cumulative bulk air-sea CO_2 flux

The air-sea CO_2 flux (F) was calculated for each calendar month of the eddy trajectory using a bulk parameterisation as:

$$F = k\,(\alpha_W\, pCO_{2\,(sw)} - \alpha_s\, pCO_{2\,(atm)}) \qquad (5.1)$$

Where k is the gas transfer velocity estimated from median wind speeds following the parameterisation of Nightingale et al. (2000). α_w and α_s are the solubility of CO_2 at the base and top of the mass boundary layer at the sea surface (Woolf et al., 2016). α_w was calculated as a function of the skin SST and SSS (Weiss, 1974), applying a cool skin bias of +0.17K to convert the skin SST

to sub skin SST (Donlon et al., 1999; Woolf et al., 2016). α_s was calculated as a function of the eddy skin SST and the SSS with a salinity gradient of +0.1 salinity units between the base and top of the mass boundary layer (Woolf et al., 2016). The CO_2 flux calculations were carried out with the open source FluxEngine toolbox (Shutler et al., 2016; Holding et al., 2019) using the 'rapid transport' approximation (described in Woolf et al., 2016) and using a monthly time step.

The monthly average daily flux of CO_2 (mmol C m^{-2} d^{-1}) was multiplied by the number of days and the area of the eddy, assuming a circular eddy with the mean eddy radius, in the respective month. The fluxes (Tg C mon^{-1}) were then added cumulatively to retrieve the net cumulative CO_2 flux for each eddy. The uncertainties in $pCO_{2\,(sw)}$ (temporally varying), $pCO_{2\,(atm)}$ (1 µatm), SST (0.441 °C) and the gas transfer velocity (assumed to be ± 10%; Woolf et al., 2019) were propagated through the cumulative flux calculations using a Monte Carlo uncertainty propagation (N = 1000), and the 95% confidence interval (2 standard deviations) on the cumulative net CO_2 flux extracted.

5.2.5 Thermal and non-thermal decomposition of $pCO_{2\,(sw)}$ timeseries

The eddy $pCO_{2\,(sw)}$ timeseries was separated into its thermal and non-thermal components as described in Takahashi et al. (2002). The thermal component ($pCO_{2\,(therm)}$) was calculated as:

$$pCO_{2\,(therm)} = pCO_{2\,(sw)} \times e^{(0.0423 \times (\overline{SST} - SST))} \quad (5.2)$$

$\overline{SST}$ and SST are the mean subskin SST across the eddy timeseries and the monthly subskin SST respectively. The non-thermal component ($pCO_{2\,(bio)}$) was calculated as:

$$pCO_{2\,(bio)} = \overline{pCO_{2\,(sw)}} \times e^{(0.0423 \times (SST - \overline{SST}))} \quad (5.3)$$

$\overline{pCO_{2\,(sw)}}$ was the mean $pCO_{2\,(sw)}$ for the eddy timeseries. The contributions of the two competing components to the $pCO_{2\,(sw)}$ timeseries can be determined from the seasonal amplitude of the $pCO_{2\,(therm)}$ and $pCO_{2\,(bio)}$;

$$\Delta pCO_{2\,(therm)} = \left[pCO_{2\,(therm)}\right]_{max} - \left[pCO_{2\,(therm)}\right]_{min} \quad (5.4)$$

$$\Delta pCO_{2\,(bio)} = \left[pCO_{2\,(bio)}\right]_{max} - \left[pCO_{2\,(bio)}\right]_{min} \quad (5.5)$$

The seasonal amplitudes were calculated using a 12 month moving window for the lifetime of the eddy, and the ratio between the thermal and non-thermal component (R) was determined as:

$$R = {\Delta pCO_{2\ (therm)}}\Big/{\Delta pCO_{2\ (bio)}} \quad (5.6)$$

In cases where R is greater (less) than 1, the thermal (non-thermal) contribution was the dominant driver. The anomaly in R was determined by subtracting the mean R across the eddy's lifetime.

5.3 Results

Both anticyclonic (Agulhas; median = -0.54 Tg C per eddy) and cyclonic (Benguela; median = -0.27 Tg C per eddy) eddies acted as cumulative net CO_2 sinks (Fig 5.1 a, d). Anticyclonic eddies displayed an exponential decay in the increase of the net cumulative CO_2 sink, compared to a more linear increase in cyclonic eddies when fit with the same functional equation (Fig. 5.1 b, e). The anomaly in the thermal to non-thermal contribution to $pCO_{2\ (sw)}$ variability in anticyclonic eddies changed over their lifetimes (Fig. 5.2a), where a positive anomaly indicates an increasing dominance of temperature on controlling $pCO_{2\ (sw)}$. For cyclonic eddies the anomaly in R did not change significantly over time (Fig. 5.2b).

The anticyclonic (-3.7 %, Mann-Whitney U-Test, $p < 0.001$, $n = 36$) and cyclonic (-1.4%, Mann-Whitney U-Test, $p = 0.005$, $n = 31$) eddies significantly enhance the cumulative CO_2 sink compared the water surrounding each eddy (Fig. 5.3). No significant differences between the ability of anticyclonic and cyclonic eddies to modify the CO_2 sink were observed (Fig. 5.3; Mann-Whitney U-Test, $p = 0.16$), although the anticyclonic modification (-3.7 %) was double that of the cyclonic eddies (-1.4 %; Fig. 5.3).

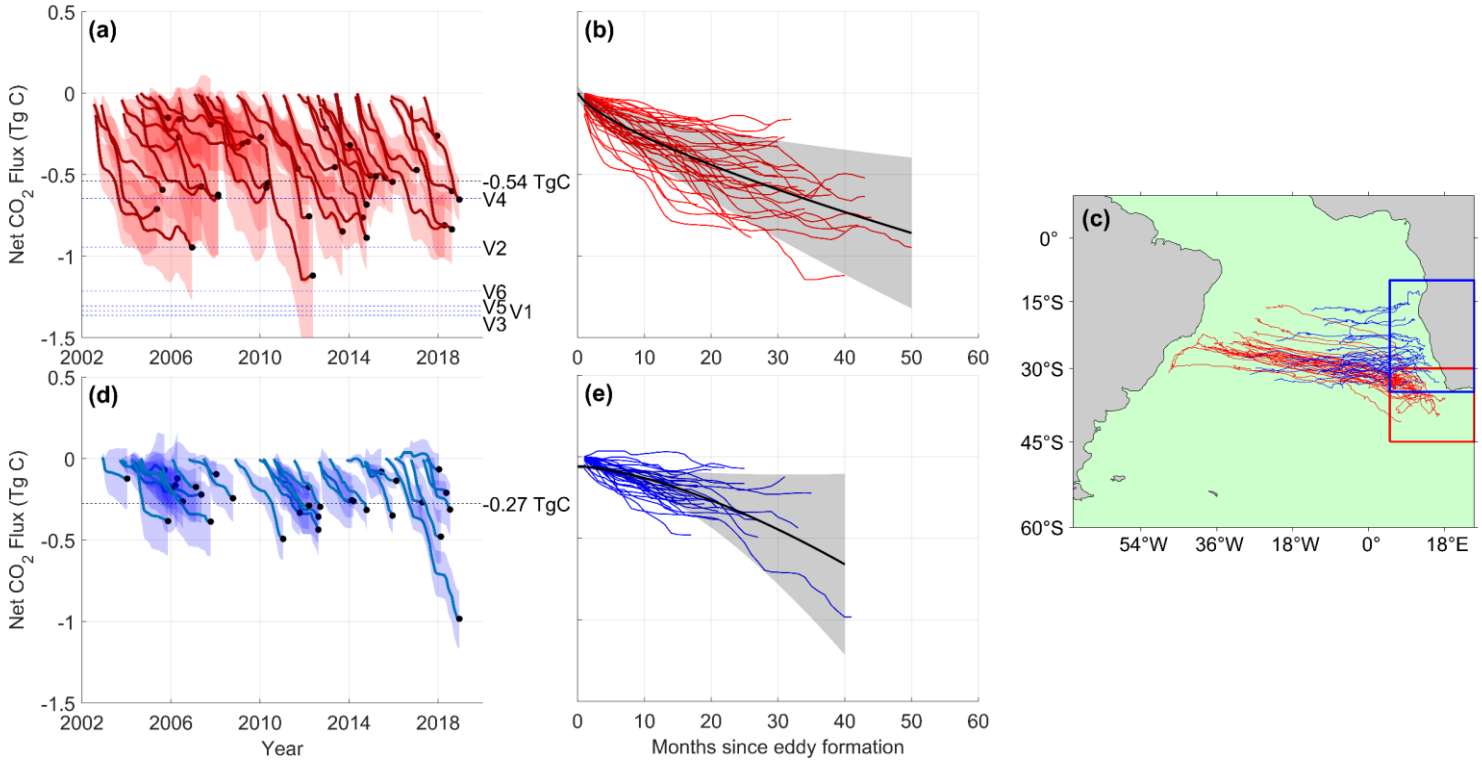

Figure 5.1 - (a) Red lines indicate the cumulative net CO_2 flux for the 36 anticyclonic eddies, where shading is the propagated uncertainty. Black dots indicate the cumulative net CO_2 flux at eddy dissipation. Black dashed line indicates the mean cumulative net CO_2 flux at eddy dissipation (i.e. mean of black dots). Blue dashed lines indicate the estimates for 6 anticyclonic eddies presented in Orselli et al. (2019b). (b) Cumulative net CO_2 flux for the 36 anticyclonic eddies plotted since eddy formation. Black line indicates a power law fit ($y = a*x^b+c$) for the temporal evolution of the net CO_2 flux of the 36 anticyclonic eddies, where shading indicates the 95% confidence limits. (c) Trajectories of the 36 anticyclonic (red lines) and 31 cyclonic (blue lines) eddies. Red and blue boxes indicate the formation region for the anticyclonic and cyclonic eddies respectively. (d) the same as (a) but for the 31 cyclonic eddies. (e) the same as (b) but for the 31 cyclonic eddies.

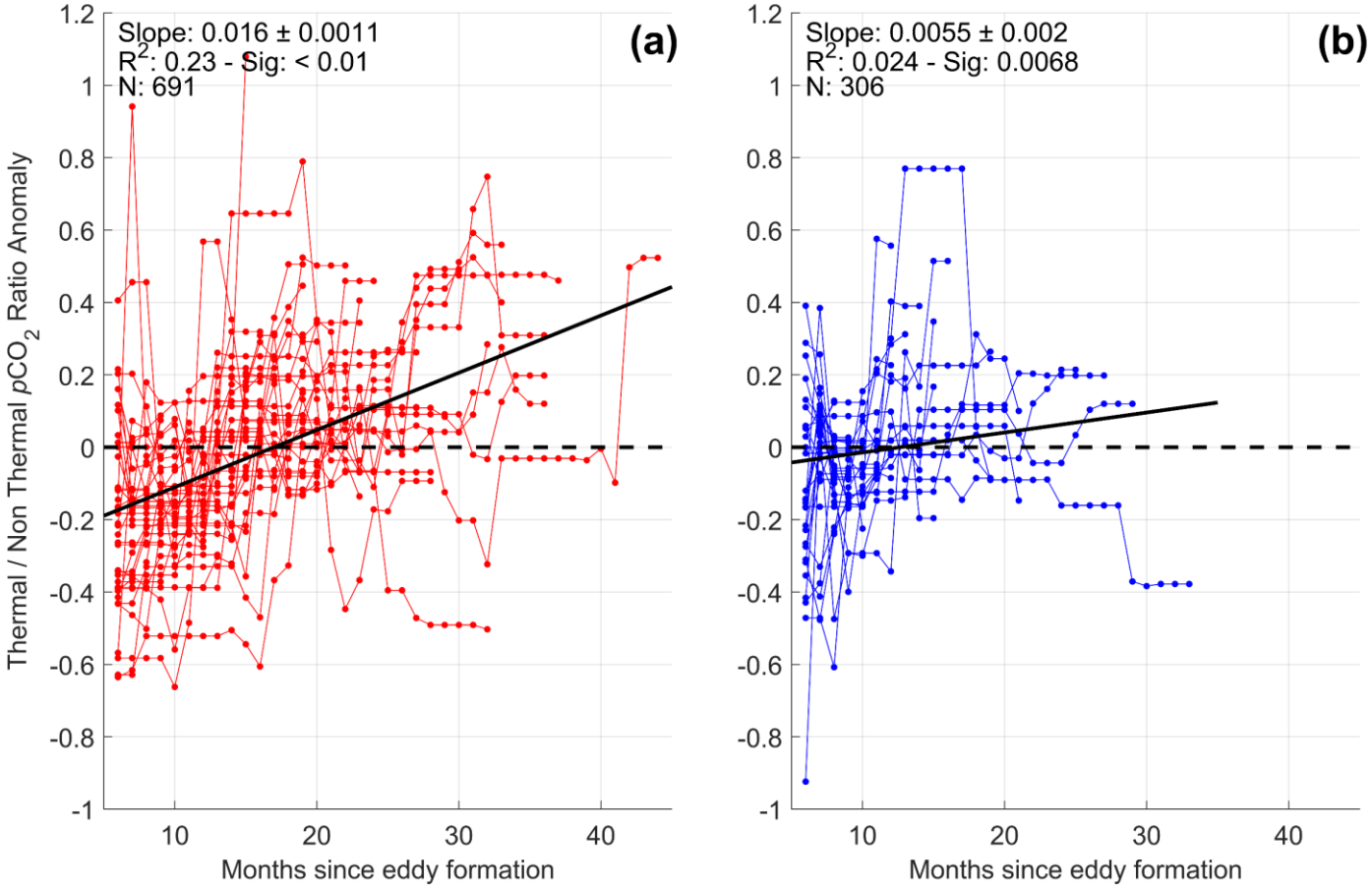

Figure 5.2 - (a) Anomaly in the 12 month running thermal to the non-thermal ratio of $pCO_{2\,(sw)}$ for the 36 anticyclonic eddies. Black solid line indicates the linear fit since the formation of the eddy. Black dashed line indicates an anomaly of 0. Statistics within the plot are: Slope is the slope of the linear fit, R^2 is the coefficient of determination, Sig is the significance of the linear fit and N is number of samples. (b) Same as (a) but for the 31 cyclonic eddies.

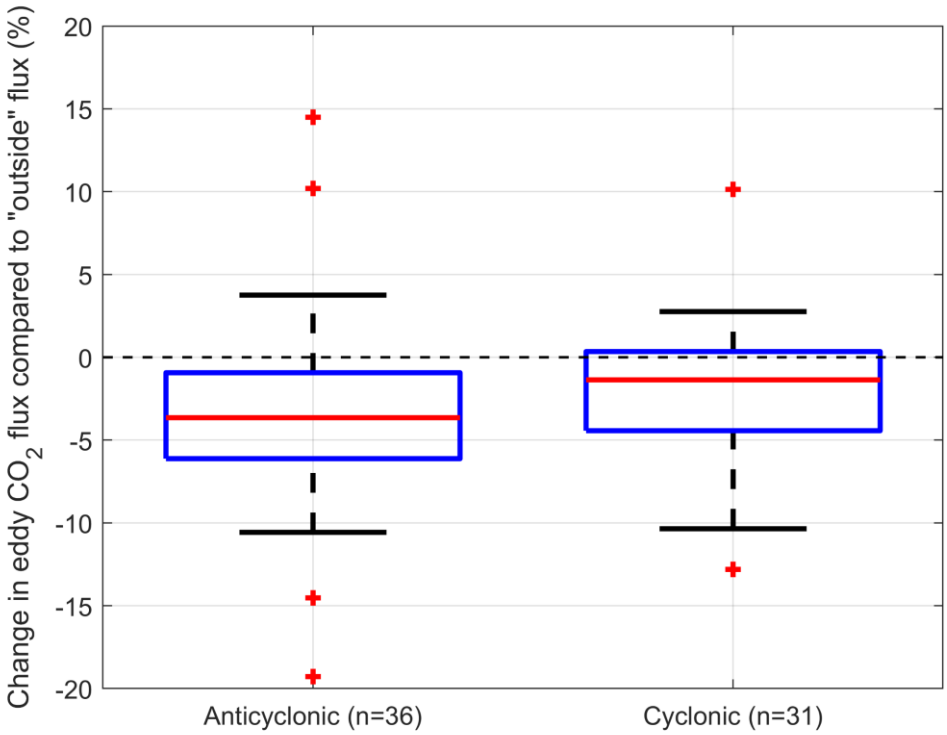

Figure 5.3 - Box plots indicating the percentage change in the cumulative net CO_2 flux at eddy dissipation with respect to theoretical eddies containing waters surrounding the eddy. Negative (positive) percentages indicate a stronger (weaker) flux

5.4 Discussion

This is the first study to provide an observation-based assessment of the cumulative net CO_2 flux of 67 long-lived mesoscale eddies. Chen et al. (2007) reported SST-$pCO_{2\,(sw)}$ relationships from in situ measurements made outside of a cyclonic eddy, but were not able to reproduce the $pCO_{2\,(sw)}$ within the eddy. We performed a comparison between the SA-FNN_{NCP} estimated $pCO_{2\,(sw)}$ and in situ $pCO_{2\,(sw)}$ observations within both anticyclonic (n = 6) and cyclonic eddies (n = 2; Fig. A5.2). The SA-FNN_{NCP} was accurate and precise within anticyclonic eddies (root mean square deviation = 10.2 µatm; bias = 0.4 µatm; n = 6) but showed larger differences in $pCO_{2\,(sw)}$ for the cyclonic eddies, albeit from just two crossovers (root mean square deviation = 20.9 µatm; bias 11.1 µatm; n = 2).

In this study, we followed the trajectory of 36 anticyclonic eddies over their lifetime and found that they were a net cumulative CO_2 sink (median = 0.54 Tg C). Anticyclonic (Agulhas) eddies have previously been identified as a net sink for CO_2 varying from ~0.6 Tg C to ~1.4 Tg C (median = 1.26 Tg C; Fig. 5.1a;

Orselli et al. 2019b). This was based on extrapolation of a snapshot of the eddies CO_2 uptake potential from ship observations that crossed the paths of six eddies. Two of these eddies were tracked in this study (V1, V3; Fig. 5.1a) and were identified as CO_2 sinks of 0.64 and 0.40 Tg C compared to 1.34 and 1.36 Tg C by Orselli et al. (2019b). The lower cumulative CO_2 sink in this study are likely due to the effect of seasonality whereby the study of Orselli et al. (2019b) sampled eddies in austral winter which acted as stronger CO_2 sinks, compared to our estimates which accounted for the seasonal variability in the air-sea CO_2 flux.

Both the cyclonic and anticyclonic eddies showed an increasing CO_2 sink over their lifetime (Fig. 5.1b, e). For the latter, the rate of CO_2 uptake decreased exponentially over this period (Fig. 5.1b). This is consistent with the geographical propagation of the eddies in the oligotrophic South Atlantic gyre (Fig. 5.1c), and eddy stirring of the environment (McGillicuddy, 2016). The significant increase in the anomalies of the seasonal thermal to non-thermal $pCO_{2\,(sw)}$ ratio (becoming more temperature driven; Fig. 5.2a), mainly driven by a reduction in the non-thermal contribution (not shown), highlights the changing role of biological activity and/or circulation over time as the eddies propagated into the gyre. Carvalho et al. (2019) showed phytoplankton community succession where younger anticyclonic (Agulhas) eddies were dominated by haptophytes (small flagellates) followed by prokaryotes as these eddies aged. Sarkar et al. (2021) highlighted that haptophytes are crucial for the biological CO_2 drawdown in the Agulhas retroflection, reinforcing a weaker biological pump as the eddies age. In contrast, the cyclonic eddies displayed a linear increase in the cumulative CO_2 sink (Fig. 5.1e). This may be because the cyclonic eddies do not propagate as far as anticyclonic eddies into the South Atlantic gyre (Fig. 5.1e), which is also illustrated by no significant change in the thermal to non-thermal $pCO_{2\,(sw)}$ ratio anomaly (Fig. 5.2b).

Both the anticyclonic and cyclonic eddies were shown to significantly increase the CO_2 drawdown in the South Atlantic Ocean (Fig. 5.3), with respect to the surrounding waters. Jones et al. (2017) showed that both anticyclonic and cyclonic eddies were hotspots for CO_2 drawdown of similar magnitude in the Antarctic Circumpolar Current. Dufois et al. (2016) examined Chl *a* variability in anticyclonic eddies using a rotated empirical orthogonal function (REOF)

analysis, which decomposes the spatial variability into dominant components. This showed the first two modes of variability were consistent with eddy stirring, and the third mode highlighted the mesoscale modification. In this study, by comparing the cumulative CO_2 fluxes of the eddies to a theoretical eddy consisting of surface waters surrounding the eddy, the mesoscale modulation of the air-sea CO_2 flux is highlighted.

The cyclonic eddies generally showed lower SST, and higher NCP (Fig. A5.3; Fig. A5.4) compared to the surrounding waters, suggesting a biological and physical amplification of the CO_2 sink. Chen et al. (2007) showed $pCO_{2\,(sw)}$ to be elevated at the core of a cyclonic eddy in the North Pacific, due to the upwelling of CO_2 rich waters into the surface layer and the eddy acting as a weaker CO_2 sink compared to the surrounding. By comparison, Lovecchio et al. (2022) identified that cyclonic eddies around the Canary upwelling system entrain nearshore nutrient rich waters into the eddy core at formation, where upwelled nutrients as a result of mesoscale processes were a small component of the total nutrients sustaining the biological production. This indicated that the CO_2 rich water supplied by upwelling, is a minor component of the CO_2 flux caused by cyclonic eddies which ultimately create a CO_2 sink induced by the associated physical and biological processes.

The anticyclonic eddies were associated with elevated SST at formation, which rapidly changed to depressed SST for the remainder of their lifetimes (Fig. A5.3) compared to the surrounding waters. NCP remained lower than the surroundings (Fig. A5.4). These characteristics suggest opposing physical and biological forces on the modification of the air-sea CO_2 flux. Similarly, Laxenaire et al. (2019) showed that the SST anomaly associated with surface water of an anticyclonic (Agulhas) eddy switched from positive to negative over its lifetime, also implying a change from a CO_2 source to sink as it propagated over the South Atlantic basin. Thus, indicating the physical component exerts the greatest control on amplifying the air-sea CO_2 sink into these anticyclonic eddies.

This study has identified that the variability in the modification of the air-sea CO_2 flux by eddies (Fig. 5.3) is driven by intrinsic differences between individual eddies (Fig. A5.3, A5.4). Lehahn et al. (2011) observed an isolated patch of elevated Chl *a* associated with an anticyclonic eddy that was transported into

the South Atlantic gyre, perhaps suggesting enhanced biological drawdown of CO_2, but whether this is a common feature of all anticyclonic eddies was not verified. Entrainment of nutrient rich nearshore waters into the cyclonic eddies as identified by Lovecchio et al. (2022), is likely to be highly variable depending on the location and interaction with other water bodies, which will in turn lead to a different biological response and therefore modulation of the air-sea CO_2 flux. Many of these studies are limited by the availability of in situ data. The expanding use of Bio-Argo profilers, especially those with pH sensors (Roemmich et al., 2019), is improving the potential to assess the air-sea CO_2 flux both globally and regionally (e.g. Gray et al., 2018), but coverage still remains a limitation for studying eddies.

Based on a recent assessment by Ford et al. (2022) of the South Atlantic Ocean (20 °S to 44 °S) which estimated the region to be a CO_2 sink of 76 Tg C yr^{-1}, the contribution to this by anticyclonic eddies would be 0.06 % (Table 5.1). This suggesting that these eddies play a more significant role in modifying the air-sea CO_2 flux within this region. Orselli et al. (2019b) showed that anticyclonic (Agulhas) eddies enhance the CO_2 sink in the South Atlantic Ocean (14 °S to 50 °S) by ~1.55 10^{-6} %, assuming that the region is a CO_2 sink of ~300 Tg C yr^{-1} (Takahashi et al., 2002). In contrast, assuming the same South Atlantic CO_2 sink as Orselli et al. (2019b) we find the contribution of anticyclonic eddies to be 0.01% (Table 5.1).

In combination, anticyclonic and cyclonic eddies contribute to the oceanic CO_2 sink into the South Atlantic Ocean (20 °S to 44 °S) by a further 0.08 % (Table 1). Globally, long lived mesoscale eddies, such as those studied here, make up 0.4% of the eddy trajectories in the AVISO+ dataset (Pegliasco et al., 2022). This suggests that the effect of all eddies on the CO_2 flux could be globally and regionally significant as shown by modelling studies. Harrison et al. (2018) for example, showed that mesoscale resolving models may have a modest effect on the global balance of carbon export (<2%), but regionally the effect can be large (±50%). Jersild et al. (2021) highlighted that an Earth System Model (ESM) that explicitly resolved mesoscale eddies was able to produce the observed seasonal biological productivity and $pCO_{2\,(sw)}$ cycles in the Southern Ocean, but when the eddies were not included, the seasonal cycle was not well reproduced. Both the methods utilised and results from this study have

significant implications on the air-sea CO_2 flux for use in current global ESM, which parameterise the oceanographic effects of eddies (Hewitt et al., 2020, 2017). Eddy kinetic energy, as a proxy for mesoscale eddies, has been increasing at a rate between 2 and 5 % per decade (Martínez-Moreno et al., 2021), indicating that the role of mesoscale eddies on the oceanic CO_2 sink maybe becoming more significant. In the context of climate change and increasing global temperatures, further work is required to quantify whether this will reduce the capacity of eddies as a CO_2 sink.

Table 5.1 - The calculation of the modification to the South Atlantic CO_2 sink that mesoscale eddies may contribute. The median percentage change in the eddy flux compared to the surrounding environment is converted to a median Tg C yr^{-1} equivalent and compared to three estimates of the South Atlantic CO_2 sink in the region the eddies propagate.

	Anticyclonic	Cyclonic	
Median cumulative CO_2 flux (Fig. 5.1a, d; Tg C per eddy)	-0.54	-0.27	
Median percentage change in CO_2 flux (Fig. 5.3; %)	-3.7	-1.4	
Additional flux into eddy (Tg C per eddy)	-0.02	-0.004	
Mean eddy lifetime (yr)	2.5	1.7	
Additional flux into eddy per year (Tg C yr^{-1})	-0.008	-0.002	
Spawn Rate (yr)	6 (Guerra et al., 2018)	4 (Chaigneau et al., 2009)	
Additional flux into eddies (Tg C yr^{-1})	-0.05	-0.01	
			Total
Ford et al. (2022) (-76 Tg C yr^{-1}) 20 °S to 44 °S	-0.06 %	-0.02 %	-0.08 %
Woolf et al. (2019; Holding et al., 2019) (-261 Tg C yr^{-1}) 20 °S to 44 °S	-0.02 %	-0.005 %	-0.03 %
Takahashi et al. (2002) (-300 Tg C yr^{-1}) 14 °S to 50 °S	-0.01 %	-0.006 %	-0.02 %

5.5 Conclusions

Our analysis presents a novel approach to assess the impact of long-lived mesoscale eddies on the air-sea CO_2 flux in the South Atlantic Ocean. Using satellite observations and Lagrangian tracking we show that anticyclonic and cyclonic eddies are cumulative net CO_2 sinks of 0.54 Tg C and 0.27 Tg C per eddy, respectively. Anticyclonic eddies exhibited an exponential decay in the rate of CO_2 uptake, and significant changes in the thermal to non-thermal drivers of the $pCO_{2\,(sw)}$ ratio anomaly. This suggests a reduction in the role of biology to the CO_2 sink as the eddies age and propagation over different geographic trajectories in the South Atlantic gyre. The cyclonic eddies showed a more linear rate of CO_2 uptake, and there was no significant change in the drivers of the seasonal $pCO_{2\,(sw)}$ ratio anomaly.

Both anticyclonic and cyclonic eddies amplified the CO_2 sink into the South Atlantic Ocean significantly by 3.7 % and 1.4 %, respectively. For the anticyclonic eddies, physical drivers acted to increase the CO_2 sink, whereas the biological component worked to oppose the uptake. In cyclonic eddies both physical and biological components worked synergistically to increase the CO_2 sink.

In combination, these mesoscale eddies could amplify the CO_2 sink into the South Atlantic Ocean (20 °S to 44 °S) by 0.08 %. Although this modification appears subtle, these long-lived eddies make up only 0.4 % of eddies in the global ocean, and therefore the amplification of the global CO_2 sink from all eddies is likely to be much larger than previously estimated. Therefore, the inclusion of these mesoscale features within models used to estimate the global ocean carbon sink could be important.

Appendices

Appendix 5.1 – Eddy tracking example

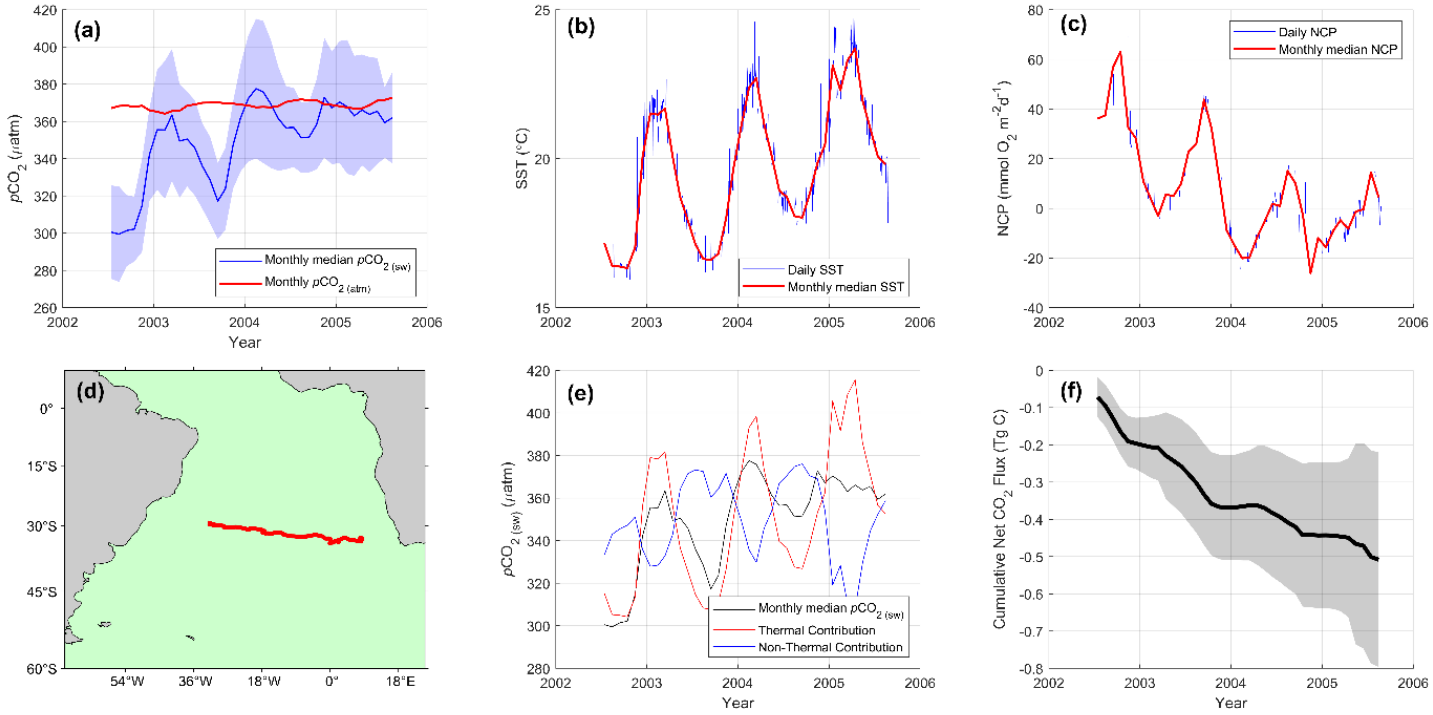

Figure A5.1 - Example output from the Lagrangian eddy tracking approach for an anticyclonic eddy. (a) Blue line indicates the monthly $pCO_{2\ (sw)}$ estimated with the SA-FNN_{NCP}, and shading indicates the uncertainty on the SA-FNN_{NCP} retrieval. Red line indicates the monthly atmospheric pCO_2 for the mean location of the eddy in the respective month. (b) Blue line indicates the daily sea surface temperature (SST) for the eddy lifetime. Red line shows the calendar month medians of SST. (c) Blue line indicates the daily net community production (NCP) for the eddy lifetime. Red line shows the calendar month medians of NCP. (d) Red line shows the geographic track of the eddy over the lifetime. (e) Black line indicates the monthly $pCO_{2\ (sw)}$. Red line indicates the thermal contribution and blue line indicates the non-thermal contribution to the $pCO_{2\ (sw)}$ variability. (f) Black line shows the cumulative net CO_2 flux, where the shading indicates he 95% confidence interval.

Appendix 5.2 – Comparison of SA-FNN$_{NCP}$ and in situ $pCO_{2\ (sw)}$ within mesoscale eddies

The global ocean ship-based hydrographic investigations program (GO-SHIP) research cruises conduct hydrographic observations which include Dissolved Inorganic Carbon (DIC) and Total Alkalinity (TA) along CLIVAR/WOCE repeat hydrographic sections. Transects within the South Atlantic Ocean between 2002 and 2018 were downloaded from the NODC/NOAA data centre (https://www.ncei.noaa.gov/access/ocean-carbon-data-system/oceans/RepeatSections/, last accessed: 29/09/2021), which included sections A10 (2003; 2011; 2017), A9.5 (2009; 2018), A13.5 (2013) and A16S (2005; 2013; Fig. A5.2 a). Each transect was analysed for measurements which coincided with anticyclonic or cyclonic eddies tracked in this study. $pCO_{2\ (sw)}$ was calculated from DIC and TA using CO2SYSv3 (Sharp et al., 2021; van Heuven et al., 2011; Orr et al., 2018; Lewis et al., 1998), and the reported uncertainties in DIC (~2 µmolkg^{-1}), TA (~2 µmolkg^{-1}), carbonic acid (Waters et al., 2014) and H_2SO_4 dissociation constants (Dickson, 1990) were propagated to retrieve the $pCO_{2\ (sw)}$ uncertainty. The in situ $pCO_{2\ (sw)}$ were corrected to a consistent temperature and depth dataset (Reynolds et al., 2002), following the methodology described in Goddijn-Murphy et al. (2015), to be consistent with the SA-FNN$_{NCP}$ sub skin $pCO_{2\ (sw)}$ observations (Woolf et al., 2016).

The Following Ocean Rings in the South Atlantic (FORSA) cruise, sampled six anticyclonic eddies with a continuous underway $pCO_{2\ (sw)}$ system, described in Orselli et al. (2019b). These $pCO_{2\ (sw)}$ observations were reanalysed to a consistent temperature and depth dataset (Reynolds et al., 2002; Goddijn-Murphy et al., 2015) using the “fe_reanalyse_socat.py” functions within the open source FluxEngine (Shutler et al., 2016; Holding et al., 2019), and the cruise track analysed for anticyclonic and cyclonic eddies tracked in this study. The mean and standard deviation of in situ $pCO_{2\ (sw)}$ for matching eddies were extracted for the region within the AVISO+ eddy radius.

In total six anticyclonic (GO-SHIP = 4; FORSA = 2; Fig. A5.2 a) and two cyclonic (GO-SHIP = 1; FORSA = 1; Fig. A5.2 b) eddies tracked in this study were sampled in situ. The in situ $pCO_{2\ (sw)}$ were compared with the SA-FNN$_{NCP}$ $pCO_{2\ (sw)}$ estimates for the month the eddy was sampled in situ (Fig. A5.2 c). The SA-FNN$_{NCP}$ $pCO_{2\ (sw)}$ estimates were accurate compared to the $pCO_{2\ (sw)}$ in

anticyclonic eddies with a low root mean square difference(RMSD; 10.2 µatm; Fig. A5.2 c) but showed a higher RMSD for the cyclonic eddies (20.9 µatm; Fig A5.2 c), although this was lower than the SA-FNN$_{NCP}$ accuracy (21.48 µatm).

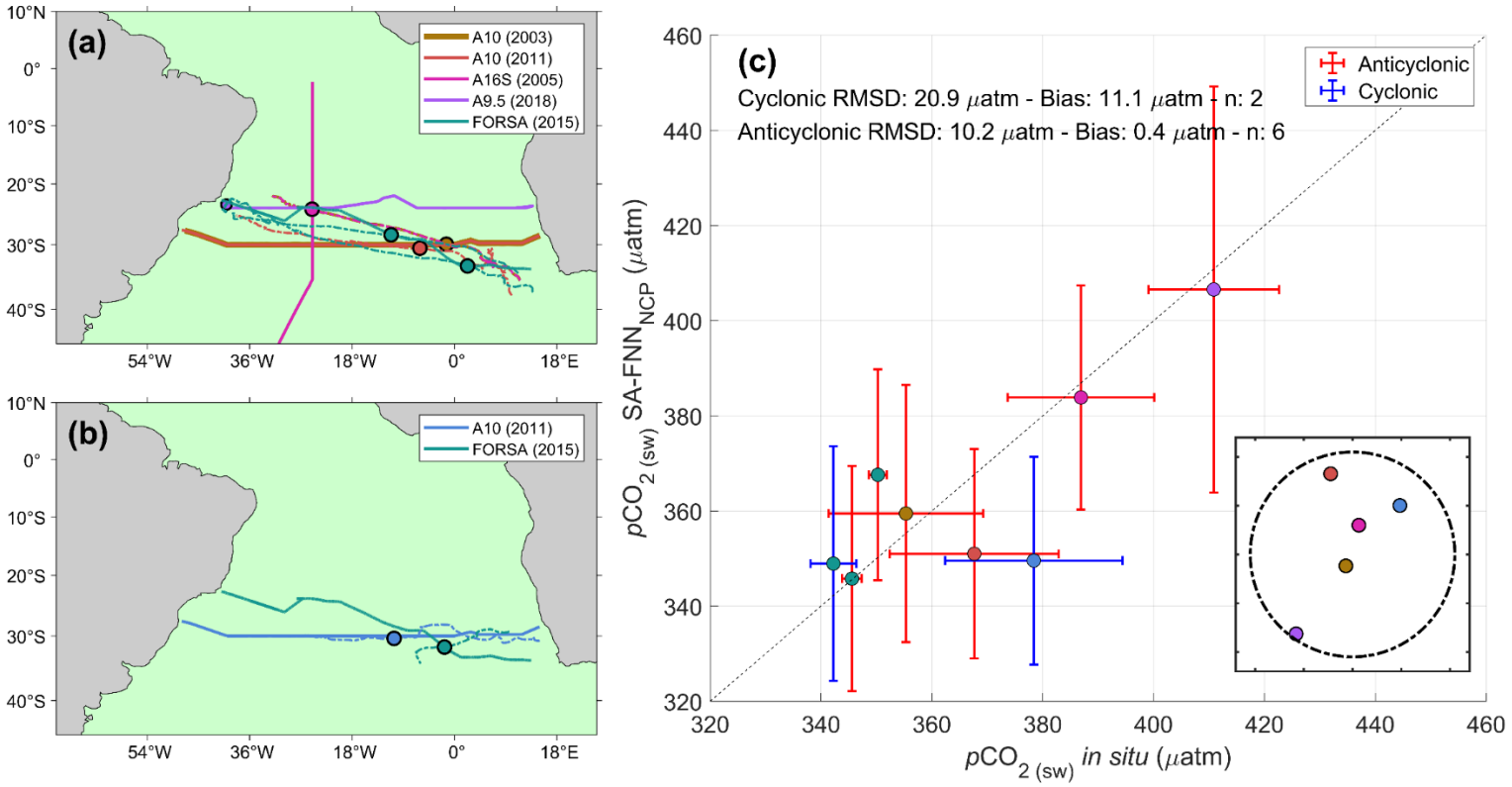

Figure A5.2 - (a) Dashed coloured lines indicate the trajectories of tracked anticyclonic eddies that were sampled in situ, where the sampling location is highlighted by the same coloured point. Solid coloured lines indicate cruise tracks which sampled the respective eddy. (b) Same as (a) but for cyclonic eddies. (c) Comparision of in situ $pCO_{2\ (sw)}$ with SA-FNN_{NCP} $pCO_{2\ (sw)}$ for anticyclonic (red errorbars) and cyclonic eddies (blue errorbars). Central coloured point represents the respective eddy sampled in (a) or (b). In plot statistics are root mean square deviation (RMSD), bias and the number of eddies (n). Inset indicates an eddy centric diagram identifying the location the in situ stations sampled (coloured points) with respect to the eddy radius (dashed line). Note the FORSA cruise sampled $pCO_{2\ (sw)}$ continuously and therefore does not appear on the inset.

Appendix 5.3 – Are mesoscale eddies distinct from their environment?

Daily anomalies in MODIS-A SST, SSS and NCP within both anticyclonic and cyclonic eddies were calculated with respect to the environmental conditions surrounding the eddy (described in section 5.2.2). The daily anomalies were fit with a 'smoothing spline' function within MATLAB (smoothing parameter = 4.14×10^{-7}) to identify the longer term variations in the anomalies for each eddy (Fig. A5.3; Fig. A5.4).

The anticyclonic eddies generally showed initial positive SST (Fig. A5.3a) and SSS (Fig. A5.3b) anomalies, which were converted to negative SST anomalies within ~6 months from the start of eddy tracking. The strength of negative SST anomalies were generally greater in austral winter, than summer. SSS anomalies indicated a linear decrease over time, as the eddy moved into the South Atlantic gyre. The cyclonic eddies showed initial negative SST anomalies which rapidly increase to ~ 0, but with seasonal fluctuations (Fig. A5.3 c). The SSS anomalies however showed no clear pattern and were generally weak (Fig.A5.3 d).

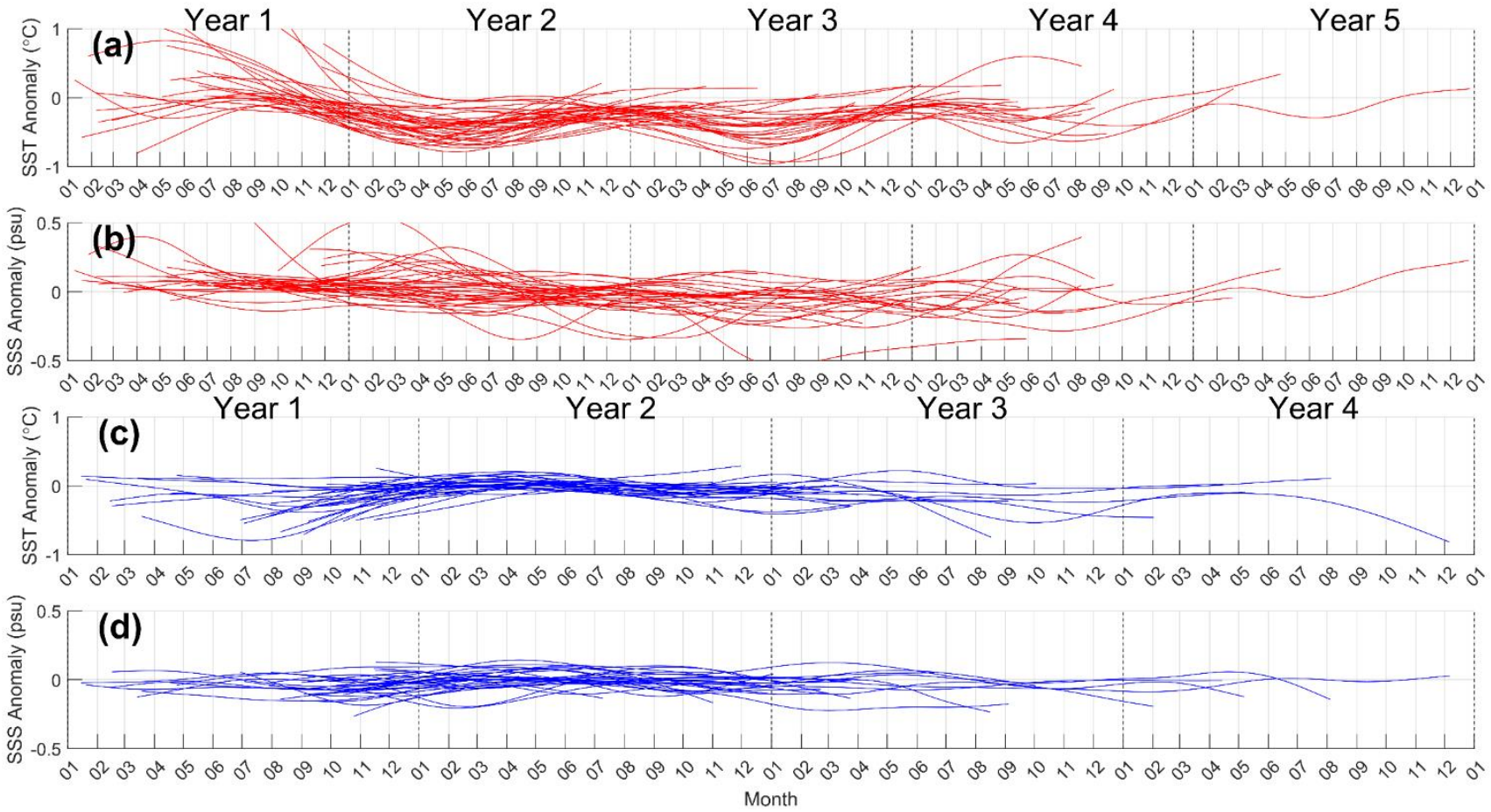

Figure A5.3 - Smoothed anomalies in physical parameters (SST and SSS) within mesoscales eddies with respect to the environmental conditions. (a) and (c) show SST anomalies for anticyclonic and cyclonic eddies respectively. (b) and (d) show SSS anomalies for Agulhas and cyclonic eddies respectively.

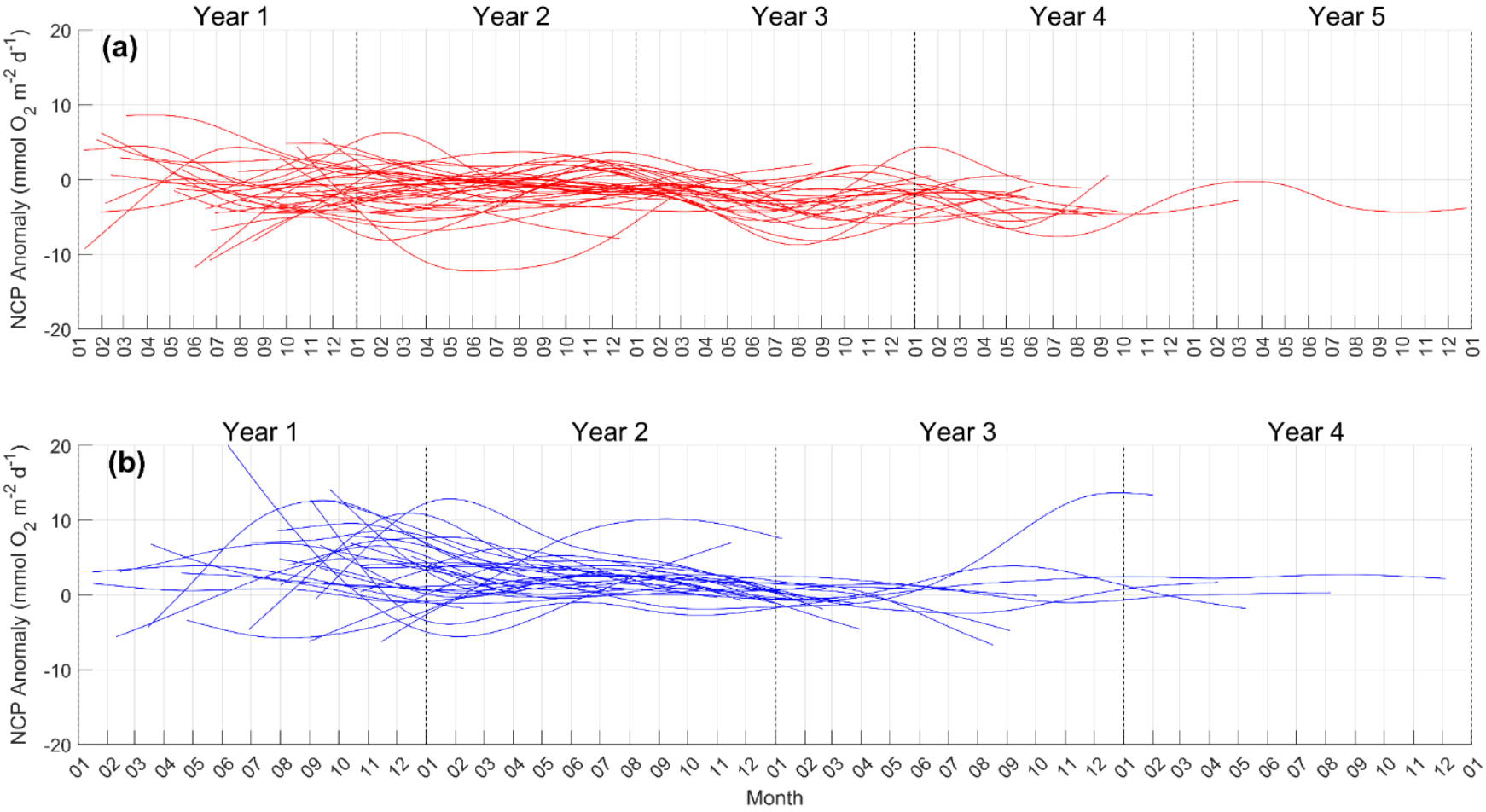

Figure A5.4 - Smoothed anomalies in NCP within mesoscale eddies with respect to the environmental conditions. (a) shows the NCP anomalies for anticyclonic eddies, and (b) the same for cyclonic eddies.

Chapter 6: General discussion and future directions

With the onset of the United Nations decade of ocean science (2021 – 2030), the role of biology in the global ocean CO_2 sink, and how it is changing was highlighted as a key issue to address by the IOC-R (Aricò et al., 2021). This thesis set out to understand the plankton contribution to the air-sea CO_2 flux and its variability using satellite and in situ observations in the South Atlantic Ocean.

6.1 Observing plankton from space using satellite ocean colour

Satellite ocean colour provide synoptic scale estimates of phytoplankton pigments and productivity globally (Behrenfeld et al., 2006; Kahru et al., 2010). MODIS-A is the longest single sensor ocean colour record (2002 to present; 20 years at the time of this thesis), however NASA have launched multiple ocean colour sensors, including SeaWiFS (1997 to 2010) and two Visible Infrared Imaging Radiometer Suites (VIIRS; VIIRS SNNP: 2012 to present; VIIRS-JPSS1: 2017 to present). In parallel the European Space Agency (ESA) also launched a series of ocean colour sensors that included the Medium Resolution Imaging Spectroradiometer (MERIS; 2002 to 2012) and more recently, two Ocean and Land Colour Instruments (OLCI; S3A: 2016 to present; S3B: 2018 to present). Individually these sensors provide useful observations but by merging (bias correcting and cross-calibrating) individual sensors into a coherent continuous record has provided a long climate data record timeseries (Sathyendranath et al., 2019). These individual sensors and merged products (Maritorena et al., 2010; Sathyendranath et al., 2019) all require continual accuracy assessments, especially when operating outside their designed lifetimes (e.g. MODIS designed lifetime was 6 years) and/or when individual sensor teams provide updated dataset versions.

The accuracy of MODIS-A has continually been assessed throughout its lifetime in many studies (Dogliotti et al., 2014, 2009; Kampel et al., 2009b, a; Garcia et al., 2005; Brewin et al., 2016) however these assume the in situ observations are “100% accurate”, or truth, which is not feasible. The same situation is true for the limited number of accuracy assessments of merged ocean colour products (Brewin et al., 2015; Maritorena et al., 2010; Sathyendranath et al., 2019). Chapter 2 (Ford et al., 2021a) assessed the accuracy of MODIS-A Chl *a*,

NPP and NCP in the South Atlantic Ocean, whilst accounting for uncertainties in the in situ measurements. The in situ observation uncertainties were accounted for using weighted statistics (an established statistical method), which showed that uncertainties in the in situ measurements were negatively influencing the resulting estimates of the satellite observation accuracy and precision. At the time of this thesis, Mckinna et al. (2021) also used a weighting scheme to account for in situ uncertainties when developing and assessing the accuracy of particulate backscattering coefficient algorithms. Both the approaches apply weighted statistics and highlighted that accounting for in situ observation uncertainties provides a more equitable assessment and identified that the satellite approaches were actually performing better than previously thought.

The approach of accounting for in situ observation uncertainties should be applied when evaluating satellite accuracy and bias more widely. However, current global datasets of Chl *a* which have been complied to assess the accuracy of satellite observations (Valente et al., 2019, 2016; Werdell and Bailey, 2005) do not contain the necessary in situ data uncertainties. There is a clear desire from space agencies to include in situ uncertainties within datasets used for satellite validation, and more recently this desire can be seen in the formation of Fiducial reference measurements (FRM) datasets. These are in situ observations that are traceable to standards, referenced to inter-comparison exercises and with a full uncertainty budget (Banks et al., 2020). In the future it is likely satellite accuracy assessments will only use datasets that include in situ uncertainties meaning that weighted statistics can be used.

Mckinna et al. (2021) showed these in situ uncertainties can also be accounted for within the development of new algorithms. This is especially important for NCP algorithms, since for both NPP and NCP the uncertainties are unlikely to be consistent. Weighted statistics could also be applied within algorithm intercomparisons. Brewin et al. (2015) identified the most accurate algorithms for a range of ocean colour based parameters using a statistical point based system. The statistics applied could be exchanged for weighted variants to account for the in situ uncertainties but this would require that these be included within the in situ observation datasets.

6.2 Biological contribution to $pCO_{2\,(sw)}$ and air-sea CO_2 flux

Chapter 3 showed that the SA-$FNN_{NO\text{-}BIO}$ variants were not able to fully reproduce the variability of $pCO_{2\,(sw)}$ in the South Atlantic Ocean. Watson et al. (2020b) produced global $fCO_{2\,(sw)}$ fields using a SOM-FNN that used only physical parameters as input, similar to the SA-$FNN_{NO\text{-}BIO\text{-}2}$. These results suggest that using only physical parameters to extrapolate $pCO_{2\,(sw)}$ observations cannot fully represent the biological contribution to $pCO_{2\,(sw)}$ variability. Global $pCO_{2\,(sw)}$ extrapolation schemes have also included Chl *a* as a biological proxy (Landschützer et al., 2014; Denvil-Sommer et al., 2019), and therefore include a representation of the biological contribution to $pCO_{2\,(sw)}$. Schloss et al. (2007) showed a weak linear relationship between NCP and Chl *a* on the southwestern Atlantic shelf, highlighting that Chl *a* can act as a proxy for NCP. However, Chapter 3 showed the SA-FNN_{CHLA} was not able to fully represent the $pCO_{2\,(sw)}$ in the South Atlantic Ocean but did improve on the SA-$FNN_{NO\text{-}BIO}$ variants. This improvement is likely due to Chl *a* acting as proxy for NCP (Schloss et al., 2007), but does not quantify variations in photosynthesis and respiration that are modulated by other environmental conditions, such as temperature, nutrient and light availability.

NCP, as the biological contribution to $pCO_{2\,(sw)}$ variability, improved the estimation of $pCO_{2\,(sw)}$ and modified the regional air-sea CO_2 fluxes in the South Atlantic Ocean as shown in Chapter 3 (Ford et al., 2022). Although the SA-FNN_{NCP} had a similar accuracy (21.56 µatm) compared to the other SA-FNN variants, it was shown to accurately reproduce the $pCO_{2\,(sw)}$ as measured by independent buoy observations and literature descriptions. Therefore, the incorporation of NCP into global $pCO_{2\,(sw)}$ extrapolation schemes is the next step to improving the biological contribution to the global ocean CO_2 sink estimates.

The satellite based NCP algorithms evaluated in Chapter 2 were developed using in situ observations in the Atlantic Ocean (Tilstone et al., 2015b). Serret et al. (2015) showed differences in the NPP to respiration scaling between the North and South Atlantic Oceans, which also varied seasonally. Therefore, it cannot be assumed that the same algorithms presented for the Atlantic Ocean

will be applicable to other ocean basins. A comparison of the best performing NCP algorithms from Chapter 2 (NCP-C and NCP-D) driven using in situ observations from the Hawaii Ocean Timeseries (HOTS; https://hahana.soest.hawaii.edu/hot/) suggests differences in the NPP to NCP scaling between the North Pacific and Atlantic Oceans (Fig. 6.1). This may be due to differences in the respiration rates, as NCP tends to be lower at HOTS (Fig. 6.1a) for NPP rates observed in the Atlantic Ocean. The observed bias when applying NCP-D (Fig. 6.1b) to these in situ observations reinforces this evaluation. This is beyond the scope of this thesis, but highlights that applying these NCP algorithms to other ocean basins needs to be taken with caution. Until a more extensive global database of NCP observations is available to assess the accuracy of these algorithms, the use of NCP for global $pCO_{2\,(sw)}$ extrapolation may be hindered.

Chapter 3 highlighted that reducing satellite NCP uncertainties would provide the greatest reduction in the uncertainty of $pCO_{2\,(sw)}$, and these estimates were verified with in situ observations from the AMT cruises. Chapter 2 showed that 40% of the satellite NCP uncertainties were due to the NPP algorithm. This suggests that improvements in satellite NPP estimation will lead to further improvements in $pCO_{2\,(sw)}$ estimates from NCP. These could be achieved through improvements in the estimation of the water column light field (Sathyendranath et al., 2020), assignment of photosynthetic rates or vertical variability in input parameters (Kulk et al., 2020), for example. The use of autonomous platforms, such as Bio-Argo profilers (Roemmich et al., 2019), could provide important information on the spatial and vertical distribution of parameters that can synergistically be applied to satellite observations. Lee et al. (2015) provide a thorough review on improving satellite NPP estimates, and provide a strategic assessment on where efforts should be focused.

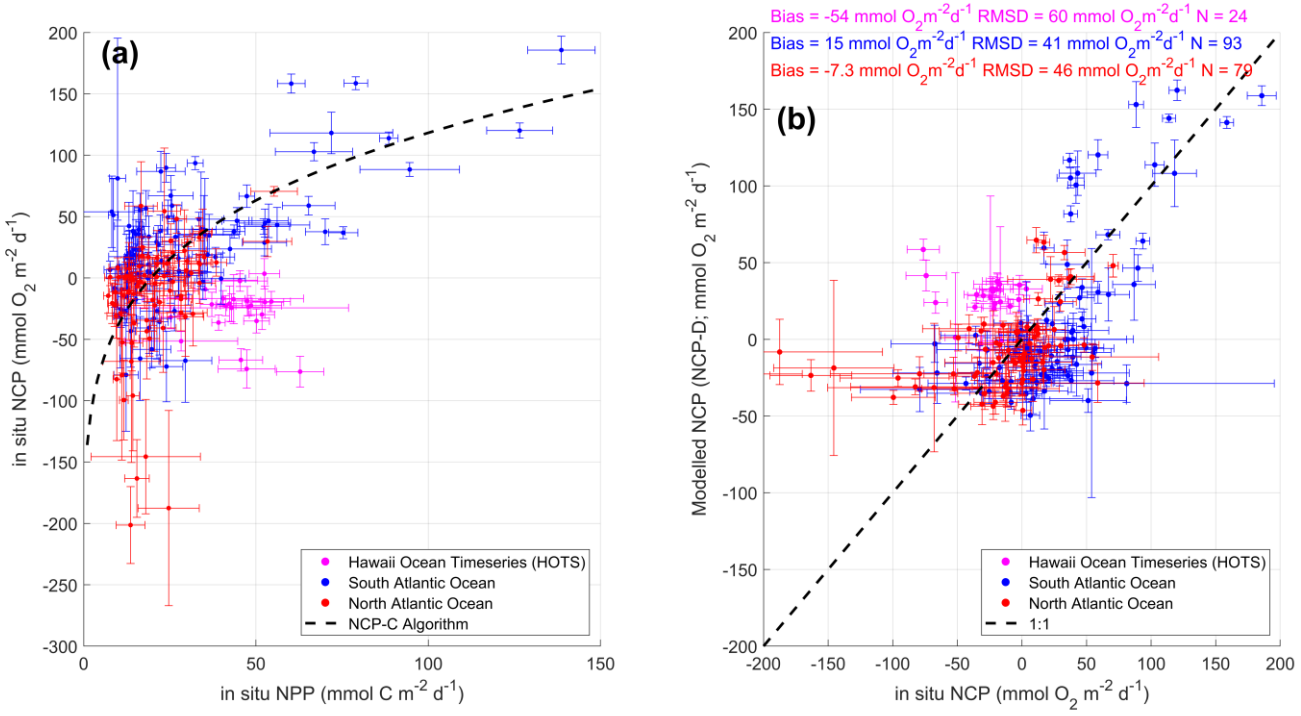

Figure 6.1 - (a) Power law relationship between in situ NPP (mmol C $m^{-2}d^{-1}$) and NCP (mmol O_2 $m^{-2}d^{-1}$) using NCP-C algorithm (black dashed line) tested in the Chapter 2. Blue points indicate in situ data presented in Chapter 2 for the South Atlantic Ocean. Red points indicate data from the AMT cruises in the North Atlantic Ocean removed from the Chapter 2 analysis. Magenta points indicate in situ observations at the Hawaii Ocean Timeseries (HOTS), downloaded from https://hahana.soest.hawaii.edu/hot/ (last accessed: 04/05/2022). Horizontal error-bars indicate the per station in situ NPP uncertainty, and vertical error-bars indicate the per station NCP uncertainty. (b) Comparision of in situ NCP observations against modelled NCP using NCP-D driven with in situ observations from the regions in (a). Horizontal error-bars indicate the in situ NCP uncertainty, and vertical error-bars indicate the uncertainty in modelled NCP by propagating uncertainties in NPP (variable) and SST (assumed to be 0.01 °C). The NCP-D algorithm uncertainty (35 mmol O_2 $m^{-2}d^{-1}$) was not incorporated into the overall uncertainty to improve visibility of points in the figure. Statistics in figure are Bias and Root Mean Square Deviation (RMSD).

Improving NCP estimates from satellite observations could also be achieved by explicitly quantifying respiration variability. Serret et al. (2015) showed NCP is determined by changes in both respiration and NPP. The satellite NCP algorithm applied in this thesis accounts for some of the respiration heterogeneity through an empirical NCP to SST relationship (Tilstone et al., 2015b). However by assessing the performance of NCP-D at HOTS (Fig. 6.1) this relationship may not account for respiration variability both in the South Atlantic and globally. Semi-analytical models could improve on empirical estimates by dynamically adjusting NPP to NCP relationships to account for respiration variability (Serret et al., 2015, 2009), and therefore become globally applicable. However, this still requires increased in situ observations globally to tune these models and therefore a concerted effort to understand respiration variability in the surface oceans is required.

6.3 Plankton induced variability in the air-sea CO_2 flux

Chapter 4 investigated the drivers of the air-sea CO_2 flux at different timescales using the SA-FNN$_{NCP}$ $pCO_{2\,(sw)}$ estimates and highlighted that biology contributed to seasonal, interannual and long term trends in the air-sea CO_2 flux. On seasonal timescales, the analysis was consistent with previous studies (Takahashi et al., 2002; Landschützer et al., 2013) showing that SST is a dominant driver in the subtropics, and biology and circulation control in the Equatorial and subpolar regions. On interannual timescales, biological induced variability in the air-sea CO_2 flux was observed that could be linked to the MEI. Chapter 2 showed a response in NCP to the El Niño South Oscillation (ENSO) but this was at the limits of the uncertainties in satellite NCP.

The interannual variability and long-term trends in Chapter 4 could be attributed to changes in biological activity, induced by changes in circulation. For example, offshore from the Benguela upwelling system strong negative trends in the CO_2 flux (i.e an increasing CO_2 sink) were observed (Fig. 4.5b). This trend was linked to changes in biological activity as observed by Kulk et al. (2020), that could be driven by increasing nutrient export offshore through changes in circulation and mesoscale eddies (Rubio et al., 2009; Xiu et al., 2018). Therefore, it may be difficult to decompose the two signals separately when

determining the contributions of biology and circulation due to the linkages between them. DeVries (2022) showed that ocean circulation and biological activity are more important than the rise in atmospheric CO_2 concentrations and changes in SST for driving decadal variability in the global CO_2 sink. It is therefore clear that NCP cannot be assumed to be steady state in both $pCO_{2\,(sw)}$ extrapolation schemes and when assessing the seasonal, interannual and decadal variability of the ocean CO_2 sink.

6.4 Mesoscale eddies in the oceans

The role that mesoscale eddies contribute to variability in the global ocean is an active area of research due to their ability to modify and transport physical, biological and chemical properties within the oceans (Chen et al., 2007; Orselli et al., 2019b, a; Pezzi et al., 2021; Souza et al., 2021; Lovecchio et al., 2022; Laxenaire et al., 2019; Nencioli et al., 2018). Long lived mesoscale eddies were shown in Chapter 5 to enhance the air-sea CO_2 sink with respect to the surrounding waters, using a novel Lagrangian tracking approach that implemented the SA-FNN_{NCP}. Long lived mesoscale eddies make up only 0.4 % of the AVISO+ mesoscale trajectories dataset (Pegliasco et al., 2022), and the enhancement of the CO_2 sink by eddies globally could be significant.

This approach could therefore be applied to shorter lived and assess a larger proportion of these mesoscale eddies providing an opportunity to investigate the total effect of all eddies on the air-sea CO_2 flux in the South Atlantic Ocean but could also be expanded globally.

However, the expansion of the approach requires in situ observations of $pCO_{2\,(sw)}$ to further assess the accuracy of the SA-FNN_{NCP} within mesoscale eddies. Chapter 5 showed the SA-FNN_{NCP} $pCO_{2\,(sw)}$ was accurate within eddies, however this was based on a small number of in situ observations (n = 8). The sampling of eddies on research cruises is generally unintentional, except in a few cases (e.g. Following Ocean Rings in the South Atlantic; FORSA), and following a single eddy over its lifetime is also unfeasible. The use of autonomous platforms could provide the increase in observations that is needed. For example, the physical properties of Agulhas eddies have been tracked with Argo profiles that become entrained within the eddy for a period,

allowing for the evolution of the eddy physical properties to be evaluated (Laxenaire et al., 2019). Chemical properties of an Agulhas eddy have been sampled by a Bio-Argo profiler (Nencioli et al., 2018). The increasing number of Bio-Argo profilers (Roemmich et al., 2019), especially those with pH sensors, will provide valuable in situ observations to assess $pCO_{2\,(sw)}$ within mesoscale eddies.

The results of Chapter 5 also have implications for current Earth System Models (ESM), where eddy induced modifications to oceanographic fields are generally parameterised. Harrison et al. (2018) showed that mesoscale resolving models may have a small effect on global balance of carbon export (< 2%), but regionally this effect can be large (± 50%). This is particularly important for ESMs used to assess future climate change under different emission targets (Coupled Model Intercomparison Project Phase 6; CMIP6) which are used to inform the IPCC assessment reports (IPCC, 2021). The parameterisation of mesoscale eddies within these models could neglect changes in eddy activity, which has been increasing (Martínez-Moreno et al., 2021), and whether this modification of the air-sea CO_2 flux by eddies is changing with time.

Mesoscale eddies are contained water masses that can be tracked through satellite altimetry fields (Pegliasco et al., 2022; Mason et al., 2014). But the waters outside of the eddies are also advected by the surface currents and geostrophic flows in the oceans. These waters can travel large distances through the ocean in a single month and move through difference biogeochemical regions (Fig. 6.2). The desire for higher temporal and spatial resolution $pCO_{2\,(sw)}$ datasets may rely on the use of Lagrangian tracking of surface waters, to understand the processes that have previously acted on the water mass. This is particularly important for biological activity, where the signature of previous biological drawdown can be maintained on the order of months (Broecker and Peng, 1974). Dall'Olmo et al. (2021) produced daily global Lagrangian trajectories that could be applied within a $pCO_{2\,(sw)}$ extrapolation, to incorporate the processes that have previously acted on the surface water, for example, the biological "history". This could be a promising approach to increase the spatial and temporal resolution of current $pCO_{2\,(sw)}$ extrapolation approaches.

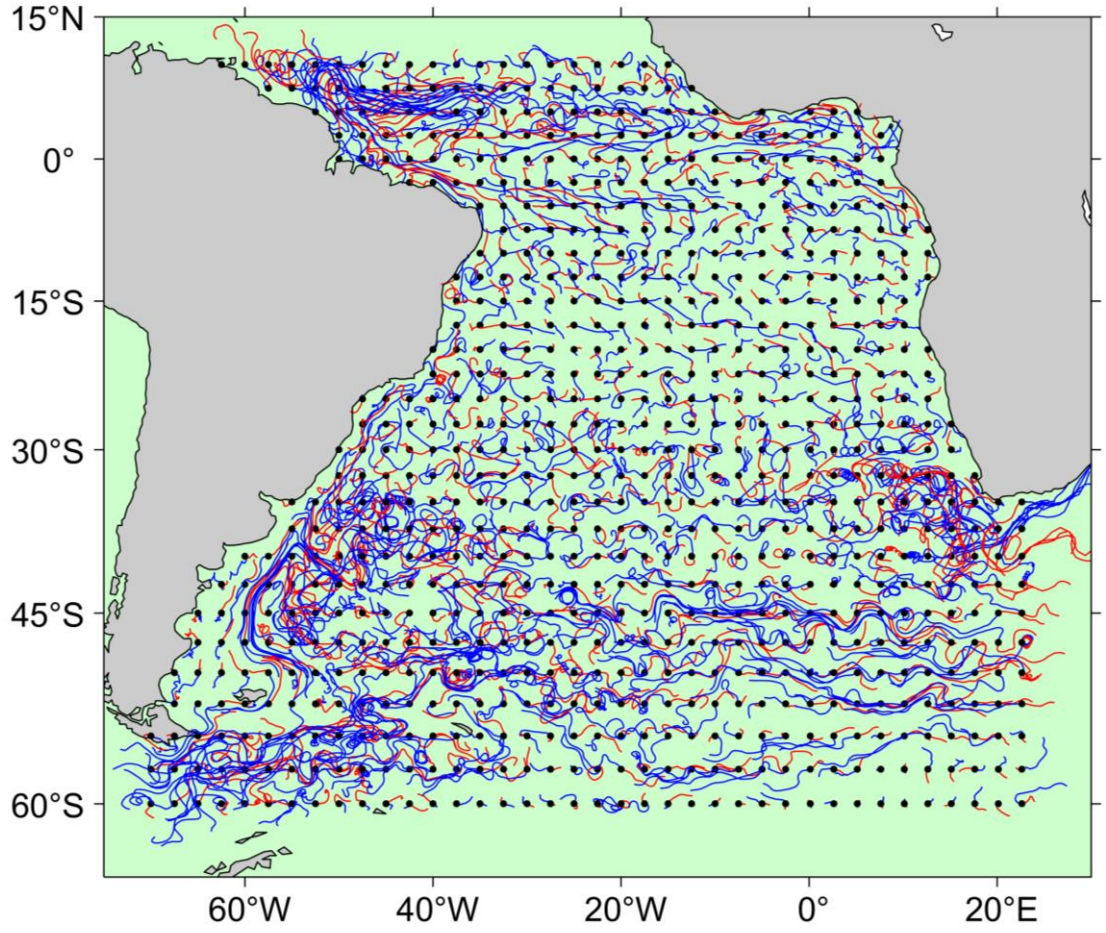

Figure 6.2 - Lagrangian trajectories of surface water for 1st January 2010 from the ocean Lagrangian trajectories (OLTraj) dataset (Dall'Olmo et al., 2021) in the South Atlantic Ocean. Black dots indicate the initial location, spaced at 3° intervals. Blue lines indicate the 1 month backwards trajectory (i.e where the water mass has travelled from). Red lines indicate the 1 month forward trajectory (i.e where the water mass will travel to).

6.5 Conclusions and future work

This thesis has shown that the plankton community in the oceans plays a key role in the CO_2 sink in the South Atlantic Ocean, and this is likely similar across the global oceans. Chapter 2 illustrated that NCP can be accurately estimated from satellite observations. Chapter 3 showed that including NCP within a $pCO_{2\,(sw)}$ extrapolation scheme improved the complete fields of $pCO_{2\,(sw)}$ and modified the regional air-sea CO_2 flux. Chapter 4 highlighted interannual and long-term variability in the air-sea CO_2 flux could be attributed to changes in NCP.

Chapter 5 indicated that mesoscale eddies are important in modifying the air-sea CO_2 flux, and this can be through the mesoscale modification of NCP.

As a result of the advancements and findings of this thesis, recommendations for future work are presented in the following research questions:

From Chapter 2:

- Are NCP algorithms for the Atlantic Ocean applicable globally?
- What is the effect of in situ uncertainties on the global performance of Chl *a*, NPP and NCP algorithms?
- How does plankton respiration vary in the global ocean? Can respiration be quantified or estimated from satellite observations?
- Are regions of plankton autotrophy becoming more or less prevalent?
- What is the performance of NCP algorithms when applied to climate data records of ocean colour data (The only one of which is the European Space Agency Ocean Colour Climate Change Initiative; OC-CCI)?
- What is the effect of accounting for in situ observation uncertainties when developing new NCP algorithms? Are current algorithms biased by uncertain in situ observations used during their development?

From Chapter 3:

- To what extent does including NCP in global $pCO_{2\,(sw)}$ extrapolation schemes modify the global ocean CO_2 sink?
- Can $pCO_{2\,(sw)}$ estimates be improved by including in situ buoy observations into the SA-FNN? Does this improve the $pCO_{2\,(sw)}$ estimates in the Equatorial Atlantic?

From Chapter 4:

- What is the contribution of biological activity to interannual and decadal changes in the global ocean CO_2 sink?
- Are there instances where changes in global biological activity are more important than changes in ocean circulation in controlling the variability in the ocean CO_2 sink? Are these processes tightly coupled?

From Chapter 5:

- What is the contribution of long-lived mesoscale eddies to the global ocean CO_2 sink?
- What is the contribution of all mesoscale eddies to the South Atlantic CO_2 sink?
- Can Lagrangian tracking of surface waters improve the temporal and spatial resolution of $pCO_{2\,(sw)}$ estimates?
- Does the increased air-sea CO_2 flux into Agulhas eddies account for their higher levels of anthropogenic carbon, as proposed by Orselli et al. (2019a)?

References

Aguiar, A. L., Cirano, M., Marta-Almeida, M., Lessa, G. C., and Valle-Levinson, A.: Upwelling processes along the South Equatorial Current bifurcation region and the Salvador Canyon (13°S), Brazil, Cont. Shelf Res., 171, 77–96, https://doi.org/10.1016/j.csr.2018.10.001, 2018.

Aguirre, C., Rojas, M., Garreaud, R. D., and Rahn, D. A.: Role of synoptic activity on projected changes in upwelling-favourable winds at the ocean's eastern boundaries, npj Clim. Atmos. Sci., 2, 44, https://doi.org/10.1038/s41612-019-0101-9, 2019.

Amari, S. I., Murata, N., Müller, K. R., Finke, M., and Yang, H. H.: Asymptotic statistical theory of overtraining and cross-validation, IEEE Trans. Neural Networks, 8, 985–996, https://doi.org/10.1109/72.623200, 1997.

Araujo, M., Noriega, C., Medeiros, C., Lefèvre, N., Ibánhez, J. S. P., Flores Montes, M., Silva, A. C. da, and Santos, M. de L.: On the variability in the CO_2 system and water productivity in the western tropical Atlantic off North and Northeast Brazil, J. Mar. Syst., 189, 62–77, https://doi.org/10.1016/j.jmarsys.2018.09.008, 2019.

Arhan, M., Speich, S., Messager, C., Dencausse, G., Fine, R., and Boye, M.: Anticyclonic and cyclonic eddies of subtropical origin in the subantarctic zone south of Africa, J. Geophys. Res. Ocean., 116, 1–22, https://doi.org/10.1029/2011JC007140, 2011.

Aricò, S., Arrieta, J. M., Bakker, D. C. E., Boyd, P. W., Cotrim da Cunha, L., Chai, F., Dai, M., Gruber, N., Isensee, K., Ishii, M., Jiao, N., Lauvset, S. K., McKinley, G. A., Monteiro, P., Robinson, C., Sabine, C., Sanders, R., Schoo, K. L., Schuster, U., Shutler, J. D., Thomas, H., Wanninkhof, R., Watson, A. J., Bopp, L., Boss, E., Bracco, A., Cai, W., Fay, A., Feely, R. A., Gregor, L., Hauck, J., Heinze, C., Henson, S., Hwang, J., Post, J., Suntharalingam, P., Telszewski, M., Tilbrook, B., Valsala, V., and Rojas, A.: Integrated Ocean Carbon Research: A Summary of Ocean Carbon Research, and Vision of Coordinated Ocean Carbon Research and Observations for the Next Decade., edited by: Wanninkhof, R., Sabine, C., and Aricò, S., UNESCO, Paris, 46 pp., https://doi.org/10.25607/h0gj-pq41, 2021.

Arnone, V., González-Dávila, M., and Magdalena Santana-Casiano, J.: CO_2 fluxes in the South African coastal region, Mar. Chem., 195, 41–49, https://doi.org/10.1016/j.marchem.2017.07.008, 2017.

Bailey, S. W. and Werdell, P. J.: A multi-sensor approach for the on-orbit validation of ocean color satellite data products, Remote Sens. Environ., 102, 12–23, https://doi.org/10.1016/j.rse.2006.01.015, 2006.

Bakker, D. C. E., Pfeil, B., Landa, C. S., Metzl, N., O'Brien, K. M., Olsen, A., Smith, K., Cosca, C., Harasawa, S., Jones, S. D., Nakaoka, S. I., Nojiri, Y., Schuster, U., Steinhoff, T., Sweeney, C., Takahashi, T., Tilbrook, B., Wada, C., Wanninkhof, R., Alin, S. R., Balestrini, C. F., Barbero, L., Bates, N. R., Bianchi, A. A., Bonou, F., Boutin, J., Bozec, Y., Burger, E. F., Cai, W. J., Castle, R. D., Chen, L., Chierici, M., Currie, K., Evans, W., Featherstone, C., Feely, R. A.,

Fransson, A., Goyet, C., Greenwood, N., Gregor, L., Hankin, S., Hardman-Mountford, N. J., Harlay, J., Hauck, J., Hoppema, M., Humphreys, M. P., Hunt, C. W., Huss, B., Ibánhez, J. S. P., Johannessen, T., Keeling, R., Kitidis, V., Körtzinger, A., Kozyr, A., Krasakopoulou, E., Kuwata, A., Landschützer, P., Lauvset, S. K., Lefèvre, N., Lo Monaco, C., Manke, A., Mathis, J. T., Merlivat, L., Millero, F. J., Monteiro, P. M. S., Munro, D. R., Murata, A., Newberger, T., Omar, A. M., Ono, T., Paterson, K., Pearce, D., Pierrot, D., Robbins, L. L., Saito, S., Salisbury, J., Schlitzer, R., Schneider, B., Schweitzer, R., Sieger, R., Skjelvan, I., Sullivan, K. F., Sutherland, S. C., Sutton, A. J., Tadokoro, K., Telszewski, M., Tuma, M., Van Heuven, S. M. A. C., Vandemark, D., Ward, B., Watson, A. J., and Xu, S.: A multi-decade record of high-quality fCO_2 data in version 3 of the Surface Ocean CO_2 Atlas (SOCAT), Earth Syst. Sci. Data, 8, 383–413, https://doi.org/10.5194/essd-8-383-2016, 2016.

Banks, A. C., Vendt, R., Alikas, K., Bialek, A., Kuusk, J., Lerebourg, C., Ruddick, K., Tilstone, G., Vabson, V., Donlon, C., and Casal, T.: Fiducial reference measurements for satellite ocean colour (FRM4SOC), Remote Sens., 12, https://doi.org/10.3390/RS12081322, 2020.

Barlow, R., Cummings, D., and Gibb, S.: Improved resolution of mono- and divinyl chlorophylls a and b and zeaxanthin and lutein in phytoplankton extracts using reverse phase C-8 HPLC, Mar. Ecol. Prog. Ser., 161, 303–307, https://doi.org/10.3354/meps161303, 1997.

Bates, N. R., Astor, Y. M., Church, M. J., Currie, K., Dore, J. E., González-Dávila, M., Lorenzoni, L., Muller-Karger, F., Olafsson, J., and Santana-Casiano, J. M.: A time-series view of changing surface ocean chemistry due to ocean uptake of anthropogenic CO_2 and ocean acidification, 27, 126–141, https://doi.org/10.5670/oceanog.2014.16, 2014.

Behrenfeld, M. J. and Falkowski, P. G.: A consumer's guide to phytoplankton primary productivity models, Limnol. Oceanogr., 42, 1479–1491, https://doi.org/10.4319/lo.1997.42.7.1479, 1997a.

Behrenfeld, M. J. and Falkowski, P. G.: Photosynthetic rates derived from satellite-based chlorophyll concentration, Limnol. Oceanogr., 42, 1–20, https://doi.org/10.4319/lo.1997.42.1.0001, 1997b.

Behrenfeld, M. J. and Milligan, A. J.: Photophysiological Expressions of Iron Stress in Phytoplankton, Ann. Rev. Mar. Sci., 5, 217–246, https://doi.org/10.1146/annurev-marine-121211-172356, 2012.

Behrenfeld, M. J., Marañón, E., Siegel, D. A., and Hooker, S. B.: Photoacclimation and nutrient-based model of light-saturated photosynthesis for quantifying oceanic primary production, Mar. Ecol. Prog. Ser., 228, 103–117, https://doi.org/10.3354/meps228103, 2002.

Behrenfeld, M. J., O'Malley, R. T., Siegel, D. A., McClain, C. R., Sarmiento, J. L., Feldman, G. C., Milligan, A. J., Falkowski, P. G., Letelier, R. M., and Boss, E. S.: Climate-driven trends in contemporary ocean productivity, Nature, 444, 752–755, https://doi.org/10.1038/nature05317, 2006.

Behrenfeld, M. J., Westberry, T. K., Boss, E. S., O'Malley, R. T., Siegel, D. A.,

Wiggert, J. D., Franz, B. A., McClain, C. R., Feldman, G. C., Doney, S. C., Moore, J. K., Dall'Olmo, G., Milligan, A. J., Lima, I., and Mahowald, N.: Satellite-detected fluorescence reveals global physiology of ocean phytoplankton, 6, 779–794, https://doi.org/10.5194/bg-6-779-2009, 2009.

Behrenfeld, M. J., O'Malley, R. T., Boss, E. S., Westberry, T. K., Graff, J. R., Halsey, K. H., Milligan, A. J., Siegel, D. A., and Brown, M. B.: Revaluating ocean warming impacts on global phytoplankton, Nat. Clim. Chang., 6, 323–330, https://doi.org/10.1038/nclimate2838, 2016.

Benallal, M. A., Moussa, H., Lencina-Avila, J. M., Touratier, F., Goyet, C., El Jai, M. C., Poisson, N., and Poisson, A.: Satellite-derived CO_2 flux in the surface seawater of the Austral Ocean south of Australia, Int. J. Remote Sens., 38, 1600–1625, https://doi.org/10.1080/01431161.2017.1286054, 2017.

BIPM: Evaluation of measurement data—Guide to the expression of uncertainty in measurement., 2008.

Bonou, F. K., Noriega, C., Lefèvre, N., and Araujo, M.: Distribution of CO_2 parameters in the Western Tropical Atlantic Ocean, Dyn. Atmos. Ocean., 73, 47–60, https://doi.org/10.1016/j.dynatmoce.2015.12.001, 2016.

Bouman, H., Platt, T., Sathyendranath, S., and Stuart, V.: Dependence of light-saturated photosynthesis on temperature and community structure, Deep Sea Res. Part I Oceanogr. Res. Pap., 52, 1284–1299, https://doi.org/10.1016/j.dsr.2005.01.008, 2005.

Bouman, H. A., Platt, T., Doblin, M., Figueiras, F. G., Gudmundsson, K., Gudfinnsson, H. G., Huang, B., Hickman, A., Hiscock, M., Jackson, T., Lutz, V. A., Mélin, F., Rey, F., Pepin, P., Segura, V., Tilstone, G. H., van Dongen-Vogels, V., and Sathyendranath, S.: Photosynthesis–irradiance parameters of marine phytoplankton: synthesis of a global data set, Earth Syst. Sci. Data, 10, 251–266, https://doi.org/10.5194/essd-10-251-2018, 2018.

Bourlès, B., Lumpkin, R., McPhaden, M. J., Hernandez, F., Nobre, P., Campos, E., Yu, L., Planton, S., Busalacchi, A., Moura, A. D., Servain, J., and Trotte, J.: THE PIRATA PROGRAM, Bull. Am. Meteorol. Soc., 89, 1111–1126, https://doi.org/10.1175/2008BAMS2462.1, 2008.

Boyd, P. W., Watson, A. J., Law, C. S., Abraham, E. R., Trull, T., Murdoch, R., Bakker, D. C. E., Bowie, A. R., Buesseler, K. O., Chang, H., Charette, M., Croot, P., Downing, K., Frew, R., Gall, M., Hadfield, M., Hall, J., Harvey, M., Jameson, G., LaRoche, J., Liddicoat, M., Ling, R., Maldonado, M. T., McKay, R. M., Nodder, S., Pickmere, S., Pridmore, R., Rintoul, S., Safi, K., Sutton, P., Strzepek, R., Tanneberger, K., Turner, S., Waite, A., and Zeldis, J.: A mesoscale phytoplankton bloom in the polar Southern Ocean stimulated by iron fertilization, Nature, 407, 695–702, https://doi.org/10.1038/35037500, 2000.

Brewin, R. J. W., Sathyendranath, S., Müller, D., Brockmann, C., Deschamps, P. Y., Devred, E., Doerffer, R., Fomferra, N., Franz, B., Grant, M., Groom, S., Horseman, A., Hu, C., Krasemann, H., Lee, Z. P., Maritorena, S., Mélin, F., Peters, M., Platt, T., Regner, P., Smyth, T., Steinmetz, F., Swinton, J., Werdell, J., and White, G. N.: The Ocean Colour Climate Change Initiative: III. A round-

robin comparison on in-water bio-optical algorithms, Remote Sens. Environ., 162, 271–294, https://doi.org/10.1016/j.rse.2013.09.016, 2015.

Brewin, R. J. W., Dall'Olmo, G., Pardo, S., van Dongen-Vogels, V., and Boss, E. S.: Underway spectrophotometry along the Atlantic Meridional Transect reveals high performance in satellite chlorophyll retrievals, Remote Sens. Environ., https://doi.org/10.1016/j.rse.2016.05.005, 2016.

Broecker, W. S. and Peng, T.-H.: Gas exchange rates between air and sea, 26, 21–35, https://doi.org/10.3402/tellusa.v26i1-2.9733, 1974.

Brown, O. B. and Minnett, P. J.: MODIS Infrared Sea Surface Temperature Algorithm, 1999.

Bruto, L., Araujo, M., Noriega, C., Veleda, D., and Lefèvre, N.: Variability of CO_2 fugacity at the western edge of the tropical Atlantic Ocean from the 8°N to 38°W PIRATA buoy, Dyn. Atmos. Ocean., 78, 1–13, https://doi.org/10.1016/j.dynatmoce.2017.01.003, 2017.

Cai, W.-J., Arthur Chen, C. T., and Borges, A.: Carbon dioxide dynamics and fluxes in coastal waters influenced by river plumes, in: Biogeochemical Dynamics at Major River-Coastal Interfaces, edited by: Bianchi, T., Allison, M., and Cai, W.-J., Cambridge University Press, New York, 155–173, https://doi.org/10.1017/CBO9781139136853.010, 2013.

Campbell, J., Antoine, D., Armstrong, R., Arrigo, K., Balch, W., Barber, R., Behrenfeld, M., Bidigare, R., Bishop, J., Carr, M.-E., Esaias, W., Falkowski, P., Hoepffner, N., Iverson, R., Kiefer, D., Lohrenz, S., Marra, J., Morel, A., Ryan, J., Vedernikov, V., Waters, K., Yentsch, C., and Yoder, J.: Comparison of algorithms for estimating ocean primary production from surface chlorophyll, temperature, and irradiance, Global Biogeochem. Cycles, 16, 9-1-9–15, https://doi.org/10.1029/2001GB001444, 2002.

Campbell, J. W. and O'Reilly, J. E.: Role of satellites in estimating primary productivity on the northwest Atlantic continental shelf, Cont. Shelf Res., 8, 179–204, https://doi.org/10.1016/0278-4343(88)90053-2, 1988.

Carr, M. E., Friedrichs, M. A. M., Schmeltz, M., Noguchi Aita, M., Antoine, D., Arrigo, K. R., Asanuma, I., Aumont, O., Barber, R., Behrenfeld, M., Bidigare, R., Buitenhuis, E. T., Campbell, J., Ciotti, A., Dierssen, H., Dowell, M., Dunne, J., Esaias, W., Gentili, B., Gregg, W., Groom, S., Hoepffner, N., Ishizaka, J., Kameda, T., Le Quéré, C., Lohrenz, S., Marra, J., Mélin, F., Moore, K., Morel, A., Reddy, T. E., Ryan, J., Scardi, M., Smyth, T., Turpie, K., Tilstone, G., Waters, K., and Yamanaka, Y.: A comparison of global estimates of marine primary production from ocean color, Deep. Res. Part II Top. Stud. Oceanogr., 53, 741–770, https://doi.org/10.1016/j.dsr2.2006.01.028, 2006.

Carvalho, A. da C. de O., Mendes, C. R. B., Kerr, R., Azevedo, J. L. L. de, Galdino, F., and Tavano, V. M.: The impact of mesoscale eddies on the phytoplankton community in the South Atlantic Ocean: HPLC-CHEMTAX approach, Mar. Environ. Res., 144, 154–165, https://doi.org/10.1016/j.marenvres.2018.12.003, 2019.

Chaigneau, A., Eldin, G., and Dewitte, B.: Eddy activity in the four major

upwelling systems from satellite altimetry (1992–2007), Prog. Oceanogr., 83, 117–123, https://doi.org/10.1016/j.pocean.2009.07.012, 2009.

Chang, C. H., Johnson, N. C., and Cassar, N.: Neural network-based estimates of Southern Ocean net community production from in situ O2/Ar and satellite observation: A methodological study, 11, 3279–3297, https://doi.org/10.5194/bg-11-3279-2014, 2014.

Chelton, D. B., Schlax, M. G., and Samelson, R. M.: Global observations of nonlinear mesoscale eddies, Prog. Oceanogr., 91, 167–216, https://doi.org/10.1016/j.pocean.2011.01.002, 2011.

Chen, C. T. A., Huang, T. H., Fu, Y. H., Bai, Y., and He, X.: Strong sources of CO_2 in upper estuaries become sinks of CO_2 in large river plumes, Curr. Opin. Environ. Sustain., 4, 179–185, https://doi.org/10.1016/j.cosust.2012.02.003, 2012a.

Chen, F., Cai, W. J., Benitez-Nelson, C., and Wang, Y.: Sea surface pCO_2-SST relationships across a cold-core cyclonic eddy: Implications for understanding regional variability and air-sea gas exchange, Geophys. Res. Lett., 34, https://doi.org/10.1029/2006GL028058, 2007.

Chen, Z., Yan, X. H., Jo, Y. H., Jiang, L., and Jiang, Y.: A study of Benguela upwelling system using different upwelling indices derived from remotely sensed data, Cont. Shelf Res., 45, 27–33, https://doi.org/10.1016/j.csr.2012.05.013, 2012b.

Chierici, M., Signorini, S. R., Mattsdotter-Björk, M., Fransson, A., and Olsen, A.: Surface water fCO_2 algorithms for the high-latitude Pacific sector of the Southern Ocean, Remote Sens. Environ., 119, 184–196, https://doi.org/10.1016/j.rse.2011.12.020, 2012.

CMEMS: Copernicus Marine Modelling Service global ocean physics reanalysis product (GLORYS12V1), Copernicus Mar. Model. Serv. [data set], https://doi.org/10.48670/moi-00021, 2021.

Coale, K. H., Johnson, K. S., Fitzwater, S. E., Gordon, R. M., Tanner, S., Chavez, F. P., Ferioli, L., Sakamoto, C., Rogers, P., Millero, F., Steinberg, P., Nightingale, P., Cooper, D., Cochlan, W. P., Landry, M. R., Constantinou, J., Rollwagen, G., Trasvina, A., and Kudela, R.: A massive phytoplankton bloom induced by an ecosystem-scale iron fertilization experiment in the equatorial Pacific Ocean, Nature, 383, 495–501, https://doi.org/10.1038/383495a0, 1996.

Colberg, F., Reason, C. J. C., and Rodgers, K.: South Atlantic response to El Niño-Southern Oscillation induced climate variability in an ocean general circulation model, J. Geophys. Res. C Ocean., 109, 1–14, https://doi.org/10.1029/2004JC002301, 2004.

Coles, V. J., Brooks, M. T., Hopkins, J., Stukel, M. R., Yager, P. L., and Hood, R. R.: The pathways and properties of the Amazon river plume in the tropical North Atlantic Ocean, J. Geophys. Res. Ocean., 118, 6894–6913, https://doi.org/10.1002/2013JC008981, 2013.

Cooley, S. R., Coles, V. J., Subramaniam, A., and Yager, P. L.: Seasonal

variations in the Amazon plume-related atmospheric carbon sink, Global Biogeochem. Cycles, 21, 1–15, https://doi.org/10.1029/2006GB002831, 2007.

Dai, A. and Trenberth, K. E.: Estimates of freshwater discharge from continents: Latitudinal and seasonal variations, J. Hydrometeorol., 3, 660–687, https://doi.org/10.1175/1525-7541(2002)003<0660:EOFDFC>2.0.CO;2, 2002.

Dall'Olmo, G., Westberry, T. K., Behrenfeld, M. J., Boss, E., and Slade, W. H.: Significant contribution of large particles to optical backscattering in the open ocean, https://doi.org/10.5194/bg-6-947-2009, 2009.

Dall'Olmo, G., Boss, E., Behrenfeld, M. J., and Westberry, T. K.: Particulate optical scattering coefficients along an Atlantic Meridional Transect, Opt. Express, 20, 21532, https://doi.org/10.1364/OE.20.021532, 2012.

Dall'Olmo, G., Nencioli, F., Jackson, T., Brewin, R. J. W., Gittings, J. A., and Raitsos, D. E.: Ocean Lagrangian Trajectories (OLTraj): Lagrangian analysis for non-expert users, Open Res. Eur., 1, 117, https://doi.org/10.12688/openreseurope.14133.2, 2021.

Demuth, H., Beale, M., and Hagan, M.: Neural Network Toolbox 6 Users Guide, 3 Apple Hill Drive, Natick, MA, 846 pp., 2008.

Denvil-Sommer, A., Gehlen, M., Vrac, M., and Mejia, C.: LSCE-FFNN-v1: A two-step neural network model for the reconstruction of surface ocean pCO_2 over the global ocean, Geosci. Model Dev., 12, 2091–2105, https://doi.org/10.5194/gmd-12-2091-2019, 2019.

DeVries, T.: The oceanic anthropogenic CO2 sink: Storage, air-sea fluxes, and transports over the industrial era, Global Biogeochem. Cycles, 28, 631–647, https://doi.org/10.1002/2013GB004739, 2014.

Dickson, A. G.: Standard potential of the Standard potential of the reaction - AgCl(s)+1/2H-2(g)=Ag(s)+HCl(aq) and the standard acidity constant of the ion HSO4- in synthetic sea-water from 273.15-K to 318.15-K, J. Chem. Thermodyn., 22, 113–127, https://doi.org/10.1016/0021-9614(90)90074-Z, 1990.

Dickson, A. G., Sabine, C. L., and Christian, J. R.: Guide to Best Practices for Ocean CO_2 measurements, PICES Special Publication, IOCCP Report No . 8, 191 pp. pp., 2007.

Dogliotti, A. I., Schloss, I. R., Almandoz, G. O., and Gagliardini, D. A.: Evaluation of SeaWiFS and MODIS chlorophyll- a products in the Argentinean Patagonian Continental Shelf (38° S–55° S), Int. J. Remote Sens., 30, 251–273, https://doi.org/10.1080/01431160802311133, 2009.

Dogliotti, A. I., Lutz, V. A., and Segura, V.: Estimation of primary production in the southern Argentine continental shelf and shelf-break regions using field and remote sensing data, Remote Sens. Environ., 140, 497–508, https://doi.org/10.1016/j.rse.2013.09.021, 2014.

Dong, Y., Yang, M., Bakker, D. C. E., Kitidis, V., and Bell, T. G.: Uncertainties in eddy covariance air–sea CO_2 flux measurements and implications for gas transfer velocity parameterisations, Atmos. Chem. Phys., 21, 8089–8110,

https://doi.org/10.5194/acp-21-8089-2021, 2021.

Donlon, C., Robinson, I., Casey, K. S., Vazquez-Cuervo, J., Armstrong, E., Arino, O., Gentemann, C., May, D., LeBorgne, P., Piollé, J., Barton, I., Beggs, H., Poulter, D. J. S., Merchant, C. J., Bingham, A., Heinz, S., Harris, A., Wick, G., Emery, B., Minnett, P., Evans, R., Llewellyn-Jones, D., Mutlow, C., Reynolds, R. W., Kawamura, H., and Rayner, N.: The Global Ocean Data Assimilation Experiment High-resolution Sea Surface Temperature Pilot Project, Bull. Am. Meteorol. Soc., 88, 1197–1214, https://doi.org/10.1175/BAMS-88-8-1197, 2007.

Donlon, C., Robinson, I. S., Reynolds, M., Wimmer, W., Fisher, G., Edwards, R., and Nightingale, T. J.: An infrared sea surface temperature autonomous radiometer (ISAR) for deployment aboard volunteer observing ships (VOS), J. Atmos. Ocean. Technol., 25, 93–113, https://doi.org/10.1175/2007JTECHO505.1, 2008.

Donlon, C. J., Nightingale, T. J., Sheasby, T., Turner, J., Robinson, I. S., and Emergy, W. J.: Implications of the oceanic thermal skin temperature deviation at high wind speed, Geophys. Res. Lett., 26, 2505–2508, https://doi.org/10.1029/1999GL900547, 1999.

Donlon, C. J., Minnett, P. J., Gentemann, C., Nightingale, T. J., Barton, I. J., Ward, B., and Murray, M. J.: Toward Improved Validation of Satellite Sea Surface Skin Temperature Measurements for Climate Research, J. Clim., 15, 353–369, https://doi.org/10.1175/1520-0442(2002)015<0353:TIVOSS>2.0.CO;2, 2002.

Duarte, C. M., Regaudie-de-Gioux, A., Arrieta, J. M., Delgado-Huertas, A., and Agustí, S.: The Oligotrophic Ocean Is Heterotrophic, Ann. Rev. Mar. Sci., 5, 551–569, https://doi.org/10.1146/annurev-marine-121211-172337, 2013.

Ducklow, H. W. and Doney, S. C.: What Is the Metabolic State of the Oligotrophic Ocean? A Debate, Ann. Rev. Mar. Sci., 5, 525–533, https://doi.org/10.1146/annurev-marine-121211-172331, 2013.

Dufois, F., Hardman-Mountford, N. J., Greenwood, J., Richardson, A. J., Feng, M., and Matear, R. J.: Anticyclonic eddies are more productive than cyclonic eddies in subtropical gyres because of winter mixing, Sci. Adv., 2, 1–7, https://doi.org/10.1126/sciadv.1600282, 2016.

Dunstan, P. K., Foster, S. D., King, E., Risbey, J., O'Kane, T. J., Monselesan, D., Hobday, A. J., Hartog, J. R., and Thompson, P. A.: Global patterns of change and variation in sea surface temperature and chlorophyll a, Sci. Rep., 8, 1–9, https://doi.org/10.1038/s41598-018-33057-y, 2018.

Dutkiewicz, S., Morris, J. J., Follows, M. J., Scott, J., Levitan, O., Dyhrman, S. T., and Berman-Frank, I.: Impact of ocean acidification on the structure of future phytoplankton communities, Nat. Clim. Chang., 5, 1002–1006, https://doi.org/10.1038/nclimate2722, 2015.

Eppley, R. W., Stewart, E., Abbott, M. R., and Heyman, U.: Estimating ocean primary production from satellite chlorophyll. Introduction to regional differences and statistics for the Southern California Bight, J. Plankton Res., 7, 57–70,

https://doi.org/10.1093/plankt/7.1.57, 1985.

Fay, A. R. and McKinley, G. A.: Global trends in surface ocean pCO_2 from in situ data, Global Biogeochem. Cycles, 27, 541–557, https://doi.org/10.1002/gbc.20051, 2013.

Field, C. B., Behrenfeld, M. J., Randerson, J. T., and Falkowski, P.: Primary production of the biosphere: Integrating terrestrial and oceanic components, Science (80-.)., 281, 237–240, https://doi.org/10.1126/science.281.5374.237, 1998.

Fogt, R. L., Bromwich, D. H., and Hines, K. M.: Understanding the SAM influence on the South Pacific ENSO teleconnection, Clim. Dyn., 36, 1555–1576, https://doi.org/10.1007/s00382-010-0905-0, 2011.

Ford, D., Tilstone, G. H., Shutler, J. D., Kitidis, V., Lobanova, P., Schwarz, J., Poulton, A. J., Serret, P., Lamont, T., Chuqui, M., Barlow, R., Lozano, J., Kampel, M., and Brandini, F.: Wind speed and mesoscale features drive net autotrophy in the South Atlantic Ocean, Remote Sens. Environ., 260, 112435, https://doi.org/10.1016/j.rse.2021.112435, 2021a.

Ford, D. J., Tilstone, G. H., Shutler, J. D., and Kitidis, V.: Interpolated surface ocean carbon dioxide partial pressure for the South Atlantic Ocean (2002-2018) using different biological parameters, PANGAEA [data set], https://doi.org/10.1594/PANGAEA.935936, 2021b.

Ford, D. J., Tilstone, G. H., Shutler, J. D., and Kitidis, V.: Derivation of seawater pCO_2 from net community production identifies the South Atlantic Ocean as a CO_2 source, 19, 93–115, https://doi.org/10.5194/bg-19-93-2022, 2022.

Frenger, I., Gruber, N., Knutti, R., and Münnich, M.: Imprint of Southern Ocean eddies on winds, clouds and rainfall, Nat. Geosci., 6, 608–612, https://doi.org/10.1038/ngeo1863, 2013.

Friedlingstein, P., O'Sullivan, M., Jones, M. W., Andrew, R. M., Hauck, J., Olsen, A., Peters, G. P., Peters, W., Pongratz, J., Sitch, S., Le Quéré, C., Canadell, J. G., Ciais, P., Jackson, R. B., Alin, S., Aragão, L. E. O. C., Arneth, A., Arora, V., Bates, N. R., Becker, M., Benoit-Cattin, A., Bittig, H. C., Bopp, L., Bultan, S., Chandra, N., Chevallier, F., Chini, L. P., Evans, W., Florentie, L., Forster, P. M., Gasser, T., Gehlen, M., Gilfillan, D., Gkritzalis, T., Gregor, L., Gruber, N., Harris, I., Hartung, K., Haverd, V., Houghton, R. A., Ilyina, T., Jain, A. K., Joetzjer, E., Kadono, K., Kato, E., Kitidis, V., Korsbakken, J. I., Landschützer, P., Lefèvre, N., Lenton, A., Lienert, S., Liu, Z., Lombardozzi, D., Marland, G., Metzl, N., Munro, D. R., Nabel, J. E. M. S., Nakaoka, S.-I., Niwa, Y., O'Brien, K., Ono, T., Palmer, P. I., Pierrot, D., Poulter, B., Resplandy, L., Robertson, E., Rödenbeck, C., Schwinger, J., Séférian, R., Skjelvan, I., Smith, A. J. P., Sutton, A. J., Tanhua, T., Tans, P. P., Tian, H., Tilbrook, B., van der Werf, G., Vuichard, N., Walker, A. P., Wanninkhof, R., Watson, A. J., Willis, D., Wiltshire, A. J., Yuan, W., Yue, X., and Zaehle, S.: Global Carbon Budget 2020, Earth Syst. Sci. Data, 12, 3269–3340, https://doi.org/10.5194/essd-12-3269-2020, 2020.

Friedrichs, M. A. M., Carr, M.-E., Barber, R. T., Scardi, M., Antoine, D.,

Armstrong, R. A., Asanuma, I., Behrenfeld, M. J., Buitenhuis, E. T., Chai, F., Christian, J. R., Ciotti, A. M., Doney, S. C., Dowell, M., Dunne, J., Gentili, B., Gregg, W., Hoepffner, N., Ishizaka, J., Kameda, T., Lima, I., Marra, J., Mélin, F., Moore, J. K., Morel, A., O'Malley, R. T., O'Reilly, J., Saba, V. S., Schmeltz, M., Smyth, T. J., Tjiputra, J., Waters, K., Westberry, T. K., and Winguth, A.: Assessing the uncertainties of model estimates of primary productivity in the tropical Pacific Ocean, J. Mar. Syst., 76, 113–133, https://doi.org/10.1016/j.jmarsys.2008.05.010, 2009.

García-Corral, L. S., Barber, E., Regaudie-De-Gioux, A., Sal, S., Holding, J. M., Agustí, S., Navarro, N., Serret, P., Mozetič, P., and Duarte, C. M.: Temperature dependence of planktonic metabolism in the subtropical North Atlantic Ocean, 11, 4529–4540, https://doi.org/10.5194/bg-11-4529-2014, 2014.

Garcia, C. A. E., Sarma, Y. V. B., Mata, M. M., and Garcia, V. M. T.: Chlorophyll variability and eddies in the Brazil-Malvinas Confluence region, Deep. Res. Part II Top. Stud. Oceanogr., https://doi.org/10.1016/j.dsr2.2003.07.016, 2004.

Garcia, C. A. E., Garcia, V. M. T., and McClain, C. R.: Evaluation of SeaWiFS chlorophyll algorithms in the Southwestern Atlantic and Southern Oceans, Remote Sens. Environ., https://doi.org/10.1016/j.rse.2004.12.006, 2005.

Garcia, V. M. T., Signorini, S., Garcia, C. A. E., and McClain, C. R.: Empirical and semi-analytical chlorophyll algorithms in the south-western Atlantic coastal region (25-40°S and 60-45°W), Int. J. Remote Sens., 27, 1539–1562, https://doi.org/10.1080/01431160500382857, 2006.

Garnesson, P., Mangin, A., Fanton d'Andon, O., Demaria, J., and Bretagnon, M.: The CMEMS GlobColour chlorophyll-a product based on satellite observation: multi-sensor merging and flagging strategies, Ocean Sci., 15, 819–830, https://doi.org/10.5194/os-15-819-2019, 2019.

Garver, S. A. and Siegel, D. A.: Inherent optical property inversion of ocean color spectra and its biogeochemical interpretation: 1. Time series from the Sargasso Sea, J. Geophys. Res. Ocean., 102, 18607–18625, https://doi.org/10.1029/96JC03243, 1997.

Gaube, P., McGillicuddy, D. J., Chelton, D. B., Behrenfeld, M. J., and Strutton, P. G.: Regional variations in the influence of mesoscale eddies on near-surface chlorophyll, J. Geophys. Res. Ocean., 119, 8195–8220, https://doi.org/10.1002/2014JC010111, 2014.

Gist, N., Serret, P., Woodward, E. M. S., Chamberlain, K., and Robinson, C.: Seasonal and spatial variability in plankton production and respiration in the Subtropical Gyres of the Atlantic Ocean, Deep. Res. Part II Top. Stud. Oceanogr., 56, 931–940, https://doi.org/10.1016/j.dsr2.2008.10.035, 2009.

Goddijn-Murphy, L. M., Woolf, D. K., Land, P. E., Shutler, J. D., and Donlon, C.: The OceanFlux Greenhouse Gases methodology for deriving a sea surface climatology of CO_2 fugacity in support of air-sea gas flux studies, Ocean Sci., 11, 519–541, https://doi.org/10.5194/os-11-519-2015, 2015.

Gohin, F., Druon, J. N., and Lampert, L.: A five channel chlorophyll concentration algorithm applied to SeaWiFS data processed by SeaDAS in

coastal waters, Int. J. Remote Sens., 23, 1639–1661, https://doi.org/10.1080/01431160110071879, 2002.

González-Dávila, M., Santana-Casiano, J. M., and Ucha, I. R.: Seasonal variability of fCO_2 in the Angola-Benguela region, Prog. Oceanogr., 83, 124–133, https://doi.org/10.1016/j.pocean.2009.07.033, 2009.

Gray, A. R., Johnson, K. S., Bushinsky, S. M., Riser, S. C., Russell, J. L., Talley, L. D., Wanninkhof, R., Williams, N. L., and Sarmiento, J. L.: Autonomous Biogeochemical Floats Detect Significant Carbon Dioxide Outgassing in the High-Latitude Southern Ocean, Geophys. Res. Lett., 45, 9049–9057, https://doi.org/10.1029/2018GL078013, 2018.

Gregg, W. W. and Carder, K. L.: A simple spectral solar irradiance model for cloudless maritime atmospheres, Limnol. Oceanogr., https://doi.org/10.4319/lo.1990.35.8.1657, 1990.

Gregor, L. and Monteiro, P. M. S.: Is the southern benguela a significant regional sink of CO_2?, S. Afr. J. Sci., 109, 1–5, https://doi.org/10.1590/sajs.2013/20120094, 2013.

Gregor, L., Lebehot, A. D., Kok, S., and Scheel Monteiro, P. M.: A comparative assessment of the uncertainties of global surface ocean CO_2 estimates using a machine-learning ensemble (CSIR-ML6 version 2019a)-Have we hit the wall?, Geosci. Model Dev., 12, 5113–5136, https://doi.org/10.5194/gmd-12-5113-2019, 2019.

Gruber, N., Gloor, M., Mikaloff Fletcher, S. E., Doney, S. C., Dutkiewicz, S., Follows, M. J., Gerber, M., Jacobson, A. R., Joos, F., Lindsay, K., Menemenlis, D., Mouchet, A., Müller, S. A., Sarmiento, J. L., and Takahashi, T.: Oceanic sources, sinks, and transport of atmospheric CO_2, Global Biogeochem. Cycles, 23, 1–21, https://doi.org/10.1029/2008GB003349, 2009.

Guerra, L. A. A., Paiva, A. M., and Chassignet, E. P.: On the translation of Agulhas rings to the western South Atlantic Ocean, Deep. Res. Part I Oceanogr. Res. Pap., 139, 104–113, https://doi.org/10.1016/j.dsr.2018.08.005, 2018.

Harrison, C. S., Long, M. C., Lovenduski, N. S., and Moore, J. K.: Mesoscale Effects on Carbon Export: A Global Perspective, Global Biogeochem. Cycles, 32, 680–703, https://doi.org/10.1002/2017GB005751, 2018.

He, Q., Zhan, H., Cai, S., and Li, Z.: Eddy effects on surface chlorophyll in the northern South China Sea: Mechanism investigation and temporal variability analysis, Deep. Res. Part I Oceanogr. Res. Pap., 112, 25–36, https://doi.org/10.1016/j.dsr.2016.03.004, 2016.

Henson, S. A., Sanders, R., Madsen, E., Morris, P. J., Le Moigne, F., and Quartly, G. D.: A reduced estimate of the strength of the ocean's biological carbon pump, Geophys. Res. Lett., 38, 10–14, https://doi.org/10.1029/2011GL046735, 2011.

Henson, S. A., Humphreys, M. P., Land, P. E., Shutler, J. D., Goddijn-Murphy, L., and Warren, M.: Controls on Open-Ocean North Atlantic ΔpCO_2 at Seasonal

and Interannual Time Scales Are Different, Geophys. Res. Lett., 45, 9067–9076, https://doi.org/10.1029/2018GL078797, 2018.

Hernández-Hernández, N., Arístegui, J., Montero, M. F., Velasco-Senovilla, E., Baltar, F., Marrero-Díaz, Á., Martínez-Marrero, A., and Rodríguez-Santana, Á.: Drivers of Plankton Distribution Across Mesoscale Eddies at Submesoscale Range, Front. Mar. Sci., 7, 1–13, https://doi.org/10.3389/fmars.2020.00667, 2020.

Hersbach, H., Bell, B., Berrisford, P., Biavati, G., Horányi, A., Muñoz Sabater, J., Nicolas, J., Peubey, C., Radu, R., Rozum, I., Schepers, D., Simmons, A., Soci, C., Dee, D., and Thépaut, J.-N.: ERA5 monthly averaged data on single levels from 1979 to present, Copernicus Clim. Chang. Serv. Clim. Data Store [dataset], https://doi.org/10.24381/cds.f17050d7, 2019.

van Heuven, S., D. Pierrot, J. W. B. R., Lewis, E., and Wallace, D. W. R.: MATLAB Program Developed for CO_2 System Calculations, Carbon Dioxide Information Analysis Center, Oak Ridge National Laboratory, Oak Ridge, TN, https://doi.org/10.3334/CDIAC/otg.CO2SYS_MATLAB_v1.1, 2011.

Hewitt, H. T., Bell, M. J., Chassignet, E. P., Czaja, A., Ferreira, D., Griffies, S. M., Hyder, P., McClean, J. L., New, A. L., and Roberts, M. J.: Will high-resolution global ocean models benefit coupled predictions on short-range to climate timescales?, Ocean Model., 120, 120–136, https://doi.org/10.1016/j.ocemod.2017.11.002, 2017.

Hewitt, H. T., Roberts, M., Mathiot, P., Biastoch, A., Blockley, E., Chassignet, E. P., Fox-Kemper, B., Hyder, P., Marshall, D. P., Popova, E., Treguier, A. M., Zanna, L., Yool, A., Yu, Y., Beadling, R., Bell, M., Kuhlbrodt, T., Arsouze, T., Bellucci, A., Castruccio, F., Gan, B., Putrasahan, D., Roberts, C. D., Van Roekel, L., and Zhang, Q.: Resolving and Parameterising the Ocean Mesoscale in Earth System Models, Curr. Clim. Chang. Reports, 6, 137–152, https://doi.org/10.1007/s40641-020-00164-w, 2020.

Ho, D. T., Law, C. S., Smith, M. J., Schlosser, P., Harvey, M., and Hill, P.: Measurements of air-sea gas exchange at high wind speeds in the Southern Ocean: Implications for global parameterizations, Geophys. Res. Lett., 33, L16611, https://doi.org/10.1029/2006GL026817, 2006.

Holding, T., Ashton, I. G., Shutler, J. D., Land, P. E., Nightingale, P. D., Rees, A. P., Brown, I., Piolle, J.-F., Kock, A., Bange, H. W., Woolf, D. K., Goddijn-Murphy, L., Pereira, R., Paul, F., Girard-Ardhuin, F., Chapron, B., Rehder, G., Ardhuin, F., and Donlon, C. J.: The FluxEngine air–sea gas flux toolbox: simplified interface and extensions for in situ analyses and multiple sparingly soluble gases, Ocean Sci., 15, 1707–1728, https://doi.org/10.5194/os-15-1707-2019, 2019.

Hooker, S. B., Rees, N. W., and Aiken, J.: An objective methodology for identifying oceanic provinces, Prog. Oceanogr., 45, 313–338, https://doi.org/10.1016/S0079-6611(00)00006-9, 2000.

Hopkins, J., Lucas, M., Dufau, C., Sutton, M., Stum, J., Lauret, O., and Channelliere, C.: Detection and variability of the Congo River plume from

satellite derived sea surface temperature, salinity, ocean colour and sea level, Remote Sens. Environ., 139, 365–385, https://doi.org/10.1016/j.rse.2013.08.015, 2013.

Howard, E. M., Durkin, C. A., Hennon, G. M. M., Ribalet, F., and Stanley, R. H. R.: Biological production, export efficiency, and phytoplankton communities across 8000 km of the South Atlantic, Global Biogeochem. Cycles, 31, 1066–1088, https://doi.org/10.1002/2016GB005488, 2017.

Hu, C., Lee, Z., and Franz, B.: Chlorophyll a algorithms for oligotrophic oceans: A novel approach based on three-band reflectance difference, J. Geophys. Res. Ocean., 117, 1–25, https://doi.org/10.1029/2011JC007395, 2012.

Hutchings, L., van der Lingen, C. D., Shannon, L. J., Crawford, R. J. M., Verheye, H. M. S., Bartholomae, C. H., van der Plas, A. K., Louw, D., Kreiner, A., Ostrowski, M., Fidel, Q., Barlow, R. G., Lamont, T., Coetzee, J., Shillington, F., Veitch, J., Currie, J. C., and Monteiro, P. M. S.: The Benguela Current: An ecosystem of four components, Prog. Oceanogr., 83, 15–32, https://doi.org/10.1016/j.pocean.2009.07.046, 2009.

Ibánhez, J. S. P., Diverrès, D., Araujo, M., and Lefèvre, N.: Seasonal and interannual variability of sea-air CO_2 fluxes in the tropical Atlantic affected by the Amazon River plume, Global Biogeochem. Cycles, 29, 1640–1655, https://doi.org/10.1002/2015GB005110, 2015.

Ibánhez, J. S. P., Araujo, M., and Lefèvre, N.: The overlooked tropical oceanic CO_2 sink, Geophys. Res. Lett., 43, 3804–3812, https://doi.org/10.1002/2016GL068020, 2016.

Iida, Y., Kojima, A., Takatani, Y., Nakano, T., Sugimoto, H., Midorikawa, T., and Ishii, M.: Trends in pCO_2 and sea–air CO_2 flux over the global open oceans for the last two decades, J. Oceanogr., 71, 637–661, https://doi.org/10.1007/s10872-015-0306-4, 2015.

IPCC: Climate Change 2013: The Physical Science Basis. Contribution of Working Group I to the Fifth Assessment Report of the Intergovernmental Panel on Climate Change, edited by: Stocker, T. F., Qin, D., Plattner, G.-K., Tignor, M. B., Allen, S. K., Boschung, J., Nauels, A., Xia, Y., Bex, V., and Midgley, P. M., Cambridge University Press, Cambridge, UK, 1535 pp., 2013.

IPCC: Climate Change 2021: The Physical Science Basis. Contribution of Working Group I to the Sixth Assessment Report of the Intergovernmental Panel on Climate Change, edited by: Masson-Delmotte, V., Zhai, P., Pirani, A., Connors, S. L., Péan, C., Berger, S., Caud, N., Chen, Y., Goldfarb, L., Gomis, M. I., Huang, M., Leitzell, K., Lonnoy, E., Matthews, J. B. R., Maycock, T. K., Waterfield, T., Yelekçi, O., Yu, R., and Zhou, B., Cambridge University Press, 2021.

Jean-Michel, L., Eric, G., Romain, B.-B., Gilles, G., Angélique, M., Marie, D., Clément, B., Mathieu, H., Olivier, L. G., Charly, R., Tony, C., Charles-Emmanuel, T., Florent, G., Giovanni, R., Mounir, B., Yann, D., and Pierre-Yves, L. T.: The Copernicus Global 1/12° Oceanic and Sea Ice GLORYS12 Reanalysis, Front. Earth Sci., 9, 1–27,

https://doi.org/10.3389/feart.2021.698876, 2021.

Jersild, A., Delawalla, S., and Ito, T.: Mesoscale Eddies Regulate Seasonal Iron Supply and Carbon Drawdown in the Drake Passage, Geophys. Res. Lett., 48, https://doi.org/10.1029/2021GL096020, 2021.

Jiang, Z. P., Cai, W. J., Lehrter, J., Chen, B., Ouyang, Z., Le, C., Roberts, B. J., Hussain, N., Scaboo, M. K., Zhang, J., and Xu, Y.: Spring net community production and its coupling with the CO_2 dynamics in the surface water of the northern Gulf of Mexico, 16, 3507–3525, https://doi.org/10.5194/bg-16-3507-2019, 2019.

Jones, E. M., Hoppema, M., Strass, V., Hauck, J., Salt, L., Ossebaar, S., Klaas, C., van Heuven, S. M. A. C., Wolf-Gladrow, D., Stöven, T., and de Baar, H. J. W.: Mesoscale features create hotspots of carbon uptake in the Antarctic Circumpolar Current, Deep. Res. Part II Top. Stud. Oceanogr., 138, 39–51, https://doi.org/10.1016/j.dsr2.2015.10.006, 2017.

Kahru, M., Gille, S. T., Murtugudde, R., Strutton, P. G., Manzano-Sarabia, M., Wang, H., and Mitchell, B. G.: Global correlations between winds and ocean chlorophyll, J. Geophys. Res. Ocean., 115, 1–11, https://doi.org/10.1029/2010JC006500, 2010.

Kaiser, J., Reuer, M. K., Barnett, B., and Bender, M. L.: Marine productivity estimates from continuous O_2/Ar ratio measurements by membrane inlet mass spectrometry, Geophys. Res. Lett., 32, n/a-n/a, https://doi.org/10.1029/2005GL023459, 2005.

Kampel, M., Sathyendranath, S., Platt, T., and Gaeta, S. A.: Satellite estimates of phytoplankton primary production at santos bight, southwestern-south Atlantic: Comparison of algorithms, in: 2009 IEEE International Geoscience and Remote Sensing Symposium, II-286-II–289, https://doi.org/10.1109/IGARSS.2009.5418066, 2009a.

Kampel, M., Lorenzzetti, J. A., Bentz, C. M., Nunes, R. A., Paranhos, R., Rudorff, F. M., and Politano, A. T.: Simultaneous measurements of chlorophyll concentration by lidar, fluorometry, above-water radiometry, and ocean color MODIS images in the Southwestern Atlantic, 9, 528–541, https://doi.org/10.3390/s90100528, 2009b.

Kendall, M. G.: Rank Correlation Methods, 4th ed., Charles Griffin, London, UK, 1975.

Keppler, L. and Landschützer, P.: Regional Wind Variability Modulates the Southern Ocean Carbon Sink, Sci. Rep., 9, 1–10, https://doi.org/10.1038/s41598-019-43826-y, 2019.

Kim, H. J., Kim, T., Hyeong, K., Yeh, S., Park, J., Yoo, C. M., and Hwang, J.: Suppressed CO_2 Outgassing by an Enhanced Biological Pump in the Eastern Tropical Pacific, J. Geophys. Res. Ocean., 124, 7962–7973, https://doi.org/10.1029/2019JC015287, 2019.

Kitidis, V., Tilstone, G. H., Serret, P., Smyth, T. J., Torres, R., and Robinson, C.: Oxygen photolysis in the Mauritanian upwelling: Implications for net community

production, Limnol. Oceanogr., 59, 299–310, https://doi.org/10.4319/lo.2014.59.2.0299, 2014.

Kitidis, V., Brown, I., Hardman-mountford, N., and Lefèvre, N.: Surface ocean carbon dioxide during the Atlantic Meridional Transect (1995 – 2013); evidence of ocean acidification, Prog. Oceanogr., 158, 65–75, https://doi.org/10.1016/j.pocean.2016.08.005, 2017.

Kitidis, V., Shutler, J. D., Ashton, I., Warren, M., Brown, I., Findlay, H., Hartman, S. E., Sanders, R., Humphreys, M., Kivimäe, C., Greenwood, N., Hull, T., Pearce, D., McGrath, T., Stewart, B. M., Walsham, P., McGovern, E., Bozec, Y., Gac, J.-P., van Heuven, S. M. A. C., Hoppema, M., Schuster, U., Johannessen, T., Omar, A., Lauvset, S. K., Skjelvan, I., Olsen, A., Steinhoff, T., Körtzinger, A., Becker, M., Lefevre, N., Diverrès, D., Gkritzalis, T., Cattrijsse, A., Petersen, W., Voynova, Y. G., Chapron, B., Grouazel, A., Land, P. E., Sharples, J., and Nightingale, P. D.: Winter weather controls net influx of atmospheric CO_2 on the north-west European shelf, Sci. Rep., 9, 20153, https://doi.org/10.1038/s41598-019-56363-5, 2019.

Koffi, U., Lefèvre, N., Kouadio, G., and Boutin, J.: Surface CO_2 parameters and air-sea CO_2 flux distribution in the eastern equatorial Atlantic Ocean, J. Mar. Syst., 82, 135–144, https://doi.org/10.1016/j.jmarsys.2010.04.010, 2010.

Koffi, U., Kouadio, G., and Kouadio, Y. K.: Estimates and Variability of the Air-Sea CO_2 Fluxes in the Gulf of Guinea during the 2005-2007 Period, Open J. Mar. Sci., 06, 11–22, https://doi.org/10.4236/ojms.2016.61002, 2016.

Körtzinger, A.: A significant CO_2 sink in the tropical Atlantic Ocean associated with the Amazon River plume, Geophys. Res. Lett., 30, 2–5, https://doi.org/10.1029/2003GL018841, 2003.

Kroopnick, P.: Isotopic fractionations during oxygen consumption and carbonate dissolution within the North Atlantic Deep Water, Earth Planet. Sci. Lett., 49, 485–498, https://doi.org/10.1016/0012-821X(80)90089-8, 1980.

Kulk, G., Platt, T., Dingle, J., Jackson, T., Jönsson, B. F., Bouman, H. A., Babin, M., Brewin, R. J. W., Doblin, M., Estrada, M., Figueiras, F. G., Furuya, K., González-Benítez, N., Gudfinnsson, H. G., Gudmundsson, K., Huang, B., Isada, T., Kovač, Ž., Lutz, V. A., Marañón, E., Raman, M., Richardson, K., Rozema, P. D., van de Poll, W. H., Segura, V., Tilstone, G. H., Uitz, J., van Dongen-Vogels, V., Yoshikawa, T., and Sathyendranath, S.: Primary production, an index of climate change in the ocean: Satellite-based estimates over two decades, Remote Sens., 12, https://doi.org/10.3390/rs12050826, 2020.

Lamont, T., Barlow, R. G., and Kyewalyanga, M. S.: Physical drivers of phytoplankton production in the southern Benguela upwelling system, Deep. Res. Part I Oceanogr. Res. Pap., 90, 1–16, https://doi.org/10.1016/j.dsr.2014.03.003, 2014.

Lamont, T., Brewin, R. J. W., and Barlow, R. G.: Seasonal variation in remotely-sensed phytoplankton size structure around southern Africa, Remote Sens. Environ., 204, 617–631, https://doi.org/10.1016/j.rse.2017.09.038, 2018a.

Lamont, T., García-Reyes, M., Bograd, S. J., van der Lingen, C. D., and

Sydeman, W. J.: Upwelling indices for comparative ecosystem studies: Variability in the Benguela Upwelling System, J. Mar. Syst., 188, 3–16, https://doi.org/10.1016/j.jmarsys.2017.05.007, 2018b.

Lamont, T., Barlow, R. G., and Brewin, R. J. W.: Long-Term Trends in Phytoplankton Chlorophyll a and Size Structure in the Benguela Upwelling System, J. Geophys. Res. Ocean., 124, 1170–1195, https://doi.org/10.1029/2018JC014334, 2019.

Land, P. E., Bailey, T. C., Taberner, M., Pardo, S., Sathyendranath, S., Zenouz, K. N., Id, V. B., Shutler, J. D., and Id, G. D. Q.: A Statistical Modeling Framework for Characterising Uncertainty in Large Datasets : Application to Ocean Colour, Remote Sens., 10, https://doi.org/https://doi.org/10.3390/rs10050695, 2018.

Landschützer, P., Gruber, N., Bakker, D. C. E., Schuster, U., Nakaoka, S., Payne, M. R., Sasse, T. P., and Zeng, J.: A neural network-based estimate of the seasonal to inter-annual variability of the Atlantic Ocean carbon sink, 10, 7793–7815, https://doi.org/10.5194/bg-10-7793-2013, 2013.

Landschützer, P., Gruber, N., Bakker, D. C. E., and Schuster, U.: Recent variability of the global ocean carbon sink, Global Biogeochem. Cycles, 28, 927–949, https://doi.org/10.1002/2014GB004853, 2014.

Landschützer, P., Gruber, N., Haumann, F. A., Rödenbeck, C., Bakker, D. C. E., van Heuven, S., Hoppema, M., Metzl, N., Sweeney, C., Takahashi, T., Tilbrook, B., and Wanninkhof, R.: The reinvigoration of the Southern Ocean carbon sink, Science (80-.)., 349, 1221–1224, https://doi.org/10.1126/science.aab2620, 2015.

Landschützer, P., Gruber, N., and Bakker, D. C. E.: Decadal variations and trends of the global ocean carbon sink, Global Biogeochem. Cycles, 30, 1396–1417, https://doi.org/10.1002/2015GB005359, 2016.

Landschützer, P., Gruber, N., and Bakker, D. C. E.: An observation-based global monthly gridded sea surface pCO_2 product from 1982 onward and its monthly climatology (NCEI Accession 0160558), NOAA Natl. Centers Environ. Information. Dataset, https://doi.org/10.7289/v5z899n6, 2017.

Landschützer, P., Laruelle, G. G., Roobaert, A., and Regnier, P.: A uniform pCO_2 climatology combining open and coastal oceans, Earth Syst. Sci. Data, 12, 2537–2553, https://doi.org/10.5194/essd-12-2537-2020, 2020.

Laruelle, G. G., Lauerwald, R., Pfeil, B., and Regnier, P.: Regionalized global budget of the CO_2 exchange at the air-water interface in continental shelf seas, Global Biogeochem. Cycles, 28, 1199–1214, https://doi.org/10.1002/2014GB004832, 2014.

Lavender, S. J., Pinkerton, M. H., Froidefond, J.-M., Morales, J., Aiken, J., and Moore, G. F.: SeaWiFS validation in European coastal waters using optical and bio-geochemical measurements, Int. J. Remote Sens., 25, 1481–1488, https://doi.org/10.1080/01431160310001592481, 2004.

Laws, E. A., Falkowski, P. G., Smith, W. O., Ducklow, H., and McCarthy, J. J.:

Temperature effects on export production in the open ocean, Global Biogeochem. Cycles, 14, 1231–1246, https://doi.org/10.1029/1999GB001229, 2000.

Laxenaire, R., Speich, S., and Stegner, A.: Evolution of the Thermohaline Structure of One Agulhas Ring Reconstructed from Satellite Altimetry and Argo Floats, J. Geophys. Res. Ocean., 124, 8969–9003, https://doi.org/10.1029/2018JC014426, 2019.

Lee, Z., Marra, J., Perry, M. J., and Kahru, M.: Estimating oceanic primary productivity from ocean color remote sensing: A strategic assessment, J. Mar. Syst., 149, 50–59, https://doi.org/10.1016/j.jmarsys.2014.11.015, 2015.

Lefévre, N., Diverrés, D., and Gallois, F.: Origin of CO_2 undersaturation in the western tropical Atlantic, Tellus, Ser. B Chem. Phys. Meteorol., 62, 595–607, https://doi.org/10.1111/j.1600-0889.2010.00475.x, 2010.

Lefèvre, N. and Taylor, A.: Estimating pCO_2 from sea surface temperatures in the Atlantic gyres, Deep. Res. Part I Oceanogr. Res. Pap., 49, 539–554, https://doi.org/10.1016/S0967-0637(01)00064-4, 2002.

Lefèvre, N., Aiken, J., Rutllant, J., Daneri, G., Lavender, S., and Smyth, T.: Observations of pCO_2 in the coastal upwelling off Chile: Spatial and temporal extrapolation using satellite data, J. Geophys. Res., 107, 3055, https://doi.org/10.1029/2000JC000395, 2002.

Lefèvre, N., Watson, A. J., and Watson, A. R.: A comparison of multiple regression and neural network techniques for mapping in situ pCO_2 data, Tellus, Ser. B Chem. Phys. Meteorol., 57, 375–384, https://doi.org/10.1111/j.1600-0889.2005.00164.x, 2005.

Lefèvre, N., Guillot, A., Beaumont, L., and Danguy, T.: Variability of fCO_2 in the Eastern Tropical Atlantic from a moored buoy, J. Geophys. Res. Ocean., 113, https://doi.org/10.1029/2007JC004146, 2008.

Lefèvre, N., Caniaux, G., Janicot, S., and Gueye, A. K.: Increased CO_2 outgassing in February-May 2010 in the tropical Atlantic following the 2009 Pacific El Niño, J. Geophys. Res. Ocean., 118, 1645–1657, https://doi.org/10.1002/jgrc.20107, 2013.

Lefèvre, N., Veleda, D., Araujo, M., and Caniaux, G.: Variability and trends of carbon parameters at a time series in the eastern tropical Atlantic, Tellus, Ser. B Chem. Phys. Meteorol., 68, https://doi.org/10.3402/tellusb.v68.30305, 2016.

Lefèvre, N., Montes, M. F., Gaspar, F. L., Rocha, C., Jiang, S., De Araújo, M. C., and Severino Pino Ibánhez, J.: Net heterotrophy in the Amazon continental shelf changes rapidly to a sink of CO_2 in the outer Amazon plume, Front. Mar. Sci., 4, 1–16, https://doi.org/10.3389/fmars.2017.00278, 2017.

Lefèvre, N., Tyaquiçã, P., Veleda, D., Perruche, C., and van Gennip, S. J.: Amazon River propagation evidenced by a CO_2 decrease at 8°N, 38°W in September 2013, J. Mar. Syst., 211, 103419, https://doi.org/10.1016/j.jmarsys.2020.103419, 2020.

Lefèvre, N., Mejia, C., Khvorostyanov, D., Beaumont, L., and Koffi, U.: Ocean

Circulation Drives the Variability of the Carbon System in the Eastern Tropical Atlantic, 2, 126–148, https://doi.org/10.3390/oceans2010008, 2021.

Lehahn, Y., D'Ovidio, F., Lévy, M., Amitai, Y., and Heifetz, E.: Long range transport of a quasi isolated chlorophyll patch by an Agulhas ring, Geophys. Res. Lett., 38, https://doi.org/10.1029/2011GL048588, 2011.

Lencina-Avila, J. M., Ito, R. G., Garcia, C. A. E., and Tavano, V. M.: Sea-air carbon dioxide fluxes along 35°S in the South Atlantic Ocean, Deep. Res. Part I Oceanogr. Res. Pap., 115, 175–187, https://doi.org/10.1016/j.dsr.2016.06.004, 2016.

Lewis, E., Wallace, D., and Allison, L. J.: Program developed for CO_2 system calculations, Oak Ridge, TN, https://doi.org/10.2172/639712, 1998.

Li, J., Jamet, C., Zhu, J., Han, B., Li, T., Yang, A., Guo, K., and Jia, D.: Error Budget in the validation of radiometric products derived from OLCI around the China Sea from Open Ocean to Coastal Waters Compared with MODIS and VIIRS, Remote Sens., 11, 1997–2010, https://doi.org/10.3390/rs11202400, 2019.

Li, Z. and Cassar, N.: Satellite estimates of net community production based on O2/Ar observations and comparison to other estimates, Global Biogeochem. Cycles, 30, 735–752, https://doi.org/10.1002/2015GB005314, 2016.

Liu, F., Yin, K., He, L., Tang, S., and Yao, J.: Influence on phytoplankton of different developmental stages of mesoscale eddies off eastern Australia, J. Sea Res., 137, 1–8, https://doi.org/10.1016/j.seares.2018.03.004, 2018.

Liu, W. T. and Xie, X.: Space Observation of Carbon Dioxide Partial Pressure at Ocean Surface, IEEE J. Sel. Top. Appl. Earth Obs. Remote Sens., 10, 5472–5484, https://doi.org/10.1109/JSTARS.2017.2766138, 2017.

Liutti, C. C., Kerr, R., Monteiro, T., Orselli, I. B. M., Ito, R. G., and Garcia, C. A. E.: Sea surface CO_2 fugacity in the southwestern South Atlantic Ocean: An evaluation based on satellite-derived images, Mar. Chem., 236, 104020, https://doi.org/10.1016/j.marchem.2021.104020, 2021.

Lobanova, P., Tilstone, G. H., Bashmachnikov, I., and Brotas, V.: Accuracy assessment of primary production models with and without photoinhibition using Ocean-Colour climate change initiative data in the North East Atlantic Ocean, Remote Sens., 10, 1–24, https://doi.org/10.3390/rs10071116, 2018.

Longhurst, A.: Ecological geography of the sea, Academic Press, San Diego, 1998.

Longhurst, A., Sathyendranath, S., Platt, T., and Caverhill, C.: An estimate of global primary production in the ocean from satellite radiometer data, J. Plankton Res., 17, 1245–1271, https://doi.org/10.1093/plankt/17.6.1245, 1995.

Lovecchio, E., Gruber, N., Münnich, M., and Frenger, I.: On the Processes Sustaining Biological Production in the Offshore Propagating Eddies of the Northern Canary Upwelling System, J. Geophys. Res. Ocean., 127, 1–28, https://doi.org/10.1029/2021JC017691, 2022.

Luz, B. and Barkan, E.: Assessment of Oceanic Productivity with the Triple-Isotope Composition of Dissolved Oxygen, Science (80-.)., 288, 2028–2031, https://doi.org/10.1126/science.288.5473.2028, 2000.

Mann, H. B.: Nonparametric Tests Against Trend, 13, 245, https://doi.org/10.2307/1907187, 1945.

Marañón, E., Behrenfeld, M. J., González, N., Mouriño, B., and Zubkov, M. V.: High variability of primary production in oligotrophic waters of the Atlantic Ocean: Uncoupling from phytoplankton biomass and size structure, Mar. Ecol. Prog. Ser., 257, 1–11, https://doi.org/10.3354/meps257001, 2003.

Marañón, E., Lorenzo, M. P., Cermeño, P., and Mouriño-Carballido, B.: Nutrient limitation suppresses the temperature dependence of phytoplankton metabolic rates, ISME J., 12, 1836–1845, https://doi.org/10.1038/s41396-018-0105-1, 2018.

Maritorena, S., Siegel, D. A., and Peterson, A. R.: Optimization of a semianalytical ocean color model for global-scale applications, Appl. Opt., 41, 2705, https://doi.org/10.1364/AO.41.002705, 2002.

Maritorena, S., d'Andon, O. H. F., Mangin, A., and Siegel, D. A.: Merged satellite ocean color data products using a bio-optical model: Characteristics, benefits and issues, Remote Sens. Environ., 114, 1791–1804, https://doi.org/10.1016/j.rse.2010.04.002, 2010.

Martínez-Moreno, J., Hogg, A. M. C., England, M. H., Constantinou, N. C., Kiss, A. E., and Morrison, A. K.: Global changes in oceanic mesoscale currents over the satellite altimetry record, Nat. Clim. Chang., 11, 397–403, https://doi.org/10.1038/s41558-021-01006-9, 2021.

Mason, E., Pascual, A., and C., M. J.: A New Sea Surface Height – Based Code for Oceanic Mesoscale Eddy Tracking, J. Atmos. Ocean. Technol., 31, 1181–1188, https://doi.org/10.1175/JTECH-D-14-00019.1, 2014.

Mason, E., Pascual, A., Gaube, P., Ruiz, S., Pelegrí, J. L., and Delepoulle, A.: Subregional characterization of mesoscale eddies across the Brazil-Malvinas Confluence, J. Geophys. Res. Ocean., 122, 3329–3357, https://doi.org/10.1002/2016JC012611, 2017.

McGillicuddy, D. J.: Mechanisms of Physical-Biological-Biogeochemical Interaction at the Oceanic Mesoscale, Ann. Rev. Mar. Sci., 8, 125–159, https://doi.org/10.1146/annurev-marine-010814-015606, 2016.

Mcgillis, W. R. and Wanninkhof, R.: Aqueous CO_2 gradients for air – sea flux estimates, Mar. Chem., 98, 100–108, https://doi.org/10.1016/j.marchem.2005.09.003, 2006.

McKinna, L. I. W., Cetinić, I., and Werdell, P. J.: Development and Validation of an Empirical Ocean Color Algorithm with Uncertainties: A Case Study with the Particulate Backscattering Coefficient, J. Geophys. Res. Ocean., 126, https://doi.org/10.1029/2021JC017231, 2021.

Meister, G. and Franz, B. A.: Corrections to the MODIS aqua calibration derived from MODIS aqua ocean color products, IEEE Trans. Geosci. Remote Sens.,

52, 6534–6541, https://doi.org/10.1109/TGRS.2013.2297233, 2014.

Morel, A.: Light and marine photosynthesis: a spectral model with geochemical and climatological implications, Prog. Oceanogr., 26, 263–306, https://doi.org/10.1016/0079-6611(91)90004-6, 1991.

Morel, A. and Prieur, L.: Analysis of variations in ocean color, Limnol. Oceanogr., 22, 709–722, https://doi.org/10.4319/lo.1977.22.4.0709, 1977.

Morel, A., Antoine, D., Babin, M., and Dandonneau, Y.: Measured and modeled primary production in the northeast Atlantic (EUMELI JGOFS program): The impact of natural variations in photosynthetic parameters on model predictive skill, Deep. Res. Part I Oceanogr. Res. Pap., https://doi.org/10.1016/0967-0637(96)00059-3, 1996.

Morel, A., Huot, Y., Gentili, B., Werdell, P. J., Hooker, S. B., and Franz, B. A.: Examining the consistency of products derived from various ocean color sensors in open ocean (Case 1) waters in the perspective of a multi-sensor approach, Remote Sens. Environ., 111, 69–88, https://doi.org/10.1016/j.rse.2007.03.012, 2007.

Moussa, H., Benallal, M. A., Goyet, C., and Lefèvre, N.: Satellite-derived CO_2 fugacity in surface seawater of the tropical Atlantic Ocean using a feedforward neural network, Int. J. Remote Sens., 37, 580–598, https://doi.org/10.1080/01431161.2015.1131872, 2016.

MODIS-A Reprocessing R2018: https://oceancolor.gsfc.nasa.gov/reprocessing/r2018/aqua/, last access: 29 April 2020.

NASA OBPG: MODIS Aqua Level 3 SST Thermal IR Daily 4km Daytime v2014.0, NASA Phys. Oceanogr. DAAC [data set], https://doi.org/10.5067/MODSA-1D4D4, 2015.

NASA OBPG: MODIS-Aqua Level 3 Mapped Photosynthetically Available Radiation Data Version R2018.0, NASA Ocean Biol. DAAC [data set], https://doi.org/10.5067/AQUA/MODIS/L3M/PAR/2018, 2017.

Nencioli, F., Dall'Olmo, G., and Quartly, G. D.: Agulhas Ring Transport Efficiency From Combined Satellite Altimetry and Argo Profiles, J. Geophys. Res. Ocean., 123, 5874–5888, https://doi.org/10.1029/2018JC013909, 2018.

Nightingale, P. D., Malin, G., Law, C. S., Watson, A. J., Liss, P. S., Liddicoat, M. I., Boutin, J., and Upstill-Goddard, R. C.: In situ evaluation of air-sea gas exchange parameterizations using novel conservative and volatile tracers, Global Biogeochem. Cycles, 14, 373–387, https://doi.org/10.1029/1999GB900091, 2000.

O'Reilly, J. E. and Werdell, P. J.: Chlorophyll algorithms for ocean color sensors - OC4, OC5 & OC6, Remote Sens. Environ., 229, 32–47, https://doi.org/10.1016/j.rse.2019.04.021, 2019.

O'Reilly, J. E., Maritorena, S., Mitchell, B. G., Siegel, D. A., Carder, K. L., Garver, S. A., Kahru, M., and Mcclain, C.: Ocean color chlorophyll algorithms for SeaWiFS encompassing chlorophyll concentrations between, J. Geophys.

Res., 103, 24937–24953, 1998.

Olsen, A., Triñanes, J. A., and Wanninkhof, R.: Sea-air flux of CO_2 in the Caribbean Sea estimated using in situ and remote sensing data, Remote Sens. Environ., 89, 309–325, https://doi.org/10.1016/j.rse.2003.10.011, 2004.

Ono, T., Saino, T., Kurita, N., and Sasaki, K.: Basin-scale extrapolation of shipboard pCO_2 data by using satellite SST and Chla, Int. J. Remote Sens., 25, 3803–3815, https://doi.org/10.1080/01431160310001657515, 2004.

Organelli, E. and Claustre, H.: Small Phytoplankton Shapes Colored Dissolved Organic Matter Dynamics in the North Atlantic Subtropical Gyre, Geophys. Res. Lett., 46, 12183–12191, https://doi.org/10.1029/2019GL084699, 2019.

Orr, J. C., Epitalon, J.-M., Dickson, A. G., and Gattuso, J.-P.: Routine uncertainty propagation for the marine carbon dioxide system, Mar. Chem., 207, 84–107, https://doi.org/10.1016/j.marchem.2018.10.006, 2018.

Orselli, I. B. M., Goyet, C., Kerr, R., de Azevedo, J. L. L., Araujo, M., Galdino, F., Touratier, F., and Garcia, C. A. E.: The effect of Agulhas eddies on absorption and transport of anthropogenic carbon in the South Atlantic Ocean, 7, 1–25, https://doi.org/10.3390/CLI7060084, 2019a.

Orselli, I. B. M., Kerr, R., Azevedo, J. L. L. d., Galdino, F., Araujo, M., and Garcia, C. A. E.: The sea-air CO_2 net fluxes in the South Atlantic Ocean and the role played by Agulhas eddies, Prog. Oceanogr., 170, 40–52, https://doi.org/10.1016/j.pocean.2018.10.006, 2019b.

Parard, G., Lefévre, N., and Boutin, J.: Sea water fugacity of CO_2 at the PIRATA mooring at 6°S, 10°W, Tellus, Ser. B Chem. Phys. Meteorol., 62, 636–648, https://doi.org/10.1111/j.1600-0889.2010.00503.x, 2010.

Pegliasco, C., Delepoulle, A., and Faugere, Y.: Mesoscale Eddy Trajectories Atlas Delayed-Time all satellites: version META3.1exp DT allsat, Avis. [dataset], https://doi.org/10.24400/527896/a01-2021.001, 2021.

Pegliasco, C., Delepoulle, A., Mason, E., Morrow, R., Faugère, Y., and Dibarboure, G.: META3.1exp: a new global mesoscale eddy trajectory atlas derived from altimetry, Earth Syst. Sci. Data, 14, 1087–1107, https://doi.org/10.5194/essd-14-1087-2022, 2022.

Peylin, P., Law, R. M., Gurney, K. R., Chevallier, F., Jacobson, A. R., Maki, T., Niwa, Y., Patra, P. K., Peters, W., Rayner, P. J., Rödenbeck, C., Van Der Laan-Luijkx, I. T., and Zhang, X.: Global atmospheric carbon budget: Results from an ensemble of atmospheric CO_2 inversions, 10, 6699–6720, https://doi.org/10.5194/bg-10-6699-2013, 2013.

Pezzi, L. P., de Souza, R. B., Santini, M. F., Miller, A. J., Carvalho, J. T., Parise, C. K., Quadro, M. F., Rosa, E. B., Justino, F., Sutil, U. A., Cabrera, M. J., Babanin, A. V., Voermans, J., Nascimento, E. L., Alves, R. C. M., Munchow, G. B., and Rubert, J.: Oceanic eddy-induced modifications to air–sea heat and CO_2 fluxes in the Brazil-Malvinas Confluence, Sci. Rep., 11, 10648, https://doi.org/10.1038/s41598-021-89985-9, 2021.

Pezzulli, S., Stephenson, D. B., and Hannachi, A.: The variability of seasonality,

J. Clim., 18, 71–88, https://doi.org/10.1175/JCLI-3256.1, 2005.

Pfeil, B., Olsen, A., Bakker, D. C. E., Hankin, S., Koyuk, H., Kozyr, A., Malczyk, J., Manke, A., Metzl, N., Sabine, C. L., Akl, J., Alin, S. R., Bates, N., Bellerby, R. G. J., Borges, A., Boutin, J., Brown, P. J., Cai, W. J., Chavez, F. P., Chen, A., Cosca, C., Fassbender, A. J., Feely, R. A., González-Dávila, M., Goyet, C., Hales, B., Hardman-Mountford, N., Heinze, C., Hood, M., Hoppema, M., Hunt, C. W., Hydes, D., Ishii, M., Johannessen, T., Jones, S. D., Key, R. M., Körtzinger, A., Landschützer, P., Lauvset, S. K., Lefèvre, N., Lenton, A., Lourantou, A., Merlivat, L., Midorikawa, T., Mintrop, L., Miyazaki, C., Murata, A., Nakadate, A., Nakano, Y., Nakaoka, S., Nojiri, Y., Omar, A. M., Padin, X. A., Park, G. H., Paterson, K., Perez, F. F., Pierrot, D., Poisson, A., Ríos, A. F., Santana-Casiano, J. M., Salisbury, J., Sarma, V. V. S. S., Schlitzer, R., Schneider, B., Schuster, U., Sieger, R., Skjelvan, I., Steinhoff, T., Suzuki, T., Takahashi, T., Tedesco, K., Telszewski, M., Thomas, H., Tilbrook, B., Tjiputra, J., Vandemark, D., Veness, T., Wanninkhof, R., Watson, A. J., Weiss, R., Wong, C. S., and Yoshikawa-Inoue, H.: A uniform, quality controlled Surface Ocean CO_2 Atlas (SOCAT), Earth Syst. Sci. Data, 5, 125–143, https://doi.org/10.5194/essd-5-125-2013, 2013.

Platt, T. and Sathyendranath, S.: Oceanic Primary Production: Estimation by Remote Sensing at Local and Regional Scales, Science (80-.)., 241, 1613–1620, https://doi.org/10.1126/science.241.4873.1613, 1988.

Platt, T., Caverhill, C., and Sathyendranath, S.: Basin-scale estimates of oceanic primary production by remote sensing: The North Atlantic, J. Geophys. Res. Ocean., 96, 15147–15159, https://doi.org/10.1029/91JC01118, 1991.

Pope, R. M. and Fry, E. S.: Absorption spectrum (380–700 nm) of pure water. II. Integrating cavity measurements, Appl. Opt., 36, 8710, https://doi.org/10.1364/AO.36.008710, 1997.

Poulton, A. J., Holligan, P. M., Hickman, A., Kim, Y. N., Adey, T. R., Stinchcombe, M. C., Holeton, C., Root, S., and Woodward, E. M. S.: Phytoplankton carbon fixation, chlorophyll-biomass and diagnostic pigments in the Atlantic Ocean, Deep. Res. Part II Top. Stud. Oceanogr., 53, 1593–1610, https://doi.org/10.1016/j.dsr2.2006.05.007, 2006.

Radenac, M. H., Jouanno, J., Carine Tchamabi, C., Awo, M., Bourlès, B., Arnault, S., and Aumont, O.: Physical drivers of the nitrate seasonal variability in the Atlantic cold tongue, 17, 529–545, https://doi.org/10.5194/bg-17-529-2020, 2020.

Raven, J., Caldeira, K., Elderfield, H., Hoegh-Guldberg, O., Liss, P., Riebesell, U., Shepherd, J., Turley, C., and Watson, A.: Ocean acidification due to increasing atmospheric carbon dioxide, The Royal Society, London, 68 pp., 2005.

Reboita, M. S., Ambrizzi, T., Silva, B. A., Pinheiro, R. F., and da Rocha, R. P.: The south atlantic subtropical anticyclone: Present and future climate, Front. Earth Sci., 7, 1–15, https://doi.org/10.3389/feart.2019.00008, 2019.

Reed, R. K.: On Estimating Insolation over the Ocean, J. Phys. Oceanogr., 7,

482–485, https://doi.org/10.1175/1520-0485(1977)007<0482:OEIOTO>2.0.CO;2, 1977.

Regaudie-De-Gioux, A. and Duarte, C. M.: Temperature dependence of planktonic metabolism in the ocean, Global Biogeochem. Cycles, 26, 1–10, https://doi.org/10.1029/2010GB003907, 2012.

Reverdin, G., Weiss, R. F., and Jenkins, W. J.: Ventilation of the Atlantic Ocean equatorial thermocline, J. Geophys. Res., 98, 16289, https://doi.org/10.1029/93JC00976, 1993.

Reynolds, R. W., Rayner, N. A., Smith, T. M., Stokes, D. C., and Wang, W.: An improved in situ and satellite SST analysis for climate, J. Clim., 15, 1609–1625, https://doi.org/10.1175/1520-0442(2002)015<1609:AIISAS>2.0.CO;2, 2002.

Robinson, C. and Williams, P. J. le B.: Respiration and its measurement in surface marine waters, in: Respiration in Aquatic Ecosystems, Oxford University Press, 147–180, https://doi.org/10.1093/acprof:oso/9780198527084.003.0009, 2005.

Robinson, C., Widdicombe, C. E., Zubkov, M. V., Tarran, G. A., Miller, A. E. J., and Rees, A. P.: Plankton community respiration during a coccolithophore bloom, Deep. Res. Part II Top. Stud. Oceanogr., 49, 2929–2950, https://doi.org/10.1016/S0967-0645(02)00064-4, 2002a.

Robinson, C., Serret, P., Tilstone, G., Teira, E., Zubkov, M. V, Rees, A. P., and Woodward, E. M. S.: Plankton respiration in the Eastern Atlantic Ocean, Deep Sea Res. Part I Oceanogr. Res. Pap., 49, 787–813, https://doi.org/10.1016/S0967-0637(01)00083-8, 2002b.

Rodenbeck, C., Keeling, R. F., Bakker, D. C. E., Metzl, N., Olsen, A., Sabine, C., and Heimann, M.: Global surface-ocean pCO_2 and sea – air CO_2 flux variability from an observation-driven ocean mixed-layer scheme, Ocean Sci., 9, 193–216, https://doi.org/10.5194/os-9-193-2013, 2013.

Rödenbeck, C., Bakker, D. C. E., Gruber, N., Iida, Y., Jacobson, A. R., Jones, S., Landschützer, P., Metzl, N., Nakaoka, S., Olsen, A., Park, G.-H., Peylin, P., Rodgers, K. B., Sasse, T. P., Schuster, U., Shutler, J. D., Valsala, V., Wanninkhof, R., and Zeng, J.: Data-based estimates of the ocean carbon sink variability – first results of the Surface Ocean pCO_2 Mapping intercomparison (SOCOM), 12, 7251–7278, https://doi.org/10.5194/bg-12-7251-2015, 2015.

Rodrigues, R. R., Campos, E. J. D., and Haarsma, R.: The impact of ENSO on the south Atlantic subtropical dipole mode, J. Clim., 28, 2691–2705, https://doi.org/10.1175/JCLI-D-14-00483.1, 2015.

Roemmich, D., Alford, M. H., Claustre, H., Johnson, K. S., King, B., Moum, J., Oke, P. R., Owens, W. B., Pouliquen, S., Purkey, S., Scanderbeg, M., Suga, T., Wijffels, S. E., Zilberman, N., Bakker, D., Baringer, M. O., Belbeoch, M., Bittig, H. C., Boss, E., Calil, P., Carse, F., Carval, T., Chai, F., Conchubhair, D. O., D'Ortenzio, F., Dall'Olmo, G., Desbruyères, D., Fennel, K., Fer, I., Ferrari, R., Forget, G., Freeland, H., Fujiki, T., Gehlen, M., Greenan, B., Hallberg, R., Hibiya, T., Hosoda, S., Jayne, S., Jochum, M., Johnson, G. C., Kang, K. R., Kolodziejczyk, N., Koertzinger, A., Le Traon, P. Y., Lenn, Y. D., Maze, G., Mork,

K. A., Morris, T., Nagai, T., Nash, J., Garabato, A. N., Olsen, A., Pattabhi, R. R., Prakash, S., Riser, S., Schmechtig, C., Shroyer, E., Sterl, A., Sutton, P., Talley, L., Tanhua, T., Thierry, V., Thomalla, S., Toole, J., Troisi, A., Trull, T., Turton, J. D., Velez-Belchi, P. J., Walczowski, W., Wang, H., Wanninkhof, R., Waterhouse, A., Watson, A., Wilson, C., Wong, A. P., Xu, J., and Yasuda, I.: On the future of Argo: A global, full-depth, multi-disciplinary array, Front. Mar. Sci., 6, 1–28, https://doi.org/10.3389/fmars.2019.00439, 2019.

Rouault, M., Pohl, B., and Penven, P.: Coastal oceanic climate change and variability from 1982 to 2009 around South Africa, African J. Mar. Sci., 32, 237–246, https://doi.org/10.2989/1814232x.2010.501563, 2010.

Roughan, M., Keating, S. R., Schaeffer, A., Cetina Heredia, P., Rocha, C., Griffin, D., Robertson, R., and Suthers, I. M.: A tale of two eddies: The biophysical characteristics of two contrasting cyclonic eddies in the East Australian Current System, J. Geophys. Res. Ocean., 122, 2494–2518, https://doi.org/10.1002/2016JC012241, 2017.

Rubio, A., Blanke, B., Speich, S., Grima, N., and Roy, C.: Mesoscale eddy activity in the southern Benguela upwelling system from satellite altimetry and model data, Prog. Oceanogr., 83, 288–295, https://doi.org/10.1016/j.pocean.2009.07.029, 2009.

Saba, V. S., Friedrichs, M. A. M., Carr, M. E., Antoine, D., Armstrong, R. A., Asanuma, I., Aumont, O., Bates, N. R., Behrenfeld, M. J., Bennington, V., Bopp, L., Bruggeman, J., Buitenhuis, E. T., Church, M. J., Ciotti, A. M., Doney, S. C., Dowell, M., Dunne, J., Dutkiewicz, S., Gregg, W., Hoepffner, N., Hyde, K. J. W., Ishizaka, J., Kameda, T., Karl, D. M., Lima, I., Lomas, M. W., Marra, J., McKinley, G. A., Melin, F., Moore, J. K., Morel, A., O'Reilly, J., Salihoglu, B., Scardi, M., Smyth, T. J., Tang, S., Tjiputra, J., Uitz, J., Vichi, M., Waters, K., Westberry, T. K., and Yool, A.: Challenges of modeling depth-integrated marine primary productivity over multiple decades: A case study at BATS and HOT, Global Biogeochem. Cycles, 24, 1–21, https://doi.org/10.1029/2009GB003655, 2010.

Saba, V. S., Friedrichs, M. A. M., Antoine, D., Armstrong, R. A., Asanuma, I., Behrenfeld, M. J., Ciotti, A. M., Dowell, M., Hoepffner, N., Hyde, K. J. W., Ishizaka, J., Kameda, T., Marra, J., Mélin, F., Morel, A., O'reilly, J., Scardi, M., Smith, W. O., Smyth, T. J., Tang, S., Uitz, J., Waters, K., and Westberry, T. K.: An evaluation of ocean color model estimates of marine primary productivity in coastal and pelagic regions across the globe, 8, 489–503, https://doi.org/10.5194/bg-8-489-2011, 2011.

Sabine, C. L., Hankin, S., Koyuk, H., Bakker, D. C. E., Pfeil, B., Olsen, A., Metzl, N., Kozyr, A., Fassbender, A., Manke, A., Malczyk, J., Akl, J., Alin, S. R., Bellerby, R. G. J., Borges, A., Boutin, J., Brown, P. J., Cai, W. J., Chavez, F. P., Chen, A., Cosca, C., Feely, R. A., González-Dávila, M., Goyet, C., Hardman-Mountford, N., Heinze, C., Hoppema, M., Hunt, C. W., Hydes, D., Ishii, M., Johannessen, T., Key, R. M., Körtzinger, A., Landschützer, P., Lauvset, S. K., Lefèvre, N., Lenton, A., Lourantou, A., Merlivat, L., Midorikawa, T., Mintrop, L., Miyazaki, C., Murata, A., Nakadate, A., Nakano, Y., Nakaoka, S., Nojiri, Y., Omar, A. M., Padin, X. A., Park, G. H., Paterson, K., Perez, F. F., Pierrot, D.,

Poisson, A., Ríos, A. F., Salisbury, J., Santana-Casiano, J. M., S. Sarma, V. V. S., Schlitzer, R., Schneider, B., Schuster, U., Sieger, R., Skjelvan, I., Steinhoff, T., Suzuki, T., Takahashi, T., Tedesco, K., Telszewski, M., Thomas, H., Tilbrook, B., Vandemark, D., Veness, T., Watson, A. J., Weiss, R., Wong, C. S., and Yoshikawa-Inoue, H.: Surface Ocean CO_2 Atlas (SOCAT) gridded data products, Earth Syst. Sci. Data, 5, 145–153, https://doi.org/10.5194/essd-5-145-2013, 2013.

Santana-Casiano, J. M., González-Dávila, M., and Ucha, I. R.: Carbon dioxide fluxes in the Benguela upwelling system during winter and spring: A comparison between 2005 and 2006, Deep Sea Res. Part II Top. Stud. Oceanogr., 56, 533–541, https://doi.org/10.1016/j.dsr2.2008.12.010, 2009.

Sarkar, A., Mishra, R., Bhaskar, P. V., Anilkumar, N., Sabu, P., and Soares, M.: Potential Role of Major Phytoplankton Communities on pCO2 Modulation in the Indian Sector of Southern Ocean, 37, 531–548, https://doi.org/10.1007/s41208-021-00323-2, 2021.

Sarma, V. V. S. S., Sampath Kumar, G., Yadav, K., Dalabehera, H. B., Rao, D. N., Behera, S., and Loganathan, J.: Impact of eddies on dissolved inorganic carbon components in the Bay of Bengal, Deep Sea Res. Part I Oceanogr. Res. Pap., 147, 111–120, https://doi.org/10.1016/j.dsr.2019.04.005, 2019.

Sarmiento, J. L. and Gruber, N.: Ocean Biogeochemical Dynamics, 2004.

Sathyendranath, S., Platt, T., Caverhill, C. M., Warnock, R. E., and Lewis, M. R.: Remote sensing of oceanic primary production: computations using a spectral model, Deep Sea Res. Part A, Oceanogr. Res. Pap., 36, 431–453, https://doi.org/10.1016/0198-0149(89)90046-0, 1989.

Sathyendranath, S., Longhurst, A., Caverhill, C. M., and Platt, T.: Regionally and seasonally differentiated primary production in the North Atlantic, Deep. Res. Part I, 42, 1773–1802, https://doi.org/10.1016/0967-0637(95)00059-F, 1995.

Sathyendranath, S., Brewin, R. J. W., Brockmann, C., Brotas, V., Calton, B., Chuprin, A., Cipollini, P., Couto, A. B., Dingle, J., Doerffer, R., Donlon, C., Dowell, M., Farman, A., Grant, M., Groom, S., Horseman, A., Jackson, T., Krasemann, H., Lavender, S., Martinez-Vicente, V., Mazeran, C., Mélin, F., Moore, T. S., Müller, D., Regner, P., Roy, S., Steele, C. J., Steinmetz, F., Swinton, J., Taberner, M., Thompson, A., Valente, A., Zühlke, M., Brando, V. E., Feng, H., Feldman, G., Franz, B. A., Frouin, R., Gould, R. W., Hooker, S. B., Kahru, M., Kratzer, S., Mitchell, B. G., Muller-Karger, F. E., Sosik, H. M., Voss, K. J., Werdell, J., and Platt, T.: An ocean-colour time series for use in climate studies: The experience of the ocean-colour climate change initiative (OC-CCI), 19, https://doi.org/10.3390/s19194285, 2019.

Sathyendranath, S., Platt, T., Kovač, Ž., Dingle, J., Jackson, T., Brewin, R. J. W., Franks, P., Marañón, E., Kulk, G., and Bouman, H. A.: Reconciling models of primary production and photoacclimation [Invited], Appl. Opt., 59, C100, https://doi.org/10.1364/AO.386252, 2020.

Schloss, I. R., Ferreyra, G. A., Ferrario, M. E., Almandoz, G. O., Codina, R.,

Bianchi, A. A., Balestrini, C. F., Ochoa, H. A., Pino, D. R., and Poisson, A.: Role of plankton communities in sea-air variations in pCO_2 in the SW Atlantic Ocean, Mar. Ecol. Prog. Ser., 332, 93–106, https://doi.org/10.3354/meps332093, 2007.

Sen, P. K.: Estimates of the Regression Coefficient Based on Kendall's Tau, J. Am. Stat. Assoc., 63, 1379–1389, https://doi.org/10.1080/01621459.1968.10480934, 1968.

Serret, P., Fernández, E., Sostres, J., and Anadón, R.: Seasonal compensation of microbial production and respiration in a temperate sea, Mar. Ecol. Prog. Ser., 187, 43–57, https://doi.org/10.3354/meps187043, 1999.

Serret, P., Fernandez, E., and Robinson, C.: Biogeographic Differences in the Net Ecosystem Metabolism of the Open Ocean, Ecology, 83, 3225, https://doi.org/10.2307/3071855, 2002.

Serret, P., Robinson, C., Fernández, E., Teira, E., Tilstone, G., and Pérez, V.: Predicting plankton net community production in the Atlantic Ocean, Deep. Res. Part II Top. Stud. Oceanogr., 56, 941–953, https://doi.org/10.1016/j.dsr2.2008.10.006, 2009.

Serret, P., Robinson, C., Aranguren-Gassis, M., García-Martín, E. E., Gist, N., Kitidis, V., Lozano, J., Stephens, J., Harris, C., and Thomas, R.: Both respiration and photosynthesis determine the scaling of plankton metabolism in the oligotrophic ocean, Nat. Commun., 6, 1–10, https://doi.org/10.1038/ncomms7961, 2015.

Sharp, J. D., Pierrot, D., Humphreys, M. P., Epitalon, J.-M., Orr, J. C., Lewis, E. R., and Wallace, D. W. R.: CO2SYSv3 for MATLAB, https://doi.org/10.5281/ZENODO.4774718, 2021.

Shiskin, J., Young, A. J., and Musgrave, J. C.: The X-11 variant of the Census Method II Seasonal Adjustment Program, US Dept of Commerce, 68 pp., 1967.

Shutler, J. D., Land, P. E., Piolle, J. F., Woolf, D. K., Goddijn-Murphy, L., Paul, F., Girard-Ardhuin, F., Chapron, B., and Donlon, C. J.: FluxEngine: A flexible processing system for calculating atmosphere-ocean carbon dioxide gas fluxes and climatologies, J. Atmos. Ocean. Technol., 33, 741–756, https://doi.org/10.1175/JTECH-D-14-00204.1, 2016.

Shutler, J. D., Wanninkhof, R., Nightingale, P. D., Woolf, D. K., Bakker, D. C., Watson, A., Ashton, I., Holding, T., Chapron, B., Quilfen, Y., Fairall, C., Schuster, U., Nakajima, M., and Donlon, C. J.: Satellites will address critical science priorities for quantifying ocean carbon, Front. Ecol. Environ., 18, 27–35, https://doi.org/10.1002/fee.2129, 2020.

Slade, W. H., Boss, E., Dall'olmo, G., Langner, M. R., Loftin, J., Behrenfeld, M. J., Roesler, C., and Westberry, T. K.: Underway and moored methods for improving accuracy in measurement of spectral particulate absorption and attenuation, J. Atmos. Ocean. Technol., https://doi.org/10.1175/2010JTECHO755.1, 2010.

Smith, W. O. and Demaster, D. J.: Phytoplankton biomass and productivity in the Amazon River plume: Correlation with seasonal river discharge, Cont. Shelf

Res., 16, 291–319, https://doi.org/10.1016/0278-4343(95)00007-N, 1996.

Smyth, T. J., Tilstone, G. H., and Groom, S. B.: Integration of radiative transfer into satellite models of ocean primary production, J. Geophys. Res. C Ocean., 110, 1–11, https://doi.org/10.1029/2004JC002784, 2005.

Song, H., Marshall, J., Munro, D. R., Dutkiewicz, S., Sweeney, C., McGillicuddy, D. J., and Hausmann, U.: Mesoscale modulation of air-sea CO_2 flux in Drake Passage, J. Geophys. Res. Ocean., 121, 6635–6649, https://doi.org/10.1002/2016JC011714, 2016.

Souza, R., Pezzi, L., Swart, S., Oliveira, F., and Santini, M.: Air-sea interactions over eddies in the Brazil-malvinas confluence, Remote Sens., 13, https://doi.org/10.3390/rs13071335, 2021.

Stephens, M. P., Samuels, G., Olson, D. B., Fine, R. A., and Takahashi, T.: Sea-air flux of CO_2 in the North Pacific using shipboard and satellite data, J. Geophys. Res., 100, 13571, https://doi.org/10.1029/95JC00901, 1995.

Szeto, M., Werdell, P. J., Moore, T. S., and Campbell, J. W.: Are the world's oceans optically different?, J. Geophys. Res. Ocean., 116, 1–14, https://doi.org/10.1029/2011JC007230, 2011.

Takahashi, T., Feely, R. A., Weiss, R. F., Wanninkhof, R. H., Chipman, D. W., Sutherland, S. C., and Takahashi, T. T.: Global air-sea flux of CO_2: An estimate based on measurements of sea-air pCO2 difference, Proc. Natl. Acad. Sci. U. S. A., 94, 8292–8299, https://doi.org/10.1073/pnas.94.16.8292, 1997.

Takahashi, T., Wanninkhof, W. H., Feely, R. A., Weiss, R. F., Chipman, D. W., Bates, N. R., Olafsson, J., Sabine, C. L., and Sutherland, S. G.: Net sea-air CO_2 flux over the global oceans: An improved estimate based on the sea-air pCO_2 difference, 1999.

Takahashi, T., Sutherland, S. C., Sweeney, C., Poisson, A., Metzl, N., Tilbrook, B., Bates, N., Wanninkhof, R., Feely, R. A., Sabine, C., Olafsson, J., and Nojiri, Y.: Global sea–air CO_2 flux based on climatological surface ocean pCO_2, and seasonal biological and temperature effects, Deep Sea Res. Part II Top. Stud. Oceanogr., 49, 1601–1622, https://doi.org/10.1016/S0967-0645(02)00003-6, 2002.

Takahashi, T., Sutherland, S. C., Wanninkhof, R., Sweeney, C., Feely, R. A., Chipman, D. W., Hales, B., Friederich, G., Chavez, F., Sabine, C., Watson, A., Bakker, D. C. E., Schuster, U., Metzl, N., Yoshikawa-Inoue, H., Ishii, M., Midorikawa, T., Nojiri, Y., Körtzinger, A., Steinhoff, T., Hoppema, M., Olafsson, J., Arnarson, T. S., Tilbrook, B., Johannessen, T., Olsen, A., Bellerby, R., Wong, C. S., Delille, B., Bates, N. R., and de Baar, H. J. W.: Climatological mean and decadal change in surface ocean pCO_2, and net sea-air CO_2 flux over the global oceans, Deep. Res. Part II Top. Stud. Oceanogr., 56, 554–577, https://doi.org/10.1016/j.dsr2.2008.12.009, 2009.

Takahashi, T., Sutherland, S. C., and Kozyr, A.: LDEO Database (Version 2019): Global Ocean Surface Water Partial Pressure of CO_2 Database: Measurements Performed During 1957-2019, NOAA Natl. Centers Environ. Inf. [dataset], https://doi.org/10.3334/cdiac/otg.ndp088(v2015), 2017.

Tans, P. P., Fung, I. Y., and Takahashi, T.: Observational constraints on the global atmospheric CO_2 budget, Science (80-.)., 247, 1431–1438, https://doi.org/10.1126/science.247.4949.1431, 1990.

Taylor, J. R.: An introduction to error analysis, University Science Books, Sausalito, Calif., 1997.

Telszewski, M., Chazottes, A., Schuster, U., Watson, A. J., Moulin, C., Bakker, D. C. E., González-Dávila, M., Johannessen, T., Körtzinger, A., Lüger, H., Olsen, A., Omar, A., Padin, X. A., Ríos, A. F., Steinhoff, T., Santana-Casiano, M., Wallace, D. W. R., and Wanninkhof, R.: Estimating the monthly pCO_2 distribution in the north Atlantic using a self-organizing neural network, 6, 1405–1421, https://doi.org/10.5194/bg-6-1405-2009, 2009.

Tilstone, G. H., Smyth, T. J., Gowen, R. J., Martinez-Vicente, V., and Groom, S. B.: Inherent optical properties of the Irish Sea and their effect on satellite primary production algorithms, J. Plankton Res., 27, 1127–1148, https://doi.org/10.1093/plankt/fbi075, 2005.

Tilstone, G. H., Smyth, T., Poulton, A., and Hutson, R.: Measured and remotely sensed estimates of primary production in the Atlantic Ocean from 1998 to 2005, Deep. Res. Part II Top. Stud. Oceanogr., 56, 918–930, https://doi.org/10.1016/j.dsr2.2008.10.034, 2009.

Tilstone, G. H., Angel-Benavides, I. M., Pradhan, Y., Shutler, J. D., Groom, S., and Sathyendranath, S.: An assessment of chlorophyll-a algorithms available for SeaWiFS in coastal and open areas of the Bay of Bengal and Arabian Sea, Remote Sens. Environ., 115, 2277–2291, https://doi.org/10.1016/j.rse.2011.04.028, 2011.

Tilstone, G. H., Taylor, B. H., Blondeau-Patissier, D., Powell, T., Groom, S. B., Rees, A. P., and Lucas, M. I.: Comparison of new and primary production models using SeaWiFS data in contrasting hydrographic zones of the northern North Atlantic, Remote Sens. Environ., 156, 473–489, https://doi.org/10.1016/j.rse.2014.10.013, 2015a.

Tilstone, G. H., Xie, Y. yuan, Robinson, C., Serret, P., Raitsos, D. E., Powell, T., Aranguren-Gassis, M., Garcia-Martin, E. E., and Kitidis, V.: Satellite estimates of net community production indicate predominance of net autotrophy in the Atlantic Ocean, Remote Sens. Environ., 164, 254–269, https://doi.org/10.1016/j.rse.2015.03.017, 2015b.

Tilstone, G. H., Lange, P. K., Misra, A., Brewin, R. J. W., and Cain, T.: Micro-phytoplankton photosynthesis, primary production and potential export production in the Atlantic Ocean, Prog. Oceanogr., 158, 109–129, https://doi.org/10.1016/j.pocean.2017.01.006, 2017.

Valente, A., Sathyendranath, S., Brotas, V., Groom, S., Grant, M., Taberner, M., Antoine, D., Arnone, R., Balch, W. M., Barker, K., Barlow, R., Belanger, S., Berthon, J. F., Besiktepe, S., Brando, V., Canuti, E., Chavez, F., Claustre, H., Crout, R., Frouin, R., Garcia-Soto, C., Gibb, S. W., Gould, R., Hooker, S., Kahru, M., Klein, H., Kratzer, S., Loisel, H., McKee, D., Mitchell, B. G., Moisan, T., Muller-Karger, F., O'Dowd, L., Ondrusek, M., Poulton, A. J., Repecaud, M.,

Smyth, T., Sosik, H. M., Twardowski, M., Voss, K., Werdell, J., Wernand, M., and Zibordi, G.: A compilation of global bio-optical in situ data for ocean-colour satellite applications, Earth Syst. Sci. Data, 8, 235–252, https://doi.org/10.5194/essd-8-235-2016, 2016.

Valente, A., Sathyendranath, S., Brotas, V., Groom, S., Grant, M., Taberner, M., Antoine, D., Arnone, R., Balch, W. M., Barker, K., Barlow, R., Bélanger, S., Berthon, J.-F., Beşiktepe, Ş., Borsheim, Y., Bracher, A., Brando, V., Canuti, E., Chavez, F., Cianca, A., Claustre, H., Clementson, L., Crout, R., Frouin, R., García-Soto, C., Gibb, S. W., Gould, R., Hooker, S. B., Kahru, M., Kampel, M., Klein, H., Kratzer, S., Kudela, R., Ledesma, J., Loisel, H., Matrai, P., McKee, D., Mitchell, B. G., Moisan, T., Muller-Karger, F., O'Dowd, L., Ondrusek, M., Platt, T., Poulton, A. J., Repecaud, M., Schroeder, T., Smyth, T., Smythe-Wright, D., Sosik, H. M., Twardowski, M., Vellucci, V., Voss, K., Werdell, J., Wernand, M., Wright, S., and Zibordi, G.: A compilation of global bio-optical in situ data for ocean-colour satellite applications – version two, Earth Syst. Sci. Data, 11, 1037–1068, https://doi.org/10.5194/essd-11-1037-2019, 2019.

Valerio, A. M., Kampel, M., Ward, N. D., Sawakuchi, H. O., Cunha, A. C., and Richey, J. E.: CO_2 partial pressure and fluxes in the Amazon River plume using in situ and remote sensing data, Cont. Shelf Res., 215, 104348, https://doi.org/10.1016/j.csr.2021.104348, 2021.

Varela, R., Álvarez, I., Santos, F., DeCastro, M., and Gómez-Gesteira, M.: Has upwelling strengthened along worldwide coasts over 1982-2010?, Sci. Rep., 5, 1–15, https://doi.org/10.1038/srep10016, 2015.

Varona, H. L., Veleda, D., Silva, M., Cintra, M., and Araujo, M.: Amazon River plume influence on Western Tropical Atlantic dynamic variability, Dyn. Atmos. Ocean., 85, 1–15, https://doi.org/10.1016/j.dynatmoce.2018.10.002, 2019.

Wanninkhof, R.: Relationship between wind speed and gas exchange over the ocean, J. Geophys. Res., 97, 7373, https://doi.org/10.1029/92JC00188, 1992.

Wanninkhof, R.: Relationship between wind speed and gas exchange over the ocean revisited, Limnol. Oceanogr. Methods, 12, 351–362, https://doi.org/10.4319/lom.2014.12.351, 2014.

Wanninkhof, R. and Triñanes, J.: The impact of changing wind speeds on gas transfer and its effect on global air-sea CO_2 fluxes, Global Biogeochem. Cycles, 31, 961–974, https://doi.org/10.1002/2016GB005592, 2017.

Wanninkhof, R., Park, G. H., Takahashi, T., Sweeney, C., Feely, R., Nojiri, Y., Gruber, N., Doney, S. C., McKinley, G. A., Lenton, A., Le Quere, C., Heinze, C., Schwinger, J., Graven, H., and Khatiwala, S.: Global ocean carbon uptake: Magnitude, variability and trends, 10, 1983–2000, https://doi.org/10.5194/bg-10-1983-2013, 2013.

Waters, J., Millero, F. J., and Woosley, R. J.: Corrigendum to "The free proton concentration scale for seawater pH", [MARCHE: 149 (2013) 8–22], Mar. Chem., 165, 66–67, https://doi.org/10.1016/j.marchem.2014.07.004, 2014.

Watson, A. J., Schuster, U., Shutler, J. D., Holding, T., Ashton, I. G. C., Landschützer, P., Woolf, D. K., and Goddijn-Murphy, L.: Interpolated Global

surface ocean carbon dioxide partial pressure and ocean-atmosphere fluxes 1992-2018, corrected for surface temperature deviations, https://doi.org/10.1594/PANGAEA.922985, 2020a.

Watson, A. J., Schuster, U., Shutler, J. D., Holding, T., Ashton, I. G. C., Landschützer, P., Woolf, D. K., and Goddijn-Murphy, L.: Revised estimates of ocean-atmosphere CO_2 flux are consistent with ocean carbon inventory, Nat. Commun., 11, 1–6, https://doi.org/10.1038/s41467-020-18203-3, 2020b.

Weiss, R. F.: Carbon dioxide in water and seawater: the solubility of a non-ideal gas, Mar. Chem., 2, 203–215, https://doi.org/10.1016/0304-4203(74)90015-2, 1974.

Welschmeyer, N. A.: Fluorometric analysis of chlorophyll a in the presence of chlorophyll b and pheopigments, Limnol. Oceanogr., 39, 1985–1992, https://doi.org/10.4319/lo.1994.39.8.1985, 1994.

Wentz, F. J., Scott, J., Hoffman, R., Leidner, M., Atlas, R., and Ardizzone, J.: Remote Sensing Systems Cross-Calibrated Multi-Platform (CCMP) 6-hourly ocean vector wind analysis product on 0.25 deg grid, Version 2.0, Remote Sens. Syst. St. Rosa, CA [dataset], Available online www.remss.com/measurements/ccmp. [Accessed 08-11-2021], 2015.

Werdell, P. J. and Bailey, S. W.: An improved in-situ bio-optical data set for ocean color algorithm development and satellite data product validation, Remote Sens. Environ., 98, 122–140, https://doi.org/10.1016/j.rse.2005.07.001, 2005.

Werdell, P. J., Franz, B. A., Bailey, S. W., Feldman, G. C., Boss, E., Brando, V. E., Dowell, M., Hirata, T., Lavender, S. J., Lee, Z. P., Loisel, H., Maritorena, S., Mélin, F., Moore, T. S., Smyth, T. J., Antoine, D., Devred, E., D'Andon, O. H. F., and Mangin, A.: Generalized ocean color inversion model for retrieving marine inherent optical properties, Appl. Opt., 52, 2019–2037, https://doi.org/10.1364/AO.52.002019, 2013.

Wilks, D. S.: On "field significance" and the false discovery rate, J. Appl. Meteorol. Climatol., 45, 1181–1189, https://doi.org/10.1175/JAM2404.1, 2006.

Williams, P. J. L. B.: The balance of plankton respiration and photosynthesis in the open oceans, Nature, 394, 55–57, https://doi.org/10.1038/27878, 1998.

Williams, P. J. le B., Quay, P. D., Westberry, T. K., and Behrenfeld, M. J.: The Oligotrophic Ocean Is Autotrophic, Ann. Rev. Mar. Sci., 5, 535–549, https://doi.org/10.1146/annurev-marine-121211-172335, 2013.

Wimmer, W. and Robinson, I. S.: The ISAR instrument uncertainty model, J. Atmos. Ocean. Technol., 33, 2415–2433, https://doi.org/10.1175/JTECH-D-16-0096.1, 2016.

Woolf, D. K.: Bubbles and their role in gas exchange, in: The Sea Surface and Global Change, Cambridge University Press, 173–206, https://doi.org/10.1017/CBO9780511525025.007, 1997.

Woolf, D. K.: Parametrization of gas transfer velocities and sea-state-dependent wave breaking, Tellus B, 57, 87–94, https://doi.org/10.1111/j.1600-

0889.2005.00139.x, 2005.

Woolf, D. K., Land, P. E., Shutler, J. D., Goddijn-Murphy, L. M., and Donlon, C. J.: On the calculation of air-sea fluxes of CO_2 in the presence of temperature and salinity gradients, J. Geophys. Res. Ocean., 121, 1229–1248, https://doi.org/10.1002/2015JC011427, 2016.

Woolf, D. K., Shutler, J. D., Goddijn-Murphy, L., Watson, A. J., Chapron, B., Nightingale, P. D., Donlon, C. J., Piskozub, J., Yelland, M. J., Ashton, I., Holding, T., Schuster, U., Girard-Ardhuin, F., Grouazel, A., Piolle, J. F., Warren, M., Wrobel-Niedzwiecka, I., Land, P. E., Torres, R., Prytherch, J., Moat, B., Hanafin, J., Ardhuin, F., and Paul, F.: Key Uncertainties in the Recent Air-Sea Flux of CO_2, Global Biogeochem. Cycles, 33, 1548–1563, https://doi.org/10.1029/2018GB006041, 2019.

Woosley, R. J., Millero, F. J., and Wanninkhof, R.: Rapid anthropogenic changes in CO_2 and pH in the Atlantic Ocean: 2003-2014, Global Biogeochem. Cycles, 30, 70–90, https://doi.org/10.1002/2015GB005248, 2016.

Xiong, X., Masuda, Y., Hashioka, T., Ono, T., and Yamanaka, Y.: Effect of seasonal change in gas transfer coefficient on air–sea CO_2 flux in the western North Pacific, J. Oceanogr., 71, 685–701, https://doi.org/10.1007/s10872-015-0313-5, 2015.

Xiu, P., Chai, F., Curchitser, E. N., and Castruccio, F. S.: Future changes in coastal upwelling ecosystems with global warming: The case of the California Current System, Sci. Rep., 8, 1–9, https://doi.org/10.1038/s41598-018-21247-7, 2018.

Young, I. R. and Ribal, A.: Multiplatform evaluation of global trends in wind speed and wave height, Science (80-.)., 364, 548–552, https://doi.org/10.1126/science.aav9527, 2019.

Yvon-Durocher, G., Caffrey, J. M., Cescatti, A., Dossena, M., Giorgio, P. del, Gasol, J. M., Montoya, J. M., Pumpanen, J., Staehr, P. A., Trimmer, M., Woodward, G., and Allen, A. P.: Reconciling the temperature dependence of respiration across timescales and ecosystem types, Nature, 487, 472–476, https://doi.org/10.1038/nature11205, 2012.

Zapata, M., Rodríguez, F., and Garrido, J.: Separation of chlorophylls and carotenoids from marine phytoplankton:a new HPLC method using a reversed phase C8 column and pyridine-containing mobile phases, Mar. Ecol. Prog. Ser., 195, 29–45, https://doi.org/10.3354/meps195029, 2000.

Zeng, J., Nojiri, Y., Landschützer, P., Telszewski, M., and Nakaoka, S.: A global surface ocean fCO_2 climatology based on a feed-forward neural network, J. Atmos. Ocean. Technol., 31, 1838–1849, https://doi.org/10.1175/JTECH-D-13-00137.1, 2014.

Zeng, J., Nojiri, Y., Nakaoka, S. ichiro, Nakajima, H., and Shirai, T.: Surface ocean CO_2 in 1990–2011 modelled using a feed-forward neural network, Geosci. Data J., 2, 47–51, https://doi.org/10.1002/gdj3.26, 2015.